The Pennsylvania State University
The Graduate School
College of Engineering

LOW POWER, SECURE AND ROBUST DESIGNS OF NON-VOLATILE MEMORIES

A Dissertation in
Computer Science and Engineering
by
Seyedhamidreza Motaman

© 2018 Seyedhamidreza Motaman

Submitted in Partial Fulfillment
of the Requirements
for the Degree of

Doctor of Philosophy

December 2018

The dissertation of Seyedhamidreza Motaman was reviewed and approved* by the following:

Swaroop Ghosh
Assistant Professor of EE
Dissertation Advisor and Chair of Committee

Mahmut Kandemir
Professor of EECS

Saptarshi Das
Assistant Professor of ESM

Mehdi Kiani
Assistant Professor of EECS

Chitaranjan Das
Head of the Department of CSE

*Signatures are on file in the Graduate School

Abstract

In the last few decades, computation power has been increasing, thanks to CMOS scaling, which in turn results in growing demand for high-density memories to meet the large bandwidth requirement. However, CMOS scaling is approaching the end of roadmap and it is experiencing significant challenges such as high power-density, process variation, high standby power, and reliability issues. In addition, the increasing demand for high performance computing (HPC) and integration of multiple cores on a single die have widened the speed gap between logic and memory, that is known as the "memory-wall". Process variability and standby power are posing severe obstruction towards SRAM/DRAM scaling to future nodes. On one hand, industry and academia began investigating alternative memory technologies, such as Spin-Torque Transfer RAM (STT-RAM), Domain Wall memory (DWM), Phase-Change RAM (PCRAM), Ferro-electric RAM (FeRAM), Resistive RAM (RRAM), and Magnetic RAM (MRAM). These emerging non-volatile memory technologies offer the speed of SRAM, the high density of DRAM, and the non-volatility of Flash memory. On the other hand, the speed gap between the processor and memory impedes the continuous performance improvement of the traditional von Neumann architecture. In order to address this challenge, extensive amount of research is performed to explore the alternative non-von Neumann architectures based on the concept of computing in memory.

Among these memories, spintronic memories (i.e. STTRAM, DWM) have proven to be potential alternatives to replace on-chip SRAM owing to their remarkable high density, zero standby power, high speed, high endurance and CMOS compatibility. Nevertheless, STTRAM suffers from crucial challenges such as high write energy, long write time and poor sense margin. Furthermore, it suffers from process variation induced write latency and write power degradation. Moreover, the sensitivity of magnets to ambient parameters and data persistence makes the spintronic memories vulnerable to tampering and data leakage. In addition to the aforementioned

challenges associated with STTRAM, DWM suffers from shift latency and shift power overhead, aspect ratio mismatch, and segregated read and write heads. The recent experimental studies have revealed that RRAM is a promising alternative to implement main memory due to their small footprint and zero standby power. Therefore, realizing logic operations within RRAM crossbar arrays is a promising approach to implement computing-in-memory systems. However, RRAM crossbar array suffers from sneak-path problem which leads to poor sense margin, higher power consumption, and limited array size.

In the first part of this thesis, we propose the circuit and architectural techniques to improve read yield, write latency, write power and data security of STTRAM. We introduce slope sensing, a destructive sensing technique for elimination of the reference resistance variation in order to enhance read yield of STTRAM arrays. Further, we propose a non-destructive sensing scheme which exploits a voltage feedback and boosting (VFAB) approach to develop large sense margin and substantially reduce sensing power. We introduce a novel and adaptive write current boosting to mitigate process variation induced write latency and write power degradation. In this technique, the bits experiencing worst-case write latency are fixed through write current boosting. Next, we investigate data security of STTRAM last level cache under magnetic attack where we apply low-overhead micro-architecture methods to avoid errors in presence of the magnetic attack.

In the second part of this thesis, we propose circuit and architectural techniques to overcome the design challenges associated with DWM. We apply layout techniques such as sharing of diffusion, bitlines and shift lines in order to enhance bitcell density. Circuit methods such as merged read-write head for improvement of bitcell density and shift gating to reduce shift power are proposed. Furthermore, we apply the micro-architecture techniques such as cache segregation using a novel replacement policy as well as dynamic current boosting based on workload monitoring in order to mitigate shift power and shift latency. Moreover, adaptive write and shift

current boosting is proposed to mitigate process variation induced performance and power degradation.

Lastly, we propose a low-power dynamic computing in memory system which can implement various functions in the Sum of Product (SoP) form in RRAM crossbar array architecture. This technique benefits from the nonlinear characteristic of a selector diode for improvement of the sense margin in order to implement higher fan-in logic gates.

Table of Contents

List of Figures xi
List of Tables xviii
List of Abbreviations xix
Acknowledgements xxii

Chapter 1 1

1. Introduction 1
   1.1. Contributions 6

Chapter 2 8

2. Introduction to Non-Volatile Memories 8
   2.1. Basics Principles of STTRAM 9
      2.1.1. Design Fundamentals of STTRAM 9
      2.1.2. Modeling of STTRAM Switching Dynamics 10
      2.1.3. STTRAM Design Challenges 12
         2.1.3.1. Tunneling Magnetoresistance (TMR) 12
         2.1.3.2. Oxide Breakdown 12
         2.1.3.3. Process Variation and Thermal Effects 13
         2.1.3.4. Sense Margin 15
         2.1.3.5. Read disturb 15
         2.1.3.6. Data Security 15
   2.2. Design Fundamentals of DWM 17
      2.2.1. Basics of DWM 17
      2.2.2. Modeling of DWM 18
      2.2.3. DWM Challenges 19
         2.2.3.1. Shift Latency 19
         2.2.3.2. Segregated Read and Write Head 19
         2.2.3.3. Aspect Ratio Mismatch 20
         2.2.3.4. Utilization Factor (UF) 20
   2.3. Design Fundamentals of RRAM 21
      2.3.1. Basics of RRAM 21
      2.3.2. RRAM Design Challenges 22

Chapter 3 24

3. Robust and Low Power STTRAM Design....24
3.1. Introduction....24
3.2. Improving Read Yield of STTRAM Array....26
3.2.1. Classification of Sensing Techniques....28
3.2.2. Background....29
3.2.2.1. Non-destructive Voltage Sensing Scheme [59]....29
3.2.2.1.1. Impact of process variation....29
3.2.2.2. Destructive Self-reference Sensing Scheme [67]....32
3.2.2.2.1. Impact of process variation:....34
3.2.3. Proposed Slope Sensing Technique....36
3.2.3.1. Slope Sensing Basic Operation....37
3.2.3.2. Double Sampling....39
3.2.3.3. Test Chip Implementation....40
3.2.3.3.1. Slope Sensing Circuit Design....40
3.2.3.3.2. Impact of Process Variation....42
3.2.3.3.3. Array Architecture....44
3.2.3.4. Test Results....46
3.2.3.4.1. Conventional Sensing Test Results....46
3.2.3.4.2. Slope Sensing Test Results....48
3.2.3.5. Applications....51
3.2.4. VFAB: A Novel 2-Stage STTRAM Sensing Using Voltage Feedback and Boosting....52
3.2.4.1. Proposed VFAB Sensing Scheme....52
3.2.4.1.1. Basic Operation....52
3.2.4.1.2. Simulation Results....54
3.2.4.2. Design Space Exploration....57
3.2.4.2.1. Design Method to Optimize Sense Margin....57
3.2.4.2.2. Impact of Discharge Time (t_d)....57
3.2.4.2.3. Impact of Boost Capacitors and Boost Voltage....59
3.2.4.2.4. Impact of Boost Time (t_b)....62
3.2.4.2.5. Impact of TMR....62
3.2.4.2.6. Impact of Voltage Scaling....63
3.2.4.3. Process, Temperature and Voltage Variation Analysis....64
3.2.4.3.1. Monte Carlo Simulation Setup....64
3.2.4.3.2. Read Yield....65
3.2.4.3.3. Sense Amplifier OFFSET voltage Analysis....66
3.2.4.3.4. Design Method for Process and Temperature Variation Tolerance....67
3.2.4.3.5. Simulation Results....68
3.2.4.4. Comparison with other Sensing Schemes....71
3.2.4.5. Application....73
3.3. Improving Write Performance of STTRAM....74
3.3.1. Related Works....75
3.3.2. Process Variation Analysis....76
3.3.2.1. Process Variation in Write Operation....76
3.3.2.2. Process Variation Tolerant Design....79
3.3.3. Subarray Circuit Design....79
3.3.3.1. Write Driver Design....79
3.3.3.2. Subarray Architecture....80

3.3.4. Cache Design for Adaptive Boosting 81
3.3.4.1. Methodology 81
3.3.4.2. Cache Organization 82
3.3.4.3. Simulation Setup 83
3.3.4.4. Simulation Results 84
3.4. Summary 86

Chapter 4 88

4. Secure Design of STTRAM Last Level Cache 88
4.1. Introduction 89
4.2. Related Work 92
4.3. Attack Models 93
4.3.1.1. Attack Model 93
4.3.1.2. Attack Sensing 94
4.4. Prevention Techniques 95
4.4.1. System Assumptions 95
4.4.2. Preventive Solution: Stalling 97
4.4.3. Preventive Solution: Cache Bypass 98
4.4.4. Preventive Solution: Checkpointing 101
4.4.5. Checkpointing for Write-through Policy 103
4.5. Simulation Results 104
4.6. Discussions 107
4.6.1. Usage of Stalling, Bypassing and Checkpointing 107
4.6.2. Handling I/O Requests 107
4.6.3. Ramping Attack Timing 108
4.6.4. Continuous Attack 108
4.7. Summary 109

Chapter 5 110

5. Robust, Low-Power and High Density Domain Wall Memories 110
5.1. Introduction 110
5.2. Related Works 113
5.3. Bitcell Design 115
5.3.1. Merged Read-Write Head Design 115
5.3.2. Access transistor sizing 117
5.3.3. Utilization Factor and Latency 118
5.3.3.1. Number/Positioning of merged head and UF 119
5.3.3.2. Latency 120
5.4. Bitcell Layout 121
5.4.1. Sharing of diffusion, bitlines and shift lines 121
5.4.2. Process requirements for DWM integration 123
5.5. Cache Design 124
5.5.1. Sub-Array design 125
5.5.2. Cache Organization 128
5.6. Cash Segregation and Workload Aware Current Boosting 129
5.6.1. Cache segregation 129
5.6.2. Workload-aware current boosting 130

5.6.3. Simulation Setup and Result 134
5.7. Process Variation Analysis 136
5.7.1. Process Variation in Write Head 136
5.7.2. Process Variation in Read Head 139
5.7.3. Process Variation Tolerant Design 139
5.7.4. Write Driver Design 140
5.7.5. Shift Driver Design 142
5.7.6. Subarray Architecture 143
5.8. Cache Design for Adaptive Boosting 143
5.8.1. Methodology 144
5.8.2. Cache Organization 145
5.8.3. Simulation Setup and Result 145
5.9. Summary 150

Chapter 6 152

6. Dynamic Computing in Memory in Resistive Crossbar Arrays 152
6.1. Introduction 152
6.1. Background 154
6.1.1. Basics of RRAM Crossbar Array 154
6.1.2. Static Computing in Memory (SCIM) Method 158
6.1.3. Memristor Aided LoGIC (MAGIC) [137] 160
6.2. Proposed Dynamic Computing in memory 161
6.2.1. Basic Operation 161
6.2.2. Impact of Gate Fan-in on Sense Margin 165
6.2.3. Impact of Gate Fan-in on Power 167
6.3. Process and Temperature Variation Analysis 168
6.3.1. Impact of Process and Temperature Variation on Sense Margin 168
6.4. Implementation of Carry Select Adder using DCIM 170
6.5. Evaluation and Comparison of different Computing in memory techniques 172
6.5.1. Power 172
6.5.2. Latency 173
6.6. Summary 174

Chapter 7 175

7. Future Work 175
7.1. Improving write performance of Spintronic Memories 175
7.1.1. Considerations for inter-die process variations 175
7.1.2. Static vs. dynamic boosting 176
7.2. Security 177
7.3. Computing in Memory 177

Chapter 8 179

8. Summary 179

Appendix 182

1. Referred Conferences 182
2. Referred Journals 183
3. Referred Patents 184

Bibliography 185

List of Figures

Figure 1.1 (a) Operating frequency scaling trend , and **(b)** On-chip cache size trend as reported in [143-144]. 1

Figure 1.2 (a) Percentage of area occupied by memory and logic, and **(b)** percentage of dynamic and static power in scaled technologies (static power increases due to larger on chip cache). 3

Figure 2.1 (a) Schematic of a Spin Transfer Torque Random Access Memory (STTRAM); and, (b) energy barrier separating the two MTJ magnetization states............................. 9

Figure 2.2 Simplified band diagram to demonstrate TMR effect in MTJ (a) parallel magnetization (good band matching), and (b) anti-parallel magnetization (poor band matching) of two magnetic layers. 11

Figure 2.3 (a) Illustration of R_{H}, R_{L} and R_{REF} distribution under process variation; and, (b) write latency distribution for P→AP switching for two write currents. 14

Figure 2.4 Schematic of a conventional Domain Wall Memory. The MTJ at read and write head and the overhead bits are also shown. 16

Figure 2.5 (a) Schematic of the 1T1R structure of RRAM; **(b)** schematic of the 1D1R structure of RRAM; and, **(c)** I-V curve of bipolar switching. 20

Figure 2.6 Forming, SET and RESET switching mechanism in RRAM. 21

Figure 3.1 Taxonomy of STTRAM sensing schemes. 27

Figure 3.2 (a) Non-destructive sensing scheme; (b) Data0, reference and Data1 voltage distributions.. 30

Figure 3.3 SM0 and SM1 distribution for 10000 Monte-Carlo points; (a) original scheme [59]; and, (b) with source degeneration [60]... 30

Figure 3.4 The impact of clamp voltage on sense margin for V_{Clamp}=0.7V and V_{Clamp}=0.9V. 31

Figure 3.5 (a) Self-reference sensing scheme; and, (b) sense circuit timing diagram is also shown. 33

Figure 3.6 I-R characteristics of the two MTJs under process-variation. A variation in resistance can change the sense margin. 33

Figure 3.7 (a) V-I curves of an MTJ with high and low resistance states initially; and, (b) optimum data current variation. 35

Figure 3.8 Sense margin distribution for 5000 Monte Carlo points. 35

Figure 3.9 (a) Slope detection sense circuit; and, (b) simplified timing diagram. 36

Figure 3.10 Sampling voltage across MTJ: (a) sampling with frequency f_1 *and* $\emptyset_1$-$\emptyset_{1d}$ clock phases which provides poor SM0 and large SM1; (b) sampling with frequency f_2 (f_2= $f1/2$) and $\emptyset_1$-$\emptyset_{1d}$ clock phases which provides large SM0 but poor SM1; and, (c) double sampling with frequency f_2, $\emptyset_1$-$\emptyset_{1d}$ and $\emptyset_2$-$\emptyset_{2d}$ clock phases which results in large SM0 and SM1 while ensure capturing negative slope. 38

Figure 3.11 Implementation details of slope detection sense circuit. 40

Figure 3.12 Post layout simulation of slope sensing scheme along with timing diagram for sense circuit-1(SC1) and SC2. 41

Figure 3.13 Low and high resistance distribution for 1000 points Monte Carlo simulation for, (a) 5K-10K, and (b) 2.5K-5K. 43

Figure 3.14 MTJ switching time distribution for 6uA/nS and 12uA/nS ramp current slopes for 1000 Monte Carlo points. 43

Figure 3.15 Subarray architecture. The sector architecture is shown in inset. 44

Figure 3.16 Experimental results: (a)-(b) Conventional sensing failure ratio with respect to clamp voltage for 2.5K-5K and 5K-10K arrays for TMR of 100%; and, (c)-(d) failure ratio with respect to TMR for 2.5K-5K and 5K-10K arrays with optimum clamp voltage. 45

Figure 3.17 Experimental results: Conventional sensing shmoo plot with TMR of 100% and optimum clamp voltage for (a) 5K-10K array; and, (b) 2.5K-5K array. 45

Figure 3.18 Oscilloscope capture of voltage across single-bitcell. Sensing starts by activating WL1 and bitcell switches to low resistance state at the edge of WL2; and, (b) the slope of voltage across bitcell for various current slope settings. Setting 00 indicatesthe lowest and 11 indicates the highest current slope. 46

Figure 3.19 Experimental results: (a)-(b) Slope sensing failure ratio with clock frequency for 2.5K-5K and 5K-10K arrays; (c)-(d) failure ratio with ramp current slope for 2.5K-

5K and 5K-10K arrays; and, (f) failure ratio with switching time for double and single sampling method. 47

Figure 3.20 Experimental results: Slope sensing shmoo plot with TMR of 100% and optimized ramp current slope and double sampling for, (a) 2.5K-10K array; and, (b) 5K-10K array. The # of failing chips out of 10 tested chips for failing voltage and frequency is shown....49

Figure 3.21 Experimental results: Passing frequency distribution for 10 tested chips for 2.5K-5K array. 49

Figure 3.22 Experimental results: Comparison of # of failures for conventional and slope sensing....49

Figure 3.23 Chip microphotograph and features. 50

Figure 3.24 Proposed sensing circuit; (b) timing diagram; and, (c) I_D-V_{GS} curve of feedback transistor when R_{Data}=R_H at different stages of sensing. In first stage, FR is weakly ON whereas FD is strongly OFF. In second stage, FR becomes strongly ON whereas FD remains weakly OFF. 53

Figure 3.25 VRL, VBL and gate/source voltage of data feedback transistors (VG_FD and VS_FD); and, (b) gate/source voltage of reference feedback transistor (VG_FR and VS_FR) during discharge and boost stages where RData= RH 55

Figure 3.26 Sense margin development during boosting stage. It can be noted that 800mV sense-1 margin and 990mV sense-0 margin is developed using VFAB. 56

Figure 3.27 Impact of discharge time on feedback transistor V_{GS} at the end of discharge stage in TT, SS and FF corners; and, (b) impact of discharge time on sense margin and V_{GS} of feedback transistor after boosting when R_{Data}=R_H. 58

Figure 3.28 Impact of boost voltage on sense margin; and, (b) impact of C_{Boost} on sense margin for discharge time of 1.2nS. 60

Figure 3.29 Impact of boost time on sense margin. 61

Figure 3.30 Fig. 8 Impact of TMR on sense margin (optimum R_L is shown). 61

Figure 3.31 Impact of supply voltage variation on sense margin; and, (b) optimum sense margin vs supply voltage; the optimum design parameters ({V_{Boost}, C_{Boost}, t_d}) are also shown for each supply voltage. 63

Figure 3.32 Sense amplifier circuit; and, (b) SA offset voltage distribution for 1000 points Monte-Carlo simulations....66

Figure 3.33 (a) SM0 and, (b) SM1 distribution for 2000 Monte Carlo points (TT). The μ and σ are also shown. 69

Figure 3.34 RAPY of top 4 design points which maximize PVT_{SM}. The RAPY improvement achieved by tuning V_{BST} is also shown; (b) sensitivity of RAPY on temperature in TT corner; and, (c) sensitivity of RAPY with respect to supply voltage variation in TT, FF and SS corners. The W_{BST} indicates the width of PMOS gate boost capacitor. 70

Figure 3.35 (a) Various sources of variations in STTRAM bitcell and, (b) the proposed methodology that involves modeling of tail of the distribution and adaptive boosting to accelerate the tail. 74

Figure 3.36 Write latency distribution for 5000 Monte Carlo points. The curve fitting to model the tail is also shown; (b) write latency distribution using curve fitting model for three different write currents. The worst case MTJ can be accelerated through high write current. The 4 sigma delay is also shown. By boosting the current the number of bits beyond 4 sigma delay can be reduced; and, (c) min, mean and max write latency with write current. 77

Figure 3.37 Boost enabled write and sense circuit; and (b) simulation results showing write time improvement by enabling write boost. 78

Figure 3.38 Subarray architecture showing boost enabled write and read circuit; and, (b) cache organization and fuse bits. 80

Figure 3.39 (a) IPC; (b) L2 total energy comparison ; (c) L2 Dynamic energy; (d) L2 Leakage energy. 85

Figure 4.1 Two types of magnetic attacks: (a) gradually ramping attack; and, (b) sudden attack. 91

Figure 4.2 Embedded attack sensor in memory array [40]. The details of sensor array with peripheral circuits is shown in inset. Control logic is shared among the subarrays and contains the logic to generate address, read, write and data and analyze the response. 94

Figure 4.3 Look aside cache architecture. 96

Figure 4.4 (a) Control flow to activate/deactivate bypassing; and, (b) processing of read, write requests during bypassing. 98

Figure 4.5 Bypassing of (a) read, and (b) write request with look-aside cache architecture. 100

Figure 4.6 Cache bypass architecture with checkpointing. 102

Figure 4.7 Control flow diagram of checkpointing. 102

Figure 4.8 Number of forced (FCP) and periodic checkpoints (PCP) for each PARSEC benchmark. Periodic checkpointing is performed after every 2 million cycles. 103

Figure 4.9 IPC results of baseline, bypassing and checkpointing with different attack rates using; (a) SPLASH, and; (b) PARSEC benchmark suites. 105

Figure 4.10 Energy results of baseline, bypassing and checkpointing with different attack rates for SPLASH and PARSEC benchmarks: (a) total energy; and, (b) dynamic energy...106

Figure 5.1 Synergistic system design proposed in this paper..111

Figure 5.2 Proposed merged head design. The shared read/write circuit, head selection and shift select is also shown. 116

Figure 5.3 Relationship between read current, write latency and access transistor size. 118

Figure 5.4 UF vs number of Heads for NW with 40 bits. 119

Figure 5.5 Example showing that left head catering to only left shifts and the right head catering to only right shifts, (b) a better placement of the heads allowing for bi-directional shifts, (c) the ideal head placement for a shift latency of 2 and, (d) shows the NW used in our simulation with 4 heads placed at bit number 3, 7, 11, 15 of the usable bits. Buffer bits are represented by 'X'...120

Figure 5.6 Bitcell layout (4-bit, $2.56F^2$/bit). MTJs and diffusion contacts are numbered according to their connection, (b) cross section of the bitcell...122

Figure 5.7 Fig. 14 (a) Metal plan of BLB. The SL stubs are also shown, (b) metal plan of shift lines...122

Figure 5.8 Overview of proposed subarray with shift select, gating select and head selects. WL strap is also shown. (b) Shift gating circuitry. 125

Figure 5.9 Write power versus write latency for three operating voltages. 126

Figure 5.10 (a) DW velocity vs input current using 1D model [41]. The DW velocity and power of fast, medium and slow shift are indicated, (b) shift latency vs power. 126

Figure 5.11 Fig. 18 (a) Conventional shift circuit, (b) conventional write driver. (c) Proposed shift circuit, (d) proposed write driver...127

Figure 5.12 Logical to physical mapping of a bank. Shaded ends of NW are buffer bits. The set mapping on the NW is depicted. 129

Figure 5.13 Proposed cache replacement policy..129

Figure 5.14 Proposed segregated cache and replacement procedure in a Mat. 129

Figure 5.15 Fig. 23 Workload-aware write and shift current boosting. 131

Figure 5.16 Number of L2 accesses for set1 & set2. Access profile for both 200K/500K cycles are shown. 131

Figure 5.17 Shift-current scaling of set2. 132

Figure 5.18 Power and performance overhead for proposed workload-aware current boosting. 132

Figure 5.19 Fig. 27 Performance comparison across different memory technologies. 134

Figure 5.20 Fig. 28 Comparison of energy consumption of L2 cache across different memory technologies. 134

Figure 5.21 Performance comparison across different memory technologies for each workload set. 135

Figure 5.22 Energy comparison across different memory technologies for each workload set. 135

Figure 5.23 Write latency distribution for 5000 Monte Carlo points. The curve fitting to model the tail is also shown; (b) write latency distribution using curve fitting model for three different write currents. The worst-case head can be accelerated through high write current. The 4 sigma delay is also shown. By boosting the current the number of bits beyond 4 sigma delay can be reduced; and, (c) min, mean and max write latency with write current. 137

Figure 5.24 Fig. 33 Effect of process variation on maximum write latency by considering 50% and 200% of original standard deviation of parameters reported in Table 3.1. 138

Figure 5.25 Fig. 32 (a) Read latency distribution for 2000 Monte Carlo points. The curve fitting to model the tail is also shown; (b) read latency distribution for 32M heads. 139

Figure 5.26 Fig. 34 Mitigation of process variation on write latency by write and shift current boosting 140

Figure 5.27 (a)& (b) Boost enabled write and shift driver; and (c) simulation results showing write time improvement by enabling write boost. 141

Figure 5.28 Subarray architecture showing boost enabled shift and write drivers, shift gating for low power and head selection. 142

Figure 5.29 Cache organization. 142

Figure 5.30 Shift current boosting for fast shifting. 145

Figure 5.31 (a) IPC; (b) total energy comparison; 147

Figure 5.32 (a) Dynamic energy; and, (b) Leakage energy 149

Figure 6.1 Crossbar array with metal oxide RRAM and selector dio each crosspoint; and, (b) schematic of crossbar array with selector diode. 154

Figure 6.2 I-V curve RRAM model used in this study; (b) I-R characteristic of the RRAM model; (c) I-V curve of selector diode used in this study; and, (d) the I-V characteristic of bitcell composed of RRAM and selector diode. 155

Figure 6.3 RRAM crossbar array (a) GND-GND read scheme; and, (b)VDD/2 write technique. Sneak paths are shown for read and write operations. 156

Figure 6.4 Static computing in memory architecture in RRAM crossbar array. 158

Figure 6.5 V_{AND1} and V_{AND0} versus AND array size; and, (b) V_{OR1} and V_{OR0} versus OR array size in an array of 2N WLs where all WLs are utilized to implement N-input gate. 159

Figure 6.6 MAGIC NOR gate implementation. 159

Figure 6.7 XOR implementation using proposed DCIM architecture in RRAM crossbar array; and, (b) timing diagram of logical XOR operation. 162

Figure 6.8 $V_{AND,1}$,$V_{AND,0}$, V_{OR1} and V_{OR0} versus gate fan-in for, (a) conventional CIM in array of 16 WLs, (b) DCIM in array of 64 WLs. 165

Figure 6.9 Power consumption versus number of inputs; (a) Dynamic CIM and, (b) static CIM. 167

Figure 6.10 (a) V_{AND1} and V_{AND0} distribution for 1000 Monte-Carlo points @ -10°C and 90°C; and, (b) V_{OR0} and V_{OR1} distribution. 169

Figure 6.11 Implementation of 16-bit carry select adder using DCIM scheme. For sake of brevity only low resistance connections are shown. 171

Figure 6.12 (a) Power, and (b) latency comparison of various CIM schemes. 173

List of Tables

Table 1.1 Comparison of different memory technologies reported in [25-26]. 3

Table 2.1 MTJ parameters used. 10

Table 2.2 Magnetic constants used for DW dynamics. 18

Table 3.1 Parameters used for process variation study. 29

Table 3.2 Comparison with other sensing schemes. 50

Table 3.3 Sense circuit parameters..57

Table 3.4 Parameters used for process variation study. 64

Table 3.5 Comparison with conventional voltage sensing scheme. 72

Table 3.6 Comparison with other sensing scheme. 72

Table 3.7 Processor Configuration..81

Table 3.8 Design parameters for different cache configurations (22nm Technology). 83

Table 5.1 Processor configuration. 133

Table 5.2 Design parameters for different cache configurations (22 nm technology). 136

Table 6.1 List of design parameters. 157

Table 6.2 Parameters used for process variation study. 168

Table 6.3 Comparison of 16-bits adder implementation using different CIM schemes..........170

List of Abbreviations

ADC	Analog to Digital Converter
AP	Anti-Parallel
BCT	Block Counter
BL	Bit Line
DIBL	Drain Induced Barrier Lowering
DAC	Digital to Analog Converter
DRAM	Dynamic Random Access Memory
DCIM	Dynamic Computing in Memory
DMA	Direct Memory Access device
DoS	Denial of Service
DW	Domain Walls
DWM	Domain Wall Memory
ECC	Error Correction Code
EWT	Early Write Termination
eDRAM	embedded DRAMs
FeFET	Ferroelectric FET
FeRAM	Ferroelectric RAM
FF	Flip-flop
FL	Free Layer
GIDL	Gate Induced Drain Leakage
GBDP	Grouping-Based Data Placement
HRS	High Resistance State

HPC	High Performance Computing
IC	Integrated Circuit
IMA	In-plane Magnetic Anisotropy
IoT	Internet of Things
IPC	the instruction per cycle
LLG	Landau-Lifshitz-Gilbert
LLC	Last Level Cache
LS	Left-Shift (LS)
LRS	Low Resistance state
MAGIC	Memristor Aided LoGIC
MIM	Metal-Insulator-Metal
MRAM	Magnetic RAM
MTJ	Magnetic Tunnel Junction
MRU	most recently used
NBTI	Negative Bias temperature Instability
NVM	Non-Volatile Memory
NW	Nanowire
PCM	Phase Change Memory
P	Parallel
PCP	Periodic Checkpointing
PC	program counter
PMA	Perpendicular Magnetic Anisotropy
PL	Pinned Layer
PUF	Physically Unclonable Function
RAPY	Read Access Pass Yield
RDPY	Read Disturbance Pass Yield
RS	Right-Shift
RH	High Resistances

RO	Ring Oscillator
RRAM	Resistive RAM
Sa	Sense Amplifier
SCIM	Static Computing in Memory
SE	Sense Enable
SHE	Spin Hall Effect
SL	Source Line
SM	Sense Margin
SM0	Sense-0 Margin
SOP	Sum of Product
SRAM	Static Random-Access Memory
STTRAM	Spin Transfer Torque RAM
TDDB	Time Dependent Dielectric Breakdown
TMR	Tunneling Magnetoresistance
TRNG	True Random Number Generator
UF	Utilization Factor
VFAB	Voltage Feedback And Boosting
WL	Wordline

Acknowledgements

I would like to thank a few people who helped me in this journey. Firstly, I would like to express my sincere gratitude to my advisor Prof. Swaroop Ghosh, for his continuous guidance, patience, enthusiasm and support throughout my doctoral studies. He was always very welcoming to answer my questions and helping me in all the time of research. Dr Ghosh's insight and advice on both research and my career are invaluable.

I would like to thank Dr. Jaideep Kulkarni provided me insight into the industry and offered a practical perspective to my research direction. Collaborating with him on couple of publications helped me understand the industry challenges in designing non-volatile memories. I would also like to thank the committee members for their help and guidance during my PhD.

I thank my fellow labmates for the motivating discussions, for the sleepless nights we were working together before deadlines, and for all the fun we have had in the last four years. I would like to thank Jae, Asmit, Nasim, Saki, Rekha and Anirudh for their continued support, motivation, and encouragement.

This material is based on work supported by the Semiconductor Research Corporation (SRC) under award number (#2727.001), the National Science Foundation (NSF) under award numbers (#CNS-1722557, #CCF-1718474, DGE-1723687 and DGE-1821766), and the Defense Advanced Research Projects Agency (DARPA) Young Faculty Award under award number (#D15AP00089).

Any opinion, findings, and conclusions or recommendations expressed in this publication are those of the authors and do not necessarily reflect the views of the Semiconductor Research Corporation, National Science Foundation and Defense Advanced Research Projects Agency.

To my family

Chapter 1

Introduction

Embedded memories play a crucial role in computing systems to support the increasing need of data storage in various applications. For the last few decades, the process of scaling down, known as moor's law, projects an exponential increase in the number of transistors on a die, reaching up to 10 billion transistors today [1]. Moreover, not only the number of transistors on a single die increases, but also transistors become faster and cheaper each year. Hence, overall computation power increases, which in turn results in growing demand for high-density memories to meet the large data bandwidth requirement. However, power dissipation prevents the frequency scaling as shown in Fig. 1.1(a) [1]. The power densities in state-of-the-art processors are ~65W/cm^2 [2] and is reaching that of nuclear reactors. The power density issue can be mitigated by increasing

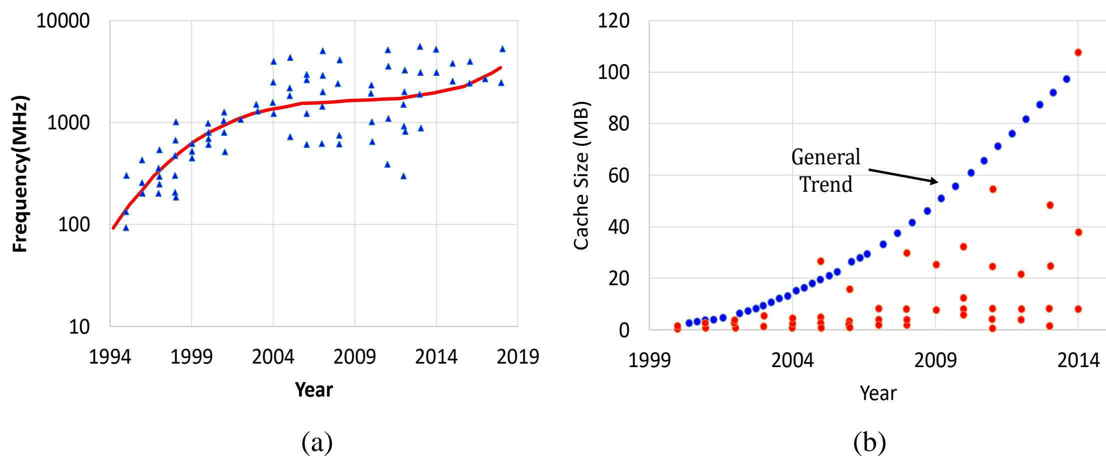

(a) (b)

Figure 1.1 **(a)** Operating frequency scaling trend , and **(b)** On-chip cache size trend as reported in [1].

the number of processor cores which in turn requires larger on-chip cache to take full advantage of multi-core systems. As shown in Fig. 1.1(b), the capacity of on-chip memory increases every year. Fig.1.2 (a) shows that as technology scales, more and more of on-chip area is dedicated to memory. So far, CMOS scaling allows smaller transistor size to increase the capacity of on-chip caches. However, Moore's law predicts exponential scaling and will not continue indefinitely because of numerous technological challenges [3], such as precision in photo lithographic process, and electrical limitations due to short channel effects. Furthermore, the CMOS scaling is associated with challenges such as increased subthreshold leakage due to Drain Induced Barrier Lowering (DIBL), Gate Induced Drain Leakage (GIDL), Hot Carrier Injection (HCI), Time Dependent Dielectric Breakdown (TDDB), Negative Bias Temperature Instability (NBTI), high power density, velocity saturation due to mobility degradation, and process variations.

In the last few years, the increasing demand for high performance computing (HPC) and integration of multiple cores on a single die have increased the speed gap between logic and memory, the so-called "memory-wall". Conventional CMOS memories i.e., Static Random Access Memory (SRAM) and Dynamic Random Access Memory (DRAM) have been the popular choices to build on-chip caches and main memory for the last several decades. However, SRAM and DRAM seem to be approaching a brick wall. SRAM and DRAM are volatile memories meaning that they require a constant power supply to retain the state. SRAM cell drastically consumes static (leakage) power, and DRAM cell requires a periodical refresh. On one hand, process variability and standby power are posing severe obstruction towards SRAM/DRAM scaling to future nodes. Fig. 1.2(b) shows that the leakage power is exceeding dynamic power in scaled technology. On the other hand, emerging energy-constrained and bandwidth hungry electronic gadgets demand for larger on-chip cache which cannot be satisfied with SRAM. Thus, the memory hierarchy design must substantially scale in performance, power, and density to sustain the processing demands of next-generation applications.

Table 1.1 Comparison of different memory technologies reported in [25-26].

Features	SRAM	DRAM	STTRAM	DWM	RRAM	FeRAM	PCRAM
Density(F^2)	50-120	6-10	4-20	~2.5	4-6	20-40	6-12
R/W power	Low	Low	Low	Low	Low	Low	High
R/W Access Time (nS)	<1/ <1	30/ 50	~2-20/ ~2-20	~2-20/ ~2-20	~100/ ~50	50/50	20-50/ 50-120
Endurance	$>10^{21}$	10^{16}	$\sim10^{16}$	$\sim10^{16}$	$\sim10^{10}$	$\sim10^{12}$	$\sim10^{10}$
Operating Voltage(V)	0.7-1.2	1.2-3.3	1-1.2	1-1.2	1.5-3	2-5	~3
Non-Volatility	No	No	Yes	Yes	Yes	Yes	Yes
Other Power	Leakage	Refresh	No	Shifting	No	No	No

To circumvent these issues, several emerging non-volatile memory technologies are investigated as an alternative to implement on-chip cache, main-memory and storage such as Spin-Torque Transfer RAM (STT-RAM) [4], Domain Wall memory (DWM) [5], Phase-Change RAM

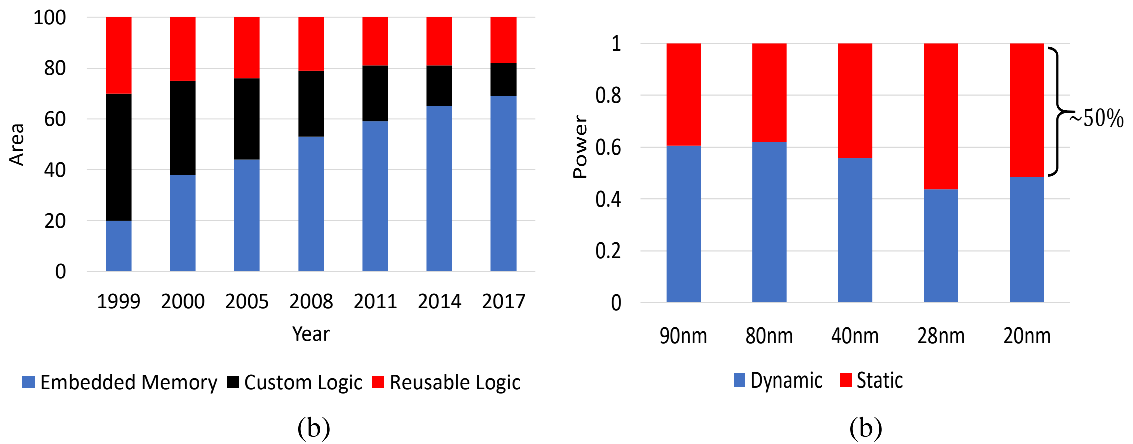

Figure 1.2 **(a)** Percentage of area occupied by memory and logic, and **(b)** percentage of dynamic and static power in scaled technologies (static power increases due to larger on chip cache)[143-144].

(PCRAM) [6-7], Ferro-electric RAM (FeRAM) [8], Resistive RAM (RRAM)) [9], and Magnetic RAM (MRAM) [10] that are explored as potential alternatives to existing memories. These emerging NVM technologies offer the speed of SRAM, high density of DRAM, and the non-volatility of Flash memory.

Table 1.1 compares memory technologies in terms of density, access time, and endurance. Among these memory technologies, spintronic memories (i.e. STTRAM, DWM) have proven to be potential alternatives to replace on-chip SRAM. These memory technologies offer high-density, zero standby power, high speed, high endurance and CMOS compatibility. STTRAM provides small footprint of ~4-20F^2, extremely good endurance of > 10^{16} and read/write access time of 2-20ns. DWM provides small footprint as low as 2.5F^2 [11] and similar endurance. Even though read/write access time of DWM is longer due to shift-based access mechanism, very small footprint makes it a promising candidate to implement large on-chip caches. From an industrial standpoint, HP and Hynix are planning to replace flash memory and later DRAM/SRAM with RRAM. Furthermore, Toshiba is planning to implement 512KB STTRAM L2 cache to save power [12]. Everspin released commercialized samples of 64MB STT-RAM [13].

On the other hand, the speed gap between the processor and memory impedes the continuous performance improvement of the traditional von Neumann architecture. To address this challenge, extensive amount of research has been conducted to explore alternative non-von Neumann architectures based on the concept of computing in memory. Von Neumann computing separates memory and processing elements leading to performance and energy bottlenecks due to frequent data transfers. With conventional von Neumann computing struggling to implement high performance and energy-efficient computing systems, there is a pressing need to explore alternative computing models. CMOS switches, although universal, fails to offer additional features to meet this end goal. Recent experimental studies have revealed that RRAM is a promising alternative to implement main memory due to small footprint and zero standby power. Therefore, realizing logic

operations within RRAM crossbar arrays is a promising approach to implement computing in memory systems. Resistive crossbar arrays possess many promising features that can not only enable high-density and low-power storage but also non-von Neumann compute models. Various computing in memory schemes have been proposed to implement dot products in RRAM crossbar array. Digital to analog converter (DAC) and analog to digital converter (ADC) are required as peripheral circuitry to implement dot product in RRAM crossbar array. These architectures can implement matrix multiplication [14] and various computing paradigms such as neuromorphic computing [15-16] and approximate computing [17]. Spintronic devices are also investigated for ultra-low power computing based on artificial neural network. Interestingly, variety of new structures have been proposed to suit particular application e.g., full adders [18], MTJ neurons [19-21] and MTJ synapses [22-24]. Two basic operations in artificial neural network are weighted summation of inputs and thresholding operation. MTJ switching basically behaves as a current thresholding device. Thus, MTJ can be exploited to implement thresholding operation of a neuron in a memristive crossbar array. However, due to small resistance difference between two states of MTJ, STT synapse cannot compete with that of RRAM to implement weighted summation.

Despite all the advantages, spintronic memories suffer from high write energy, long write time, poor sense margin (SM), read disturb and reliability issues such as oxide break down. Furthermore, they bring new data security issues that were absent in volatile memory counterparts such as SRAM. The free layer of MTJ can flip under the influence of external magnetic field that can be exploited by the adversary. In this dissertation, we explore circuit and architectural techniques to address spintronic memories design challenges. In addition, we investigate RRAM crossbar array to implement energy-efficient computing in memory paradigm.

1.1. Contributions

In this dissertation, we have explored STTRAM, DWM and RRAM as alternatives to CMOS to implement memory and computing systems. First, we describe the basic principles of these memories and their design challenges.

In the third chapter, we propose circuit and architectural techniques to improve read yield and write performance of STTRAM which is summarized as follows:

- Due to poor TMR, the voltage/current differential between low and high resistance states of STTRAM decreases which degrades the SM. Furthermore, process variation reduces this difference even further resulting in a poor sense margin. In this chapter we propose, slope sensing, a destructive sensing technique to eliminate reference resistance variation to enhance the read yield of STTRAM arrays. Additionally, we introduce a non-destructive sensing scheme that exploits a voltage feedback and boosting (VFAB) technique to develop large sense margin. Moreover, this method reduces the sensing power significantly by eliminating static current.
- Process variation along with stochastic nature of MTJ switching results in a large spread in the write latency variation. We propose a novel and adaptive write current boosting to address this issue. In this technique, the bits experiencing worst-case write latency are fixed through write current boosting.

In the fourth chapter, we investigate the data security of STTRAM last level cache under magnetic attack. We apply low-overhead micro-architecture techniques to avoid errors in presence of magnetic attack which include:

- Stalling where the system is halted during attack.
- Cache bypass during gradually ramping attack where the last level cache (LLC) is bypassed and the upper level caches interact directly with the main memory.

- Checkpointing along with bypass during sudden attack where the processor states are saved periodically, and the LLC is written back at regular intervals. During attack, the system goes back to the last checkpoint and the computation continues with bypassed cache.

In the fifth chapter, we propose circuit and architectural techniques to address the DWM design challenges as follows:

- At the circuit level, we introduce merged read-write head to increase bitcell density by merging the segregated read and write access transistors and extra wiring overhead. We propose access transistor sizing which optimizes area and latency while reducing the probability of read disturbance. Shift gating by sharing shift circuit among 8 NWs, to reduce shift current is also introduced. Moreover, the shift circuit and write driver capable to work under three operating points namely, fast, medium and slow modes is applied.
- At the architecture level, cache is segregated to take advantage of three operating modes using a novel replacement policy. A dynamic current boosting based on workload monitoring is also proposed to take advantage of proposed write driver and shift circuit.
- We also propose circuit level techniques to implement adaptive write and shift current boosting and exploit them at the micro-architecture level to mitigate process variation induced performance and power degradation.

In the sixth chapter, we propose a low-power dynamic computing in memory system which can implement various functions in Sum of Product (SoP) form in RRAM crossbar array architecture. This design benefits from the nonlinear characteristic of a selector diode to improve sense margin in order to implement higher fan-in gates. In addition, this technique reduces the power consumption associated with logical operation significantly by eliminating the static current.

Chapter 2

Introduction to Non-Volatile Memories

As discussed in the previous chapter, CMOS scaling experiencing significant challenges such as high-leakage power, process variation and thermal issues. Thus, there is a need of alternative technologies to replace CMOS technology for both computing and storage applications. This chapter describes the basic principles of STTRAM, DWM and RRAM. First, we explain magnetic tunnel junction (MTJ) which is the basic component in DWM and STTRAM. Next, we briefly explain the underlying physics in modeling the magnetization dynamics of the free layer of the MTJ. Subsequently, we discuss design challenges associated with STTRAM such as low TMR, oxide breakdown, read disturb, process variation and thermal effects, as well as the data security issues.

Afterwards, we describe the basic read and write operations in DWM. We also discuss the key design parameters of DWM and their impact on read/write latency, reliability and memory density. We describe the dynamics of DW motion in nanowire (NW), and investigate the design challenges of DWM such as shift latency, utilization factor, aspect ratio mismatch, and segregated read and write head. Finally, we present the basic principles of RRAM and characterize RRAM design challenges.

2.1. Basics Principles of STTRAM

2.1.1. Design Fundamentals of STTRAM

Spin-Torque Transfer Random Access Memory [4] is a promising memory technology for embedded cache due to high-density, low standby power and high speed. STTRAM provides high-density due to 1T-1R structure, and eliminates bitcell leakage owing to the non-volatile nature of the storage element which is a magnetic tunnel junction (MTJ). The MTJ contains a free ferromagnetic layer (FL), a metal oxide (MgO or AlO) and a pinned ferromagnetic layer (PL) (a cartoon is shown in Fig. 2.1). The resistance of the MTJ stack is high (low) if free layer magnetic orientation is anti-parallel (parallel) compared to the fixed layer. The parallel and anti-parallel magnetization state of the FL with respect to PL can represent either a logic '0' or '1', respectively. The configuration of the MTJ can be changed from anti-parallel (AP) to parallel (P) by injecting a write current (I_W) greater than critical current (I_C) from bit-line to source-line (or vice versa). STTRAM state can be read by asserting wordline (WL), applying a small read current and

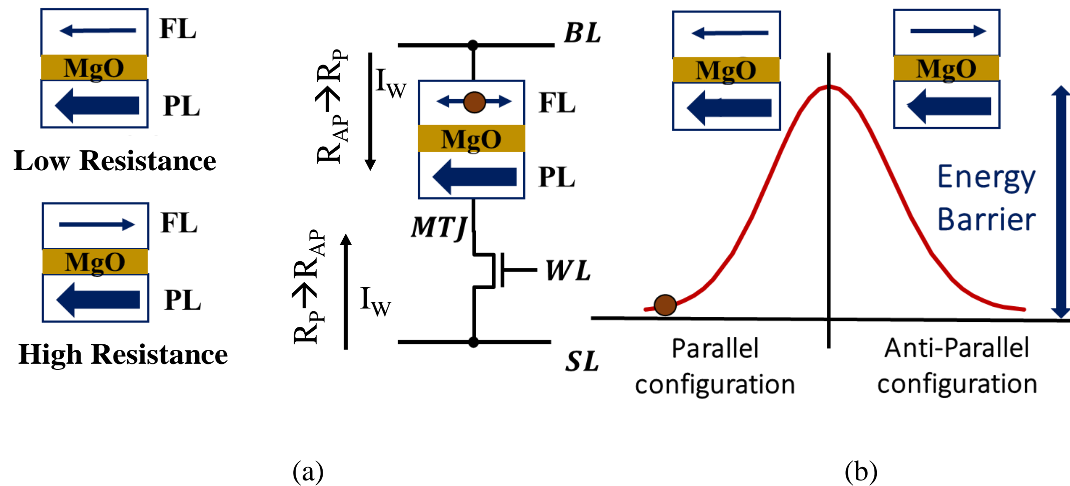

Figure 2.1 (a) Schematic of a Spin Transfer Torque Random Access Memory (STTRAM); and, (b) energy barrier separating the two MTJ magnetization states.

Table 2.1 MTJ parameters used.

Parameter	Value
Ms	700 emu/cc
Demagnetization Field	4*π*Ms
K_B	$1.38e^{-23}$
α	0.028
Exchange Constant (A)	20e-12 J/m.
Length(l)/Width(w)/Thickness(t) of NW	50e-9 m/95e-9 m/1.2e-9 m
ɣ	1.76e11 /G s
Energy Barrier (E_B)	56*k_B*T

comparing the output voltage with that of reference voltage. The two states of MTJ are separated by an energy barrier 'E_B' (Fig. 2.1(b)). By injecting a current into MTJ, the FL can be excited to overcome the corresponding energy barrier. Hence, MTJ magnetization can be switched from one state to another. There are two flavors of MTJ, perpendicular magnetic anisotropy (PMA) and in-plane magnetic anisotropy (IMA). The easy axis of in-plane DWM is aligned with the plane of the thin ferromagnetic layer, while it is perpendicular to the plane of ferromagnetic layer in PMA. PMA MTJ offers good thermal stability, low critical current and high access speed [30].

2.1.2. Modeling of STTRAM Switching Dynamics

The magnetization reversal time of MTJ is very sensitive to magnetic field. The dynamics of the MTJ free layer is described by the LLG equation [27-28].

$$\frac{\partial \vec{m}}{\partial t} = -\gamma \vec{m} \times H_{eff} - \alpha\gamma \vec{m} \times \vec{m} \times H_{eff} + \underbrace{\frac{I_s \hbar G(\psi)}{2e} \vec{m} \times (\vec{m} \times \vec{e_p})}_{\text{STT}} \tag{2.1}$$

Where $\vec{m}$ is the unit vector representing local magnetic moment, α denotes the Gilbert's damping parameter, γ is the gyromagnetic ratio, I_s is the spin current, $G(\psi)$ is the transmission co-efficient, $\hbar$ is the reduced planck's constant, e is the charge of electron and $\overrightarrow{e_p}$ is the unit vector along fixed layer magnetization. In the above expression, $\overrightarrow{\mathrm{H_{eff}}}$ is the effective field given by: $\overrightarrow{\mathrm{H_{eff}}} = \overrightarrow{\mathrm{H_a}} + \overrightarrow{\mathrm{H_k}} + \overrightarrow{\mathrm{H_d}} + \overrightarrow{\mathrm{H_{ex}}}$, where $\overrightarrow{\mathrm{H_a}}$, $\overrightarrow{\mathrm{H_k}}$, $\overrightarrow{\mathrm{H_d}}$, and $\overrightarrow{\mathrm{H_{ex}}}$ are the applied, anisotropy, demagnetization and exchange fields, respectively. The first two terms represent precession and damping torques respectively, which govern the dynamics of the magnetization in the presence of an effective magnetic field. The MTJ retention time is exponentially related to MTJ's thermal barrier (Δ) and is given by $t = t_0 \times e^{k\Delta}$, where t_0 is the inverse of attempt frequency, and k is a fitting constant. The thermal barrier, in turn, is proportional to free layer volume (V) and inversely proportional to the absolute temperature (T) and is given by $\Delta = \frac{k_u V}{k_B T}$, where k_u is the anisotropy constant, and k_B is the Boltzmann's constant. Reducing free layer volume result in lower retention time for both store-0 and store-1.

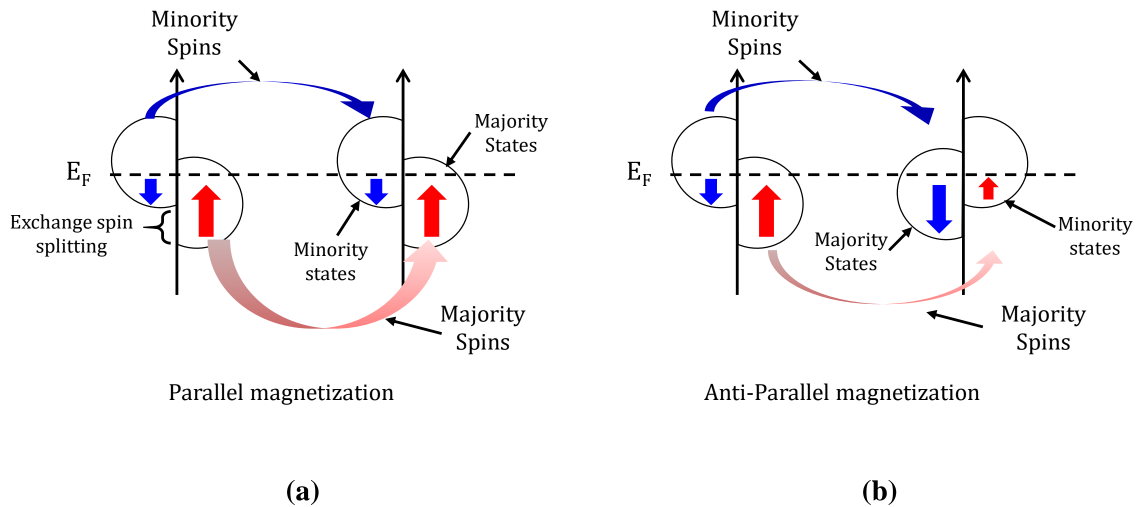

(a) **(b)**

Figure 2.2 Simplified band diagram to demonstrate TMR effect in MTJ (a) parallel magnetization (good band matching), and (b) anti-parallel magnetization (poor band matching) of two magnetic layers.

2.1.3. STTRAM Design Challenges

2.1.3.1. Tunneling Magnetoresistance (TMR)

The TMR effect is due to the difference in density of states for spin-up and spin-down electrons in ferromagnetic layers. The TMR effect can be understood by the density of state diagram demonstrated in Fig. 2.2. In the parallel magnetization configuration, electrons with the majority spins (shown by thick arrow) tunnel through the barrier and fill the majority states in the second film while the minority spins tunnel to the minority states. Therefore, there is a good band matching, which leads to a small resistance. When magnetic orientation of two ferromagnetic layers is anti-parallel, the majority spins of the first layer tunnel to the minority states in the second layer and vice versa. This results in a poor band matching which, in turn, leads to a higher resistance. The TMR is defined as [29]:

$$TMR = \frac{R_H - R_L}{R_L} \tag{2.2}$$

Where R_L and R_H indicate MTJ resistance in the low and high resistance states, respectively. Higher TMR ratio means larger difference between low and high resistance state and hence, better distinguishability in the read operation. The higher oxide thickness results in the higher TMR ratio [31]. However, thicker oxide results in higher resistance which will slow down the write operation due to the limited voltage headroom. Therefore, low resistance and higher TMR are needed for a robust STTRAM design.

2.1.3.2. Oxide Breakdown

MTJ consists of a thin metal oxide barrier (MgO or AlO) with thickness of around 1.2 nm. Almost all the applied voltage across MTJ is dropped across metal oxide. This can lead to oxide breakdown under high stress conditions known as Time Dependent Dielectric Breakdown (TDDB) [32]. The duration and amount of current flowing through the device determines the breakdown

time. The TDDB exhibits an abrupt decrease in MTJ resistance. It is important that the write voltage is below the breakdown voltage with a proper margin to prevent TDDB. Since the faster switching demands large voltage across MTJ, the maximum switching speed is limited by the breakdown voltage [33].

2.1.3.3. Process Variation and Thermal Effects

MTJ switching is inherently stochastic due to random thermal fluctuation. This results in a non-deterministic switching delay of MTJ magnetization, even for the same environmental conditions. The thermal fluctuations affect the magnetization dynamics in two ways. First, the magnetization is randomly initialized in different angles. Second, the thermal field randomly disturb the magnetization during MTJ switching. The switching probability can be expressed as follows [4][34]:

$$P_{Sw} = 1 - exp\left\{-\frac{t}{\tau_0} exp\left[-\Delta_0 (1 - \frac{I_W}{Ic_0})\right]\right\} \tag{2.3}$$

Where Δ_0 ($\frac{E_B}{K_B T}$) is the magnetic memorization energy without any applied current and field (typically 60), t is the pulse width, τ_0 is the inverse of attempt frequency (typically 1n), I_C and I_W denote critical and write currents, respectively. Equation 2.3implies that as Δ_0 or the retention time increases, the switching probability decreases. Therefore, there is a trade-off between the retention time and switching speed.

Process variation is another significant factor in memory design. Process variations in the STTRAM is modeled by incorporating variations in MTJ as well as the access transistor. The resistance of MTJ increases exponentially with increased oxide thickness (T_{OX}) and linearly with decreased cross-sectional area (A). Hence, MTJ switching time is highly sensitive to T_{OX} and A variations. In addition, process variation results in a large spread in low and high resistance states of MTJ. In non-destructive sensing, resistance of data MTJ is compared against the resistance of

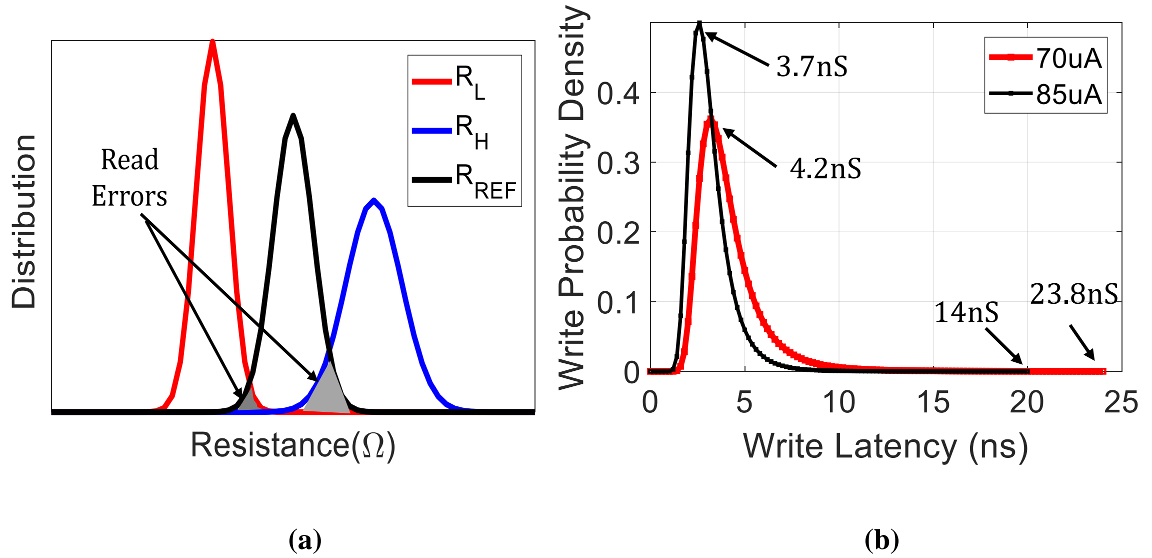

(a) **(b)**

Figure 2.3 **(a)** Illustration of R_H, R_L and R_{REF} distribution under process variation; and, (b) write latency distribution for P→AP switching for two write currents.

the reference MTJ (R_{REF}) to determine the bitcell content. Therefore, reference resistance as well as data resistance variation may result wrong interpretation of bitcell content. Sensing error occurs where reference resistance overlaps with data resistance as demonstrated in Figure 2.3(a).

The process variation along with the stochastic switching due to random thermal fluctuation leads to huge variation in MTJ switching time. In a STTRAM array with Error Correction Code (ECC), the target write error rate is 10^{-9} [36]. In order to achieve target error rate with a constant write current, longer write pulse is required. For example, using the model [37], for 70 uA of write current a write period 24 nS is needed. Note that the write latency is determined based on P→AP switching since it is the worst case of two switching delay. Figure. 2.3(b) shows the write distribution versus write latency for the write current of 70 uA and 85 uA for P→AP switching. It is evident that the worst case write latency reduces by increasing the write current. Note that this distribution has a long tail which determines the write latency.

2.1.3.4. Sense Margin

In order to sense the state of MTJ, data MTJ resistance can be compared against reference MTJ resistance (which is an average of fixed high and low MTJ resistances). In conventional non-destructive voltage sensing, sensing is performed by applying a current into both data and reference MTJ and comparing the output voltage of data MTJ against that of reference MTJ. Due to poor TMR, the voltage/current differential between R_H and R_L decreases which degrades the sense margin. Furthermore, process variation reduces this difference even further (as shown in Fig. 2.3(a)) leading to a poor sense margin. Poor sense margin results in a wrong interpretation of MTJ state.

2.1.3.5. Read disturb

As mentioned earlier, in order to prevent read disturbance I_{Read} must be less than critical current (I_C). I_C depends on current pulse width as follows [4]:

$$I_C = I_{C0}\left\{1 - \left(\frac{K_B T}{E_B}\right)\ln\left(\frac{t}{\tau_0}\right)\right\} \tag{2.4}$$

Where I_{C0} is the critical switching current at 0 K. E_B is the barrier height, τ is the switching time and τ_0 represents the inverse of the attempt frequency. The read current must be much smaller than the median I_C because repeated write cycles result in a wide variation in I_C [38-39] to ensure non-destructive read.

2.1.3.6. Data Security

STTRAM brings new data security issues that were absent in volatile memory counterparts such as Static RAM (SRAM). This is primarily due to the fundamental dependency of this memory technology on the ambient parameters such as the magnetic field and temperature that can be exploited to tamper with the stored data. The free layer of MTJ flips under the influence of external

magnetic field and temperature that can be exploited by the adversary. As described in Equation 2.1, the adversary can place an external AC/DC magnetic field to alter the $\overrightarrow{H_{eff}}$ parameter resulting in an uneven flipping of bits under read, write and/or retention [40]. The magnetic field produced by a horseshoe magnet can be used to flip the bits in a STTRAM memory array [40]. Consequently, the magnetic field can be exploited by the adversary for scrambling the data in LLC to launch denial of service (DoS) attack or simply increase the miss rate affecting the overall performance of the system. The existing countermeasures to mitigate the magnetic attack include variable strength Error Correcting Code (ECC) and forced retention [40]. The strength of the ECC is increased (1bit/2bit/4bit/8bit) depending on the magnitude of the attack. A carefully orchestrated DoS attack can result in a severe consequence during the secure data processing and financial transactions to name a few. The magnetic attack can also be carried out when the system is OFF. However, such attacks will not affect the computation as the cache is invalidated on startup. The attacker can gain access to non-volatile data after the authentic user has signed out, by launching unauthorized read and write operation and probing the data buses [92].

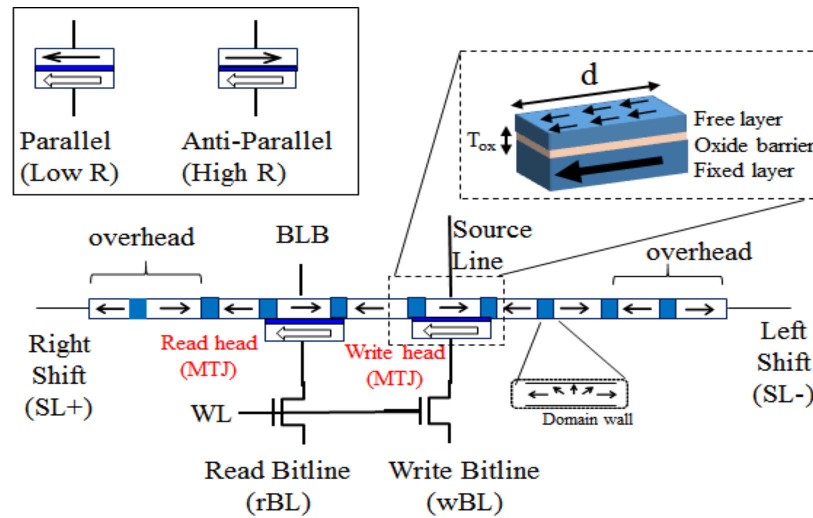

Figure 2.4 Schematic of a conventional Domain Wall Memory. The MTJ at read and write head and the overhead bits are also shown.

2.2. Design Fundamentals of DWM

2.2.1. Basics of DWM

DWM consists of three components: (a) write head, (b) read head, and (c) magnetic nanowire (NW). The read and write heads are similar to the conventional magnetic tunnel junction (MTJ) whereas NW holds the bits in the form of magnetic polarity (Fig. 2.4). The left (right) orientation can be regarded as '0' ('1'). The most interesting feature of the NW is the formation of domain walls (DWs) between domains of opposite polarities where the local magnetization changes its polarity. Dynamics of the NW is determined by the dynamics of DW. The DWs can be shifted forward and backward by injecting the charge current from left-shift (LS) and right-shift (RS) contacts. Note that the local moments change its orientation under the influence of current that gives the impression of DW propagation in the NW. In essence, the NW is analogous to a shift register. The new domains are injected by first pushing current through shift contacts to move the bits in lockstep fashion to bring the desired bit under write head. Next spin polarized current is injected through the write MTJ (using wBL and SL) in positive or negative direction to write a '1' or '0' in the NW. Read is performed by bringing the desired bit under read head using shift and sensing the resistance of MTJ formed by DW under the read head (using rBL). It should be noted that this new access mechanism makes shifting of DWs critical to the functionality of the memory. The robustness, speed and power consumption of the memory has a significant dependency on DW dynamics in the NW. A number of points that can be observed in this context are: (a) read and write operation is linked with shifting of bits, (b) buffering of bits is required to ensure that the useful bits are preserved in the NW. Therefore, only a fraction of bits from the NW can be used for computation defined as 'utilization factor' (UF), and (c) the shift latency depends on the offset from read/write heads. Hence, multiple heads are desirable to reduce the access latency, and (d) bitcell footprint depends on both the NW dimensions as well as the number and size of read/write heads.

2.2.2. Modeling of DWM

For the read and write head we utilized the hspice model of MTJ from nanohub [37]. The DW dynamics in the NW is modeled in verilog-A by solving the Landau-Lifshitz-Gilbert (LLG) for 1D motion [41]:

$$(1+\alpha^2)\dot{q} = \frac{\mu_0}{2}\gamma\Delta(H_k \sin 2\psi - \pi H_T) + \alpha\Delta\gamma\left(\mu_0 H_A - \frac{Vq}{M_s d}\right) + (1+\alpha\beta)u \tag{2.5}$$

$$(1+\alpha^2)\dot{\psi} = -\frac{\mu_0}{2}\alpha\gamma(H_k \sin 2\psi - \pi H_T) + \gamma\left(\mu_0 H_A - \frac{Vq}{M_s d}\right) + \frac{\beta-\alpha}{\Delta}u \tag{2.6}$$

Where, $\dot{q}$ and $\dot{\psi}$ are the time derivatives of the domain wall position and tilt angle respectively, α is the damping constant, β is the non-adiabatic spin torque transfer term, V is pinning potential, d is the pinning notch width, Δ is DW width parameter, M_s is saturation magnetization, H_k is demagnetization field, H_A and H_T is applied field and u is a scalar quantity having the unit of velocity. Term u depends on the current density J, the spin polarization P, saturation magnetization M_s and Bohr Magneton μ_B as follows:

$$u = \frac{\mu_B JP}{eM_s},\ \ \mu_B = \frac{\hbar e}{2m_e} \tag{2.7}$$

Table 2.2 Magnetic constants used for DW dynamics.

Parameter	Value
α	Varied (0.01 - 0.02)
β	Varied (0.0 - 0.1)
Bohr magneton(μB)	9.27e-24 J/T
Ms	8e5 A/m
Exchange Constant (A)	1.3e-11 J/m.
Length(l)/Width(w)/Thickness(t) of NW	1e-6 m/1e-7 m/10e-9 m
ɣ	1.76e11 /G s
Demagnetization Field (Hk)	1600~1800 Oe.

The detailed derivation of the above equation from LLG is provided in [11]. The values of constants used in the model are provided in Table 1. The DW velocity depends on the shift current. Higher current increases the DW velocity but increases the power consumption.

2.2.3. DWM Challenges

The DWM read and write heads are similar to conventional magnetic tunnel junction (MTJ), whereas NW acts as free magnetic layer, and holds the bits in the form of magnetic polarity. Hence, DWM design challenges includes all the challenges associated with MTJ such as limited TMR, stochastic switching, read disturb, and oxide breakdown as described in Section 2.1.3. However, there are other challenges involved with DWM:

2.2.3.1. Shift Latency

As mentioned earlier, shift operation is required to access a bitcell in DWM. The time needed to access a bitcell on a NW depends on its location with respect to the read/write port. Moreover, multiple shift operations are performed in single memory access to read/write all bits of data which poses significant latency and power overhead.

2.2.3.2. Segregated Read and Write Head

The conventional DWM contains segregated read and write heads (Fig. 2.4) to decouple read and write and make head design simple. Although it simplifies the design constraints due to separate read/write head design, this design incurs loss in bitcell density due to the dedicated access transistor and wiring for each head. Furthermore, the separate read and write heads is functionally redundant since both read and write operations cannot be performed simultaneously (unless the shifts need for read and write are identical). This makes the read head to wait until the write head has finished writing and appropriately shifts back the bits into its original place or vice versa.

2.2.3.3. Aspect Ratio Mismatch

DWM suffers from aspect ratio mismatch between NW and access transistor, since the NW is long and narrow and access transistor is wide. Therefore, DWM layout must be optimized to achieve the maximum memory density. In addition, since the shift circuitry is shared among all the local columns in a global column, the shift operation shifts all the NWs at the entire global column. This incurs substantial shift power overhead. Therefore, a gating mechanism is needed to avoid shifting of unassessed NWs.

2.2.3.4. Utilization Factor (UF)

As mentioned earlier, a certain number of bits per NW are dedicated for buffering the functional bits during shift. The number of heads and their positioning in the NW determine the amount of buffer space required for preserving the functional bits. For better bitcell density it is desirable to achieve higher UF which in turn depends on the number of heads, their positioning and the physical dimension of the NW.

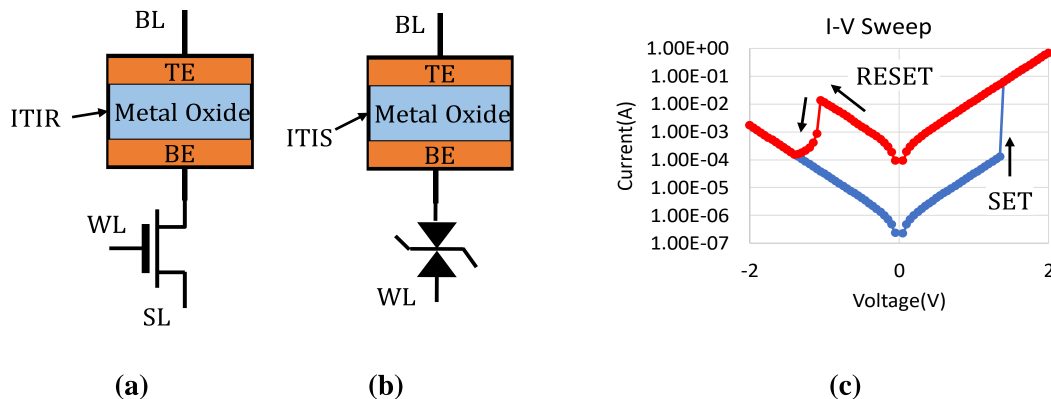

(a) (b) (c)

Figure 2.5 **(a)** Schematic of the 1T1R structure of RRAM; **(b)** schematic of the 1D1R structure of RRAM; and, **(c)** I-V curve of bipolar switching.

2.3. Design Fundamentals of RRAM

2.3.1. Basics of RRAM

As discussed in the first chapter, RRAM is a promising candidate to replace main memory due to small footprint and low standby power. The device structure is an oxide material sandwiched between two metal electrodes (i.e., Top Electrode (TE) and Bottom Electrode (BE)) called metal-insulator-metal (MIM) structure (Fig. 2.5(a)). RRAM bitcell consists of MIM and a selector device which can be either a transistor (1T1R structure as show in Fig. 2.5(a)) or a selector diode (1D1R structure) as shown in Fig. 2.5(b). The 1T1R cell provides the small footprint of 6 F^2 whereas footprint as low as 4 F^2 can be achieved by 1D1R structure in crossbar memory architecture. There are two types of resistive switching. One type is based on the formation of conductive filament (CF) consisting of oxygen vacancies which occurs in oxide-based RRAM. The second type is based on the conductive filament of metal atoms which is called conductive-bridge RAM (CBRAM). The oxide-based RRAM resistive switching is basically due to the mechanism of oxide breakdown which forms a conduction filament in the oxide. The switching from High Resistance State (HRS) to Low Resistance State (LRS) is called "SET" process, while the opposite switching is called "RESET" process. Usually, fresh RRAM samples require a voltage greater than SET voltage to

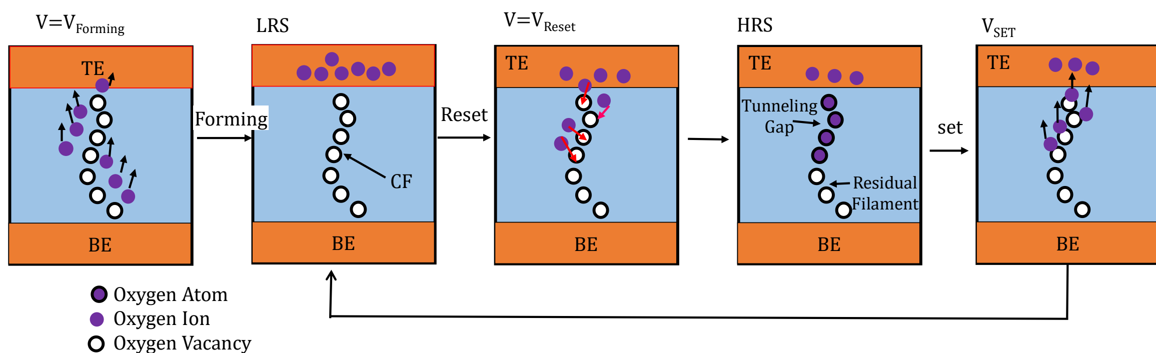

Figure 2.6 Forming, SET and RESET switching mechanism in RRAM.

trigger the resistance switching for the next cycles, which is known as the "forming" process. The resistive switching can be categorized into unipolar and bipolar switching. In unipolar RRAM, switching direction depends on the amplitude of the voltage across RRAM and does not depend on the polarity of applied voltage. Therefore, SET/RESET can take place at the same polarity. In bipolar switching, switching direction depends on the polarity of applied voltage. Thus, SET only occurs at positive polarity, while RESET occurs at negative polarity as shown in Fig. 2.5(c).

Typically, in oxide-based RRAM, resistive switching is associated with migration of oxygen ions between electrodes, resulting in the formation of conduction filament. As demonstrated in Fig. 2.6, during the forming process, soft dielectric breakdown due to high electric field leads to the drift of oxygen ions to anode interface. If the anode material is a noble metal, the oxygen ions are discharged as neutral non-lattice oxygen, while they react with oxidizable anode materials to form an interfacial oxide layer [42]. Therefore, the electrode/oxide interface acts as an oxygen reservoir [43]. In the LRS mode, the current flows through the CF. In the reset process, oxygen ions migrate back to the bulk to recombine with the oxygen vacancies which in turn reset the RRAM to HRS. In this thesis, switching model of HFO_2 based bipolar RRAM is used. HFO_2 has gained significant attention due to properties such as simplicity, low operating power and high speed [44].

2.3.2. RRAM Design Challenges

Even though RRAM provides good design metrics such as high density, low standby power, fast access time, and high resistance ratio, it suffers from low endurance, process variation, nonuniformity, and requires low-read voltage for prevention of read disturbance.

To avoid a permanent dielectric breakdown in the set process, it is essential to limit the current called compliance current. During formation/SET process, when CF is formed in the oxide material, the current flowing through RRAM increases abruptly. Therefore, a current limiter is

required to clamp the forming/SET current in order to prevent degradation of HRS and failure of memory device [45]. Due to lower high resistance at saturation region a transistor is a better current limiter. Large capacitance between transistor and RRAM must be avoided in design of 1T1R bitcell. Parasitic capacitance results in overshoot current during SET process which in turn increases the SET current.

RRAM suffers from poor nonuniformity due to extensive parameter variation such as variation of switching voltage as well as resistance variation in LRS and HRS. The variation of resistance switching includes temporal variation (cycle-to-cycle) and special variation (device-to-device). These variations are originated from the stochastic nature of the oxygen vacancies/ion process [46].

High density crossbar array which employs two terminal RRAM at the crosspoint of vertical and horizontal metal wires are proposed [47]. Nonetheless, these architectures suffer from sneak-path problem entailing a poor sense margin, higher power consumption, and limited array size.

Chapter 3

Robust and Low Power STTRAM Design

Conventional CMOS memory i.e., Static Random Access Memory (SRAM) has been the popular choice for embedded memory application for last several decades. However, SRAM seems to be approaching a brick wall. On one hand process variability and leakage power is posing severe obstruction towards SRAM scaling to future nodes and on the other hand, emerging energy-constrained and bandwidth hungry electronic gadgets demand for larger as well as energy-efficient on-chip cache which cannot be satisfied with SRAM. To address the changing landscape of consumer market, there is a corresponding need of changing the design paradigm. Several emerging memory technologies are on the horizon such as STTRAM, DWM and RRAM but there is no clear universal choice for embedded application. STTRAM is promising for Last Level Cache (LLC) due to numerous benefits such as high-density, non-volatility, high-speed, zero leakage, CMOS compatibility [48] and good endurance [4]. The crucial challenges involved in STTRAM are high write energy, long write time and poor sense margin. In this chapter, we propose circuit and architectural techniques to improve read yield, write latency and write power of STTRAM.

3.1. Introduction

Implementation of last level cache using STTRAM is widely investigated. It is accepted that STTRAM reduces the leakage power substantially. In [49] STTRAM is compared against SRAM and DRAM in a single-core processor architecture in terms of area, energy and performance. Then they have explored 3D microprocessor stacking with MRAM. Authors have explored STTRAM cache in multi-processor architecture and investigated costly write operation in

STT-RAM on power and performance [51]. Architectural evaluation of replacing on-chip DRAM with STTRAM has been investigated [50]. Authors proposed a dual-write-speed STTRAM architecture which benefits from the correlation between MTJ device write time and write current [53]. This method offers write latency improvement with relatively small memory cell size. The relationship between write latency and retention time to find optimal retention-time for STTRAM LLC has been explored in [54]. This paper explores adapting data retention time to match the required refresh time of LLC blocks to improve performance and save energy. Most of these works report more than 10% performance degradation due to employing STTRAM LLC architecture. Many works have been made to address the performance and energy overhead of STTRAM LLC. Architectural optimization has been proposed to recover dynamic energy due to store instruction by coalescing stores from L1 to the L2. The idea is to increase the residency of dirty lines in the L1 to accommodate all the stores to that line. This would prevent the line from being prematurely evicted to the L2 and being subsequently move back to the L1 on a near term store miss [58]. In [52], a hybrid design of SRAM L1 caches STTRAM L2 and L3 caches is proposed. Device-architecture space is explored to reduced write power by lowering the thermal energy to trade volatility [55-57]. It can be concluded that STTRAM is great potential to be used as an on-chip random access cache due to high density and low standby power. Moreover, circuit and architectural improvement can be employed to mitigate long write latency to achieve similar performance as that of SRAM cache. In this chapter, we investigate circuit and micro-architectural techniques to address these design challenges.

Due to poor TMR, the voltage/current differential between R_H and R_L decreases which degrades the SM. Furthermore, process variation reduces this difference even further results in poor sense margin. In this chapter, we propose, slope sensing, a destructive sensing technique to eliminate reference resistance variation. In addition, we propose a non-destructive sensing scheme

that exploits a voltage feedback and boosting (VFAB) technique to develop large sense margin. This technique reduces the sensing power significantly by eliminating static current.

We observe that process variation can result in large spread in write and read latency variations. The performance of conventionally designed STTRAM cache can degrade as much as 10% due to process variations. We propose a novel and adaptive write current boosting to address this issue. In this method, the bits experiencing worst-case write latency are fixed through write current boosting.

In summary, we make following contributions in this chapter:

- We propose a destructive slope detection technique using sampling techniques in order to detect MTJ resistance when it switches from high to low resistance state. We have designed a test-chip and performed thorough characterization. We characterized the slope sensing technique with respect to various design parameters such as sampling frequency, ramp current slope, TMR and various flavor of MTJ resistance.
- We propose a low-power and robust STTRAM sensing which exploits voltage feedback and boosting (VFAB) techniques to achieve large sense margin. We perform detailed process and temperature variation analysis to evaluate robustness of VFAB technique.
- We investigate the impact of process variations on the write latency of STTRAM and propose a methodology to enable write current modulation adaptively to mitigate process variation induced write latency degradation.

3.2. Improving Read Yield of STTRAM Array

Sense margin of STTRAM depends on TMR `which is defined as 100*(R_H-R_L/R_L) where R_L and R_H are low and high resistance of MTJ respectively. Due to poor TMR, the voltage/current differential between R_H and R_L decreases which degrades the SM. Furthermore, As described in

Section. 2.1.3.3, process variation induces large spread in low and high resistance states. The limited TMR and process variation result in poor sense margin. Poor sense margin can result in wrong interpretation of the MTJ state. The STTRAM sensing can be categorized into non-destructive and destructive sensing. In conventional non-destructive voltage sensing, data MTJ resistance is compared against reference MTJ resistance (which is an average of fixed high and low MTJ resistances). Therefore, it suffers from reference resistance variation in addition to data resistance variation. Moreover, sensing is associated with applying a static current into data leg and two reference legs which results in high power consumption. In addition, non-destructive sensing suffers from read disturb. Destructive sensing involves with writing into bitcell that results in significant power and latency overhead. However, destructive sensing eliminates bit-to-bit process variation in MTJ resistance which in turn improves read yield drastically. In addition, ` it suffers from failures due to unoptimized selection of data and reference currents.

In this Section, we investigate two sensing techniques to improve sense margin. First, we propose a novel slope detection technique to exploit MTJ resistance switching from high to low state using low-overhead sample-and-hold circuit. The proposed sensing technique is destructive in nature and eliminates reference resistance variation. Second, we propose a non-destructive and low-power sensing scheme that exploits a voltage feedback and boosting (VFAB) technique to develop large

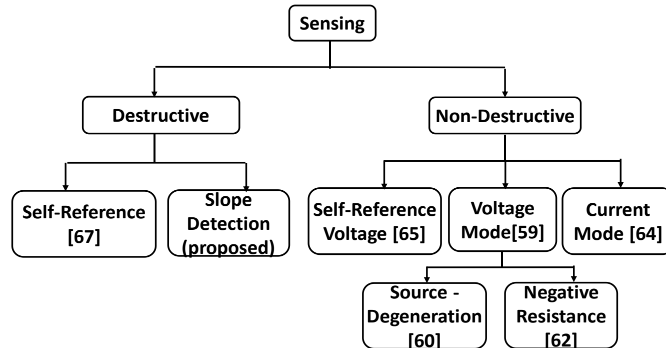

Figure 3.1 Taxonomy of STTRAM sensing schemes.

sense margin. Furthermore, VFAB does not requires a static current to be injected into data and reference STTRAMs which results in significant power saving.

3.2.1. Classification of Sensing Techniques

Fig. 3.1 shows the taxonomy of various sensing techniques. STTRAM sensing can be broadly categorized into *destructive* and *non-destructive* sensing. Several techniques have been proposed under non-destructive sensing. A non-destructive voltage sensing and a sizing methodology to improve the SM of MRAM arrays has been proposed in [59]. Source degeneration scheme is proposed in [60][91] to reduce large sense margin variation. Self-body biasing technique has been proposed in [61] to resolve the small sense margin issue in conventional voltage sensing scheme. In this scheme threshold voltage of load PMOS transistor is adaptively controlled by body bias. Negative resistance read and write technique has been described in [62] to eliminate read disturb and reduce the write power. Reference voltage (V_{ref}) biasing has been explored in [63] to shift margins between polarities to improve the robustness. A non-destructive current mode

sensing scheme using current conveyor has been proposed in [64]. In [65-66], a nondestructive self-reference sensing scheme has been proposed by leveraging the dependency of high and low resistance state of the MTJ on the cell current amplitude. Even though this scheme reduces the read latency and power by eliminating two write steps, the sense margin is much smaller than destructive self-reference scheme and conventional nondestructive voltage sensing.

Under destructive sensing, a self-reference sensing has been proposed in [67] to eliminate bit-to-bit process variation in MTJ resistance. Sensing is performed by first storing the voltage of the MTJ by passing a current (I_1), and then after a time interval storing a reference voltage of the same MTJ by passing current (I_2). The variation in MTJ resistance can be eliminated using this self-reference sensing scheme. Although this mechanism incurs high power consumption and long

Table 3.1 Parameters used for process variation study.

Device	Parameter	Mean	Std. Dev.
PMOS	V_{TH}	460 mV	$A_{V_T}/\sqrt{wL}$
NMOS	V_{TH}	500 mV	$A_{V_T}/\sqrt{wL}$
MTJ	MgO Thickness	1.2nm	2%
	Shape Area	100nm*50nm	10%

read latency due to two write steps, it provides high sense margin and eliminates the need of reference voltage.

3.2.2. Background

3.2.2.1. Non-destructive Voltage Sensing Scheme [59]

The sense circuit identifies the resistance of the data MTJ. In order to make the comparison, data MTJ resistance is compared against reference MTJ resistance (which is an average of fixed high and low MTJ resistances). Fig. 3.2 (a) shows the typical voltage sensing where a reference current is injected in both data leg and reference legs and the resulting voltage is compared by a voltage sense amplifier. Poor sense margin can result in wrong interpretation of the MTJ state. For example, if the offset voltage of the sense amplifier (SA) is +/-25mV, a sense margin of 25mV can be read as either ‘0’ or ‘1’.

3.2.2.1.1. Impact of process variation

MTJ model [37] is used in order to perform process variation analysis. Process-variations for read operation is modeled by incorporating variations in MTJ as well as access transistor [68]. For MTJ we have assumed tunnel oxide barrier and surface area variations. The variations in access transistor is lumped in threshold voltage fluctuation. The mean and standard deviation of these

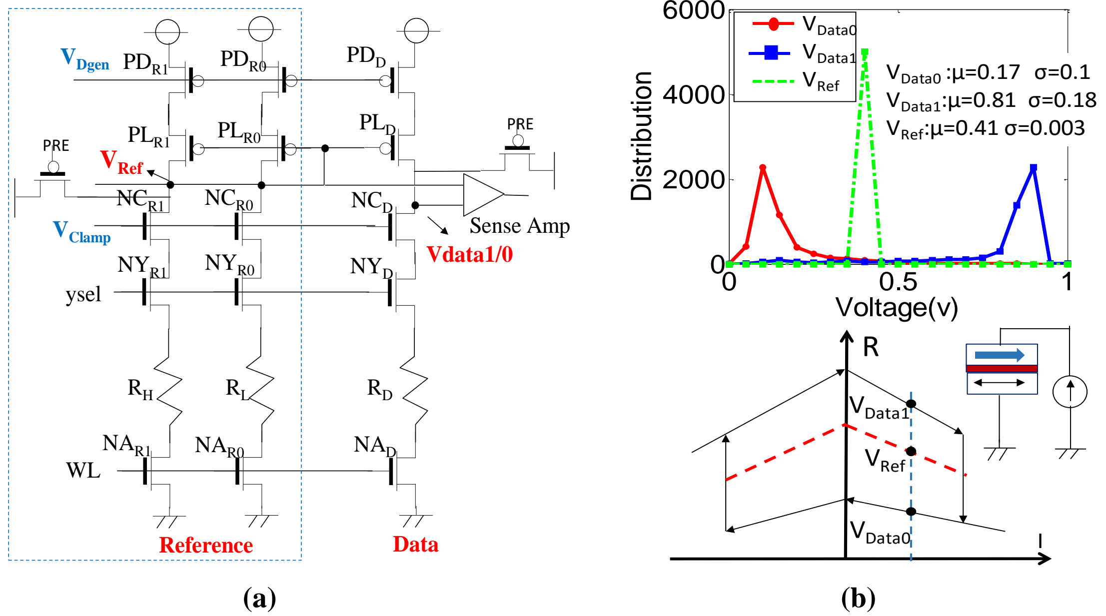

Figure 3.2 (a) Non-destructive sensing scheme; (b) Data0, reference and Data1 voltage distributions.

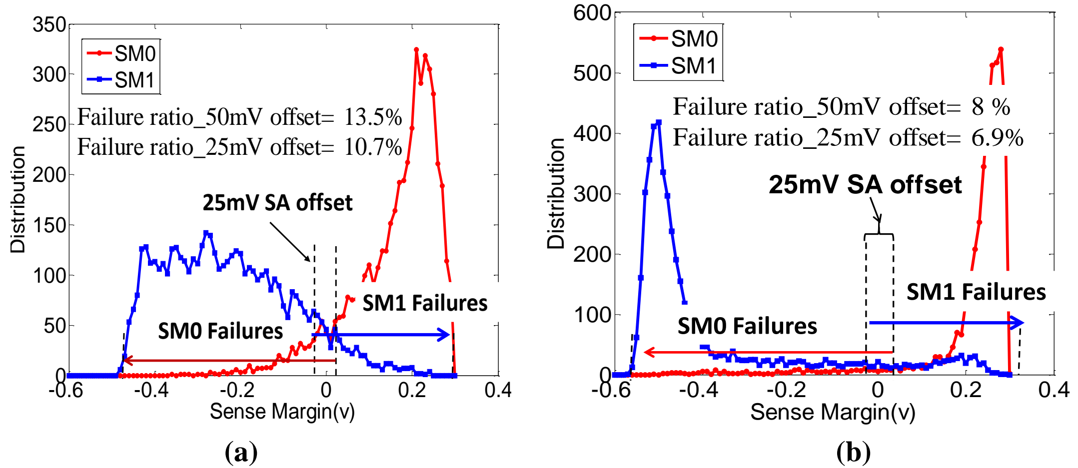

Figure 3.3 SM0 and SM1 distribution for 10000 Monte-Carlo points; (a) original scheme [59]; and, (b) with source degeneration [60].

parameters are provided in Table 3.1. In non-destructive sensing, resistance of data MTJ is compared against the resistance of reference MTJ to determine the bitcell content. Therefore, reference resistance as well as data resistance variation may result in wrong interpretation of bitcell

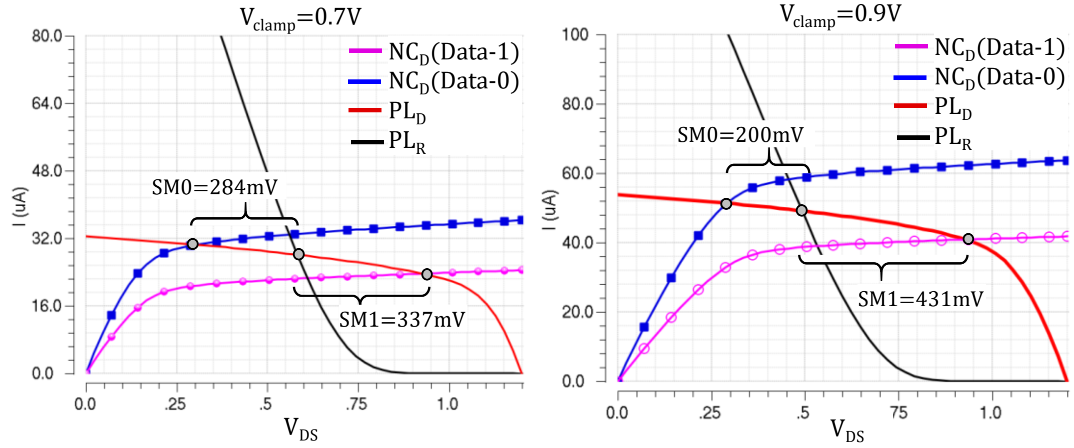

Figure 3.4 The impact of clamp voltage on sense margin for V_{Clamp}=0.7V and V_{Clamp}=0.9V.

content. Data0, Data1 and reference voltage distributions and $R_{H,}$ R_L and R_{Ref} resistance distributions are shown in Fig. 3.2(b). Sensing error occurs where reference voltage overlaps with Data0/1 voltage.

Two critical transistors in STTRAM sense circuit are the PMOS load (PL) and NMOS clamp (NC) (Fig. 3.2(a)). The clamp voltage and clamp transistor size sets the current in the leg. The load transistor sets the output voltage (where the NMOS and PMOS drain currents intersect). The mismatch between matched-pair transistors in the sense circuit degrades the sense margin. Since size of PL is smaller than NC transistor, the sense margin is most sensitive to mismatch between the PL transistors of reference legs (PL_R) with that of data leg (PL_D). One sigma of V_T variation is given by following equation [68]:

$$\sigma_{V_T} = \frac{A_{V_T}}{\sqrt{W.L}} \tag{3.1}$$

Where W and L are the width and length of the transistor and A_{V_T} is pelgrom coefficient. Sense circuit is designed to reduce the impact of process variation on SM. This goal is achieved by increasing the width and length of PL transistors to reduce the V_T mismatch between PL_D and PL_R, and optimizing other design parameters (NC width, V_{clamp} and V_{Ref}) to maximize both SM0

and SM1. Distributions of SM0 and SM1 for 10000 Monte-Carlo points are depicted in Fig. 3.3 (a). Simulations reveal that 10% of bitcells fail sensing due to SM0 failures and 11.2% fail due to SM1 failures which result in 10.7% total failures for 25mV SA offset. It is evident that non-destructive conventional sensing is prone to process variation. To reduce the large sense margin variation, the source degeneration scheme is used with longer channel length for PL transistors [60]. Source degeneration PMOS (PD) is added to the source of PL transistors to reduce current variation and increase effective resistance which results in SM improvement. Fig. 3.3(b) shows SM0 and SM1 distributions for 10000 monte-carlo points with source degeneration scheme. The simulation reveals 4.7% SM0 failures and 11% SM1 failures which result in 6.9% total failures for 25mV SA offset. Although source degeneration reduces SM0 failures, SM1 failures are still significant which underscores the need for a self-reference scheme to eliminate bit-to-bit variation as well as the mismatch between matched-pair transistors in data and reference legs.

As shown in Fig. 3.4, as clamp voltage increases SM0 reduces while SM1 increases. Therefore, clamp voltage can be exploited as a knob to make a trade of between SM0 and SM1 to minimize the sensing failures. The mismatch between matched-pair transistors in the sense circuit as well as reference resistance variation degrades the sense margin.

3.2.2.2. Destructive Self-reference Sensing Scheme [67]

In self-reference sensing, voltage generated by the data current across the MTJ, and the voltage generated by a reference current across the same MTJ are compared. Therefore, the bit-to-bit variation in MTJ resistance is eliminated. Self-reference sensing scheme works as follows (Fig. 3.5):

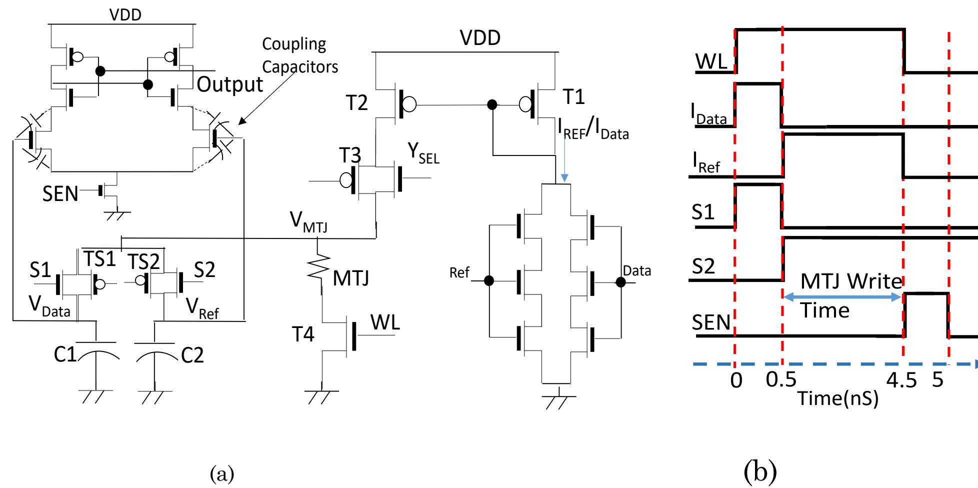

(a) (b)

Figure 3.5 (a) Self-reference sensing scheme; and, (b) sense circuit timing diagram is also shown.

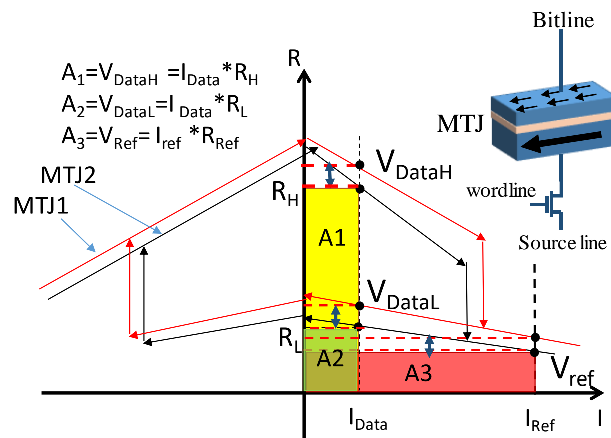

Figure 3.6 I-R characteristics of the two MTJs under process-variation. A variation in resistance can change the sense margin.

1) A read current I_{Data} is injected into bitcell and the resulting voltage is stored in a capacitor C_1. The voltage could be V_{DataH} (V_{DataL}) if the MTJ resistance is high (low).
2) A zero is written into the MTJ.
3) Another read current I_{Ref} is applied to generate voltage V_{Ref} which is stored in capacitor C_2.
4) V_{Data} and V_{Ref} are compared to determine the bitcell content.
5) The read data is written back to the MTJ.

Considerations for process-variations is important to determine appropriate values of I_{Ref} and I_{Data}. I-R curves of the two MTJs under process variation are shown in Fig. 3.6. If a current is injected from bitline to source line, MTJ switches from high-to-low resistance state. In contrast, if a current is injected from source line to bitline the MTJ is switches from low-to-high resistance state. The I_{Data} and I_{Ref} must be chosen in such a way that to make SM0 positive and SM1 negative. Therefore, the area A3 (which is essentially voltage) should be greater than A2 and less than A1, which results in following inequalities:

$$V_{DataL} < V_{Ref} < V_{DataH} \quad (3.2)$$

$$SM0 = V_{Ref} - V_{DataL} > 0$$

$$SM1 = V_{Ref} - V_{DataH} < 0$$

3.2.2.2.1. Impact of process variation:

To understand the impact of process variation on data and reference current requirement we sweep the bitcell current from bitline to source line. If the bitcell state is low, the voltage across MTJ increases monotonically with current. However, if the bitcell state is high, it switches to low resistance state beyond the critical current. Therefore, the voltage changes from high-to-low. As depicted in Fig. 3.7, I_{Ref} and I_{Data} should be chosen carefully to ensure +ve SM for high data and –ve SM for low data. Therefore, V_{Ref} should be greater than V_{DataL} and less than V_{DataH} where V_{DataL} (V_{DataH}) is the voltage across the MTJ when the stored data is low (high). From Fig. 3.7(a), the optimum I_{Data} is the current which maximizes SM0+SM1 (i.e., the current where V_{DataH} is maximum). Optimum I_{Ref} is chosen in such a way to equalize SM0 and SM1. Fig. 3.7(b) shows the optimum I_{Data} variation which results in optimum I_{Ref} variation. We have evaluated two cases for determining robust reference and data current:

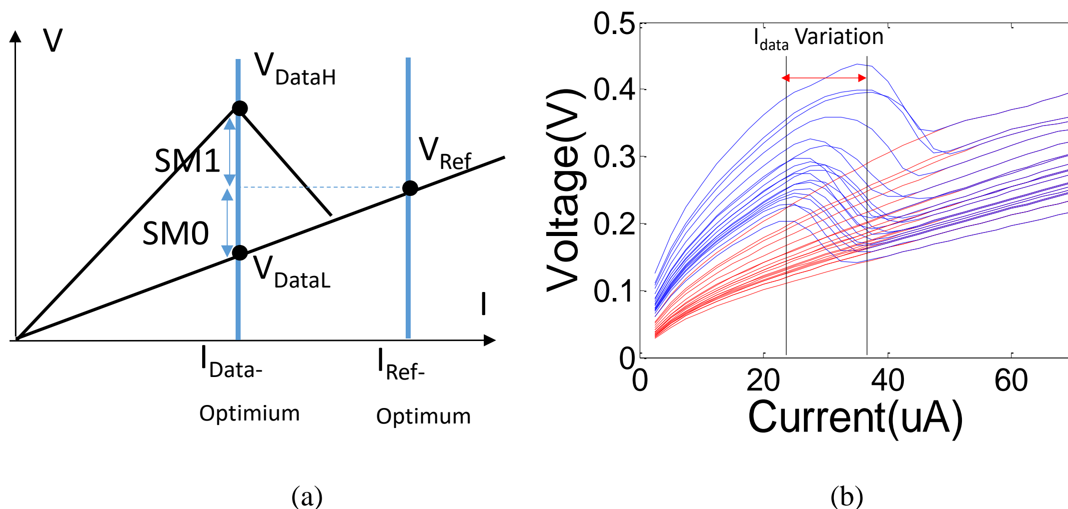

(a) (b)

Figure 3.7 (a) V-I curves of an MTJ with high and low resistance states initially; and, (b) optimum data current variation.

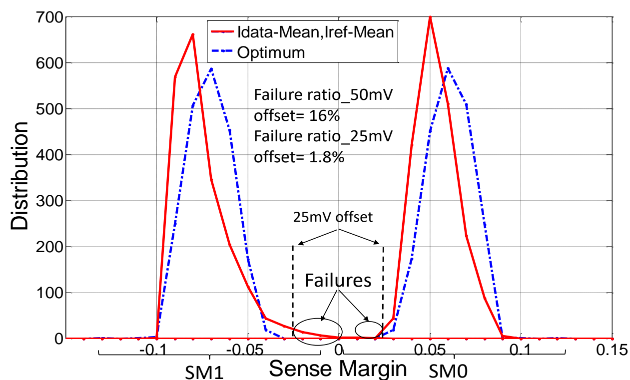

Figure 3.8 Sense margin distribution for 5000 Monte Carlo points.

Case-(a) (Optimum): data and reference currents are bit-to-bit optimal to maximize the sense margins.

Case-(b) (I_{Data}-Mean, I_{Ref} – Mean): both data and reference current are the mean value of the current distribution.

Fig. 3.8 shows the SM distribution for 5000 Monte-Carlo points for cases (a) & (b). Case-(a) provides a distribution with lowest standard deviation and higher mean value which results in good sense margins for all bitcells and provides minimum number of failures. However, the number

of failures increase significantly (failure ratio of 1.8%) in case-(b). In addition, SM failure ratio increase to 16% for case-(b) for 50mV SA offset. Even by providing optimum data and reference current for each bitcell, failure ratio is 9.5% for 50mV SA offset. *Hence, there is a need to develop a sensing scheme which eliminates data and reference current.*

3.2.3. Proposed Slope Sensing Technique

To eliminate bit-to-bit process variation as well as data and reference current, we propose a reference-less, destructive slope detection technique which exploits the MTJ switching from high to low state to detect memory state. We design a proof-of-concept test-chip using 96kb mimicked STTRAM (using passive resistors) bits in 65nm technology to validate the proposed slope sensing circuit. The resistor values are matched with the experimentally calibrated simulated models to capture the process variations in real MTJ. A single mimicked STTRAM bitcell contains both low and high resistors in parallel and the switching circuit is designed to match the switching latency of real MTJ.

(a) (b)

Figure 3.9 (a) Slope detection sense circuit; and, (b) simplified timing diagram.

3.2.3.1. Slope Sensing Basic Operation

If the MTJ resistance is low, it will only switch with a negative current. The resistance will remain low for positive current. We also note that slope of MTJ V-I curve changes from positive to negative during switching of resistance. Therefore, we propose to sense the change in slope of voltage to detect the MTJ state. A ramp current is injected into bitcell which results in a ramp voltage. If the MTJ resistance state is high initially the slope of voltage will change from positive to negative as the MTJ resistance switches from high to low resistance state while the voltage slope will remain positive if the resistance of MTJ is low initially. Therefore, sensing problem can be simplified to slope detection. If a negative slope is detected then the data is sensed as '1', else the data is sensed as '0'. We used high speed sample and hold circuit to detect the slope of voltage across bitcell (Fig. 3.9(a)).

Fig. 3.9(a) shows the proposed sensing circuit with features to inject the ramp current and sample the ramp voltage. The slope of ramp voltage will change from positive to negative if the MTJ switches from high to low resistance. The voltage slope remains positive if MTJ resistance is initially low. The slope detection is performed by sampling the ramp voltage with two sample-and-hold circuits using clocks ϕ_1 and ϕ_{1d} (delayed ϕ_1). The sampled voltages are stored in C_1 and C_{1d} respectively. Finally, V_{C1} and V_{C1d} are compared at the edge of sense amplifier enable (SE). Simplified timing diagram is shown in Fig. 3.9(b).

As shown in Fig. 3.10(a), white triangles are voltages sampled by ϕ_1 and black triangle are voltages sampled by ϕ_{1d}. The sense amplifier is enabled after the black triangles. As a result, two consecutive black and white triangle sampled voltages are compared. It is evident that the SM is

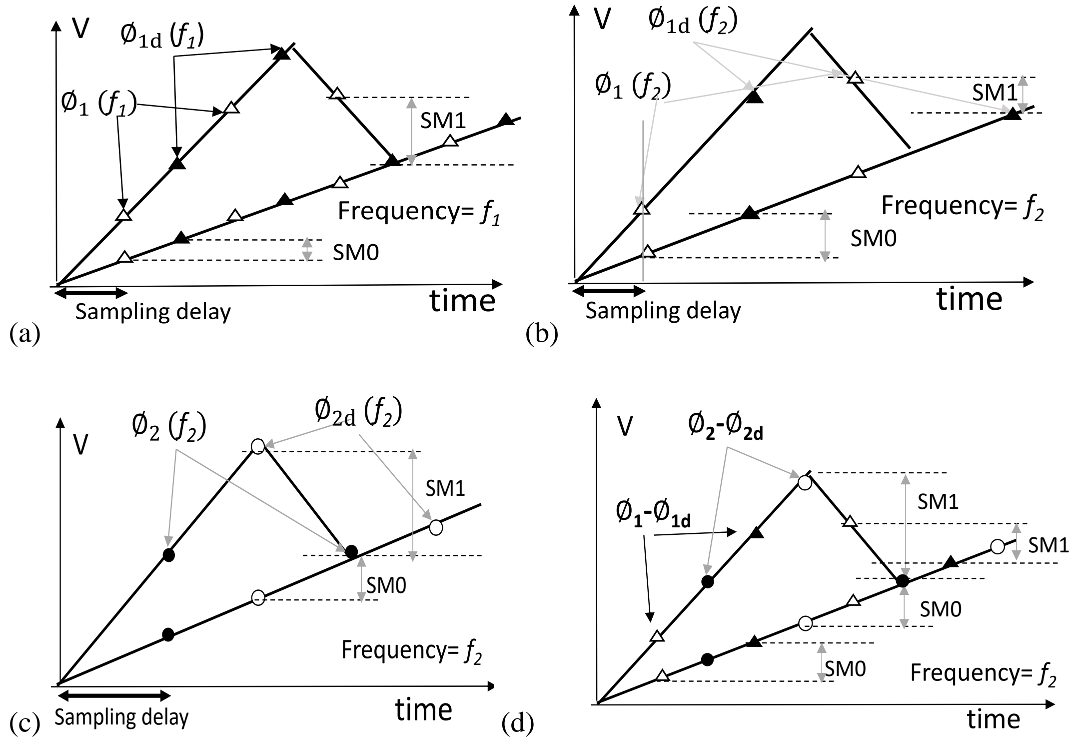

Figure 3.10 Sampling voltage across MTJ: (a) sampling with frequency f_1 *and* $\varnothing_1$-$\varnothing_{1d}$ clock phases which provides poor SM0 and large SM1; (b) sampling with frequency f_2 ($f_2 = f1/2$) and $\varnothing_1$-$\varnothing_{1d}$ clock phases which provides large SM0 but poor SM1; and, (c) double sampling with frequency f_2, $\varnothing_1$-$\varnothing_{1d}$ and $\varnothing_2$-$\varnothing_{2d}$ clock phases which results in large SM0 and SM1 while ensure capturing negative slope.

positive in positive slope region and negative in the negative slope region. Sense margin depends on sampling frequency, slope of ramp current and MTJ switching time. We have implemented design-for-test features to test the sensing failure by sweeping these parameters. By increasing the ramp current slope, the voltage difference between two consecutive samples will increase which results in higher SM. However, the buffer output voltage (V_{BUFO}) may be clamped at V_{DD} by further increasing the ramp current slope which results in SM loss.

3.2.3.2. Double Sampling

Fig. 3.10 shows impact of two sampling frequencies on sense margin. Note that lower sampling frequency results in more Sense-0 Margin (SM0) since the voltage difference of two consecutive samples is higher as shown Fig. 3.10(b). However, decreasing sampling frequency might cause an error in negative slope detection due to poor SM1. Sampling at higher frequency ensures negative slope detection. However, SM0 loss due to higher sampling frequency results in increased failures (Fig. 3.10(a)). As shown in Fig. 3.10(b), sampling with frequency f_2 (where $f_2 = f_1 /2$) and ϕ_1-ϕ_{1d} clock phases provides poor SM1 after MTJ flipping while sampling with frequency f_1, ϕ_1-ϕ_{1d}, provides larger SM1. *In order to obtain the desired number of samples at lower sampling frequency to ensure negative slope detection (higher SM1) as well as higher SM0, double sampling technique is proposed.*

Double sampling can be implemented by lowering sampling frequency and using two sets of sample-and-holds (S/H) with ϕ_1-ϕ_{1d} and ϕ_2-ϕ_{2d} clock phases (where ϕ_2 and ϕ_{2d} are delayed ϕ_1 and ϕ_{1d} respectively) to sample voltage across bitcell. Hence two groups of sample-and-hold circuits (SC) are used. From Fig. 3.10(d), sense amplifier is activated after ϕ_{2d} (black circle) and ϕ_{1d} (black triangles). Therefore, SM is the difference between black and previous white circle voltages which is sensed by 1st sense amplifier or black and previous white triangle voltages which is sensed by 2nd sense amplifier. In the proposed double sampling method, if one of sense amplifiers detects negative slope (SM1) the output is ‘1’ otherwise it is ‘0’. Therefore, the SM1 is the maximum absolute value of SM1 which is provided by two sets of S/H circuits. From Fig. 3.10(b-c), it can be noted that sampling with frequency f_2 and ϕ_1-ϕ_{1d} provides poor SM1 while sampling with frequency f_2 and ϕ_2-ϕ_{2d} provides large SM1. Therefore, double sampling with both ϕ_1-ϕ_{1d} and ϕ_2-ϕ_{2d} clock phases provides large SM1 as well as large SM0. Sampling is performed during sense time (T_{Senes}). Sense time is determined in such a way to ensure all bitcells in high resistance will switch to low

resistance state under process variation. Note that sampling accuracy and robustness can be improved by increasing the number of sample-and-holds and lowering the sampling frequency to achieve larger SM1 and SM0 at the cost of more sense amplifiers.

3.2.3.3. Test Chip Implementation

In this section, we explain the subarray architecture with integrated slope sensing circuit and the test chip design.

3.2.3.3.1. Slope Sensing Circuit Design

Fig. 3.11 depicts the implementation details of slope sensing with two SCs to enable double sampling. To mimic MTJ resistance in the test-chip we used poly resistance. The bitcell contains two high resistances (R_H) and two access transistors (Fig. 3.11). The bitcell is in high resistance state if WL1 is activated and is in low resistance state if both WL1 and WL2 are asserted (two R_H are connected in parallel). In order to mimic the switching time variation, we have incorporated a knob to fire WL2 at different times. Our design matches the real MTJ parameters such as, MTJ

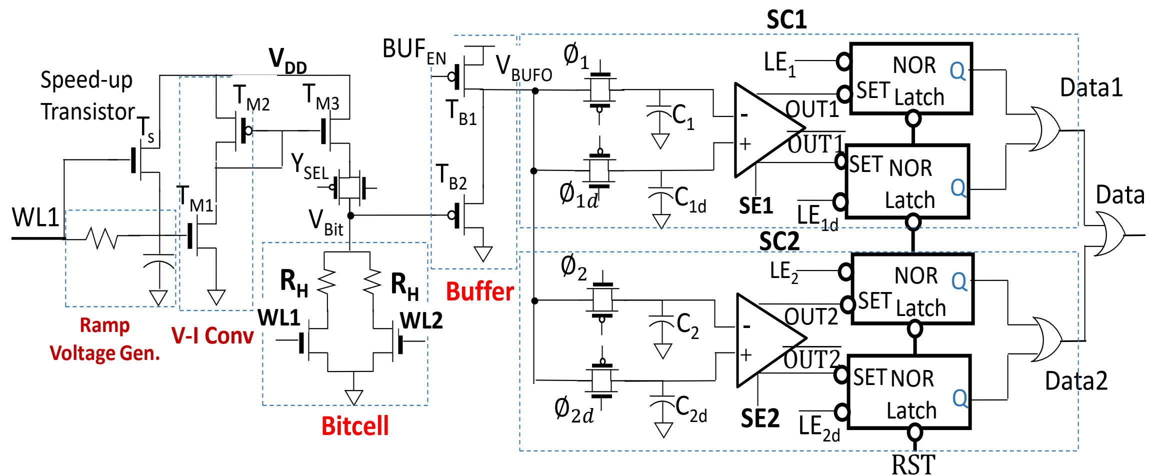

Figure 3.11 Implementation details of slope detection sense circuit.

resistance, switching time and TMR variability using experimentally calibrated simulation models [37] (details in Section 3.2.3.2.2) and serves as a solid proof-of-concept for the slope sensing scheme.

The ramp current is generated using RC low pass filter to generate a ramp voltage. The output of low pass filter is connected to gate of an NMOS transistor (T_{M1}) to generate a ramp current. Since the T_{M1} is OFF for voltages less than threshold voltage, a speedup transistor (T_S) is used to charge the capacitor rapidly to threshold voltage of T_{M1} in order to speed up the ramp current generation process. Next, the ramp current is injected in to bitcell using a PMOS current mirror

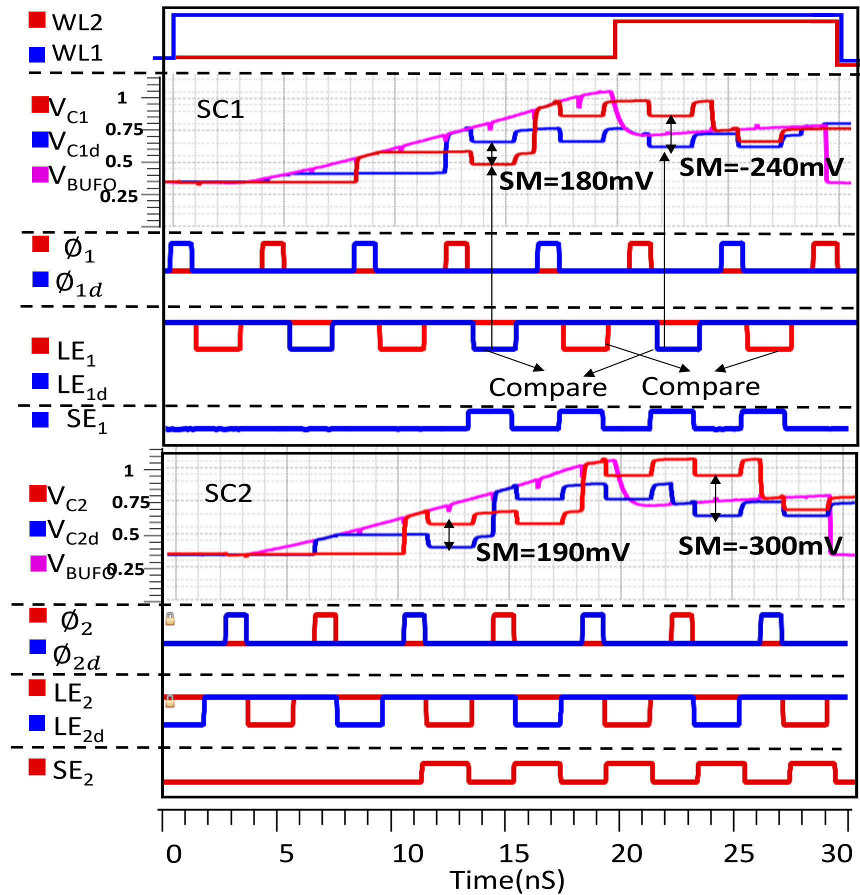

Figure 3.12 Post layout simulation of slope sensing scheme along with timing diagram for sense circuit-1(SC1) and SC2.

which in turn generates a ramp voltage (V_{BIT}) at the input of PMOS source follower buffer (T_{b1}). In order to reduce the buffer offset voltage, width of T_{b1} is larger than T_{b2}. Therefore, buffer offset is approximately the threshold voltage of T_{b1}. In order to reduce the offset voltage further, we use a transistor with low threshold voltage to provide enough headroom for output voltage swing. This reduces the buffer offset voltage to 330mV.

Fig. 3.12 shows post layout simulation of slope sensing. To perform comparison between every two consecutive samples we exploited two NOR latches and two active-low latch enables (LE_1 and LE_{1d}) for each sense circuit. Comparison is performed at the SE edge. However, the comparison result is stored in the latches at the LE edge. Since OUT1 is connected to latch with LE_1, $V_{C1}>V_{C1d}$ (OUT is 0 when $V_{C1}>V_{C1d}$) indicates negative SM as a result a '1' will be stored into latch (when OUT=0, '1' will be latched). The latch with LE_{1d} is connected to $\overline{OUT1}$, thereby, $V_{C1}<V_{C1d}$ indicates negative SM and output will be set to '1'. The outputs of two latches are ORed which indicates that the output is set to '1' if one of the latches capture the negative slope. Bottom figure shows the timing diagram of SC2. The SC2 result in higher SM1 compared to SC1 (-240mV vs -300mV). If one of the sense circuits outputs '1' the double sampling results in '1' since outputs of two SCs are ORed. We designed a test feature to select between single and double sampling to study their impact on sensing errors.

3.2.3.3.2. Impact of Process Variation

In order to mimic MTJ using poly resistance, Monte Carlo simulation is performed to characterize the behavior of MTJ under process variation. MTJ model [37] is used in order to perform process variation analysis. For MTJ we have assumed tunnel oxide barrier thickness and

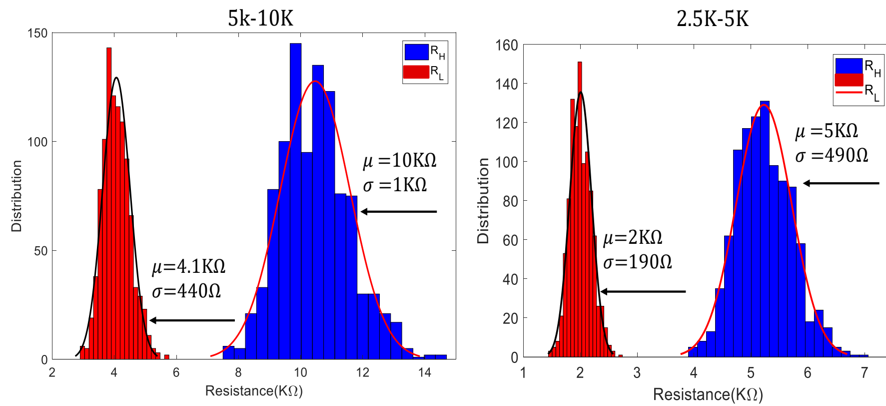

Figure 3.13 Low and high resistance distribution for 1000 points Monte Carlo simulation for, (a) 5K-10K, and (b) 2.5K-5K.

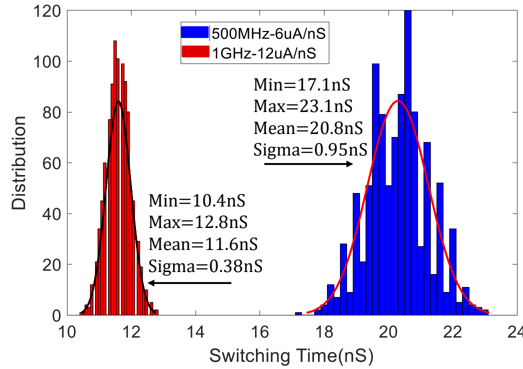

Figure 3.14 MTJ switching time distribution for 6uA/nS and 12uA/nS ramp current slopes for 1000 Monte Carlo points.

surface area variations. The mean and standard deviation of these parameters are provided in Table 3.1. MTJ is characterized in terms of switching time and resistance variation by performing 1000 points Monte-Carlo simulations. Fig. 3.13 shows the R_L and R_H variation for two MTJ configurations under the read operation condition. The model implements a MTJ with TMR of 150%. However, in order to investigate the read failures aggressively, we assume TMR of 100%. Different MTJ resistances is achieved by modifying the MTJ surface area (90nm*30nm for 5K-10K and 50nm*100nm for 2.5K-5K). We consider MTJ area and oxide thickness variation reported [69-70] using the MTJ model. It can be observed that one sigma of resistance variation is around 10% which matches the MTJ variation reported in [71][65]. We have incorporated test features in

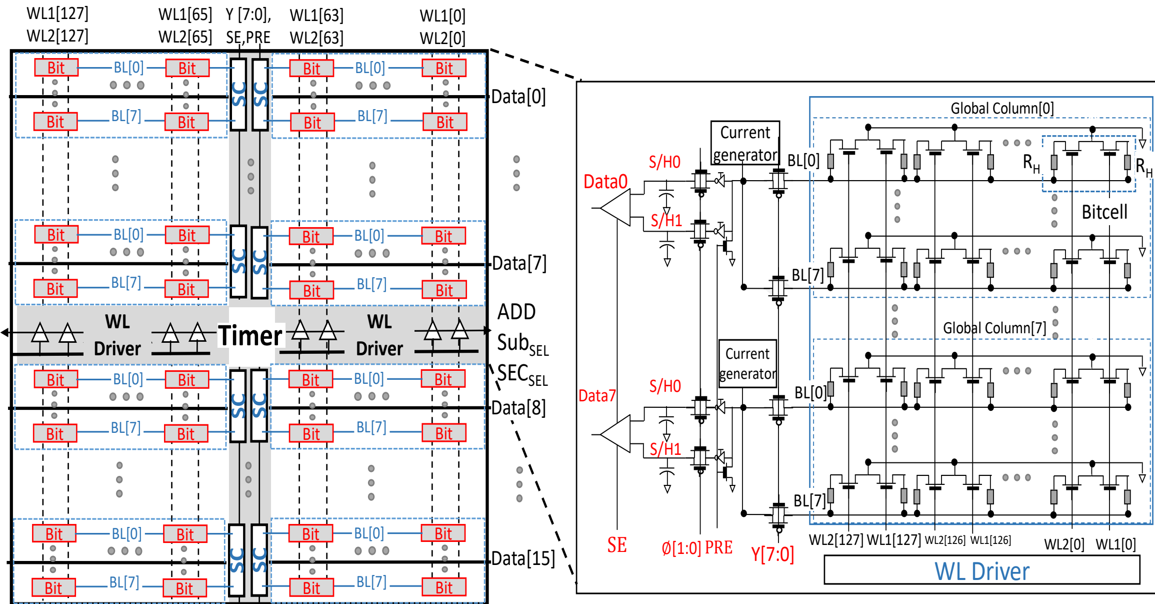

Figure 3.15 Subarray architecture. The sector architecture is shown in inset.

the test chip to tune the resistance by -10%, -20% and +10% +20% to mimic the MTJ resistance variation.

The MTJ switching time variation is obtained by performing 1000 points Monte Carlo simulation for different ramp current slope. As mentioned earlier faster system clock frequency (1GHz) results in shorter WL1 period (sensing duration) which in turn demands higher ramp current slope (12 uA/nS). Fig. 3.14 depicts the MTJ switching time for 6uA/nS and 12 uA/nS ramp current slopes. Note that the sigma for both cases are almost 5% (half of clock period). We have incorporated the test feature in the test chip to mimic the MTJ switching time by enabling the WL2 at various clock cycles.

3.2.3.3.3. Array Architecture

Fig. 3.15 shows the array architecture. To study the effect of resistance value on sensing we implemented array of 2.5K/5K and 5K/10K MTJ resistances. The resistances are tunable by +/-20% to explore the effect of TMR variation on sensing errors. To characterize slope sensing we

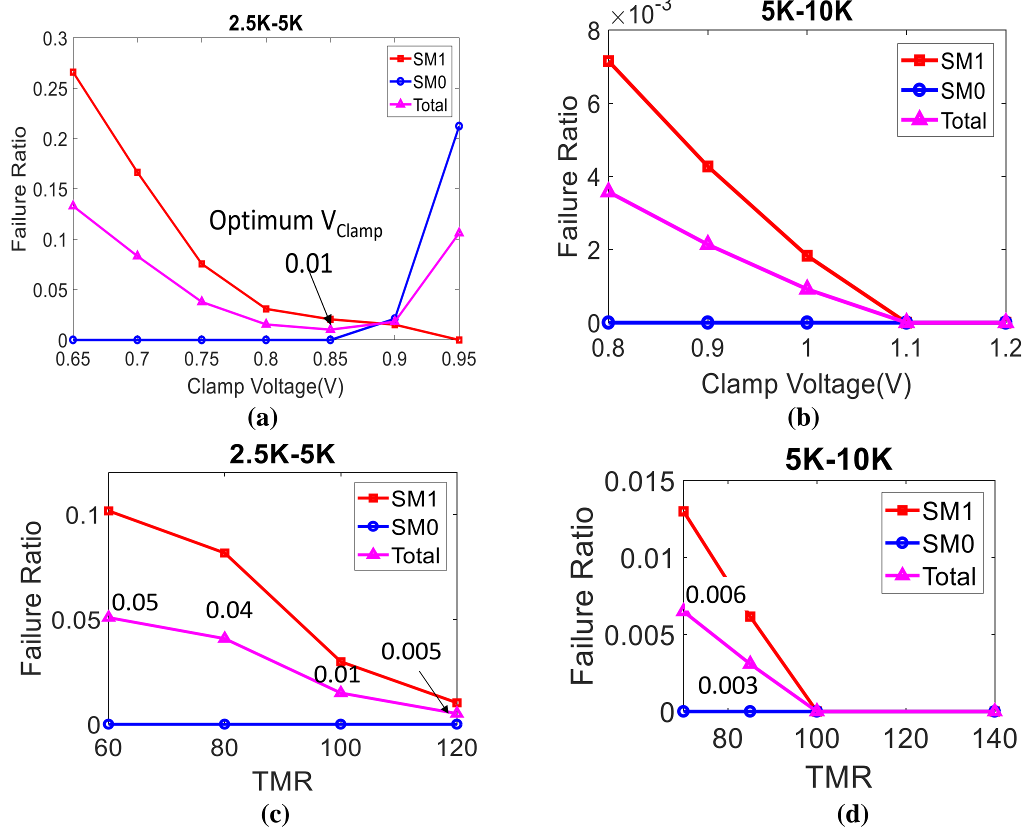

Figure 3.16 Experimental results: (a)-(b) Conventional sensing failure ratio with respect to clamp voltage for 2.5K-5K and 5K-10K arrays for TMR of 100%; and, (c)-(d) failure ratio with respect to TMR for 2.5K-5K and 5K-10K arrays with optimum clamp voltage.

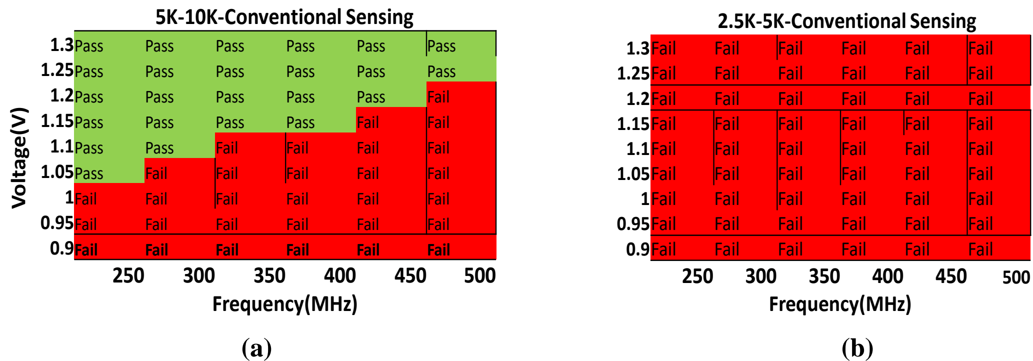

Figure 3.17 Experimental results: Conventional sensing shmoo plot with TMR of 100% and optimum clamp voltage for (a) 5K-10K array; and, (b) 2.5K-5K array.

swept clock frequency from100Mhz to 500MHz (sampling frequency is 1/4th of the clock frequency), ramp current slope (5 to 14 uA/nS) and MTJ switching time (9 to 12ns). For conventional sensing, we swept clamp voltage (V_{clamp}).

3.2.3.4. Test Results

In this section, first we explain the conventional sensing experimental result and the impact of TMR and clamp voltage on the sensing failures. Next, we describe the experiential results that presents the impact of ramp current slope, sampling frequency, switching time on sensing failure. Moreover, we depict the shmoo plot as well as impact of process variation on sensing failures. Finally, we compare the conventional sensing failures against slope sensing.

3.2.3.4.1. Conventional Sensing Test Results

Fig. 3.16(a)-(b) shows the conventional sensing failures vs V_{clamp} for 2.5K-5K and 5K-10K at TMR=100%. By increasing V_{clamp}, the SM0 failures increases while SM1 failures decreases. This plot matches the simulation results discussed in Section 3.2.2.1. A. For 2.5K-5k array the optimum V_{clamp} = 0.85V which result in minimum failure ratio (=0.01). The 5K-10K array results in zero failure ratio at V_{clamp} =1.1V. This is due the higher difference between low/high resistance and reference resistance for 5K-10K than 2.5K-5K array. Fig. 3.16(c)-(d) shows failure ratio vs TMR.

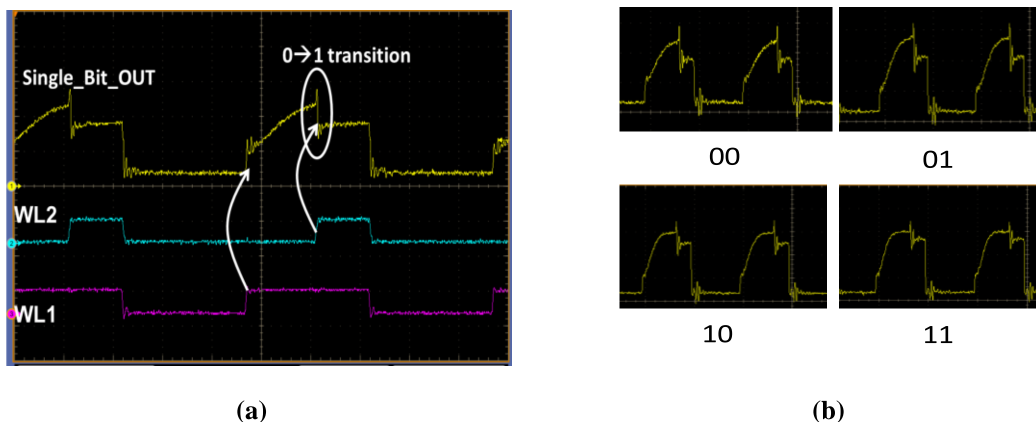

Figure 3.18 Oscilloscope capture of voltage across single-bitcell. Sensing starts by activating WL1 and bitcell switches to low resistance state at the edge of WL2; and, (b) the slope of voltage across bitcell for various current slope settings. Setting 00 indicates the lowest and 11 indicates the highest current slope.

The 5K-10K array performs better than 2.5K-5K array. Fig. 3.17(a)-(b) shows the shmoo plots of 5K-10K and 2.5K-5K

arrays with 100% TMR. Note that the 2.5K-5K array fails for all frequency and voltages.

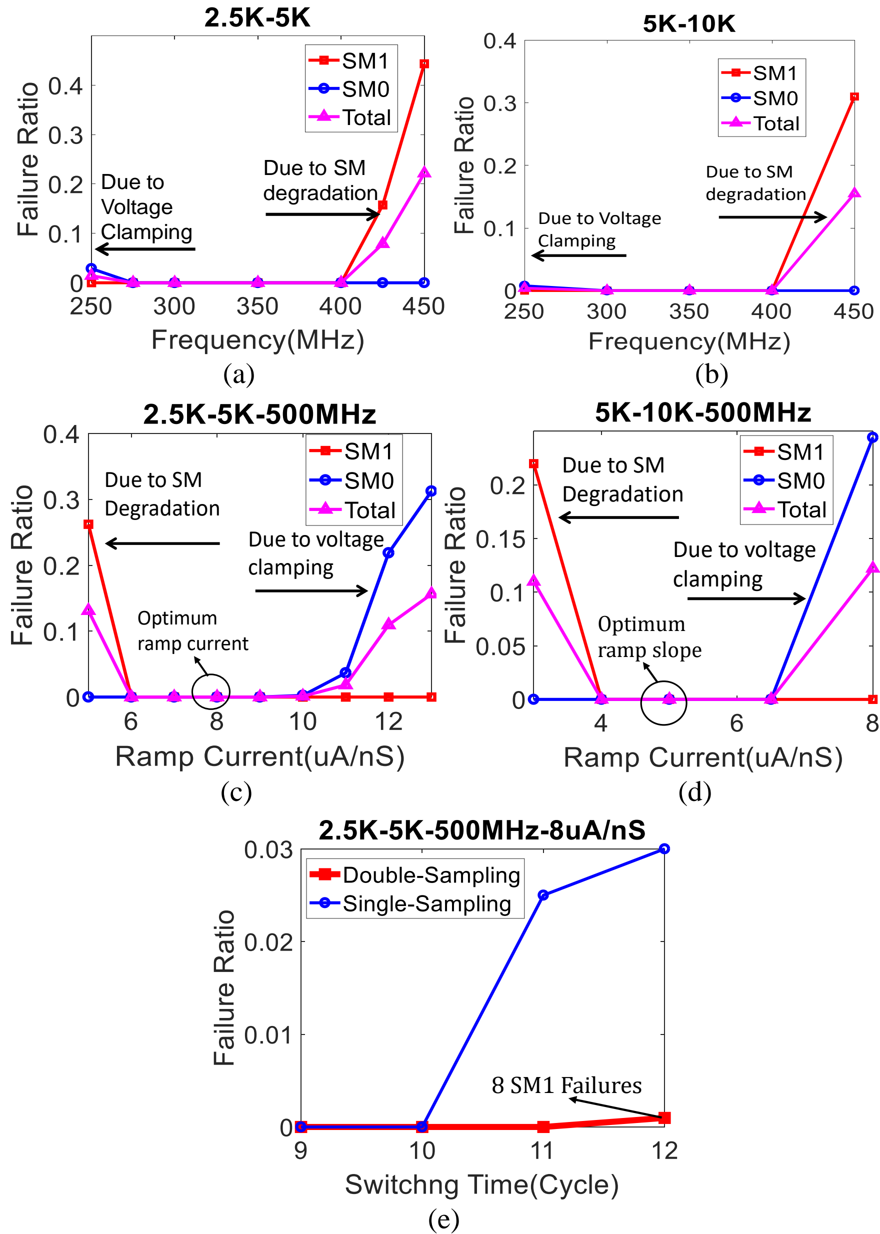

Figure 3.19 Experimental results: (a)-(b) Slope sensing failure ratio with clock frequency for 2.5K-5K and 5K-10K arrays; (c)-(d) failure ratio with ramp current slope for 2.5K-5K and 5K-10K arrays; and, (f) failure ratio with switching time for double and single sampling method.

3.2.3.4.2. Slope Sensing Test Results

To demonstrate slope sensing, we designed a single bitcell that works at low frequency to capture the high-to-low switching waveforms. Sensing starts by activating WL1 and bitcell switches to low resistance state at the edge of WL2 result in negative slope (Fig. 3.18(a)). Fig. 3.18(b) shows the slope of voltage across bitcell for various current slope settings. Setting ‘00’ (‘11’) provides lowest (highest) current slope. Thus, the negative slope can be captured to determine memory state.

Fig. 3.19(a)-(b) shows the array-level slope sensing failures vs clock frequency for 2.5K-5K and 5K-10K arrays. Note that sampling frequency is one fourth of clock frequency for each S/H circuit. Lower than 250MHz clock result in failures due to voltage clamping. Due to longer WL at slower clock for constant ramp current slope, the peak voltage across bitcell will increase and can get clamped at V_{DD} leading to SM loss. More than 400 MHz clock results in sensing failures due to SM1 loss because of sampling at higher frequency. Fig. 3.19(c)-(d) shows the failure ratio vs ramp current slope. In the case of 2.5K-5K array, the failures increase for ramp current slope lower than 6uA/nS due to SM loss. Ramp current slope greater than 10uA/nS result in sense failures due to voltage clamping. Since MTJ switching time changes significantly due to process variation we have swept it by changing the WL2 assertion time. Fig. 3.19(e) shows the failure ratio with respect to switching time for double and single sampling method for 2.5K-5K array at 500MHz. It can be observed that double sampling method reduces the SM1 failures significantly under MTJ switching time variation. Fig. 3.20(a)-(b) shows the shmoo plot for 2.5K-5K and 5K-10K arrays @ TMR = 100%. Note that slope sensing results in zero error for wide voltage and frequency range. To study the effect of process variation, we have tested 10 chips and plotted the passing frequency for 1V, 0.95V and 0.9V (Fig. 3.21). Note that the passing frequency increases for higher voltage.

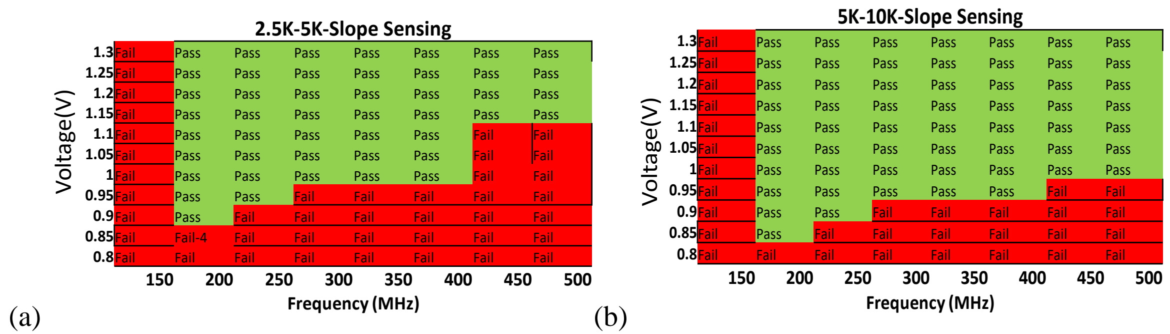

Figure 3.20 Experimental results: Slope sensing shmoo plot with TMR of 100% and optimized ramp current slope and double sampling for, (a) 2.5K-10K array; and, (b) 5K-10K array. The # of failing chips out of 10 tested chips for failing voltage and frequency is shown.

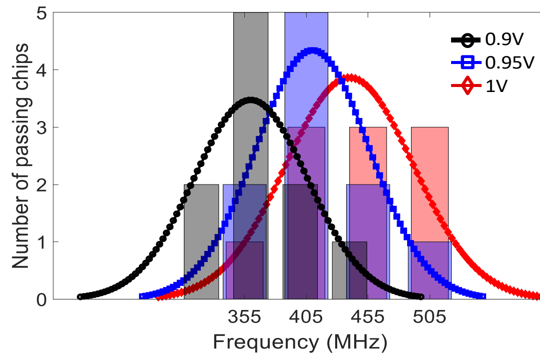

Figure 3.21 Experimental results: Passing frequency distribution for 10 tested chips for 2.5K-5K array.

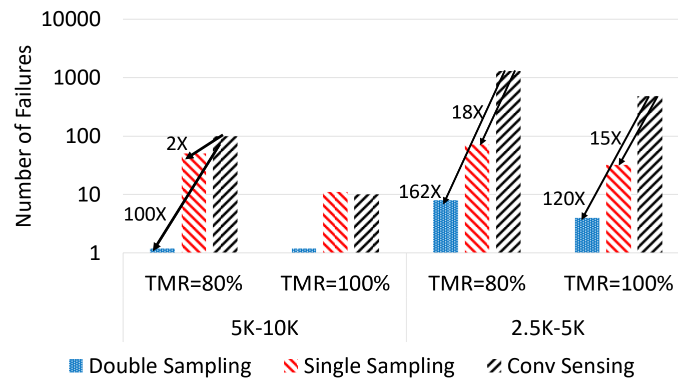

Figure 3.22 Experimental results: Comparison of # of failures for conventional and slope sensing.

Fig. 3.22 shows the comparison of slope and conventional sensing. Slope sensing results in 100X failure reduction for TMR=80% in 5K-10K array and 120X (162X) failure reduction for TMR=100% (80%) in 2.5K-5K array. Fig. 3.23 shows chip microphotograph and features. We have

Table 3.2 Comparison with other sensing schemes.

	Techn-ology	Supply Voltage	Capacity	Power (uW)	Sense Time(nS)	Average SM	Failure rate	Referen ce less
Slope Sensing (this work)	65nm	1V-1.2V	96Kb	190	32@500MHz	200mV (2.5K-5K)	0%	✓
Conventional Sensing [59-60]	65nm	1V-1.2V	96Kb	90	16@500MHz	180mV	1% (2.5K-5K) 0% (5k-10K)	-
Self-Reference [67]	240nm	2V	16Kb	-	130	~40mV	0%	✓
Non-Destructive Self-Reference [65]	130nm	1.2V-1.5V	16Kb	~100	15	~20mV	2%	✓
SPSC (Simulation)[72]	45nm	1V	-	33.5	3	600mV	Read Yield=5.7σ	-
VFAB (Simulation) Next Section	65nm	1.2V	-	16.2	5nS	800mV	Read Yield=9.8σ	

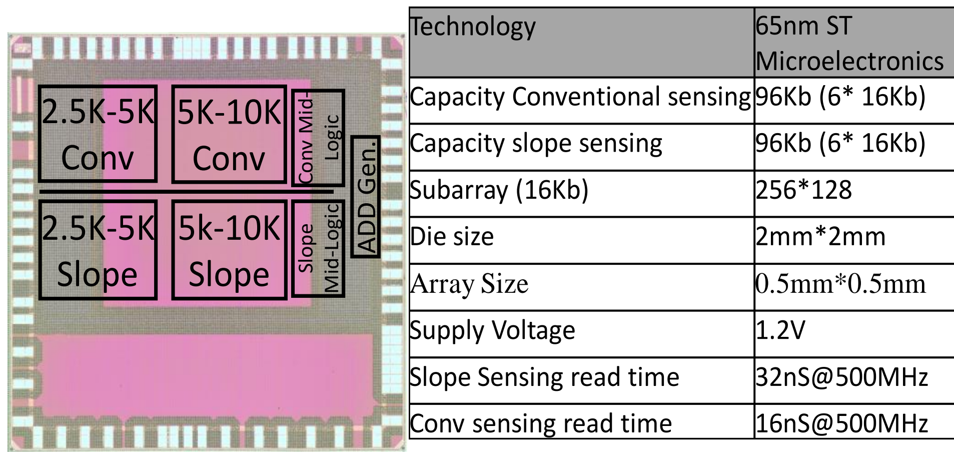

Technology	65nm ST Microelectronics
Capacity Conventional sensing	96Kb (6* 16Kb)
Capacity slope sensing	96Kb (6* 16Kb)
Subarray (16Kb)	256*128
Die size	2mm*2mm
Array Size	0.5mm*0.5mm
Supply Voltage	1.2V
Slope Sensing read time	32nS@500MHz
Conv sensing read time	16nS@500MHz

Figure 3.23 Chip microphotograph and features.

compared the proposed sensing with state-of-art sensing techniques (Table 3.2). Even though slope sensing read latency is higher and consume more power, it provides higher read yield in presence of process variation.

3.2.3.5. Applications

The proposed sensing can be exploited in applications with reliable read operation which the data will be read only one time and can be discarded afterward such as Network on chip (NOC) buffers and FIFO buffers. Moreover, it can be used in video streaming applications for buffering each video frame where data will be read only one time. In these applications, it is not required to write the data back after reading, thereby, the latency of proposed technique is comparable to conventional non-destructive sensing while the robustness under process variation is improved significantly.

3.2.4. VFAB: A Novel 2-Stage STTRAM Sensing Using Voltage Feedback and Boosting

In this Section, we propose a non-destructive and low-power sensing scheme that exploits a voltage feedback and boosting (VFAB) technique to develop large sense margin. Furthermore, VFAB does not requires a static current to be injected into data and reference STTRAMs which results in significant power saving. Significant research has been devoted to improve sense margin. However, they either result in minor improvement in sense margin or consume significant area, power and may also require restoration upon read. In contrast to existing techniques, we present a Voltage Feedback and Boosting (VFAB) technique which provides drastic improvement in sense margin at low design overhead.

3.2.4.1. Proposed VFAB Sensing Scheme

In this section, first we describe the proposed VFAB sense circuit. Next, we describe the simulation results and read disturb analysis to demonstrate the effectiveness of VFAB.

3.2.4.1.1. Basic Operation

The purpose of the sense circuit is to identify the resistance of the data STTRAM (R_{Data}). To make the comparison, data STTRAM resistance is compared against reference STTRAM resistance ($R_{Ref} = R_H + R_L/2$). The proposed VFAB sensing circuit is shown in Fig. 3.24(a). As shown in timing diagram in Fig. 3.24(b), the sensing is performed in two stages, discharge and boost stage. Sensing starts by asserting Y_{SEL} and precharging C_{RL}, C_{BL}, sense circuit output capacitors (C_{Data} & C_{Ref}) and boost capacitor (C_{Boost}) by applying active low PRE signal (precharge transistors are not shown in the sense circuit). In the discharge stage, the WL is asserted and C_{BL} and C_{RL} start

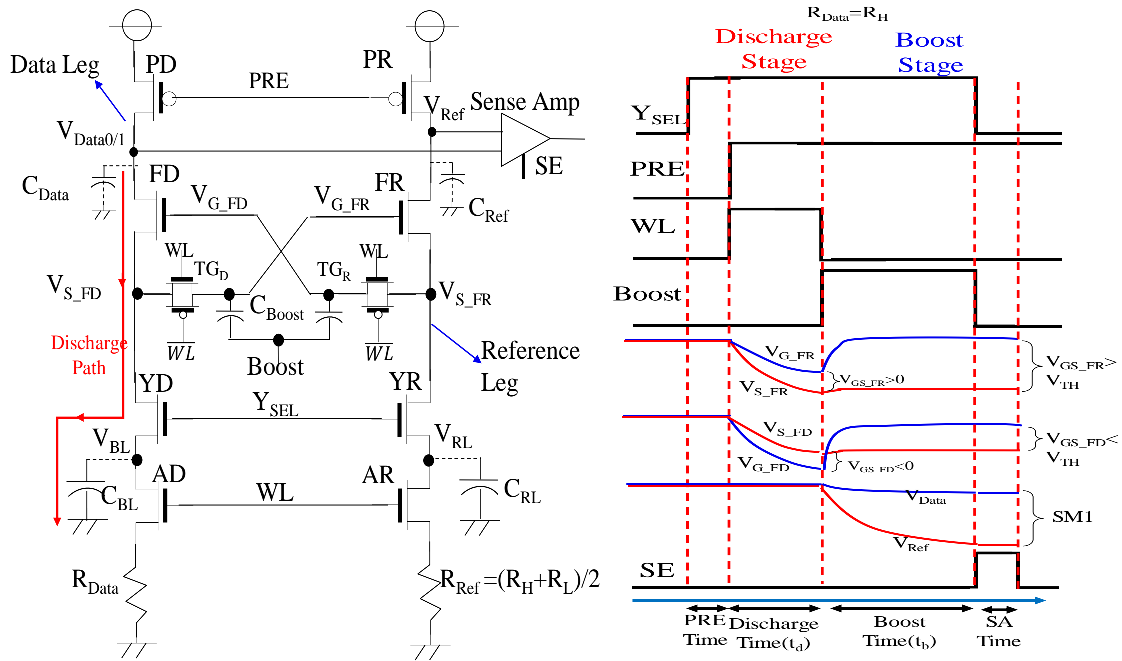

(a) (b)

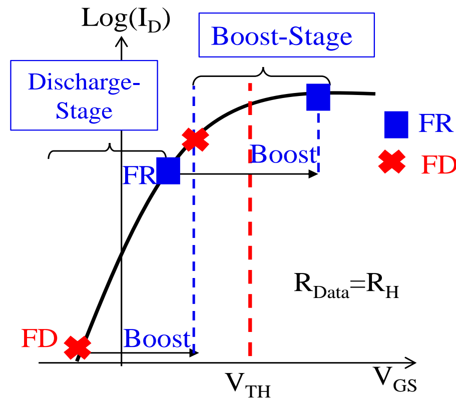

(c)

Figure 3.24 Proposed sensing circuit; (b) timing diagram; and, (c) I_D-V_{GS} curve of feedback transistor when R_{Data}=R_H at different stages of sensing. In first stage, FR is weakly ON whereas FD is strongly OFF. In second stage, FR becomes strongly ON whereas FD remains weakly OFF.

discharging at different rates based on the RC time constants. Since Y_{SEL} is asserted, V_{S_FR} (V_{S_FD}) is equal to V_{RL} (V_{BL}) approximately. In this stage, transmission gates (TG_R and TG_D) are ON, thereby, V_{S_FD} and V_{S_FR} are fed back to the gate of FR and FD respectively. Based on data STTRAM state the lower resistance leg is either data leg or reference leg. The V_{GS} of feedback

transistor in lower resistance leg is positive whereas it is negative in higher resistance leg. For example, if $R_{Data} = R_H$ then reference leg resistance will be lower than data leg. The C_{RL} discharges faster than C_{BL} since $R_{Ref}*C_{RL}$ is lower than R_H*C_{BL} (note that C_{BL} and C_{RL} are equal). Thus, V_{RL} ($V_{S\text{-}FR}$) is less than V_{BL} (V_{S_FD}) during discharge stage and $V_{GS_FR} \cong V_{S_FD} - V_{S_FR} > 0$ while $V_{GS_FD} \cong V_{S_FR} - V_{S_FD} < 0$ (Fig. 3.24 (b)).

As shown in Fig. 3.24(c), FR conducts in subthreshold region whereas FD is completely OFF due to negative V_{GS}. Since $V_{GS_FR} < V_{TH}$ at the end of discharge stage, a common mode boosting technique is employed to the gate of both feedback transistors in order to increase the V_{GS} of FR above threshold. In the boost stage, WL is disabled and transmission gates (TG_R and TG_D) are turned OFF, the feedback loop is disconnected and Boost signal is asserted. As a result of boosting, gate voltage of both feedback transistors increase while source voltage is almost fixed (Fig. 3.24(b)). Therefore, V_{GS_FR} increases above V_{TH} and FR turns ON strongly as shown in Fig. 3.24(c). Thus, C_{Ref} discharges and V_{Ref} drops exponentially. Due to boosting, V_{GS_FD} increases as well however FD stays OFF through careful selection of C_{Boost} and V_{Boost} to prevent C_{Data} from discharging. This results in large sense-1 margin (SM1). Sense-0 works in similar fashion.

3.2.4.1.2. Simulation Results

In the following paragraphs, we explain the simulation results in ST Microelectronics 65nm technology in detail. Fig. 3.25(a-b) shows the simulation waveforms when the bitcell resistance is high ($R_{Data} = R_H$). The V_{BL} and V_{RL} start discharging when WL is asserted. However, the source voltage of feedback transistors (V_{S_FD}/V_{S_FR}) remains precharged since YD/YR transistors are OFF at the beginning of discharge stage. The YD (YR) transistor turns ON when the V_{BL} (V_{RL}) drops more than V_{TH}. Therefore, there is a delay (discharge delay) before the discharging of V_{S_FD}/V_{S_FR} starts. In this case, V_{BL} is greater than V_{RL}. Thus, V_{S_FD} start decreasing after longer discharge delay compared to V_{S_FR} which aids to achieve higher V_{GS_FR} and lower V_{GS_FD} at the end of discharge

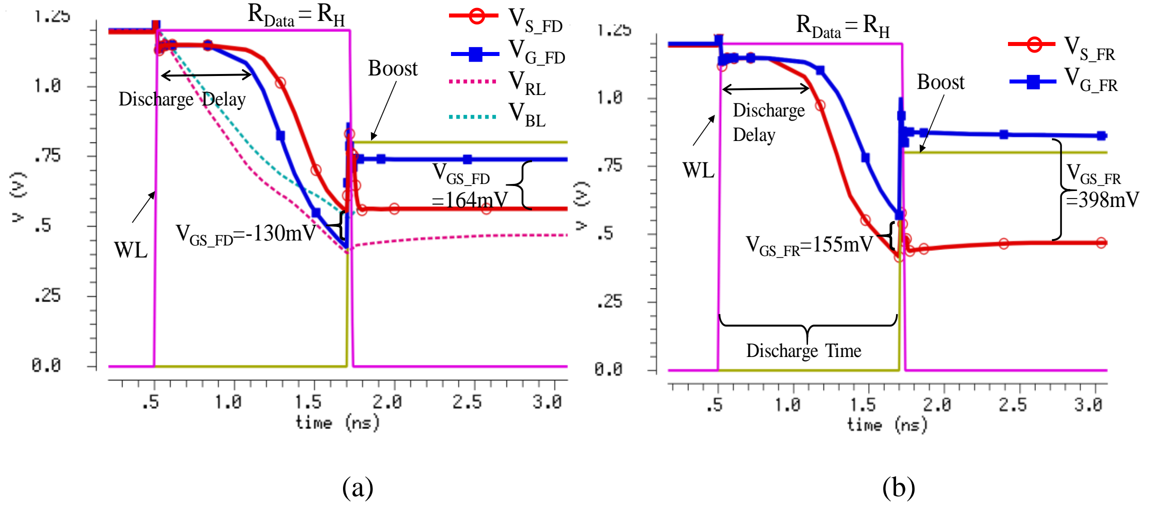

Figure 3.25 VRL, VBL and gate/source voltage of data feedback transistors (VG_FD and VS_FD); and, (b) gate/source voltage of reference feedback transistor (VG_FR and VS_FR) during discharge and boost stages where RData= RH

stage. As depicted in Fig. 3.25(a-b), V_{GS_FR} is 155mV and V_{GS_FD} is -130mV at the end of discharge stage. Higher V_{GS_FR} is desirable to ensure C_{Ref} discharges quickly and low V_{GS_FD} is desirable to prevent C_{Data} from discharging after boosting. To achieve this goal, discharge time (t_d), C_{BL}, V_{Boost} and C_{Boost} can be tuned to maximize sense margin for a given data and reference resistance. Note that, C_{BL} can be tuned by changing the size of the memory array.

In the boost stage, boost signal is asserted and feedback path is disconnected by disabling WL. Because of boosting, V_{GS_FR} (398mV) raises above V_{TH} (332mV) and FR turns ON while V_{GS_FD} (164mV) is less than V_{TH} and FD stays OFF. Consequently, C_{Ref} discharges and V_{Ref} drops exponentially while V_{Data1} stays at V_{DD} which in turn provides large SM1 (800mV) (Fig. 3.26). V_{Ref} and V_{Data} are compared at the rising edge of sense amplifier enable (SE). It is evident that V_{Ref} cannot drop more than $V_{S_FR.}$ Therefore, SM1 is limited by V_{S_FR}. The same explanation applies to sensing ‘0’ operation where $R_{Data} = R_L$. In this case, data leg’s feedback transistor turns ON, C_{Data} discharges and V_{Data0} drops exponentially which provides large SM0 (990mV(Fig. 3.26). Similarly, V_{Data0} cannot drop more than V_{S_FD}. Therefore, SM0 is limited by V_{S_FD}. The sense circuit

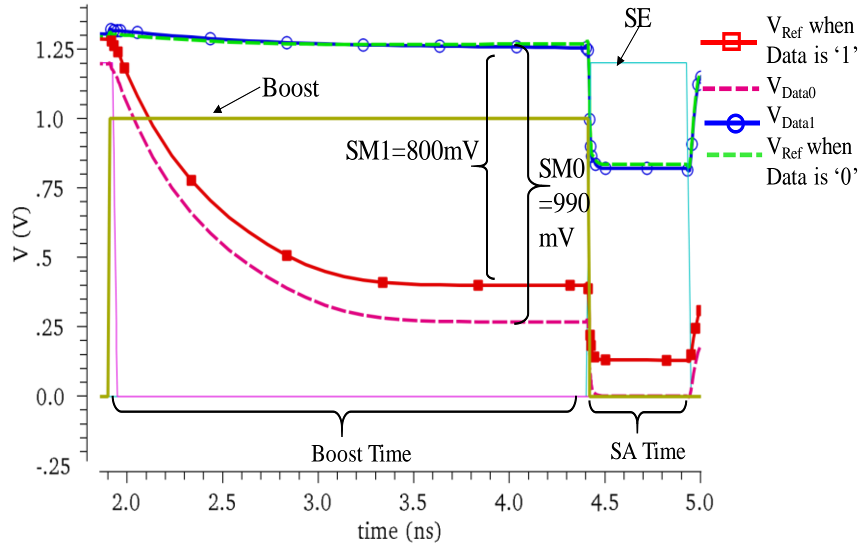

Figure 3.26 Sense margin development during boosting stage. It can be noted that 800mV sense-1 margin and 990mV sense-0 margin is developed using VFAB.

parameters are reported in Table 3.3. It can be noted that V_{RL} and V_{BL} increases after the boosting event (Fig. 3.25(a)). This is due to two factors: 1) during boosting operation, feedback transistor gate voltage is boosted and because of gate-to-source coupling, source voltage also increases which in turn increases V_{BL}/V_{RL}. However, since C_{Boost} is higher by an order of magnitude compared to gate-to-source coupling capacitance, the increase in source voltage is insignificant; 2) Since WL is disabled, in case of R_{Data}=R_H, C_{Ref} can only discharge into C_{RL} which eventually increases V_{RL} because of charge sharing between C_{Ref} and $C_{RL.}$ In other words, since FR transistors is ON and FD is OFF charge sharing only occurs between C_{Ref} and C_{RL}. Therefore, V_{RL} increases more than V_{BL} after boosting as depicted in Fig. 3.25(b). It worth mentioning that, V_{G_FR} reduces due to C_{GD_FR} coupling since V_{Ref} decreases after boosting. However, C_{GD_FR} is lower by order of magnitude compared to $C_{Boost.}$ Thus, V_{G_FR} reduction due to coupling effect is negligible (~5mV).

3.2.4.2. Design Space Exploration

In this section, we propose a design method to optimize both sense-0 and sense-1 margins. Next, we investigate the impact of various design parameters such as, discharge time (t_d), boost time (t_b), V_{Boost}, C_{Boost}, supply voltage and TMR on sense margin.

3.2.4.2.1. Design Method to Optimize Sense Margin

A metric "nominal sense margin" (NOM_{SM}) is defined as a cumulative metric to maximize and equalize both SM0 and SM1 and is defined as follows:

$$NOM_{SM} = \frac{SM0 \times SM1}{|SM1 - SM0| + 1} \tag{3.3}$$

Design parameters including feedback transistor size, boost time (t_b), discharge time (t_d), V_{Boost} and C_{Boost} are swept in order to maximize NOM_{SM}. The design point that maximizes NOM_{SM} is selected as the optimum design point. In the following paragraphs, we investigate the impact of various design parameters on the NOM_{SM} in typical, fast and slow corners. This is achieved by sweeping each design parameter while the other design parameters are optimized. Since the nominal design point does not ensure robustness under process variation. We perform further optimization for process variation in Section 3.2.4.3.

3.2.4.2.2. Impact of Discharge Time (t_d)

Higher positive V_{GS} for the feedback transistor in the low resistance leg at the end of discharge period is desirable to ensure it turns ON strongly after boosting and discharges output

Table 3.3 Sense circuit parameters

Device	Parameter	Device	Parameter
PD/PR	W=1u L=0.12u	C_{BL}/C_{RL}	60fF
FD/FR	W=0.5u L=0.18u	C_{Data}/C_{Ref}	3fF
YD/YR	W=1u L=0.12u	C_{Boost}	7.5f
AD/AR	W=1u L=0.06	R_{Data}	5K-10K

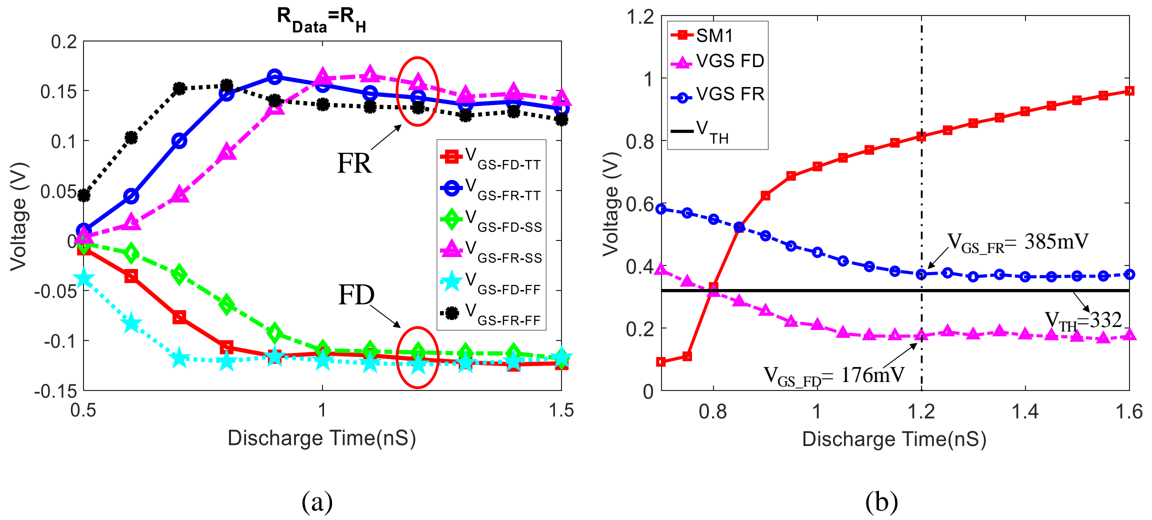

Figure 3.27 Impact of discharge time on feedback transistor V_{GS} at the end of discharge stage in TT, SS and FF corners; and, (b) impact of discharge time on sense margin and V_{GS} of feedback transistor after boosting when R_{Data}=R_H.

node which is connected to sense amplifier quickly in order to develop large sense margin. Simultaneously, a negative V_{GS} for feedback transistor in higher resistance leg is desirable to ensure it remains OFF after boosting and prevents this leg's output capacitor from discharging. Impact of discharge time on V_{GS} of feedback transistor before boosting in typical (TT), slow (SS) and fast (FF) corners when data STTRAM resistance is high is shown in Fig. 3.27(a). V_{GS_FR} is maximized (V_{GS_FD} is minimized) at 0.8nS, 0.9nS and 1.1nS in fast, typical and slow corners respectively. In slow corner, V_{TH} of YD/YR transistor is higher (460mV in slow corner for 65nm technology) and V_{S_FD}/ V_{S_FR} start falling after longer discharge delay. Thus, longer discharge time is required to achieve maximum value of V_{GS_FR} and minimum value of V_{GS_FD} compared to typical and fast corners. Note that, due to lower V_{TH} in fast corner, the discharge delay is shorter, thus, YD/YR turns ON earlier compared to typical corner and source voltage of feedback transistors drops to a lower voltage for a fixed discharge time which results in lower source voltage in fast corner.

Fig. 3.27(b) shows effect of discharge time on sense margin and V_{GS} of feedback transistors at boosting stage when R_{Data} = R_H. In this case, as discussed in Section II, the V_{Data} node stays at V_{DD} and V_{Ref} node discharges exponentially. It can be observed that both sense-0 and sense-1

margins are low at the beginning of discharge cycle since YD/YR turns ON after a delay. Shorter discharge time results in significant sense margin degradation since V_{GS_FD} rises above V_{TH}, thereby, C_{Data} discharges and V_{Data} drops which degrades sense margin. Note that sense-1 margins is improved by increasing discharge time since V_{GS_FD} is decreased drastically which prevents C_{Data} from discharging. It is evident that V_{Ref} cannot drop more than V_{S_FR}. Therefore, sense-1 margin is limited by V_{S_FR}. As discharge time increases the C_{RL} will discharge more and consequently V_{RL} and V_{S_FR} will drop to a lower voltage. Therefore, V_{Ref} is clamped at lower voltage which in turn improves sense-1 margin. The same argument applies to sense-0 margin where V_{Data} is clamped by V_{S_FD}. In this case V_{Ref} stays at V_{DD} and V_{Data} drops. Maximum NOM_{SM} for all corners is achieved at discharge time of 1.2nS.

3.2.4.2.3. Impact of Boost Capacitors and Boost Voltage

Boosting speeds up the time that is required for developing large sense margin. The proposed sensing circuit works without boosting since one of feedback transistors conducts in subthreshold region and other one is completely OFF due to negative V_{GS} at the end of discharge stage. However, since output capacitor discharges slowly longer time is required to obtain sufficient sense margin. To speed up sense margin development, boosting mechanism can be exploited which increases V_{GS} of feedback transistor in lower resistance leg which in turn reduces discharge path effective resistance and sense amplifier capacitance discharge time. Large boosting can be problematic since boosting increases V_{GS} of both feedback transistors. Thus, feedback transistor in higher resistance leg might also turn ON and reduce sense margin drastically by discharging higher resistance leg's capacitor. Therefore, C_{Boost} and V_{Boost} must be selected carefully to realize robust sensing. Feedback transistor gate voltage after boosting is given by:

$$V_{G_F}(boost) = V_{G_F}(discharge) + (V_{Boost} - V_{SF})\frac{C_{Boost}}{C_{Boost}+C_{GS}} \quad (3.4)$$

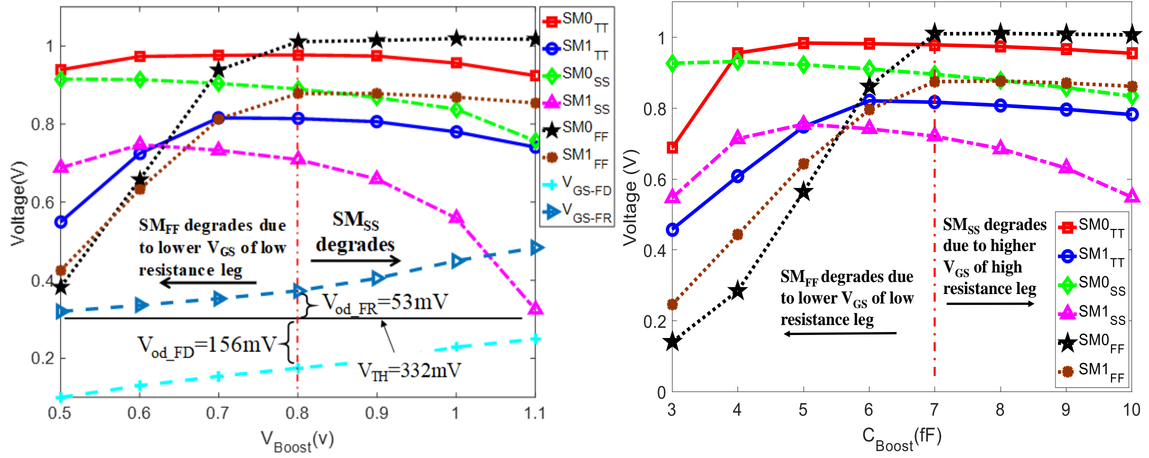

Figure 3.28 Impact of boost voltage on sense margin; and, (b) impact of C_{Boost} on sense margin for discharge time of 1.2nS.

Where $V_{G_F}(discharge)$ is the feedback transistor gate voltage at the end of discharge stage. This equation is derived by assuming feedback transistor and transmission gate leakage are zero. Therefore, we can presume that the electrical charge is conserved. Since feedback transistor's gate-source capacitance is lower by order of magnitude compared to C_{Boost}, the increase in source voltage after boosting is negligible. Based on equation 2, feedback transistor gate voltage at boost stage increases by increasing C_{Boost} and V_{Boost} (as shown in Fig. 3.28(a-b)) or by increasing gate voltage at the end of discharge stage that can be achieved by reducing discharge time.

Fig. 3.28(a) depicts the effect of boost voltage on sense margin in slow, typical and fast corners for discharge time of 1.2nS. It can be observed that the effect of V_{Boost} on sense-1 margin (where R_{Data}=R_H) in typical corner is insignificant since $V_{GS_FD} < V_{TH} < V_{GS_FR}$ for the entire range of V_{Boost} (0.5V to 1.1V). In other words, the FD transistor is OFF and FR is ON for V_{Boost} in range of 0.5V to 1.1V. Therefore, V_{Ref} drops while V_{Data} is precharged to V_{DD}. As shown in Fig. 3.28(a) V_{GS} of both feedback transistors reduces as V_{Boost} reduces. Additionally, $|V_{GS}|$ of both feedback transistors are higher in slow corner and are lower in fast corner compared to typical corner at discharge time of 1.2nS (Fig. 3.27(a)). Hence, sense margin in fast corner degrades for lower V_{Boost}.

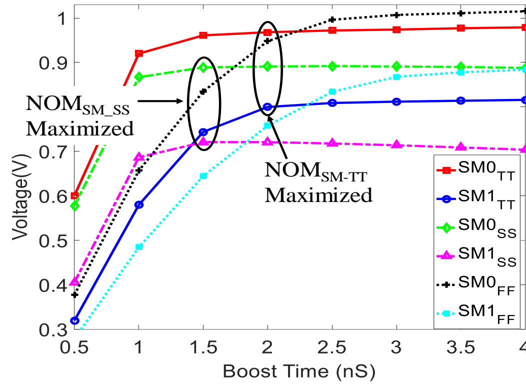

Figure 3.29 Impact of boost time on sense margin.

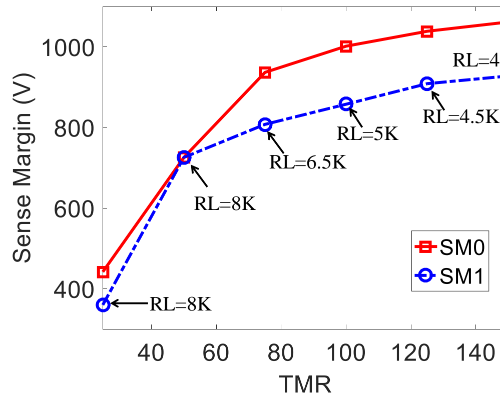

Figure 3.30 Fig. 8 Impact of TMR on sense margin (optimum R_L is shown).

This is due to reduction of V_{GS} of low resistance leg feedback transistor below V_{TH} (230mV in fast corner for 65nm technology). Thus, low resistance leg feedback transistor turns OFF which in turn degrades sense margin. In contrast, by increasing V_{Boost}, sense margin in slow corner decreases remarkably since V_{GS} of feedback transistor in higher resistance leg increases more than V_{TH} (408mV in slow corner for 65nm technology). As a result, high resistance leg feedback transistor turns ON which in turn degrades sense margin. V_{Boost}=0.8V and C_{Boost}=7fF provide maximum NOM_{SM} in all corners (Fig. 3.28(a)-(b)).

3.2.4.2.4. Impact of Boost Time (t_b)

Fig. 3.29 shows the effect of boost time on sense margin for slow, typical and fast corners. It can be observed that sense-1 and sense-0 margins do not increase beyond 1.5nS (2nS) in slow (typical) corner. Since in case of $R_{Data}= R_H$, V_{Ref} is clamped by V_{S_FR}. Similarly, in case of $R_{Data} =R_L$, V_{Data} is clamped by V_{S_FD}. As shown in Fig. 3.27(a), V_{GS_FR} is higher in slow corner compared to typical and fast corners at discharge stage. Because of higher V_{GS_FR}, C_{Ref} discharges faster and provides large sense-1 margin for shorter boost time in slow corner. In contrast, in fast corner, V_{GS_FR} is lower, C_{Ref} discharges slowly and longer boost time is required until V_{Ref} reaches its final value. As mentioned in Section 3.2.4.2, the discharge delay is shorter in fast corner due to lower V_{TH}. Therefore, YD/YR turns ON earlier compared to typical corner and source voltage of feedback transistors drop to a lower voltage for a fixed discharge time which results in lower source voltage in fast corner. Therefore, the V_{Ref} is clamped at lower voltage in fast corner since V_{S_FR} is lower at the end of discharge stage. Hence, higher sense-1 margin can be obtained if boost time is long enough to permit V_{Ref} discharges to V_{S_FR}. Same argument holds true for sense-0 margin where V_{Data0} is clamped by V_{S_FD}. As depicted in Fig. 3.29, sense-0/1 margins in fast corner is greater than slow and typical for boost time of 4nS. It worth mentioning that sense margin in slow corner degrades negligibly after it reaches its maximum value at 1.5nS since high resistance leg's feedback transistor conducts in subthreshold region, thereby, output capacitor of higher resistance leg discharges gradually which degrades sense margin. Boost time can be tuned to increase the robustness of the design (further discussed in Section 3.2.4.3).

3.2.4.2.5. Impact of TMR

TMR versus sense margin is illustrated in Fig. 3.30. The optimum R_L for each TMR is shown in the figure. This plot is obtained by sweeping R_L for a fixed TMR to achieve maximum NOM_{SM}. Note that optimum R_L decreases with TMR. The proposed sensing method provides

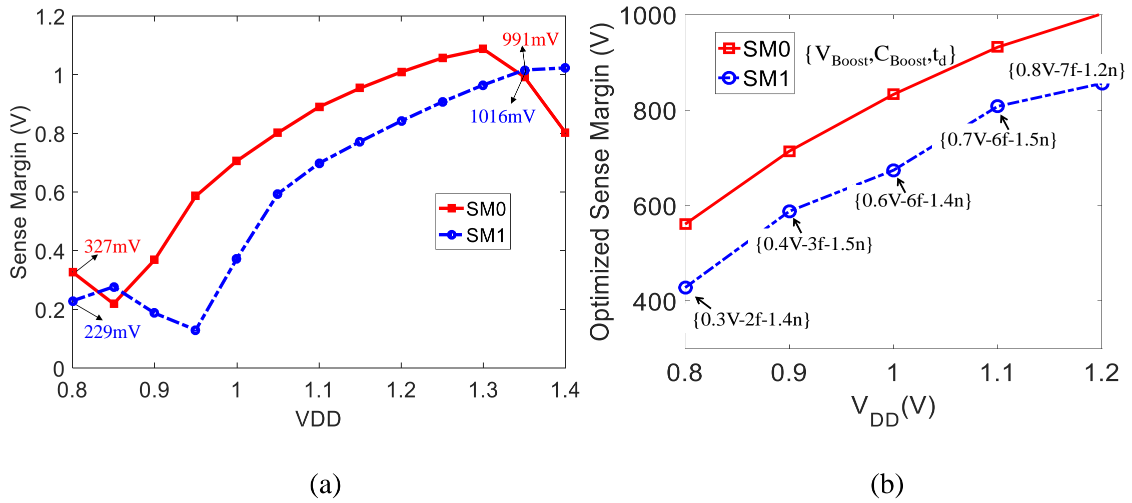

(a) (b)

Figure 3.31 Impact of supply voltage variation on sense margin; and, (b) optimum sense margin vs supply voltage; the optimum design parameters ({V_{Boost}, C_{Boost}, t_d}) are also shown for each supply voltage.

sufficient sense margin for low TMR of 25%. As the TMR increases the difference between low and high resistance increases. For higher TMR lower R_L is sufficient to provide large sense margin since the difference between R_L/R_H and reference resistance is enough to achieve sufficient V_{GS} for lower resistance leg's feedback transistor. Moreover. As mentioned in Section 3.2.4.2.2, the sense margin is limited by source voltage of low resistance leg's feedback transistor. As optimum resistance reduces the source voltage of feedback transistor reduces, thereby, the lower resistance leg's output capacitor discharges to a lower voltage resulting higher sense margin. Therefore lower R_L/R_H resistance is desirable to achieve higher sense margin for higher TMR. On the other hand, for lower TMR higher R_L is required in order to achieve higher difference between R_L and R_H in order to achieve higher V_{GS} for low resistance leg's feedback transistor and higher sense margin.

3.2.4.2.6. Impact of Voltage Scaling

The effect of V_{DD} variation on sense margin is shown in Fig. 3.31(a). It can be observed that by varying V_{DD} from 0.8V (SM1=229mV, SM0=327mV) to 1.4V (SM1=1023mV,

Table 3.4 Parameters used for process variation study.

Device	Parameter	Mean	Size	Std. Dev.
PD/PR	PMOS Standard V_{TH}	467 mV	W=1u L=0.12u	$A_{V_T}/\sqrt{wL}$ (1)
FD/FR	NMOS Low V_{TH}	332mV	W=1u L=0.12u	$A_{V_T}/\sqrt{wL}$ (1)
YD/YR	NMOS Standard V_{TH}	417mV	W=1u L=0.12u	$A_{V_T}/\sqrt{wL}$ (1)
AD/AR	NMOS Standard V_{TH}	417 mV	W=1u L=0.06u	$A_{V_T}/\sqrt{wL} \cong 20mV$ (1)
C_{BL}/C_{BR}	M2 Capacitance	60 fF	-	6fF (3)
C_{Boost}	PMOS Gate Capacitance	7.5 fF	W=10.5u L=0.12u	Variation depends on PMOS transistor variation
MTJ	R_L	5K	50*100 nm^2	0.5K (2)
	R_H	10K	50*100 nm^2	1K (2)

(1) A_{V_T} *is* Pelgroom coefficient which is 4.5mV/μm for ST 65nm technology, (2) [3, 11], (3) ST design kit

SM0=801mV) sufficient sense margin can be obtained. Unlike conventional sensing which is prone to supply voltage variation the proposed technique is functional for a wide range of supply voltage fluctuation. The NOM_{SM} is maximized at 1.35V (SM1=1016mV, SM0=991mV). The sense-1 margin degradation at 0.95V is due to increase of V_{GS_FD} beyond V_{TH}. Thus, C_{Data} is discharged which degrades sense-1 margin significantly. The optimum design solution for supply voltages in range of 0.8V to 1.2V is depicted in Fig. 3.31(b) (the respective design parameters are also shown). Note that the proposed sensing scheme provides large sense margin even at 0.8V of supply voltage.

3.2.4.3. Process, Temperature and Voltage Variation Analysis

3.2.4.3.1. Monte Carlo Simulation Setup

Table 3.4 shows the parameters which is used in the process variation study. In order to perform monte-carlo simulation, we have considered R_L, R_H and R_{Ref} as independent random

variables which means that each of these design parameters vary during each run of monte-carlo simulation. However, the reference resistance is kept same for both data leg with R_H and R_L. The mean and sigma of transistors used in sense circuit are shown in Table 3.4. The C_{Data} and C_{Ref} are equivalent capacitance of sense circuit output node and sense amplifier input capacitance. C_{Data}/C_{Ref} will fluctuate due to variation in the transistors connected to the output node. We employed the same simulation setup for conventional sensing. The simulations are performed in Cadence Spectre using 65nm ST Microelectronic design kit which is very well calibrated with experimental data. Therefore, the simulation results are close estimation of experimental results. We perform monte-carlo simulation in slow, typical and fast corners @90°C and -10°C under supply voltage variation in order to investigate effect of inter die process variation as well as temperature and supply voltage variation on read yield.

3.2.4.3.2. Read Yield

The statistical distribution of sense margin and sense amplifier offset voltage (V_{SA_OFFSET}) caused by process variation can be modeled by Gaussian distribution. Since read access pass occurs when sense margin > V_{SA_OFFSET}, read access pass yield for a bitcell with state 0 or 1 ($RAPY_0$ or $RAPY_1$) can be achieved by combining distribution of V_{SA_OS} and $SM_{0,1}$ [73]:

$$RAPY_{0,1} = \frac{\mu_{SM_{0,1}} - \mu_{V_{SA_OFFSET}}}{\sqrt{\sigma^2_{SM_{0,1}} + \sigma^2_{V_{SA_OFFSET}}}} \tag{3.5}$$

Where $\mu_{SM_{0,1}}(\mu_{V_{SA_{OFFSET}}})$ is mean sense margin and $\sigma_{SM_{0,1}}(\sigma_{V_{SA_{OFFSET}}})$ is the standard deviation of sense margin. RAPY for a bitcell is defined as the smaller of $RAPY_0$ and $RAPY_1$.

Read disturbance is the other factor which determines read yield. Since read current is injected from bitline to sourceline during read operation, disturbance can only occur when the bitcell resistance is high. In order to prevent read disturbance I_{Data1} must be less than critical current (I_C). The statistical distribution of I_{Data1} and I_C caused by process variation can be modeled by

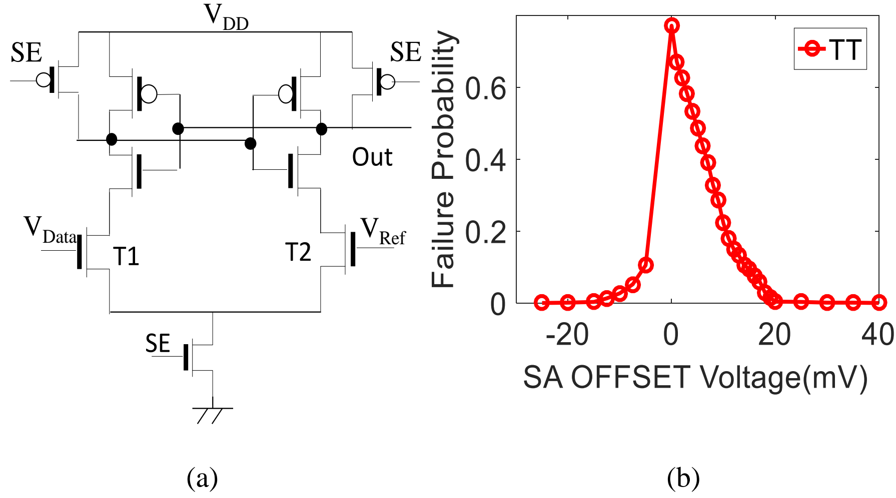

(a) (b)

Figure 3.32 Sense amplifier circuit; and, (b) SA offset voltage distribution for 1000 points Monte-Carlo simulations.

Gaussian distribution. Since read disturbance occurs when I_{Data1} is smaller than I_C, read disturbance pass yield (RDPY) in sigma is given by [73]:

$$RDPY = \frac{\mu_{I_C} - \mu_{I_{Data1}}}{\sqrt{\sigma_{I_C}^2 + \sigma_{I_{Data1}}^2}} \tag{3.6}$$

Where $\mu_{I_C}(\mu_{I_{Data1}})$ is mean of I_C (I_{Data1}) and $\sigma_{I_C}(\sigma_{I_{Data1}})$ is the standard deviation of I_C (I_{Data1}).

3.2.4.3.3. Sense Amplifier OFFSET voltage Analysis

The Sense Amplifier (SA) offset voltage depends on sense time and sense amplifier size since increasing transistor size decreases the transistor threshold voltage variation. We design the sense amplifier in such a way to reduce the offset while meet the area and delay requirements. We considered sense time of 0.5nS. In order to achieve V_{SA_OFFSET}, we fix reference voltage (V_{Ref}) at 400 mV (average reference voltage generated by sense circuit) and sweep V_{Data} (Fig. 3.32(a)). For each sweep 1000 points Monte-Carlo simulation is performed and tablethe sense amplifier failure

ontedistribution is shown in Fig. 3.33(b). The sense amplifier output node (OUT) is initially precharged to '1'. If $V_{Ref} + V_{SA_OFFSET} > V_{Data}$, node OUT is pulled down to '0'. Since OUT is initially '1', failure probability of sensing '0' is greater than sensing '1'. This distribution can be modeled by a Gaussian distribution with $\mu_{V_{SA_OFFSET}} = 8mV$ and $\sigma_{V_{SA_OFFSET}} = 16mV$.

3.2.4.3.4. Design Method for Process and Temperature Variation Tolerance

The sense margin is very sensitive to feedback transistor threshold voltage fluctuation. In order to realize a robust design in presence of process variation V_{GS} of feedback transistor in lower resistance leg must be maximized to achieve maximum sense margin during boost stage while V_{GS} of feedback transistor in higher resistance leg must be minimized to prevent higher resistance leg's output capacitor from discharging. To achieve this goal, we define a metric, PVT_{SM}, which takes these voltages into account as well as providing large sense0/1 margin as follows:

$$PVT_{SM} = NOM_{SM} \times (V_{GS_{FR_1}} - V_{TH}) \times (V_{GS_{FR_0}} - V_{TH})^2 \times (V_{GS_FD0} - V_{TH}) \times (V_{GS_FD1} - V_{TH})^2 \quad (3.7)$$

V_{GS_FR1} (V_{GS_FD1}) indicates V_{GS} of reference (data) feedback transistor when the data is '1' (R_{Data}=R_H). Similarly, V_{GS_FR0} (V_{GS_FD0}) indicates V_{GS} of reference (data) feedback transistor when the data is '0' (R_{Data}=R_L). The design point which maximizes PVT_{SM} is the best design point for process variation tolerance. The difference of V_{GS} and V_{TH} determines how strongly a transistor is OFF or ON. Therefore, the objective is to find a design solution which maximizes $V_{od} = |V_{GS} - V_{TH}|$ for both feedback transistors to ensure the feedback transistor in low resistance leg is ON while the other leg is OFF in presence of feedback transistor threshold voltage fluctuation. To achieve this goal, C_{Boost}, V_{Boost} and discharge time can be tuned.

As depicted in Fig. 3.28(a) V_{od_FR} increases while V_{od_FD} decreases with higher V_{Boost}. There is a tradeoff between V_{od_FR} and V_{od_FD}. Sense margin degradation due to lower V_{od} of lower

resistance leg can be compensated by increasing boost time and allowing this leg's output capacitor to discharge for longer time to improve sense margin. Therefore, in order to improve RAPY, boost time is determined in such a way to provide sufficient sense margin even with lower V_{od} of low resistance leg. Additionally, we select a design point where V_{od} of high resistance leg is greater than that of low resistance leg. As shown in Fig. 3.28(a), in case of R_{Data}=R_{H}, V_{od_FD} is ~3X higher than V_{od_FR} for V_{Boost}=0.8V and t_d=1.2nS. Hence, we can ensure that feedback transistor in high resistance leg would not turn ON under feedback transistor threshold voltage variation. This is achieved by increasing the impact of V_{od} of higher resistance leg (V_{od_FD1}/V_{od_FR0}) in PVT_{SM} definition.

As discussed in Section 3.2.4.2.2, slow (fast) corner obtains higher (lower) V_{GS} for both feedback transistors (Fig. 3.27(a)). *Therefore, RAPY in slow corner is limited by high V_{GS} of high resistance leg's feedback transistor and RAPY in fast corner is limited by low V_{GS} of low resistance leg's feedback transistor.* Hence, it is desirable to adjust discharge time in order to achieve lower V_{GS} for high resistance leg's feedback transistor in slow corner and higher V_{GS} for low resistance leg in fast corner. Even though longer discharge time provides higher μ_{SM}(Fig. 3.27(b)), it increases σ_{SM} (due to lower V_{od} of feedback transistor in high resistance leg) which in turn hurts RAPY significantly. Thus, by reducing discharge time μ_{SM} is sacrificed to reduce σ_{SM} in order to obtain higher RAPY. As depicted in Fig. 3.27(a)–(b), discharge time of 1.2nS provides higher positive V_{GS_FR} in fast corner and lower negative V_{GS_FD} in slow corner when data is '1'as well as higher sense margin.

3.2.4.3.5. Simulation Results

To maximize RAPY, the design parameters are swept and PVT_{SM} is computed for each design point. Next, the design solutions which provide sense margin less than 500mV are eliminated. The design points that maximize PVT_{SM} for all corners are obtained. Subsequently we

run 2000-point Monte Carlo simulation for top 10 candidates to find the maximum RAPY. The best design point results in RAPY of 14.4σ in typical corner (Fig. 3.34(a)). Even though the difference between R_L and R_{Ref} is only 5σ, we obtain RAPY of 14.4σ . This is due to following reasons: 1) The RAPY depends on many variables such as feedback and access transistor V_{TH} variation which will offset the RAPY degradation due to low difference between R_L/R_H and R_{Ref}; 2) We have considered R_H, R_L and R_{Ref} as independent variables in our simulation. For example, if due to process variation R_L is higher, R_{Ref} might be higher as well which will cancel the effect of higher R_L on sense margin degradation; 3) The reported RAPY result is for 2000 Monte-Carlo points which is an estimation of RAPY of the array. In order to achieve more accurate RAPY estimation we have performed 10000 points Monte-Carlo simulation and we achieved RAPY of 13.6σ.

The sense-0 and sense-1 margin distributions for 2000 Monte Carlo points are depicted in Fig. 3.33(a)-(b). The proposed sensing achieves 976mV of sense-0 margin and 807mV of sense-1 margin on average which significantly higher than state-of-the-art sensing methods. Based on simulation results the fast corner at -10°C and slow corner at 90°C are the worst-case corners. Fast

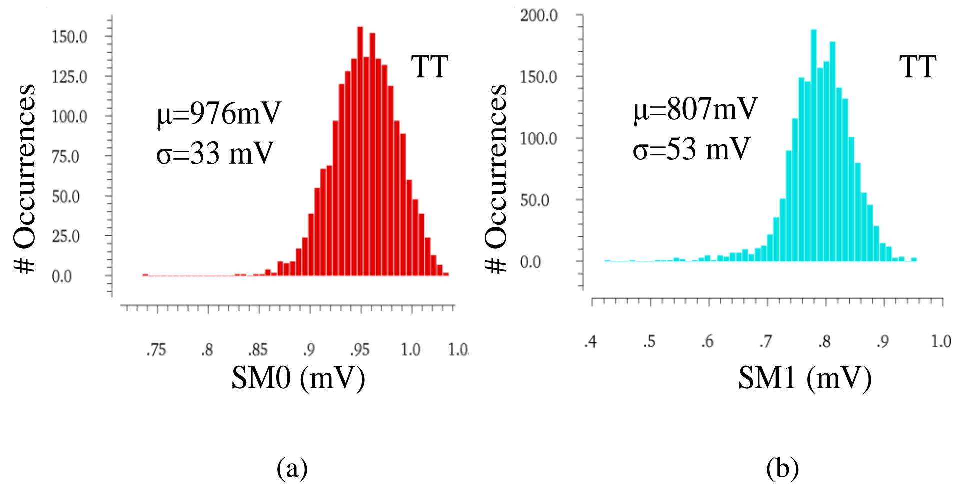

Figure 3.33 (a) SM0 and, (b) SM1 distribution for 2000 Monte Carlo points (TT). The μ and σ are also shown.

corner@-10°C (slow corner@90°C) results in RAPY of 9.8σ (10σ). V_{Boost} can be tuned to improve RAPY significantly. By increasing V_{Boost} from 0.85V to 0.95V $RAPY_{FF}$ is increased from 9.8σ to 18.2σ due to increase in V_{GS} of lower resistance leg's feedback transistor. Similarly, by decreasing V_{Boost} from 0.85V to 0.75V $RAPY_{SS}$ is increased from 10σ to 12σ due to lower V_{GS} of higher resistance leg's feedback transistor. This capability makes proposed sensing promising by providing the ability to improve RAPY significantly through post-fabrication adjustment of V_{Boost}. Fig. 3.34(b) shows the RAPY sensitivity to temperature variation in typical corner. By reducing

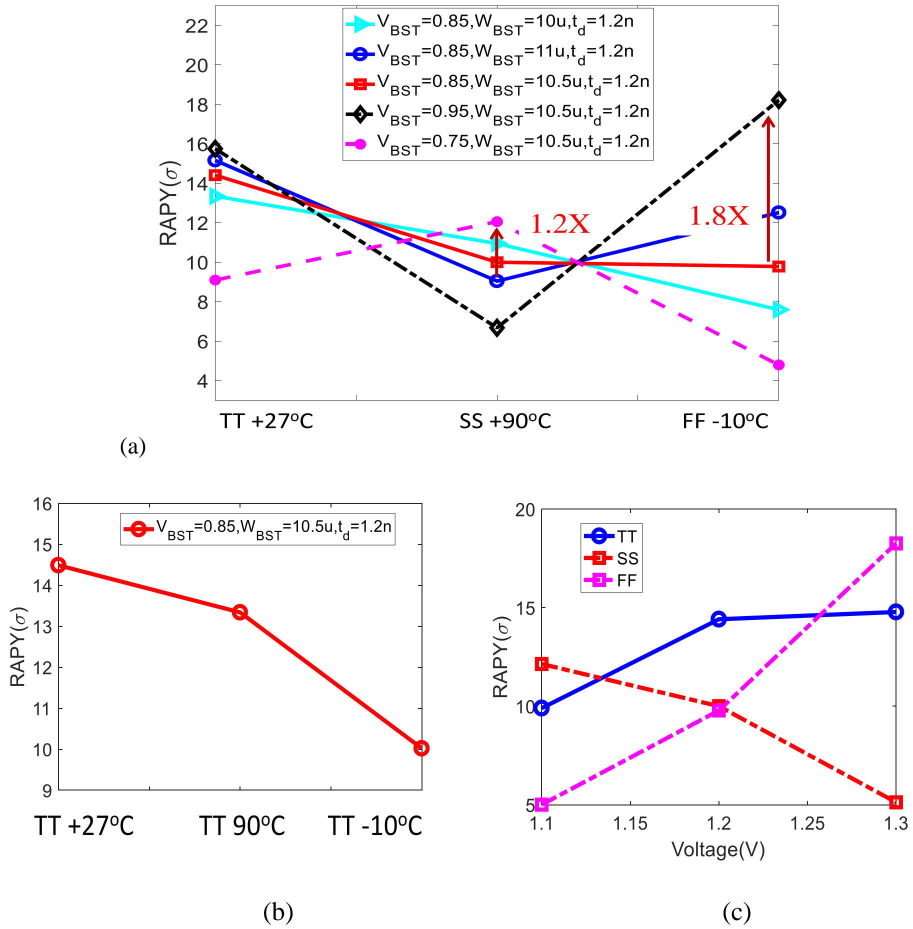

Figure 3.34 RAPY of top 4 design points which maximize PVT_{SM}. The RAPY improvement achieved by tuning V_{BST} is also shown; (b) sensitivity of RAPY on temperature in TT corner; and, (c) sensitivity of RAPY with respect to supply voltage variation in TT, FF and SS corners. The W_{BST} indicates the width of PMOS gate boost capacitor.

the temperature from 27 ºC to -10 ºC the RAPY is decreased from 14.4σ to 10σ. This is due to increase in V_{TH} of low resistance leg feedback transistor. Fig. 3.24(c) shows the RAPY with respect to supply voltage variation. RAPY is limited by high V_{GS} of high resistance leg's feedback transistor in slow corner. Since V_{GS} of high resistance leg's feedback transistor reduces by reducing the supply voltage which results in higher RAPY. Similarly, the RAPY increases in fast corner by increasing the supply voltage. By increasing supply voltage in typical corner the RAPY and sense margin improves since the difference between V_{Ref} and V_{Data} increases with supply voltage increases.

As mentioned in Equation 2.4, in order to prevent read disturbance I_{Data1} must be less than critical current (I_C). In this scheme, the C_{BL} discharge current is injected into bitcell during 1.2ns discharge period. From [38-39], critical current density J_C is $7 \times 10^6\ A/cm^2$ for switching time of 1.2nS while J_C is $3 \times 10^6\ A/cm^2$ for switching time of 4ns. The MTJ cross-sectional area is assumed to be 50nm x 100nm. Therefore, the critical current is 350uA. I_{Data1} must be less than 80% of I_C since repeated write cycles result in a wide variation in I_C [38-39]. From 2000-points Monte Carlo simulations, we obtain $\mu_{I_{Data1}} = 44\mu A$ and $\sigma_{I_{Data1}} = 3.5\mu A$. Considering the I_C variation to be 4% as reported in [9], proposed technique achieves RDPY of 16.4σ.

3.2.4.4. Comparison with other Sensing Schemes

We evaluate the proposed sensing by comparing it to conventional sensing [60] in terms of power, sense time, RAPY and RDPY. The results are reported in Table 3.5. We optimized the conventional sensing with source degeneration technique by sweeping all design parameters for 5k/10k bitcell resistance to discover the design solution which maximizes NOM_{SM}. We achieved substantially better results for conventional sensing in terms of power, RAPY and RDPY compared to [91] even with higher MTJ resistance variation. The proposed sensing technique achieves 2.43X RAPY improvement in typical corner. In conventional sensing, static current flows from V_{DD} to

ground in data leg and two reference legs which results in high power consumption. However, in [6the proposed sensing technique power is consumed during precharge phase by precharging C_{Boost}, C_{BL} and output node capacitors and there is no static current. The average power consumption for sensing '0' and '1' is reported in Table 3.5. Read power in proposed sensing is 4.7X less than conventional sensing. The sense time of proposed sensing is 5.2nS (t_{PRE}= 0.5nS, t_d=1.2nS, t_b =3nS, t_{SA} =0.5nS) while the sense time of conventional scheme is 4.5nS (t_{PRE}=0.5nS, t_{Sense}= 3.5nS, t_{SA}=0.5ns). However, the sense time can be reduced at the expense of RAPY by decreasing boost time.

We compare the proposed VFAB sensing with state-of-the-art sensing techniques in terms of power, sense time and Min (SM0, SM1)/V_{DD}. The results are reported in Table 3.6. The proposed sensing achieves significantly higher SM/V_{DD} compared to other sensing schemes. The power

Table 3.5 Comparison with conventional voltage sensing scheme.

	RAPY(σ)			**Power (uW)**	**Energy (fJ)**	**Sense Time (nS)**	**RDPY (σ)**
	SS +90°C	TT +27°C	FF -10°C				
Conv Sensing	6.1	6.5	6.3	76.9	307.6	4.5	16.3
VFAB Sensing	10	14.4	9.8	16.2	89.6	5.2	16.4

Table 3.6 Comparison with other sensing scheme.

Sense Scheme	**Power**	**Sense time**	**Min(SM0,SM1)/V_{DD}**
Proposed VFAB	**16.2uW**	**5.2nS**	**0.672**
Conventional Voltage Sensing (Source degeneration)[60][91]	76.4uW	4.5nS	0.256
Slope detection [previous section]	190uW	16nS	180mv
Self-Reference [67]	~190uW	20nS	40mV
Voltage driven Non-Destructive Self-Reference [65]	~100uW	15nS	20mV

consumption of proposed sensing is significantly lower compared to other sensing schemes. The sensing latency is acceptable compared to conventional voltage sensing and is shorter compared to other sensing techniques.

3.2.4.5. Applications

VFAB provides reliable and low-power read operation. In addition, VFAB is highly voltage scalable. The sense margin depends highly on boost voltage (V_{Boost}), and not the supply voltage (V_{DD}). As shown in Fig. 3.31(b), even low supply voltage of 0.8V achieves large sense margin. Lifetime of MTJs is usually measured with respect to the Time Dependent Dielectric Breakdown (TDDB) mechanism. Read and write operations create voltage drop across the MTJ. The thin oxide barrier experiences high electric field which degrades the reliability of the device. In VFAB, MTJ is under stress only during discharge stage which is very short (1.2ns). In addition, the voltage across MTJ can be lowered by lowering the supply voltage. Therefore, MTJ endurance increases substantially using VFAB. Hence, this technique is highly suitable for on-chip cache application where low-voltage, reliable and high endurance memory is required.

3.3. Improving Write Performance of STTRAM

STTRAM is a promising technology for high density on-chip cache due to low standby power. Additionally, it offers fast access time, good endurance and retention. One of the primary challenges of STTRAM is long write latency. Our analysis indicates that process variations in the STTRAM bitcell increases write latency significantly for large cache (Section 3.3.2). The sources of process variations are summarized in Fig. 3.35(a). Note that the process variations in combination with stochastic nature of MTJ switching result in long tail in write and read latency. This results in significant performance degradation and power overhead. The performance of conventionally designed STTRAM cache can degrade as much as 10% due to process variations. In this work, we model the tail for correct estimation of number of failing bits. We also find that write latency can be lowered by boosting the write current. We propose circuit level techniques to implement adaptive write boosting and exploit them at micro-architecture level to mitigate process variation induced performance and power degradation. The proposed approach is summarized in Fig. 3.35(b). Note that the proposed methodology can be employed dynamically. However, in this work we have investigated the static (one-time programming) column boosting for the sake of

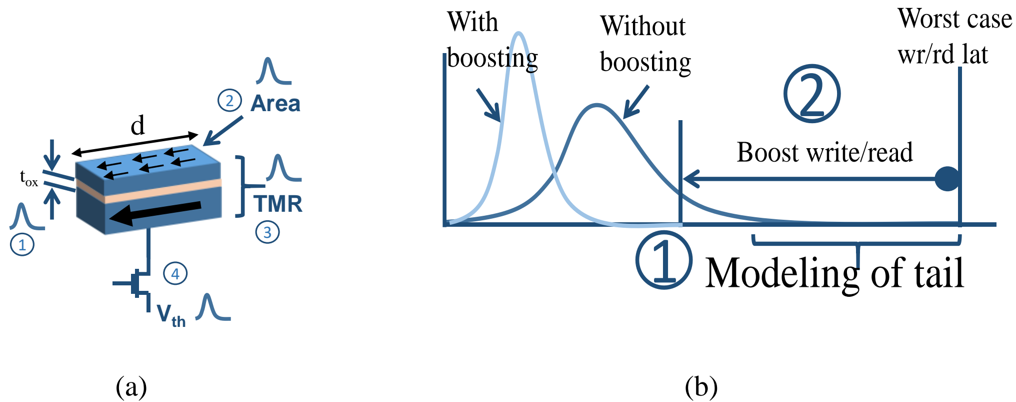

Figure 3.35 (a) Various sources of variations in STTRAM bitcell and, (b) the proposed methodology that involves modeling of tail of the distribution and adaptive boosting to accelerate the tail.

simplicity. The proposed technique can also be perceived as a repair mechanism to fix the slow columns.

3.3.1. Related Works

In [85], early write termination (EWT) to prevent redundant write operations has been employed to reduce write energy of STTRAM. This method is based on the idea that reading from MTJ consume much less energy and is much faster than writing into MTJ. The basic idea is to sample the resistance of MTJ at early stage of write operation and deactivate write current if the old value is same as new value. Although this technique is a practical and interesting scheme to improve the energy efficiency of STTRAM. it does not provide any solution to reduce the write latency of STTRAM, and also it provides area overhead due to extra sense amplifier which is used in write circuitry.

The impact of inefficient writes is minimized in STTRAM by reducing the number of write operations by using write biasing and hybrid caches in which the frequently written blocks are stored in a write cache [58]. The retention time of STTRAM is exploited to improve the write latency and write power [52]. Read-verify-rewrite scheme is proposed [74] that verifies the success of write operation and rewrites if needed. An improved idea that uses adaptive write period to improve performance while eliminating write errors in STTRAM [75]. A current source based two-step write scheme is proposed to improve the write energy and write latency [69]. Device-architecture space is explored to reduced write power by lowering the thermal energy to trade volatility [55-57]. Interesting circuit-architecture methods e.g., balanced write, flipped MTJ with sequential tag-data access and partial line update, 2T-1R with negative bitline, read optimized bitcell with stretched write cycle [76-79] have also been proposed. Process variation aware cache architectures is proposed in [80] which employs several circuit-level techniques to change the access latency of selected cache line based on the criticalities of load instruction.

For resistive memories such as Phase Change RAM (PCRAM), architectural techniques have been proposed to lower the write power through write termination [81] and improve performance by write pause, morphable MLC and bit pre-conditioning [82-84]. However, process variation induced write and read latency spread mitigation through write and shift current boosting has not been proposed which is investigated in Section 3.3.2.

3.3.2. Process Variation Analysis

In this Section, we analyze the impact of process variations in the STTRAM bitcell during read and write operation. We also investigate the modeling of read/write latency distribution and impact of current boosting.

3.3.2.1. Process Variation in Write Operation

Process variation analysis is important due to the size of cache that is employed at the last level. The process variations in the MTJ is modeled by incorporating variations in MTJ as well as access transistor as shown in Fig. 3.35(a). For MTJ we have assumed tunnel oxide barrier and surface area variations. The variations in access transistor is lumped in threshold voltage fluctuation. The mean and standard deviation of these parameters are provided in Table 3.1. The variations in the MTJ can increase the intrinsic thermal energy barrier and resistance of MTJ which in turn can increase the write time. The write latency is asymmetric in nature. We have considered the worst case polarity (high/low transition) for latency analysis.

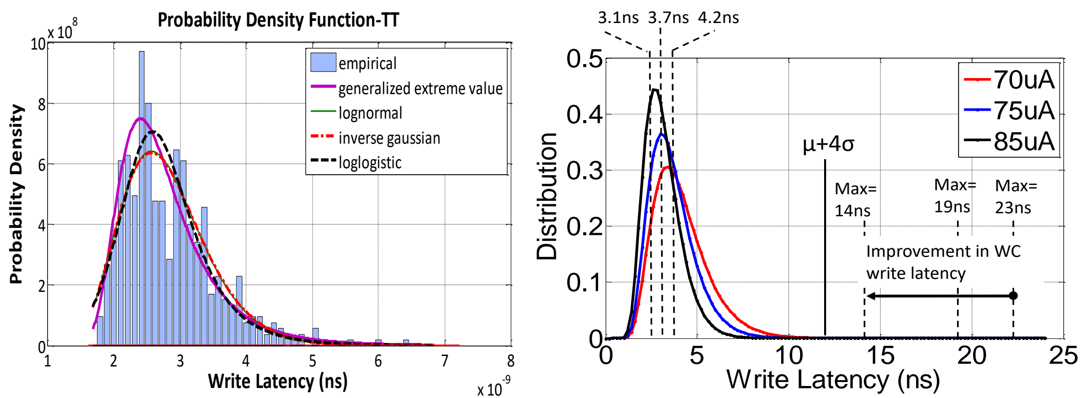

(a) (b)

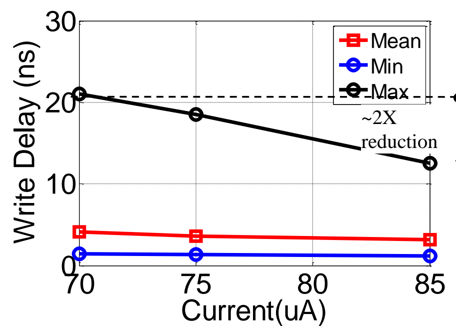

(C)

Figure 3.36 Write latency distribution for 5000 Monte Carlo points. The curve fitting to model the tail is also shown; (b) write latency distribution using curve fitting model for three different write currents. The worst case MTJ can be accelerated through high write current. The 4 sigma delay is also shown. By boosting the current the number of bits beyond 4 sigma delay can be reduced; and, (c) min, mean and max write latency with write current.

Fig. 3.36(a) shows the Monte-Carlo analysis for 5000 simulation points at typical process corner. It can be noted that performance analysis with mean write latency assumption can result in significant overestimation. The write latency also shows a long tail and the worst case write bits could eventually limit the system performance. In order to gain detailed understanding we use curve fitting based functions in Matlab to model the write latency distribution (especially the tail). Fig. 3.36(a) depicts different models (empirical, Extreme Value Theory, lognormal, inverse Gaussian and loglog) used to fit the distribution in Matlab. Empirical model indicated better match for the

tail. Therefore, we used this model for the cache level analysis. Note that the cache size for our study is 8MB. The curve fitting model is used to extrapolate the distribution to 8MB bits. At 70uA current the worst case write latency is found to be 23ns which is >5X larger than mean value underscoring the need of process variation-aware design (Fig. 3.36(b)). In order to improve the system performance it is crucial to fix the tail of the write latency. The distribution for boosted write currents are also shown in the plot. It can be observed that write current boosting can be used to speed up tail bits and mitigate the impact of process variation on write latency. The distribution also indicates that the number of MTJs beyond $\mu+4\sigma$ point is reduced when write current is boosted. Fig. 3.36(c) plots the max, mean and min latency for different write currents. It can be noted that worst case points can gain significant benefit (as much as 2X) although the mean shows minor improvement from boosting.

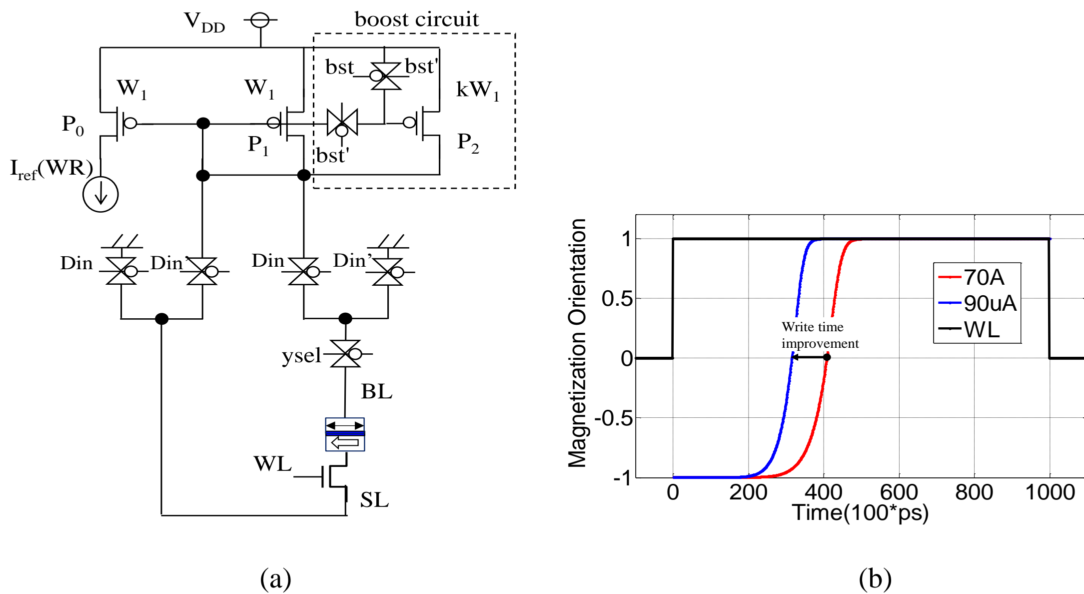

Figure 3.37 Boost enabled write and sense circuit; and (b) simulation results showing write time improvement by enabling write boost.

3.3.2.2. Process Variation Tolerant Design

From the above discussion, it is evident that write current boosting can be used as a knob to mitigate process variation. As depicted in Fig. 3.36(b), write current boosting reduces the number of MTJs beyond 4 sigma delay. Note that the current boosting for write is associated with power consumption. Therefore, these knobs should be used only for the tail bits to improve the performance with minimal impact of dynamic power. The detailed methodology is described in Section 3.3.4.

3.3.3. Subarray Circuit Design

In the previous section we studied the impact of process variation and write current boosting as design time techniques to improve performance under variability. In this Section, we will present the bitcell design, write driver design to enable boosting. The subarray architecture will also be presented to incorporate these designs.

3.3.3.1. Write Driver Design

We propose a novel current mirror based write driver to boost the write current of the column if needed (Fig. 3.37(a)). A reference write current I_{ref} (WR) is mirrored on the leg that is driving BL/SL. The direction of current flow is controlled by the polarity of data to be written (D_{in}). The BL (SL) is connected to current source (VSS) if the data to be written is 1 (0). The sizing of PMOS P_1 is ratioed wrt to reference leg to generate the required write current. We add an extra PMOS transistor P_2 with size k so that extra current needed for the boosting is generated when boost signal is asserted (i.e., bst=1). For nominal conditions P_2 is disabled by connecting the gate to V_{DD}.

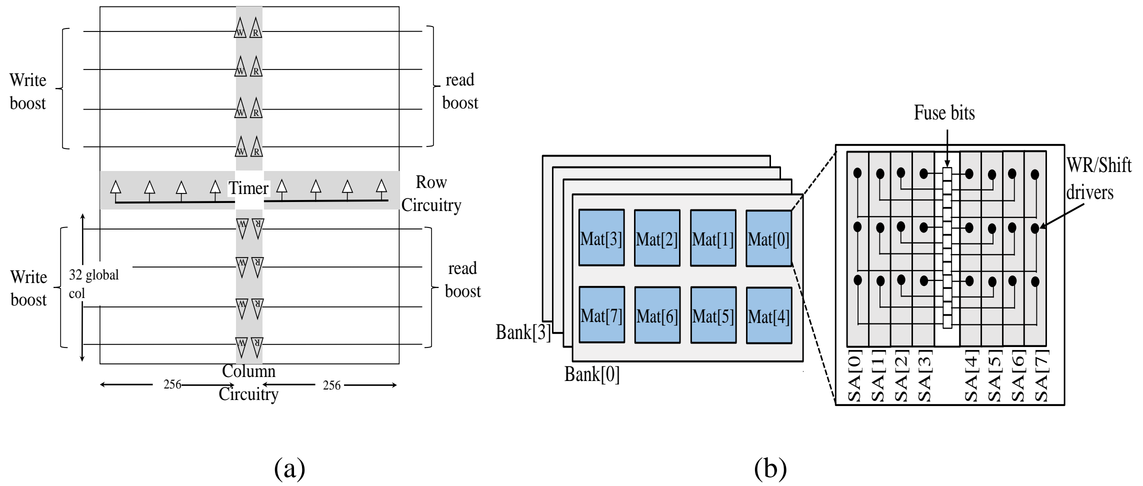

Figure 3.38 Subarray architecture showing boost enabled write and read circuit; and, (b) cache organization and fuse bits.

The proposed driver needs 4 transistors for multiplexers and an extra PMOS to generate the boosted current. Considering the fact that gate leakage is negligible and *bst* is a DC signal the multiplexers can be designed using minimum sized transistors. Therefore, the area overhead of the proposed boosting can be kept below 1%. Fig. 3.37(b) shows the hspice simulation waveform of magnetization switching during write process for nominal and boosted current.

3.3.3.2. Subarray Architecture

Fig. 3.38(a) shows the proposed sub-array design with integrated boost enabled write drivers. There are a total of 64 WLs (32 in each sector) and 512 local columns. Column muxing of 8:1 is used for one global column. A total of 64 global columns provide 64 bits of data in/out. The column area holds read/write circuitries. The write drivers are designed per global column basis. Therefore, boosting a write driver will boost the write current for the 8 local columns. *Note that it is possible to disable the boost for fast MTJs at the cost of decoding complexity*. Furthermore, the power overhead of boosting small number of global columns is found to be minimal (3.3.4).

3.3.4. Cache Design for Adaptive Boosting

In the previous section we explained the subarray circuit design techniques. This section is focused on methodology to identify the slow bits and implementation of current boosting. This is followed by cache organization and simulation results. The limitations and possible improvements are also discussed.

3.3.4.1. Methodology

The proposed boosting is employed after a test routine that screens the slow write bits. The test pattern can be any of the conventional March patterns (e.g., March C [86]) that is performed at different frequencies to determine the write time of the bits in absence of boosting. The columns containing slow write are marked individually. In this context it is worth mentioning that the entire global column is marked slow even if one of the local columns are found slow. This is due to the fact that write drivers are shared per global column basis. Next the same patterns are repeated with the boosted write currents to ensure that the bits pass. Since the amount of current boosting is determined statistically through simulations we expect that all bits will pass after this step. If not, the existing column or row redundancies can be used to replace the remaining slow bits. It is also possible to provide an extra setting in the drivers during design phase to boost the current further.

Table 3.7 Processor Configuration

Processor	Alpha,O3,4 cores, 2GHz, 8-way issue
SRAM L1-Cache	Private, Icache=16KB, Dcache=16KB, 64B Cache-line, 2 cycle Read/Write latency, Write back.
LLC Cache	Shared, 8MB, 4 banks, 8 ways, 64B cache-line, writeback, R/W latency based on memory tech.
Main Memory	4GB, DDR3, 200-cycle latency

Fuses are used to program the individual columns for boost/no-boost. The fuse bits are decoded and loaded in the flip-flops to assert the DC signals controlling boost (Fig. 3.38(b)). Note that fuse-based infrastructure is commonly used in micro-processors for redundancy programming, SRAM assist setting etc. Therefore, the proposed technique can be easily incorporated in the system.

3.3.4.2. Cache Organization

We have considered a 8MB L2 cache for this study. The L2 cache is divided into following sections (Fig. 3.38(b)): (a) Sub-array, (b) Mat that consists of a group of sub-arrays which share a common pre-decoder. Each mat contains multiple ways. A group of mats provides output cache-line (e.g., 8 mats provide 64 bits each totaling 512 bits) and, (c) Bank that operates independently.

Each subarray contains 512 rows and 512 columns. This amounts to 1Mb data. Each mat is composed of 8 subarrays (SA[7:0]). The write drivers of each subarray receives global column based boost signal. This will require 128 DC tracks (i.e., two tracks per global column) to be routed for each subarray i.e., 512 DC tracks per mat. Note that minimum pitch metals can be used for routing these signals. Each bank contains 8 mats (mat[7:0]) of total size 8MB. There are four independent banks (bank[3:0]) in the cache.

Each way in L2 is implemented in a different subarray in mat for parallelism. The column mux selects the desired BL and senseamp senses bit-cell states in either data or tag array. Each mat provides 64-bits of data by accessing a subarray. For example, way0 is accessed by enabling SA[0] of Mat[7:0] providing 512 bits of cache line. The L1 cache comprises of traditional SRAM.

3.3.4.3. Simulation Setup

We evaluate SRAM and several cases of STTRAM in terms of power and performance. The evaluations are performed on a 4-core Alpha processor in Gem5 [87]. The processor configuration is provided in Table 3.7. Gem5 is modified accordingly to implement variable read and write latencies for STTRAM cache. We simulate process variation for 5000 runs of Monte Carlo and find a model to fit the distribution in Matlab. Next the model is used to estimate the write and read latency distributions for 64 million MTJs. Next the steps described below are followed:

1. The number of MTJs with write latency greater than 4 sigma (N_{wr}) are determined from the latency distribution obtained from Matlab. Similarly, the number of MTJs with read latency greater than 4 sigma (N_{rd}) are determined.

2. N_{wr} and N_{rd} are randomly distributed among the 64 million MTJs. The slow global columns numbers are determined in Matlab and fed to Gem5.

3. Gem5 matches the global columns for each access with the list and finds the number of times the slow global columns are accessed. This information is used to estimate the dynamic power of boosted columns.

Table 3.8 Design parameters for different cache configurations (22nm Technology).

Cache parameters	Cell Size	Total Area	Read Lat.	Write Latency boost/orig.	Read Energy	Write Energy	Write Pulse (boost/orig.)	Leakage Power (W)
SRAM	$146F^2$	$17.3mm^2$	5ns	4ns	1.1nJ	0.8nJ	------	10.2
STTRAM-no-PV	$40\ F^2$	$6.9\ mm^2$	2.9ns	5.2ns	0.9nJ	1.4nJ	3.9 ns	1.72
STTRAM-WC-PV	$40\ F^2$	$6.9\ mm^2$	6.1ns	22.2ns	0.6nJ	0.7nJ	21ns	1.72
STTRAM-PV	$40\ F^2$	$6.9\ mm^2$	6.1ns	13.4ns/22.2ns	0.6 nJ	0.7nJ/1.2nJ	12.5ns/21ns	1.72

The simulations are performed over a wide range of Parsec Benchmarks [88]. For power simulation we used McPAT [89] multi-core power simulator with modified CACTI [90] integrated in Gem5 simulator. We have simulated following cases to evaluate STTRAM under process variations:

(a) STTRAM-no-PV: STTRAM without any process variation.

(b) STTRAM-WC-PV: STTRAM with worst-case write and read latency due to process variation.

(c) STTRAM-bWR: STTRAM with write boosting of slow columns.

(e) STTRAM-bAll: STTRAM with write and read boosting of all columns.

The cache latency and energy are obtained using CACTI [90] and Hspice model of STTRAM. The parameters used for simulations are provided in Table 2. Mean write latency is considered for STTRAM-no-PV whereas worst case write latency is considered for STTRAM-WC-PV (Fig. 3.36(b)). We use write current of 70uA for STTRAM-no-PV and STTRAM-WC-PV and 85uA for boosted cases. For boosted cases, we assume 4 sigma write latencies for normal columns and boosted columns. The write and read energy with and without boosting is also shown in the Table 3.

3.3.4.4. Simulation Results

Fig. 3.39(a) shows the performance result represented by the normalized (normalized to SRAM) instruction per cycle (IPC). STTRAM-no-PV provides 4% performance improvement over SRAM. However STTRAM-WC-PV indicates that process variation can degrade the IPC by 10% on average compared to STTRAM-no-PV. Boosting the write current (STTRAM-bWR) can improve the IPC by 13% compared to STTRAM-WC-PV. The maximum benefit is observed for write intensive benchmarks such as dedup.

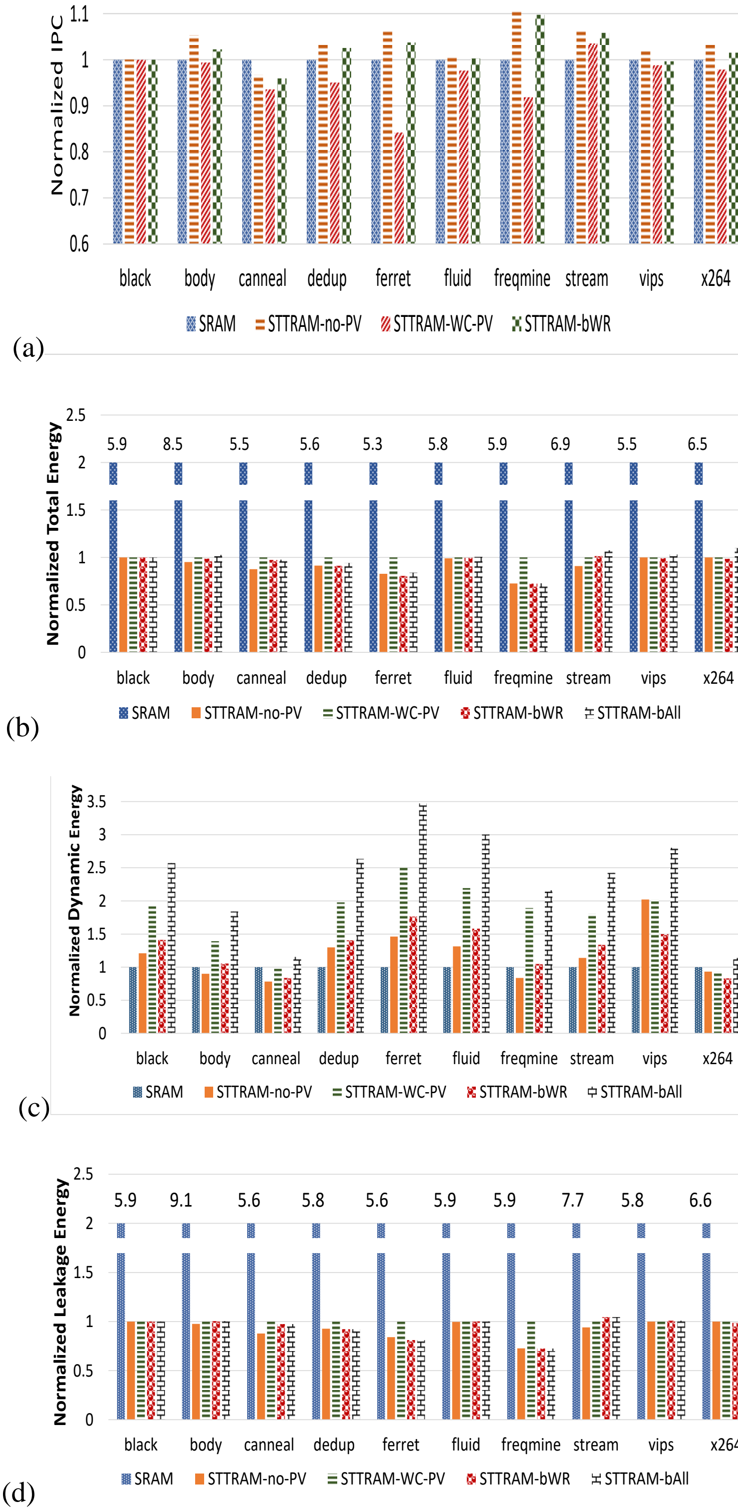

Figure 3.39 (a) IPC; (b) L2 total energy comparison ; (c) L2 Dynamic energy; (d) L2 Leakage energy.

PV). The STTRAM architecture shows ~6.4X saving compared to SRAM. This is owing to elimination of bitcell leakage and reduction in peripheral leakage (due to less number of peripherals). STTRAM-bAll increases the power for benchmarks dedup and freqmine because they are write intensive. The other benchmarks observe power reduction due to lower peripheral leakage as the run-time is faster with boosted write.

Fig. 3.39(c)-(d) shows the breakdown of total energy into leakage and dynamic energy. The proposed STTRAM-bWR decreases the dynamic energy consumption by 30% compared to STTRAM-WC-PV due to write pulse time reduction. However, it reduces the dynamic energy by 80% relative to STTRAM-bAll. Therefore, the proposed write boosting is effective in improving the IPC (13%) and the energy (30%) in compare to STTRAM-WC-PV.

3.4. Summary

STTRAM is a promising non-volatile memory technology for cache application due to high-density, low standby power, excellent retention, fast access time and good endurance. However, it can suffer from poor sense margin, and severe performance and power degradation due to process variation induced write and read latency variations. In this chapter, we proposed two flavors of sensing techniques to improve read yield of STTRAM: 1) A robust and destructive slope sensing technique to eliminate reference resistance variation; 2) a very low-power and non-destructive sensing scheme that exploits a voltage feedback and boosting (VFAB) technique to develop large sense margin as well as eliminating static current. In addition, we have proposed adaptive write current modulation to mitigate process variation induced write latency and power overhead.

We have designed a test-chip to demonstrate reference-less slope sensing technique. We characterized the slope sensing failures with respect to ramp current slope, sampling frequency and

various resistance values. A 96kb fabricated test-chip in 65nm technology shows that slope sensing reduces failure rate by 120X in 2.5K-5K array@TMR=100% and 162X in 2.5K-5K@TMR=80% array compared to conventional voltage sensing.

The proposed VFAB, outperforms conventional sensing in terms of RAPY and power substantially. Simulation results show that proposed sensing achieves RAPY of 14.4σ in typical corner and read power is reduced 4.7X compared to conventional sensing. Additionally, the proposed sensing is voltage scalable and provides excellent sense margin even with as poor TMR as 25%.

We propose a novel and adaptive write current boosting to address this issue. The bits experiencing worst-case write latency are fixed through write current boosting. Simulations show 80% power improvement compared to boosting all bit-cells and 13% performance improvement compared to worst case latency due to process variation over a wide range of PARSEC benchmarks.

Chapter 4

Secure Design of STTRAM Last Level Cache

STTRAM is promising for cache applications. However, it brings new data security issues that were absent in volatile memory counterparts such as SRAM. This is primarily due to the fundamental dependency of this memory technology on ambient parameters such as magnetic field that can be exploited to tamper with the stored data. As discussed in Section 2.1.3.6, the adversary can place an external AC/DC magnetic field to alter the $\overrightarrow{H_{eff}}$ parameter resulting in uneven flipping of bits under read, write and/or retention [40]. The objective is to launch Denial-of-Service (DoS) attack. A carefully orchestrated DoS attack can result in severe consequences during secure data processing and financial transactions to name a few.

In this chapter, we investigate data security of STTRAM last level cache under magnetic attack. The magnetic attack could be gradually ramping and/or sudden in nature. We propose three techniques to avoid errors in presence of magnetic attack, (a) stalling where the system is halted during attack; (b) cache bypass during gradually ramping attack where the last level cache (LLC) is bypassed and the upper level caches interact directly with the main memory; and, (c) checkpointing along with bypass during sudden attack where the processor states are saved periodically and the LLC is written back at regular intervals. During attack, the system goes back to the last checkpoint and the computation continues with bypassed cache.

4.1. Introduction

The free layer of MTJ flips under the influence of external magnetic field and temperature that can be exploited by the adversary. The magnetic field produced by a horseshoe magnet can be used to flip the bits in a STTRAM memory array [40]. Therefore, magnetic field can be exploited by the adversary to scramble the data in LLC to launch denial of service (DoS) attack or simply increase the miss rate affecting the overall performance of the system. The existing countermeasures to mitigate magnetic attack include variable strength Error Correcting Code (ECC) and forced retention [40]. The strength of the ECC is increased (1bit/2bit/4bit/8bit) depending on the magnitude of the attack. The ECC design is modular and during normal operation the unused ECC modules are power gated to reduce energy. Although effective ECC introduces significant design overhead. The effect of temperature on the read/write current, latency and bit error rate is presented in [93] however, the mitigation technique is not provided. Moreover, magnetic shielding can be employed to alleviate magnetic attacks [94-95]. The simulation results show that external magnetic field of H=50Oe is degraded to H=10Oe using shielding technique proposed in [94]. However, higher intensity external field may still result in failure of functional bits since the shielding cannot offset the magnetic flux completely. The proposed technique can protect the bits even at arbitrarily high magnetic field intensity. Therefore, the proposed technique can be used in addition to magnetic shielding technique to prevent failure under magnetic attack. Moreover, the shielding techniques associated with extra fabrication cost due to extra mask and materials required for fabrication process. Additionally, the associated cost and area overhead is not desirable in mobile devices such as cellphones and IoTs.

In this work, we consider two types of magnetic attack on STTRAM LLC. In the first case, the strength of the attack ramps up gradually and in the second case strength of the attack ramps suddenly. The gradual ramping attack is more practical when human entity is involved in the attack

process and a permanent magnet or electromagnet is brought closer to the memory manually. The adversary can launch DOS attack by bringing a permanent magnet close to mobile devices such as IoTs and cellphones. The sudden attack applies to scenarios where the adversary has physical access to the memory and has precise control over the magnetic field strength and proximity from the chip. An insider in a computer facility can launch DOS attack by physically accessing the memory. In sudden attack, the functional bits can fail immediately if the field strength is beyond the threshold value.

We assume that the attack signal is generated by the magnetic field sensors [40] that are distributed in the memory array. The sensors are composed of MTJ cells that are less robust than the actual functional bits. The sensor MTJs [40] can sense both gradually ramping attack as well as sudden attack through fail rate. Based on the sensor input we propose a suite of techniques to deal with the attack. A simple stalling is proposed where the execution of instructions is stalled during the ramping attack and the execution resumes from the same state after the attack is removed. Write back of dirty data to main memory is performed before stalling to update the processor state. The LLC is invalidated before resuming the execution since the data cannot be trusted after attack. Although simple, stalling is associated with performance loss during attack event.

Cache bypassing is proposed to continue error-free computation during the ramping attack (Fig. 4.1(a)). The attack sensors detect the attack ahead of time and the system is prepared to enable bypassing. The system needs to write back the dirty data in case of write-back policy to save the modifications made before the attack. Updating main memory must be performed during compensation window (i.e., the time difference between the failure of attack sensors and functional bits) to maintain functional correctness of the system. Updating main memory might consume several clock cycles before the system can continue with the LLC bypass. This step is shown in the figure as “bypass preparation”. After the write-back the bypassing is enabled, and the system runs at lower performance due to long memory latency. In ramping attack, the sensors sense the attack

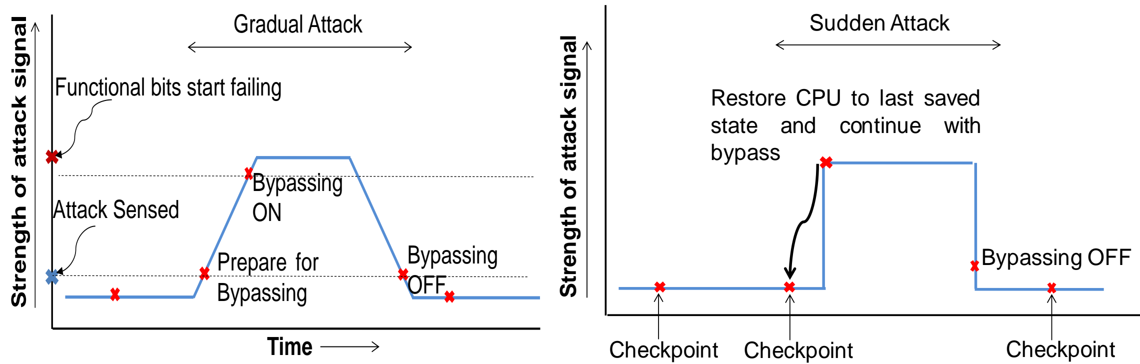

Figure 4.1 Two types of magnetic attacks: (a) gradually ramping attack; and, (b) sudden

ahead of time to perform the write back but in case of a sudden attack the functional bits start failing instantly (Fig. 4.1(b)) providing no opportunity to write back the dirty data. We propose checkpointing technique where CPU register values and program counter (PC) are saved (in hard disk) and write back is performed on all cache levels. In the event of an attack, the processor states are loaded with the last saved checkpointed data and the pipeline is flushed. The instructions executed between the last checkpoint and detection of attack are re-executed (Fig. 4.1(b)). The LLC is bypassed during the attack to prevent functional failures. Once the attack has subsided, the LLC is invalidated, and the bypass signal is de-asserted. The system continues to perform checkpointing at regular intervals.

In summary, we make following contributions in this chapter:

- CPU stalling technique to handle ramping attack with least design complexity.
- A novel dynamic LLC bypassing technique that exploits the existing design features to enable safe computing seamlessly under ramping attack.
- Periodic and forced checkpointing with LLC bypass to handle sudden attacks on LLC.

4.2. Related Work

Cache bypassing has been proposed previously to increase the performance and effective capacity of LLC without incurring power/area costs of a larger sized cache. The idea is to bypass the blocks which may pollute the cache [96][97]. A significant number of items referenced in a program are accessed very rarely and when they are fetched in cache, they evict other cache blocks. In such cases not only it nullifies the benefit in placing those items in cache, but it also incurs eviction overhead of blocks (which may be one of the frequently accessed blocks) to make way for these not so frequently accessed blocks. Furthermore, since the data is fetched from the main memory in block sizes (512KB/1024KB), fetching one word leads to the eviction of the entire cache line. In such scenarios the best option is to bypass the cache and directly send the requested word to CPU. Intel's i860 processor provides support for cache bypassing [98]. A load instruction PFLD (pipelined floating-point load) is provided to bypass the LLC to avoid cache pollution. Cache bypassing is proposed for STTRAM LLC since the latency of write operations is 2X higher than read operations which may obstruct other cache accesses on a multi-core system running multiple processes. Therefore, other accesses can be forwarded to the main memory or upper level caches [99]. Similarly, the reusability of cache blocks is very low in GPGPU applications where cache bypassing results is higher performance [100]. A performance gain of 6 %-10% is reported in these methods.

Note that the existing bypass techniques noted above are one-way, i.e., they bypass the data coming from main memory to LLC. The data coming from CPU to LLC is not bypassed. Therefore, these techniques cannot be extended for data security where bypass of LLC is desired both from CPU to main memory and vice versa. Furthermore, bypassing needs to be dynamically enabled and disabled depending on attack signal from sensors. Therefore, a bypassing technique using look-aside cache architecture is proposed to bypass LLC form CPU to main memory and vice versa. In

this method system behaves as there is no LLC and performance degrades by 13% if LLC is bypassed during the entire execution time. Before starting bypass, the dirty blocks in LLC needs to be written back to the main memory and after the bypass, the LLC needs to be invalidated.

System-level checkpointing is a mechanism used in modern systems to provide recovery in case of sudden power failure [101]. Micro-architectural checkpointing is also proposed for system recovery from transient faults [102]. The basic approach is to perform computations in epochs during which the underlying hardware is checked for errors, if any fault is detected the results of that epoch is discarded and the system is restored to last known good state. During an epoch the results are held in a speculative state and get committed at the time of checkpointing. System-level state checkpointing has been employed to improve the performance of reorder buffer (ROB) in terms of handling exceptions [103]. Application level self-checkpointing techniques also exists [104], [105]. The checkpointing mechanism proposed in this paper has been adopted from [102]. Since checkpointing is associated with IPC and energy overhead, the period of checkpointing could be tuned according to the occurrences of attack. Initially, the checkpointing can be performed at larger intervals to avoid IPC loss but after detection of an attack the frequency of checkpointing can be increased.

4.3. Attack Models

4.3.1.1. Attack Model

As described in Equation 2.1in Section 2.1.2, the adversary can place an external AC/DC magnetic field to alter the $\overrightarrow{H_{eff}}$ parameter resulting in uneven flipping of bits under read, write and/or retention [40]. The objective is to launch Denial-of-Service (DoS) attack. A carefully orchestrated DoS attack can result in severe consequences during secure data processing and financial transactions to name a few. The magnetic attack can also be carried out when the system

is OFF. However, such attacks will not affect the computation as the cache is invalidated on startup. Therefore, we focus on active attacks, i.e. when the system is operational.

4.3.1.2. Attack Sensing

The key objective of the attack sensor [40] is to sense or detect magnetic field attack ‘proactively’ in order to trigger corrective steps for the functional STTRAM array. The sensor output is used to trigger LLC bypass to avoid failures under magnetic field attacks. A small replica of the STTRAM array is used as a sensor. The sensor is embedded in the array (in the peripheral areas) to capture the spatial and temporal nature of the magnetic attack (Fig. 4.2). The sensor array is designed by modifying the actual STTRAM array. The intensity of the attack is sensed through the error rate of the sensor array. High error rate corresponds to higher intensity. The control logic resides in midlogic area and generates address, read/write signals and data and, collects responses to determine error rate from various sensor flavors.

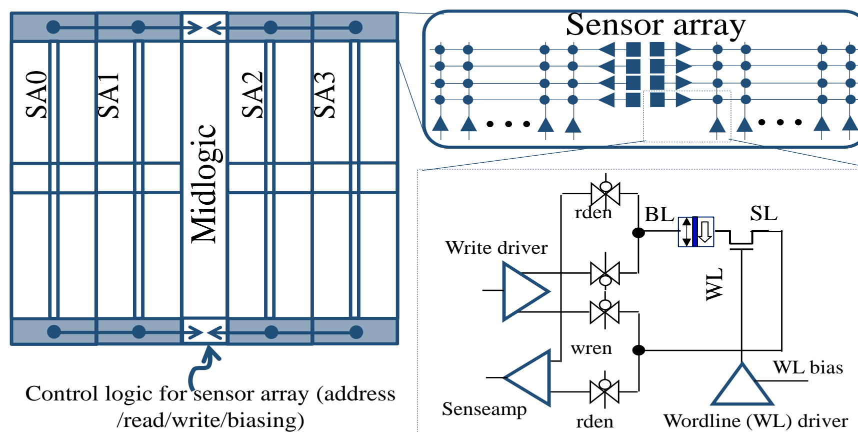

Figure 4.2 Embedded attack sensor in memory array [40]. The details of sensor array with peripheral circuits is shown in inset. Control logic is shared among the subarrays and contains the logic to generate address, read, write and data and analyze the response.

The details of sensor design is presented in [40] however, we have summarized it briefly for the sake of clarity. The key idea is to make the MTJ sensitive to magnetic field. This can be achieved by lowering its retention time which is exponentially related to MTJ's thermal barrier (Δ) and is given by $t = C \times e^{k\Delta}$, where C and k are fitting constants. The thermal barrier, in turn, is proportional to free layer volume (V) and inversely proportional to absolute temperature (T) and is given by $\Delta = \frac{k_u V}{k_B T}$, where k_u is anisotropy constant and k_B is the Boltzmann's constant. Reducing free layer volume result in lower retention time for both store-0 and store-1. Therefore, MTJs with low free layer volume can sense both attack intensity and polarity. Moreover, injection of disturb current in opposite polarity than stored value also lowers the retention time (weak write circuit is shown in Fig. 4.2). From [40], a combination of low volume and weak writing can create a timing window of *few hundred microseconds* before the functional bits start failing. Note that accurate sensing of attack while avoiding misprediction is a research challenge itself and is beyond the scope of this chapter. The sensors are placed only on top and bottom of subarray. The area overhead of the proposed sensors is less than 1% since they are embedded in the transition region of the arrays. Weak writing of sensor bits can cause power overhead. In order to reduce power consumption, the sensors with weak write could be (a) interleaved with normal sensors; and, (b) turned on periodically [40]. Therefore, power overhead can be reduced significantly.

4.4. Prevention Techniques

In this section, we present three countermeasures to protect against data security attacks on STTRAM LLC.

4.4.1. System Assumptions

We assume following features in the system for analysis:

Attack sensors: We assume that the attack signal can be asserted by the sensors [40] before the actual bits are affected. Depending on the sensor and memory error rate a signal can also be asserted to indicate whether the attack is gradual or sudden. A failure of sensor array indicates ramping attack whereas failure in both sensor and memory array indicates sudden attack. Memory failures are detected by ECC.

Look-aside cache: Look aside cache architecture [104] is a system where the cache is located on the processor bus in parallel with the main memory controller (Fig. 4.3). This design enables both the cache controller and memory controller to service CPU read and write requests simultaneously. If a cache miss occurs, then the request is completed by the memory controller. Fig. 4.3 explains the read/write operation in a look-aside cache architecture. The CPU issues a read/write request and if the requested tag is found in upper level caches (L1, L2) then it is serviced by them. If a miss occurs in upper level caches (step 1), then the request is simultaneously sent to both LLC cache controller and main memory controller as they are connected to the processor bus in parallel (step 2). The cache controller searches the requested tag in LLC and asserts the HIT signal if it is found (step 3). The assertion of HIT signal sends an ABORT signal to the memory

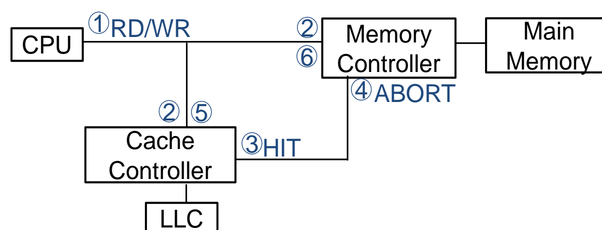

① CPU issues a read or write request. Requested tag misses in L1 and L2.
② Both cache controller and memory controller receive request simultaneously.
③ Cache controller searches tag array for requested tag and asserts HIT signal if match is found.
④ Asserted HIT signal is connected to ABORT signal of memory controller, so if HIT=1 memory controller aborts, or else continues to serve the CPU request.
⑤ If the data is found in cache the cache controller sends the data to CPU.
⑥ Else the data is received from main memory

Figure 4.3 Look aside cache architecture.

controller informing that the tag is found in LLC and the memory controller should abort searching in main memory. The corresponding data is then sent to the CPU from the LLC (step 5). If the tag is not found in LLC, then the HIT and ABORT signals stay de-asserted and the data is fetched by the memory controller. The corresponding data is sent to both CPU and LLC from the main memory (step 6). Therefore, the memory access time is reduced during LLC miss compared to traditional *look-through* cache.

4.4.2. Preventive Solution: Stalling

The simplest and robust solution is to stall the CPU and wait till the attack is over. If the cache implements write-back policy, then the dirty data is written back to the main memory to save the system state on detection of the attack (for gradually ramping attack) and the CPU is stalled. After the attack is over, the entire LLC is invalidated and the computation starts from the last saved state. The processor's register contents will remain intact and the computation can resume from the state it was halted. This technique is better than shutting down the entire system because the processor states remains intact and the computation can instantly start after the attack is over. For the user, the machine will appear to be stuck during the attack however, the user is not required to reboot the system. Although simple, this technique will not work for sudden attack since the dirty data will be corrupted (or become untrustworthy). For such scenarios the processor has to be restarted after the attack and the applications can restore the states if application level checkpointing [105][107] is implemented (which is typically the case for common applications such as Microsoft word, powerpoint, firefox). These methods prevent DoS attack successfully as the system does not consume corrupted data. However, both approaches disable computations during attack and result in power loss. The attacker can also exploit these features to drain the battery of the system.

4.4.3. Preventive Solution: Cache Bypass

Cache bypassing enhances the user experience as the computation continues with affordable IPC degradation. We show the necessary steps needed to prepare for bypassing, continue bypassing and exit bypassing (Fig. 4.4(a)). If the sensors indicate a weak attack the LLC is flushed by copying the dirty data and a bypass signal (BP) is asserted. In absence of attack, if the bypass signal is still asserted (indicating the end of attack), the entire LLC is invalidated and the BP signal is de-asserted. Otherwise, no extra steps are needed. In the following paragraphs we explain various stages of bypassing. *Preparing for bypassing (Fig. 4.4(a)):* If the sensors indicate an attack,

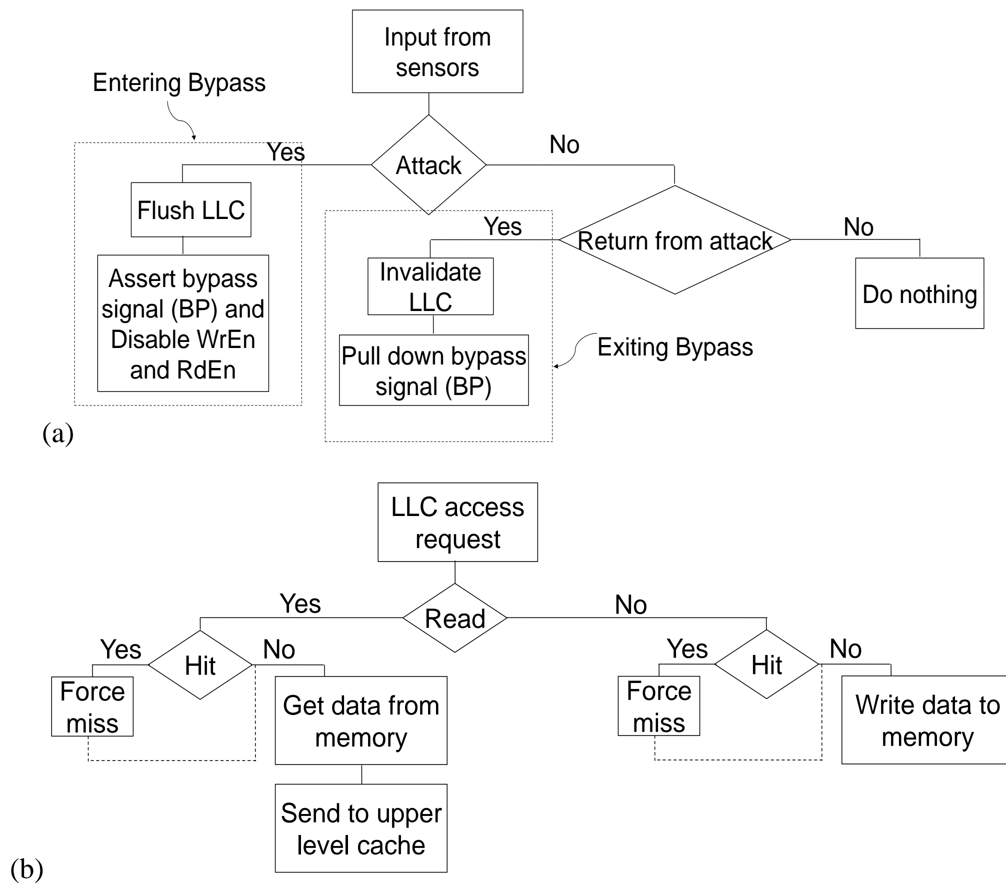

Figure 4.4 (a) Control flow to activate/deactivate bypassing; and, (b) processing of read, write requests during bypassing.

the dirty data in LLC is copied to the main memory by asserting the FLUSH signal [108] in the cache controller to ensure correctness. Note that this is possible since the sensors can sense the attack before bits start failing [40]. The FLUSH signal writes back the dirty blocks and invalidates all the cache lines after the write-back. The BP is asserted to indicate the cache controller to bypass the subsequent requests to the main memory. Note that if LLC employs write-through policy then this step is not necessary as the copy of data is immediately written back to the main memory.

Bypassing mode (Fig. 4.4(b)): There are four scenarios when the data can leave or enter the LLC namely, read hit, read miss, write hit and write miss. The read hits are forcibly converted to read misses so that the data is read from the main memory instead of cache. Read misses are served normally by sending the data from main memory. Write hits are also forcibly converted to write misses and the data is written only to main memory. In case of write misses the main memory is updated with the new data. During the attack LLC data should not be used for computation or stored anywhere (upper level caches, main memory). Note that new data may be read (written) from (to) the LLC and discarded during bypassing which results in energy overhead. In order to save dynamic energy, the LLC is prevented from performing read or write operations. This can be done by ANDing $\overline{BP}$ with WrEn (write enable) and RdEn (read enable) signals which is generated by the cache controller. In the following paragraphs, we explain the implementation of bypass during various cache accesses:

(i) LLC read hit (Fig. 4.5(a)): If the address requested by the CPU is not found in the upper level caches the request is forwarded to the LLC. If tag match happens in LLC and the corresponding valid bit is set, then the data is sent to CPU. In case of tag miss or invalid data in LLC the cycle is completed by the main memory as described earlier. To enable bypass we add a multiplexer and an AND gate to force a LLC miss. Therefore, even if the data is present in LLC the cache controller is tricked to send a miss signal and the data is fetched from main memory. The

Cache bypassing architecture (Read bypass)

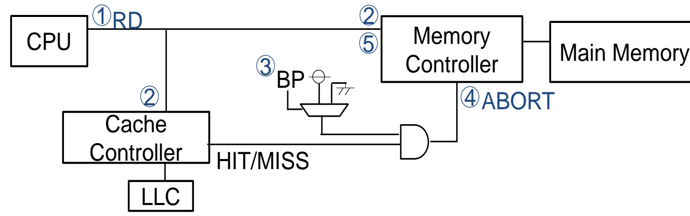

① CPU issues a read request. Requested tag misses in L1 and L2.
② Both cache controller and memory controller receive the request simultaneously.
③ Bypass signal (BP) is asserted and the output of the mux is lowered forcing LLC miss.
④ Memory controller does not receive abort signal and continues serving the read request.
⑤ The requested data is sent from the main memory, bypassing LLC. Writing of data in LLC can be masked by pulling the write signal low in write driver

(a)

Cache bypassing architecture (Write bypass)

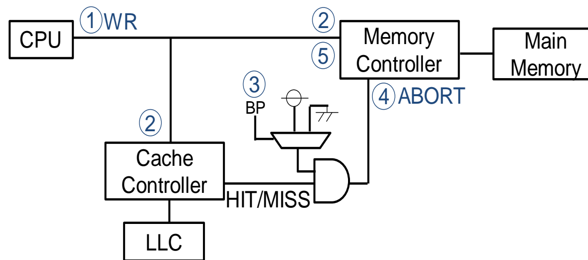

① CPU issues a write request. Requested tag misses in L1 and L2.
② Both cache controller & memory controller receive request simultaneously.
③ Bypass signal (BP) is asserted and output of the mux is lowered forcing LLC miss.
④ Memory controller does not receive the abort signal and continues serving the write request.
⑤ New data is written to main memory. We assume write-no-allocate policy, thus the data is only updated in main memory and not LLC.

(b)

Figure 4.5 Bypassing of (a) read, and (b) write request with look-aside cache architecture.

redundant writing of data in LLC with new data can be prevented by gating the write enable discussed before.

ii) LLC read miss (Fig. 4.5(a)): If the address requested by the CPU is not found in any level of cache then the request is forwarded to memory controller and the data is read from main memory. A copy of the data is also placed in LLC. In the proposed architecture all the read requests are forced to be a LLC miss and each time the data is taken from the main memory if it is not present in upper level caches.

iii) LLC write hit (Fig. 4.5(b)): If the write cycle issued by the CPU matches the tag in LLC then the corresponding data is updated. During bypass all write requests on LLC are forced to be a miss and the CPU writes to the main memory directly.

iv) LLC write miss (Fig. 4.5(b)): In case of LLC write miss when the requested address is not found the writes are automatically forwarded to the main memory. During bypass, all write requests are forced to be a miss and the main memory is always updated with the new data.

Exiting bypass mode (Fig. 4.4(a)): When the attack ends or the system is not under attack then no action is needed. If the system is in bypass mode, then we invalidate the entire LLC after attack since the data cannot be trusted. After the bypass signal is de-asserted the subsequent requests are serviced by the LLC. A hardware interrupt is forced to stall the CPU and prevent updating of LLC during the FLUSH and invalidate operations.

4.4.4. Preventive Solution: Checkpointing

We leverage the system-level checkpointing to mitigate the sudden attacks. Fig. 4.6 illustrates the high-level timeline of execution of events performed during a sudden attack. The CPU register values and PC are saved in hard drive. Additionally, LLC dirty blocks are stored in the main memory. Note that write back is performed throughout the cache hierarchy during checkpointing event. When an attack is sensed the system is restored to the last saved checkpoint and the bypass signal is asserted. The system continues to perform with the LLC bypass and the checkpointing is disabled to avoid write back of stale LLC data. After the attack ends, the bypass signal is de-asserted, the LLC is invalidated and a checkpoint is created. The system continues to perform normally with checkpointing resumed. If magnetic attack rises and falls repeatedly and attack frequency is more than checkpointing frequency, the system keeps rolling back to the

last checkpoint which is created before first attack rises, thus, CPU is stuck. Therefore, when attack is over, LLC is invalidated and a checkpoint is created.

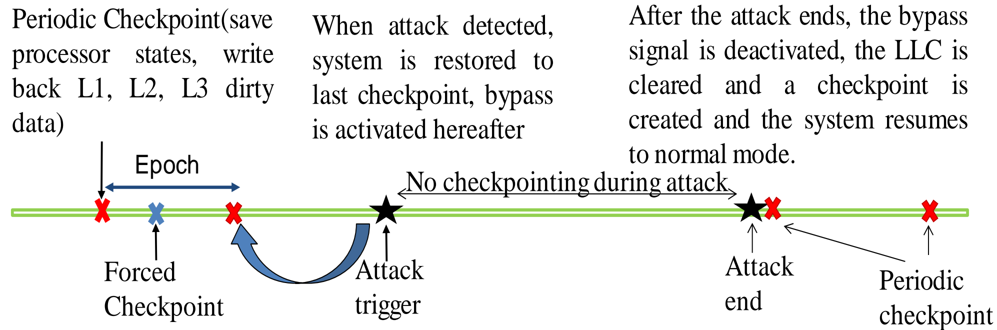

Figure 4.6 Cache bypass architecture with checkpointing.

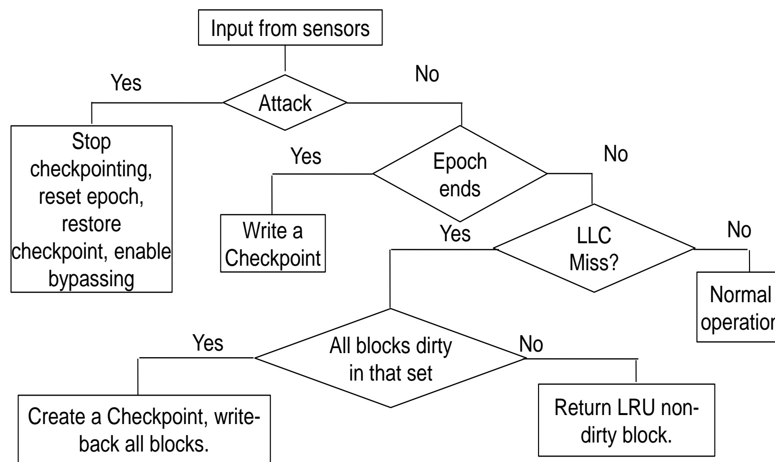

Figure 4.7 Control flow diagram of checkpointing.

Two types of checkpointing is implemented in this chapter: 1) periodic, 2) forced. Periodic checkpointing occurs at regular intervals during program execution time. Periodic checkpointing is implemented by using a checkpointing buffer (CPB) which stores indexes of dirty blocks during an epoch (the time between two periodic checkpoints). During checkpointing event, a special hardware embedded in the LLC reads the CPB contents and writes all dirty blocks to main memory. The instructions executed after the checkpoint are discarded in case of roll back. We prevent LLC from writing the data to main memory during an epoch so that the system state remains speculative and the system can recover by roll back in the event of attack.

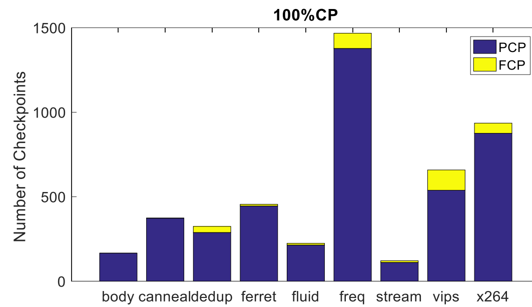

Figure 4.8 Number of forced (FCP) and periodic checkpoints (PCP) for each PARSEC benchmark. Periodic checkpointing is performed after every 2 million cycles.

Prevention of write back during epoch can result in CPU stall when all ways of a set are dirty and there is no candidate for replacement on a LLC miss. This problem is resolved by performing forced checkpointing which is implemented by modifying the LLC LRU replacement policy. On each LLC miss, non-dirty LRU block is selected to be replaced. If all ways of a set are dirty, all ways are written to write buffer and a forced checkpointing is performed. The flowchart of checkpointing is shown in Fig. 4.7. The frequency of forced checkpointing is dependent on the LLC associativity and epoch period. By increasing the associativity of LLC and reducing the epoch period forced checkpointing frequency can be reduced. Fig. 4.8 shows the number of forced and periodic checkpoints during execution time of each benchmark.

4.4.5. Checkpointing for Write-through Policy

LLC with write through policy can also be leveraged to mitigate sudden attack. In write through policy, the data is written to both cache and lower level memory. Therefore, main memory is always updated. Only CPU registers and PC needs to be saved during checkpointing. As a result, in case of both sudden and gradually ramping attack LLC can be bypassed and the system can continue to perform normally since the main memory is updated and CPU state is saved.

Compared to checkpointing, LLC bypassing with write through policy does not incur performance overhead of writing all dirty block backs to main memory and changing the LLC replacement policy. Additionally, since saving CPU state is low-overhead, checkpointing frequency can be increased to reduce the performance loss due to roll back during attack. However, write through policy can increase memory traffic resulting in performance degradation.

4.5. Simulation Results

The proposed bypass architecture is evaluated on a 2 cores Alpha processor in gem5 [87]. The configuration of the processor cores is provided in Table 1. The gem5 code is modified to implement: (a) variable read and write latency for STTRAM LLC; (b) an attack signal is added which is turned ON dynamically to mimic the actual attack signal from the sensors; and, (c) bypassing of LLC is implemented by modifying the cache access method to force a miss when the attack signal is high. (d) periodic checkpointing (PCP) is implemented to create a checkpoint at each 1mS (2 Million Cycles) interval. Forced checkpointing (FCP) is implemented by modifying LRU replacement policy of the LLC. The simulations are performed on a wide range of SPLASH and PARSEC benchmarks suite [88][109].

We have simulated following cases to evaluate performance overhead due to both ramping and sudden attack:

Baseline: processor performs normally without attack.

Full-Attack: LLC is bypassed during the entire execution time of each benchmark.

Half-Attack-Ramp: attack is asserted for 50% of each benchmark execution time and LLC is bypassed during attack.

Full-CP: checkpointing occurs during the whole execution time of a benchmark to save processor state.

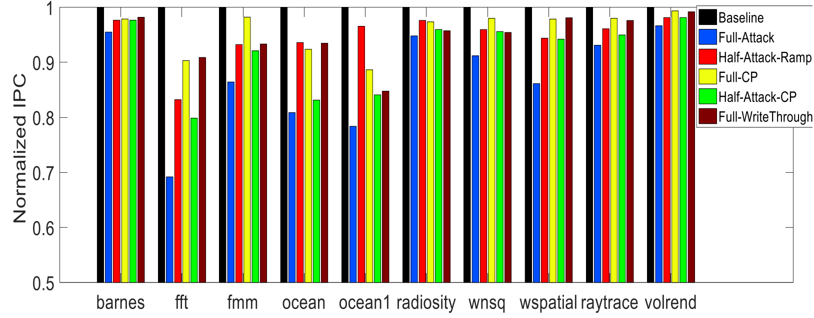

(a)

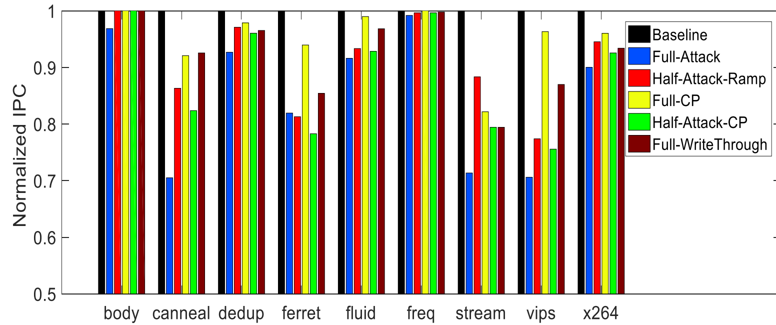

(b)

Figure 4.9 IPC results of baseline, bypassing and checkpointing with different attack rates using; (a) SPLASH, and; (b) PARSEC benchmark suites.

Half-Attack-CP: sudden attack is asserted for 50% of each benchmark execution time with LLC bypassing. Checkpointing is performed during the remaining 50% of benchmark execution time.

Full-WriteThrough: write through policy used to save processor state without LLC bypassing.

We evaluate ramping attack by simulating each benchmark when attack is asserted for 50% (Half-Attack-Ramp) and 100% (Full-Attack) of its execution time. Fig. 4.9 shows the instruction per cycle (IPC) of different cases compared with the normal execution without an attack. In case of Full-Attack the system behaves as if there is no LLC and the performance degrades by 13% (average) and 33% (max). For Half-Attack the performance degradation is 7% (average) and 24% (max). However, in both cases the system continues computation during the attack.

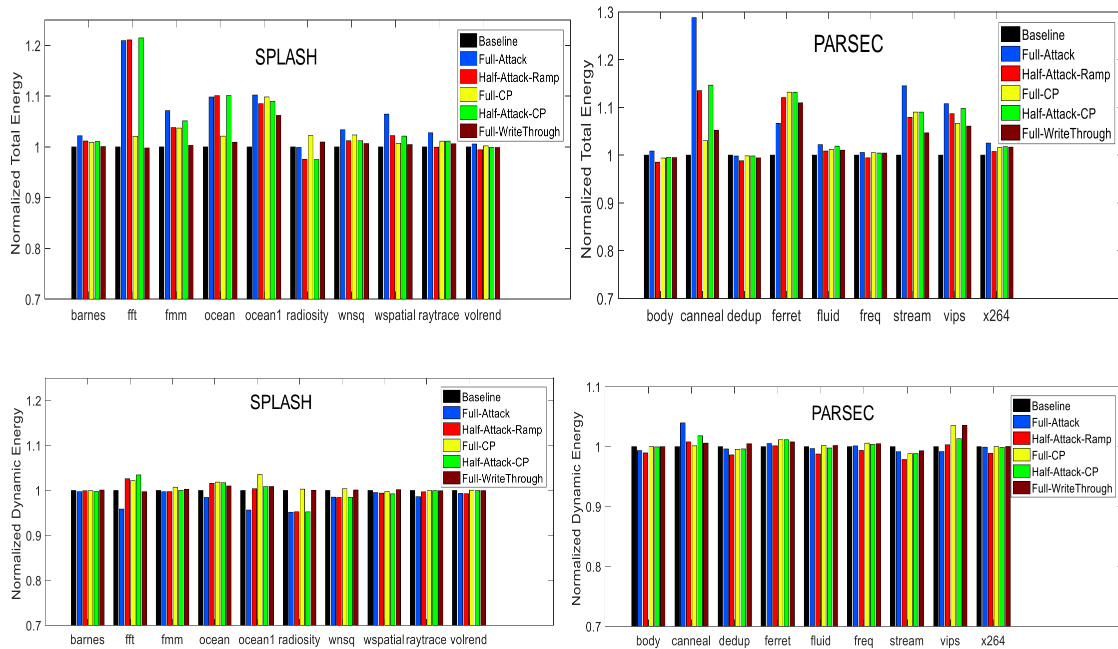

Figure 4.10 Energy results of baseline, bypassing and checkpointing with different attack rates for SPLASH and PARSEC benchmarks: (a) total energy; and, (b) dynamic energy

In case of sudden attack, we consider the attack is asserted for 50% of each benchmark execution time and checkpointing is performed during the remaining 50% of benchmark execution time. As shown in Fig. 4.9, Full-CP results in 4% performance degradation on average compare to baseline. Full-WriteThrough incurs 6% performance loss due to more memory bandwidth usage. Half-Attack-CP results in 10% performance loss. Note that Full-CP performance overhead is lower than Full-Attack for each benchmark. Hence, Half-Attack-CP scenario results in less performance degradation than Full-Attack and more than Full-CP. Half-Attack-CP incurs more performance degradation compare to Half-Attack-Ramp since in case of ramping attack, bypassing occurs once after attack is sensed while in case of Half-Attack-CP, checkpointing occurs many times at regular time intervals which results in more performance overhead.

Fig. 4.10(a) shows the normalized total energy for different cases (normalized to the baseline). Energy is calculated using the multicore power simulator McPAT [89] with modified

CACTI [21]. Full-Attack results in 6.5% (average) and 21% (max) energy overhead since LLC bypassing results in longer execution time. Full-CP increases processor energy consumption by 3% due to longer execution time because of checkpointing and dynamic energy overhead due to writing all dirty block to main memory at regular intervals. Half-Attack-CP and Half-Attack-Ramp result in 4.5% and 4% energy overhead respectively.

Fig. 4.10 (b) shows the normalized dynamic energy for different cases (normalized to the baseline). In case of Full-Attack, dynamic energy is reduced by 2%, since read/write accesses to LLC are blocked during bypassing. Full-CP result in 1% dynamic energy overhead since number of read/write accesses are increased due to checkpointing.

4.6. Discussions

4.6.1. Usage of Stalling, Bypassing and Checkpointing

Cache bypassing is low-overhead, but it can handle ramping attack only. The checkpointing technique can handle both ramping and sudden attacks at the cost of more design complexity and overhead. The high-end secure systems can employ checkpointing with adaptive checkpointing frequency to ensure robust operation at low-overhead. The mobile systems can employ simple bypassing since launching ramping attack is more plausible by the adversary. The low-cost IoTs can employ simple stalling of computation to defend against attack while minimizing the design and energy overhead of bypassing and checkpointing.

4.6.2. Handling I/O Requests

Most of modern system are equipped with Direct Memory Access device (DMA). With DMA, CPU first initiates the transfer, then it performs other operations while the transfer is in progress, and it finally receives an interrupt from the DMA controller when the operation is

finished. If DMA interrupt and sudden attack happen at the same time, interrupt can be served immediately. When the interrupt ends, the system will be restored to the last saved checkpoint and the bypass signal will be asserted. If ramping attack coincides with an I/O event, interrupt is halted till system state is saved, and then the interrupt will be served.

4.6.3. Ramping Attack Timing

The time required to save the processor state during ramping attack (for cache with write back policy) is limited by the compensation window (the time between failure of functional bits and failure of sensor bits) as shown in Fig. 4.1. In this work, DDR3 main memory with 12.8 GB/S bandwidth and 8MB L3 is used. Assuming 50% of the blocks in L3 to be dirty the total compensation time required to write all dirty blocks back to main memory can be approximated as follows:

$$Compensation\ Time \cong \frac{0.5 \times 8MB}{12.8\ GB/s} = 310\ uS$$

As reported in [40], a few hundred microseconds of compensation window is possible by using sensors with reduced MTJ volume and weak write. More sensitive sensors can be designed to enhance the compensation window further.

4.6.4. Continuous Attack

If attack is applied continuously, the system experiences performance degradation. However, without prevention techniques such as stalling, bypassing and checkpointing, either the processor is halted, or main memory is updated by corrupted data. If attack lasts longer than a user specified period of time, an interrupt can be raised to inform user regarding magnetic attack. Hence, user can perform necessary actions in order to eliminate attack.

4.7. Summary

Applicability of emerging technologies such as STTRAM in in memory hierarchy faces security challenges due to possibility of low-cost non-invasive tampering using external AC/DC magnetic field in order to launch denial-of-service attacks. We proposed three low-overhead solutions to mitigate these attacks: stalling, cache bypassing and system level checkpointing with bypassing. In case of gradually ramping attack we bypass the LLC and continue computation. For sudden attack we restore the processor to the last checkpointed state and continue computation with bypassing. The simulation results show an average of 13% (6%) overhead in IPC (energy) with the proposed bypass architecture for an attack lasting for the entire duration of execution. Checkpointing shows 10% (4.5%) overhead in IPC (energy) on average. The proposed techniques allow seamless computations even in presence of attack.

Chapter 5

Robust, Low-Power and High Density Domain Wall Memories

Domain wall memory (DWM) is gaining significant attention for embedded cache application due to low standby power, excellent retention and ability to store multiple bits per cell. Additionally, it provides fast access time, good endurance and retention. However, it suffers from poor write latency, shift latency, shift power, write power and limited sense margin. DWM is sequential in nature and latency of read/write operations depends on the offset of the bit from the read/write head. Additionally, we observe that process variation can result in large spread in write and read latency variations. The performance of conventionally designed DWM cache can degrade as much as 13% due to process variations. In this thesis, we propose DWM bitcell layout considering the access transistor size, metal pitch and number/position of heads, sharing of diffusion, bitlines and shift lines for achieving optimal density. Furthermore, circuit techniques such as merged read/write heads (for compact layout), shift gating (for shift power optimization) are proposed. Additionally, micro-architectural techniques: 1) segmented cache, 2) workload-aware dynamic shift and write current boosting are proposed to realize energy-efficient and robust DWM cache. Results reveals that proposed methods outperform SRAM and STTRAM in terms of energy and performance.

5.1. Introduction

Modern processors dominated by multi-core and graphics engines demand for greater memory bandwidth that can only be sustained by larger on-die cache. The large cache requires a

dense and an energy-efficient memory technology to substitute the current embedded memory solutions like SRAMs and embedded DRAMs (eDRAM) [110]. Emerging high-density embedded memories such as STTRAM are 4-10X denser than the standard SRAM. However, future processors would need 50-100X denser memories with extremely low standby power. RRAM is a promising candidate due to its better MLC capability but it suffers from long write-cycle time, limited write endurance, and high programming voltage. Domain wall memory (DWM) is a strong alternative for a low-power and high density on-chip memory.

The fundamental advantage of DWM is its ability to store multiple bits per cell in order to break the density barrier [117-119]. Additionally, it provides low standby power (due to its non-volatility), fast access time, good endurance and good retention [120]. Due to these properties, DWM has a great potential to be used as an on-chip random access cache. DWM based array has been proposed for cache application in [121-122] and a 256 bit in-plane DWM array has been experimentally demonstrated by IBM [116].

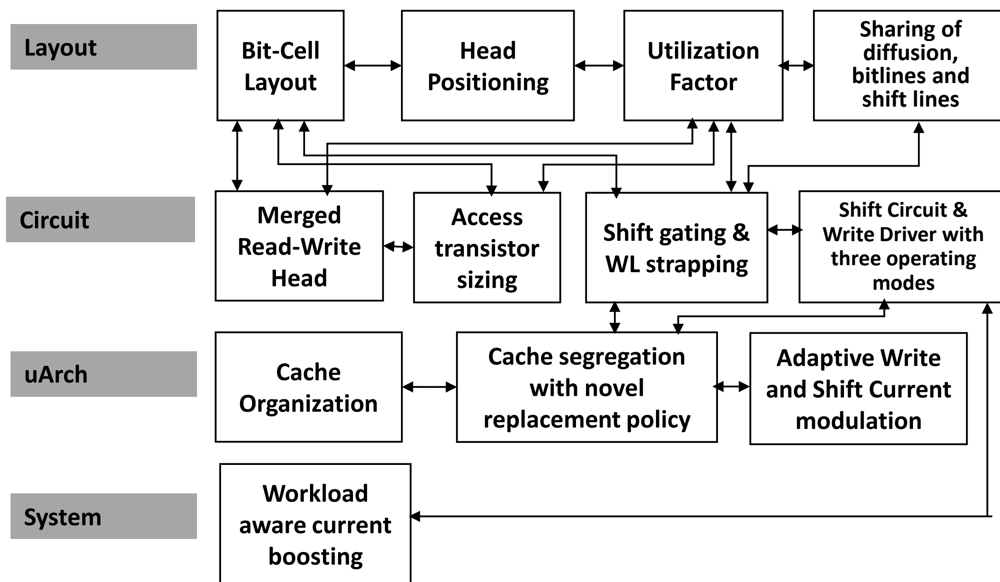

Figure 5.1 Synergistic system design proposed in this paper.

In this chapter, we propose a synergistic system design across design boundaries as illustrated in Fig. 5.1. At the layout level, we propose DWM bitcell layout considering the access transistor size, metal pitch and number/position of heads, then define a utilization factor for optimizing the number of bits in NW which can be used for computation. Furthermore, we propose sharing of diffusion, bitlines and shift lines for achieving optimal density.

At the circuit level, we introduce merged read-write head to increase bitcell density by merging the segregated read and write access transistors and extra wiring overhead. We propose access transistor sizing which optimizes area and latency while reducing the probability of read disturb. Shift gating by sharing shift circuit among 8 NWs, to reduce shift current is also introduced. Moreover, shift circuit and write driver capable to work under three operating points namely, fast, medium and slow modes is proposed.

At the architecture level, cache is segregated to take advantage of three operating modes using a novel replacement policy. A dynamic current boosting based on workload monitoring is also proposed to take advantage of proposed write driver and shift circuit. Fig. 5.1 shows the interdependence or synergy between various layout, circuit, μarch and system level techniques.

Additionally, the process variations in the MTJ increases the write latency significantly for large cache. Similarly, the read latency is also degraded due to process variations. In this work, we exploit the unique properties of the DWM to deal with this issue. We note that the write latency is lowered by boosting the write current and DW shift speed can be increased by boosting the shift current. We propose circuit level techniques to implement adaptive write and shift current boosting and exploit them at micro-architecture level to mitigate process variation induced performance and power degradation.

5.2. Related Works

The experimental results on spin valves, magnetic-tunnel junctions (MTJ), domain wall magnets (DWM) etc. [111-116] have created enormous interest in spin based computations. The most promising effect is current induced modulation of magnetization dynamics discovered in MTJ and DWM as it opens door to energy-efficient logic and memory design. Circuit level challenges in DWM such as joule heating, process variations, shift logic design have been addressed in [123-124]. The efficiency of this cache over traditional memories in terms of power, area and latency are investigated.

A cross-layer design technique using DWM is described in [125]. The features of DWM (e.g., vicinity of bits from read head) are exploited at micro-architecture level for improved performance. Each domain in the NW implement different ways of a cache set. The NW shifting during an access can be controlled by a physical to logical mapping unit, e.g., LUT. Therefore, the number of shift operations to access a block is determined by block way number. They also have proposed a data management policy, hardware-based way block reorder (HBWBR) to mitigate the number of shift operations. By tracing the data access pattern, HBWBR can identify access intensive ways and swap them with the ways under R/W head by using a block counter (BCT) which indicates the data access intensity (a data block is considered as access intensive block once its counter exceeds the predefined threshold). Even though their architectural technique is promising they have not proposed a way to hide latency overhead caused by data swap.

Architectural level propositions such as DWM as a last-level cache and the organizational framework have been described in [126]. Furthermore, a multiple port DWM optimized for read operations considering the asymmetry in the read/write characteristics has been proposed. It also provides a new cache organization and head management policies that mitigate the performance penalty arising from serial access of bits. Since tag comparison is time consuming and the tag array

represent a small fraction of area and power consumption of a cache, a hybrid cache organization which composed of DWM data array and SRAM tag array has been proposed to to take advantage of the speed of SRAM while preserving the cache density. Static and dynamic head selection policy has been proposed. In *static* policy, cache block is assigned a tape head statistically depends on its initial location. Whereas in *Dynamic* policy, the nearest head to the accessed cache block is selected. In addition, two head update policy has been proposed: 1) Eager: the heads are restored to their original position after each access; 2) Lazy: there is a status bit for each tape head to keep track of its location. Tape head is not restored to its original position after each access. This policy takes advantages of spatial locality of memory accesses.

An all-spin cache design that utilizes DWM at all level of cache hierarchy is described in [127]. A shift-based write and separate WLs for read/write access is employed at the circuit level. Domain wall motion-based write is faster and consume less energy compare to MTJ based write. This writing technique also offers the following advantages:1) *Read optimization*: the bitcell can be optimized for read and write independently; 2) *Reliability:* the write speed is mainly limited by Time-Dependent Dielectric Breakdown (TDDB) of the tunnel oxide. Pre-shifting is used at the architectural level to hide the latency of shift operations where the bit that is likely to access next is predicted and brought under the R/W port to hide the impact of shift latency from the next cache access.

current-mode majority gate to achieve a novel one bit full-adder circuit is proposed in [128]. A compiler-based optimization method for data placement on DWM where an efficient heuristic, called Grouping-Based Data Placement (GBDP) to generate near-optimal results efficiently has been proposed [129]. Although DWM have multiple R/W heads, these heads share both bitline and source line in such a way only one head per NW can be accessed at a time. Thus, accessing N-bit cache line requires shifting of N NW. A common source line array organization has been proposed to reduce the number of NW involved in one data access from N to N/M where

is M is the number of heads. This is achieved by placing multiple heads of same NW on different bitlines [130].

5.3. Bitcell Design

In this section we propose merged read and write heads for improving density and read/write latency. We also describe the sizing methodology for the heads that eventually determine the array architecture.

5.3.1. Merged Read-Write Head Design

The conventional DWM contains segregated read and write heads (Fig. 2.4) to decouple read and write and make head design simple. However, this design incurs loss in bitcell density due to the dedicated access transistor and wiring for each head. Furthermore the separate read and write heads is functionally redundant since both read and write operations cannot be performed simultaneously (unless the shifts need for read and write are identical). This makes the read head to wait until the write head has finished writing and appropriately shifts back the bits into its original place or vice versa. To improve density, we propose a merged read-write head that uses the same MTJ and access transistor for memory operations. Structurally, the read and write head are identical however the current direction and magnitude requirements are different. Write head needs bi-directional current flow (to enable writing both polarities) whereas the read head requires a unidirectional current flow. We realize that shift latency depends on the offset of the bit from the head. In order to address this issue, we reuse the extra area created by merging the heads to increase the number of R/W heads. By placing the heads at strategic locations across the NW we also improve the UF and R/W access latency (described in Section 5.3.3).

Although the merged head improves latency and density it brings design complexity due to conflicting sizing requirement for read and write. The write operation requires a large access

transistor whereas the read operation requires a small access transistor size. Therefore, the access transistor sizing should be done carefully (discussed next).

Fig. 5.2 illustrates a single NW with the proposed merged heads (two heads are shown in this example) and corresponding read-write circuitry. The bitlines (BL and BLB) are shared over all heads across the local columns, thus reducing the routing density per cell (4 tracks vs 6 tracks in original DWM bitcell). However appropriate changes in column circuitry are necessary to differentiate between read and write mode. We generate separate column selects for read and write ('ysel_r' and 'ysel_w') signals to connect the bitlines to sense-amp or write driver. Following paragraphs summarize the read and write operations with the proposed design:

Read: The BLB is switched to ground and the BL is connected to the read circuitry (comprising of a two-stage sensing circuitry). Additionally, two reference NWs are placed in each bank that are polarized in parallel and anti-parallel configurations respectively. They are used in

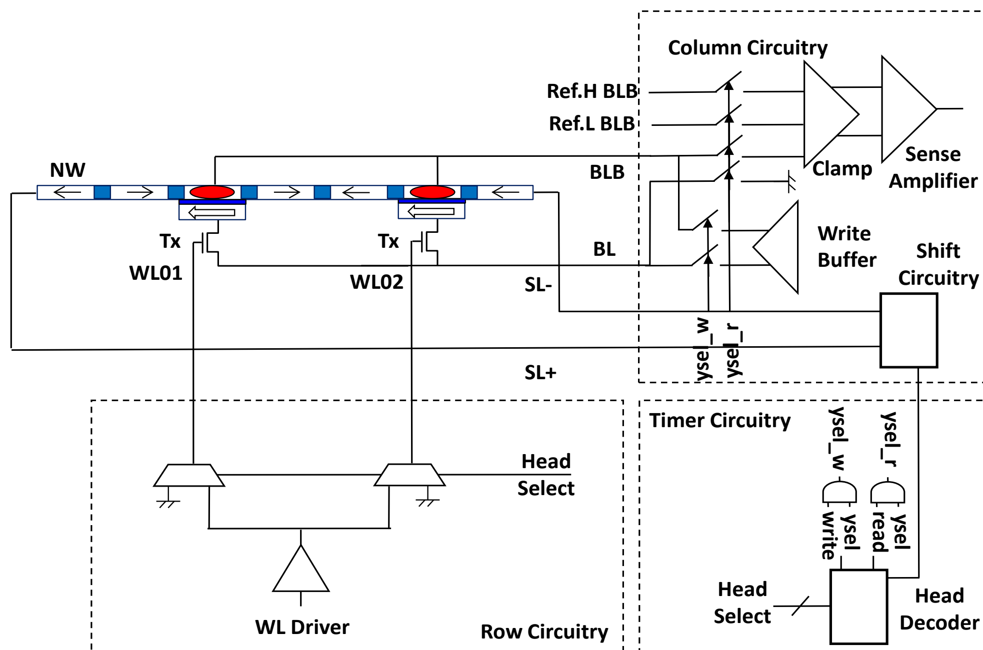

Figure 5.2 Proposed merged head design. The shared read/write circuit, head selection and shift select is also shown.

the clamping circuitry to generate current corresponding to averaged value of the high and low resistance.

Write: The BL and BLB are connected to the two ends of the write driver. In the case where a ‘0’ needs to be written the current from the write driver is made to flow from top to bottom and vice versa in the case of writing a ‘1’. This allows a bi-directional current flow. The read and write operations are atomic i.e. only one can occur at one point of time. As the read heads are spread all over the NW, bits across the NW can be accessed in the least number of shifts, thus reducing the read latency.

Head and shift selection: The selection of the head is performed dynamically using a head decoder in the timer. The decoder accepts last few bits of the address and determines the segment of the NW that needs to be accessed. The corresponding merged head closest to the accessed bit is selected. Note that the wordline (WL) driver is shared between heads since only one head is active at a time. The inactive heads are driven to ground to prevent activation of multiple heads and avoid contention on the bitlines. Furthermore, head select signals can be shared among all WL drivers in the subarray because the selected heads in unselected WL will be driven to ground by the corresponding WL driver. The sharing of head select signal, reduce interconnect overhead in tight pitch WL driver. Since the position of the bits in the NW is known ahead of time, the head decoding is also used to provide information about number of shifts required to access the desired bit. Head and shift circuit delay overhead could be hidden by performing the decoding in parallel with the WL pre-decoding.

5.3.2. Access transistor sizing

For finding the appropriate R/W head size which optimizes area and latency we have considered both read disturb and write latency. Read disturb can be controlled by reducing the read current.

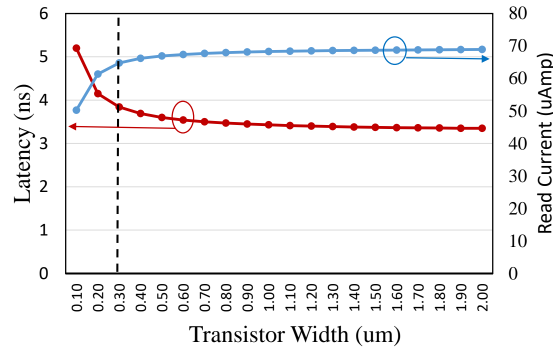

Figure 5.3 Relationship between read current, write latency and access transistor size.

Write latency can be addressed either by increasing write current or increasing access transistor size. However, increasing access transistor size may result in more read current resulting in read-disturb. Sizing access transistor requires understanding of sense circuit.

As described in Section 3.2.2.1, two critical transistors in sense circuit is the PMOS load and NMOS clamp. The clamp voltage and clamp transistor size set the current in the leg. The load transistor sets the output voltage. Hence, access transistor size has weak dependency on read current flowing in data leg. Fig. 5.3 demonstrates the relation between access transistor sizes, write latency and read current. Due to area overhead of access transistor we pick the size (0.31um in this case) that satisfies good write latency (3.9ns) and reasonable read current. The read latency is determined by finding the time needed to develop 100mV sense margin for store-0 and store-1.

5.3.3. Utilization Factor and Latency

In the previous section, we described the merged head DWM design and sizing methodology. This section presents the relationship between number and position of heads, UF and access latency.

5.3.3.1. Number/Positioning of merged head and UF

As described in the previous sections, a certain number of bits per NW are dedicated for buffering the functional bits during shift. The number of heads and their positioning in the NW determine the amount of buffer space required for preserving the functional bits. It can be observed from Fig. 5.4 that the UF increases with the increase in the number of heads due to a reduction in the number of buffer bits. For better bitcell density it is desirable to achieve higher UF which in turn depends on the number of heads, their positioning and the physical dimension of the NW. If *'n'* is the total number of bits in the NW, 'm' is the number of heads, and *SL (SR)* is the number of shifts in left (right) direction the UF is given by:

$$UF = \begin{cases} \frac{n-(SL+SR)}{n} \; if \; (\mathrm{SL}+\mathrm{SR}) > (\mathrm{n}-\mathrm{m})\%\mathrm{m} \\ \frac{n-(n-m)\%m}{n} \; otherwise \end{cases} \tag{5.1}$$

The above equation comprehends the bits wasted due to the distribution of the merged heads and the SL & SR signals required to access the bits for a particular head position. Fig. 5.5 shows few examples to illustrate the calculation of the UF for a NW containing 12 bits and 2 heads. Fig. 5.5(a) shows the scenario where the heads are placed in such a way that the number of right and left shifts required are 2 and 3 respectively. The spacing between the heads is 5. Therefore, the UF obtained from (1) is 0.58. In Fig. 5.5(b), the heads are separated by 4 bits and this change the

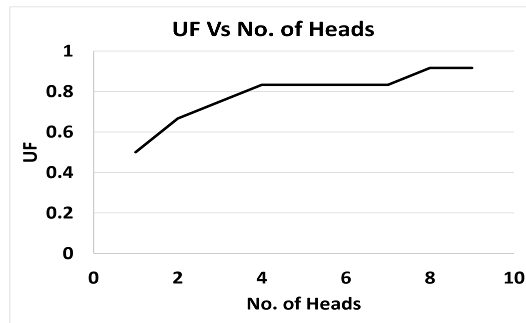

Figure 5.4 UF vs number of Heads for NW with 40 bits.

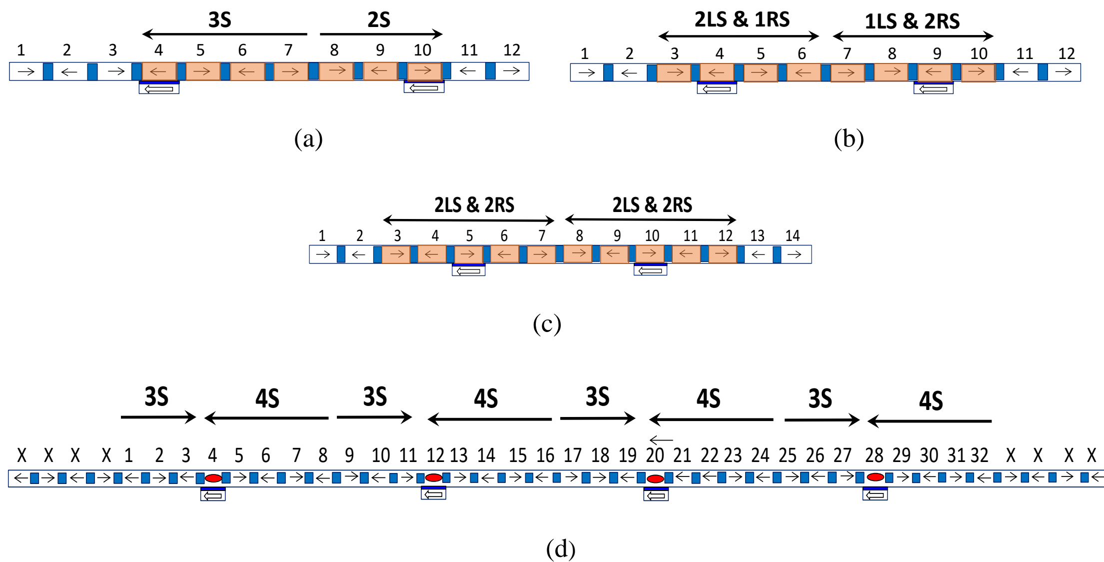

Figure 5.5 Example showing that left head catering to only left shifts and the right head catering to only right shifts, (b) a better placement of the heads allowing for bi-directional shifts, (c) the ideal head placement for a shift latency of 2 and, (d) shows the NW used in our simulation with 4 heads placed at bit number 3, 7, 11, 15 of the usable bits. Buffer bits are represented by 'X'.

number of shifts. The first (second) head require 2 left and 1 right (1 left and 2 right) shifts respectively. The UF for this arrangement is 0.67. The increase in UF is due to the more uniform bit sharing between the heads. Therefore, we infer that the number and positioning of heads directly affect the UF of the bitcell.

5.3.3.2. Latency

UF provides a tool to maximize the number of usable bits in the NW by changing the number and position of the head however it does not comprehend the shift latency optimization of the bits. In the examples described above (Fig. 5.5 (a)), the maximum latency observed by the left head is 3 cycles compared to 2 cycles from the right head. However, the configuration in Fig. 5.5(b) provides maximum latency of 2 for both the left and right heads. Fig. 5.5(c) shows the optimal design where the symmetricity of heads allows uniform left and right bit access. This increases the UF to 0.72. Therefore, it is important to take shift latency into account while determining the

number and position of heads. Fig. 5.5 (d) shows the NW used in our design. It comprises of 32 usable bits and 8 buffer bits. The physical dimension of the NW and number of bits/NW are determined during bitcell layout optimization process described in Section 5.4. The NW has 4 heads placed at strategic locations to optimize the latency and UF (=0.8 in this case).

5.4. Bitcell Layout

In the previous sections we described the NW and head design (e.g., merged head, number/position of heads in the NW, UF, access transistor sizing). In this section, we propose the DWM bitcell layout considering the access transistor size, metal pitch, number/position of heads, shift power/latency etc.

5.4.1. Sharing of diffusion, bitlines and shift lines

The proposed DWM is nT-1NW structure where n is the number of heads. The access transistor size found in Section 5.3 corresponds to 7F in Intel 22nm technology [131] whereas the width of the NW is F (the pitch is 2F). This brings the need of sharing the diffusion width to accommodate 4 NWs. There are several advantages of sharing multiple NW that belong to the same column: (a) the bitlines (BL and BLB) can be shared in 8F pitch. Therefore, the bitline widths could be increased (3.5F) and, (b) the shift lines (SL+ and SL-) can be shared with larger widths (3.5F), to reduce resistance. Plus, (c) the grouping of NWs provides a knob to segregate shift operation in the column for reducing shift power (discussed in Section 5.5).

With sharing of 4 access transistors (for 4 NWs) the width of one NW group is 11F (10F for the diffusion and 1F for NW-NW spacing). The number of bits in the NW when its length is matched with the group width is 9. This is with the assumption that the width of each domain is 1F and the space allocated for landing the shift line contact on the NW is 1F. Since one head per NW is associated with longer shift latency it is prudent to increase the number of heads which in turn

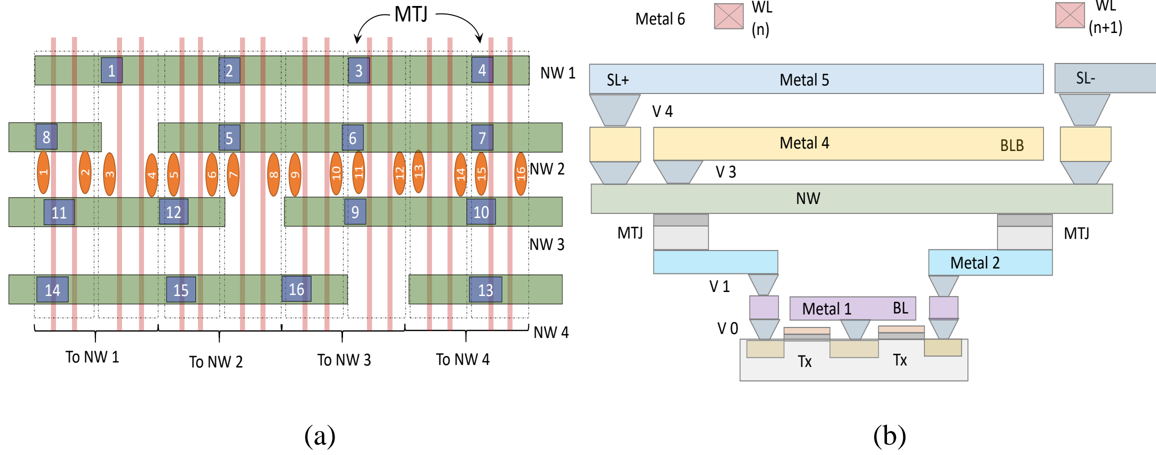

(a) (b)

Figure 5.6 Bitcell layout (4-bit, 2.56F^2/bit). MTJs and diffusion contacts are numbered according to their connection, (b) cross section of the bitcell.

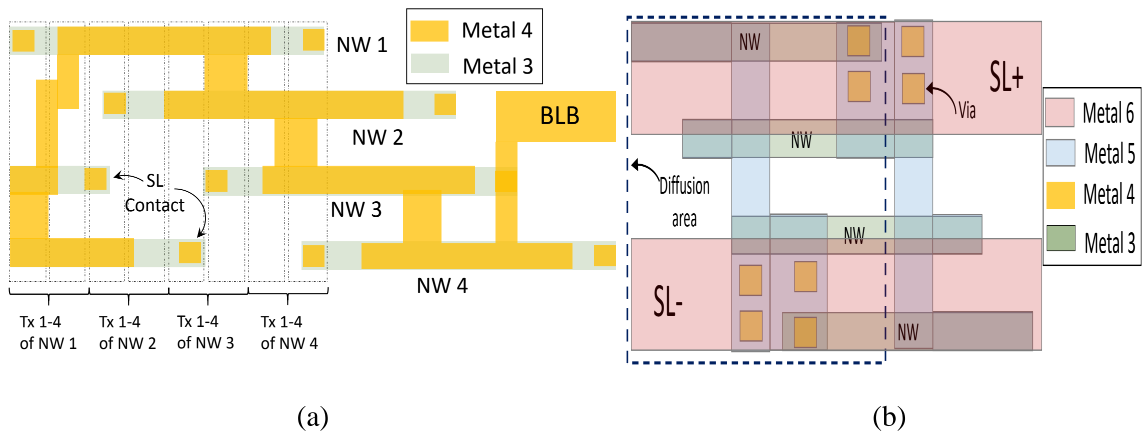

(a) (b)

Figure 5.7 Fig. 14 (a) Metal plan of BLB. The SL stubs are also shown, (b) metal plan of shift lines.

increases the NW group width and NW length. In this work we have used 4 heads per NW to optimize the shift latency, number of bits/NW, UF and architectural simplicity. The NW group width with this choice of heads is 41F. Therefore, the NW length is 40F that can hold 40 bits (where number of useful bits=32). The effective bitcell footprint for this bitcell layout is 2.56F^2 per bit and the UF is 0.8. It is important to mention that the NWs in the NW group cannot be aligned w.r.t each other because it aligns the M4 stubs in the SL+/SL- at the end of NWs and would block the routing of BLB (Fig. 5.7(b)). To create space for local routing of BLB, the NWs are staggered (Fig. 5.7(a)).

Furthermore, it also allows us to incorporate four heads per NW, without interfering with its neighboring heads.

Fig. 5.6(a) shows the proposed DWM layout. The access transistors (Txs) share the bitline (BL), and the other two ends of Txs are connected to the MTJs. There are a total of 16 MTJs on the 4 NWs that connects to the respective diffusion contacts as illustrated by numbers in Fig. 5.6(a). Each NW is controlled by single WL that is muxed and shared among 4 Txs (Fig. 5.2). Fig. 5.6 (b) provides the cross-sectional view of the DWM layout where Tx is connected to the MTJ that is built in the via space between M2 and M3. The NW rests on top of the MTJs in M3 layer. Note that M3 layer is completed occupied by NW in the bitcell area. BL is connected to the source terminal of Tx through M1 and BLB (directly above MTJ and NW) is routed in M4. The left and right shift lines (SL+ and SL-) are routed in M6 and connect to the ends of the NW through M5 and V4. M5 serves two purposes namely, shorting the SL+ and SL- for the NWs in the NW group and routing the VDD/VSS tracks. The WLs are run orthogonally in M7 for periodic connection to the poly WL for better slew rate. The details of WL strap (Fig. 5.8(a)) cell are omitted for brevity. The sizing of the bitcell is based on the Tx size, NW size and the pitch of BL, BLB, SL+/SL-1 and WL. Therefore, it is necessary to take metal pitch of each layer into account [12].

5.4.2. Process requirements for DWM integration

In the following paragraphs we list the requirements from process integration standpoint for successful integration of DWM in the logic process for embedded cache application:

- WL: The WL is routed in poly in orthogonal direction. M7 also runs orthogonally and carries WL signal. M7 is connected to poly in strap area.
- BL: This is shared between two Txs and routed in M1 in horizontal direction.

- Connection to the MTJ: The other ends of Txs are connected to the MTJs that are spatially located in the appropriate places in the NW. M2 is used for local connection to the MTJ and runs horizontally.
- MTJ: The MTJ lies in the via space between M2 and M3.
- NW: The NW is built in M3 region and also runs horizontally.
- BLB: The NW above the MTJ is connected to the BLB through V3. BLB uses M4 and runs horizontally. The routing of M4 for BLB connection to all NWs in the group is illustrated in Fig. 5.7(a).
- SL+/SL-: Fig 5.7(b) shows the routing of SL+ & SL- in M6 that runs horizontally. The SLs connect to the ends of the NW. The jogging of SLs to connect every NW is done in M5.

From above discussion it is obvious that M1, M2, M3, M4 and M6 must be routed horizontally whereas poly and M7 should be routed orthogonally and should have same pitch to enable strapping. This contradicts the logic design rules where subsequent metals are routed orthogonally. Furthermore, M1 to M7 is fully occupied in the bitcell area and cannot be used for routing other signals. Global data (in and out) should be routed in higher metal layers (M8). The pre-decoded signals and control signals can run in row and column area where the design rules are relaxed.

5.5. Cache Design

In the previous section we explained the bitcell layout and process requirements. In this section we describe the subarray design and 32MB cache architecture.

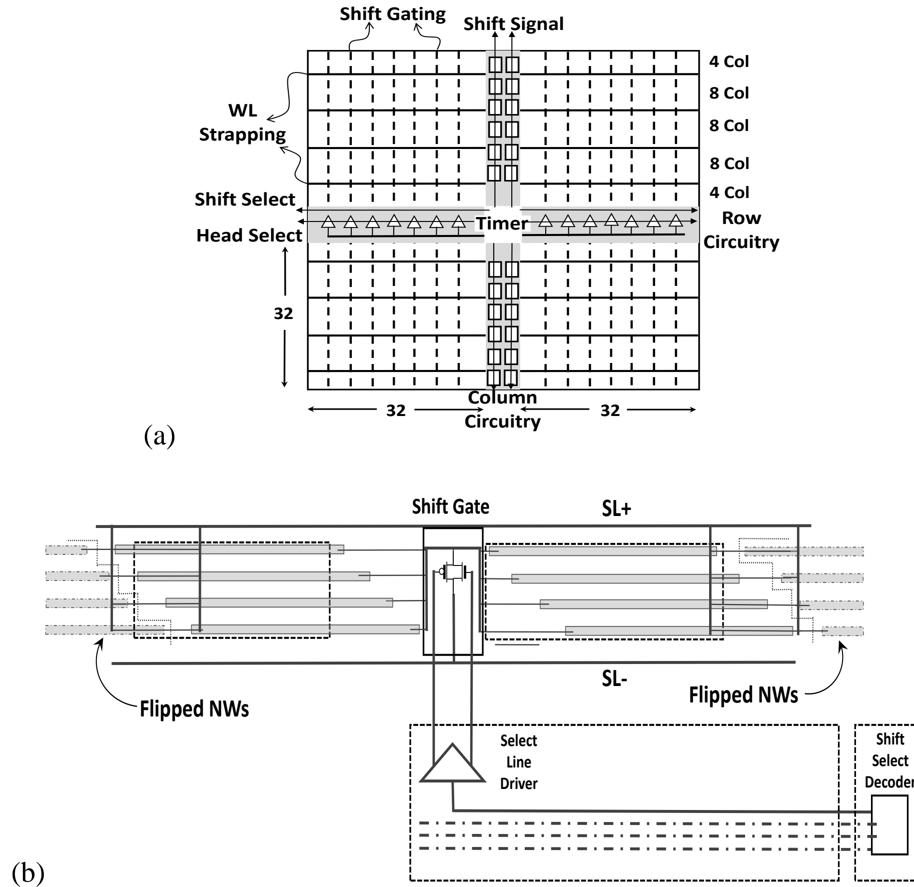

Figure 5.8 Overview of proposed subarray with shift select, gating select and head selects. WL strap is also shown. (b) Shift gating circuitry.

5.5.1. Sub-Array design

Fig. 5.8(a) shows the proposed sub-array design. There are total of 64 WLs (32 in each sector), 512 local columns that are muxed to provide 64 bits of data. The column area holds the read/write and shift circuitries. Timer contains a decoder to provide the number and direction of shift. WL decoder consists of a WL driver and head selection muxes. The select signals are provided by a decoder in the timer. Since SL+/SL- are shared, the shift operation shifts all the NWs at the entire column. This is a power consuming operation. In order to mitigate the shift power, we group

8 NWs (i.e., two NW groups) and add a transmission gate in between that is controlled by the shift gating signal. The shift gate is accommodated in Silicon by flipping the NW group so that the SL+ and SL- can be shared between NW groups eliminating the NW-NW spacing. The shift gate is full CMOS and will require an Nwell. Therefore, two extra poly space is incorporated to insert the gating mux. The gating signal is generated in the WL decoder by using the pre-decoded addresses to determine the selected NW groups. The details are described in Fig. 5.8(b). A 4X shift power reduction is gained by the proposed gating.

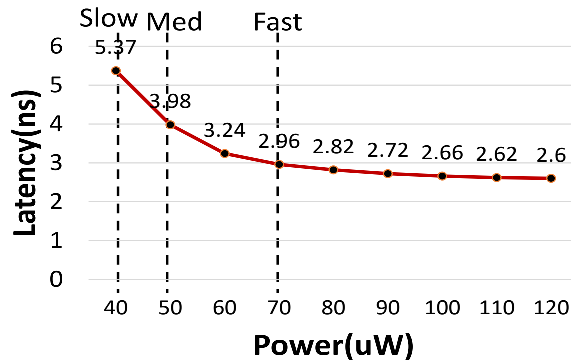

Figure 5.9 Write power versus write latency for three operating voltages.

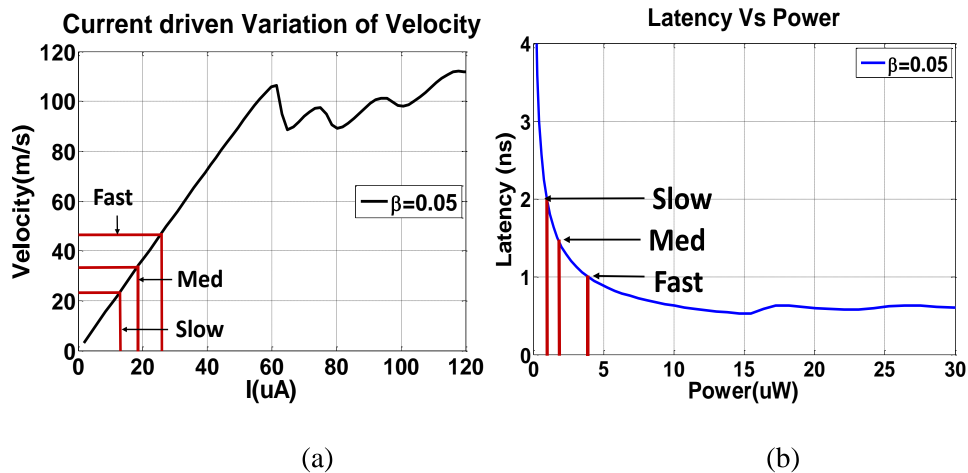

(a) (b)

Figure 5.10 (a) DW velocity vs input current using 1D model [41]. The DW velocity and power of fast, medium and slow shift are indicated, (b) shift latency vs power.

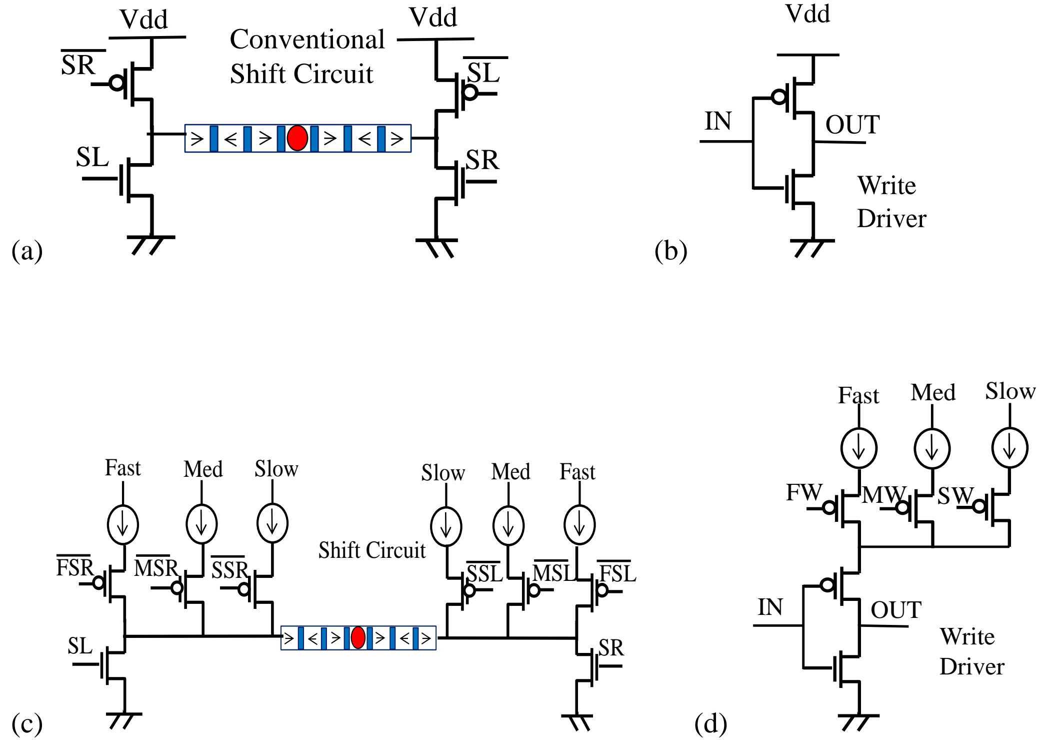

Figure 5.11 Fig. 18 (a) Conventional shift circuit, (b) conventional write driver. (c) Proposed shift circuit, (d) proposed write driver.

The write power versus write latency for each operating current is depicted in Fig. 5.9. There is a trade-off between write power and write latency - higher write current reduces latency at the cost of power whereas lower write current reduces power at the cost of higher latency. We exploit this dependency for trade-off between write power and write latency.

The DW motion depends on the shift current. Higher current increases the DW velocity but increases the power consumption as well. Fig. 5.10(a) shows the DW velocity vs shift current by using the 1D NW model described in [41]. The corresponding DW shift latency with shift power is plotted in Fig. 5.10(b). We leverage this property to trade-off between shift power and latency. The fast, medium and slow caches are shifted with high, medium and low currents respectively. In the proposed design we assume the shift latency for the fast, medium and slow cache to be 1ns,

1.5ns & 2ns respectively. The shift circuit of the fast, medium and slow cache is sized accordingly to enable variable shift latency.

The conventional shift circuit and write driver are illustrated in Fig. 5.11(a). In this chapter, we propose a new shift circuit and write driver which is capable of boosting the current. In conventional DWM circuit shift-left (right) can be done by enabling shift-left (right) signal and passing constant current. However, proposed shift circuit (Fig. 11(c)) is able to perform fast, medium and slow shift operation by varying the shift current. In order to shift the bits right with fast operating current the Fast Shift Right (FSR) signal and SR is enabled. Medium and slow shift operation can be accomplished by asserting MSL/MSR and SSL/SSR respectively. In this work, we select 15uA, 19uA and 25uA as shift current for slow, medium and fast shift operation. Similarly, in order to perform fast write operation fast write (FW) signal is enabled (Fig. 11(d)). Medium and slow write operation can be achieved by activating the MW and SW signals respectively. In this work, we select 40uA, 50uA and 70uA as write current for slow, medium and fast write operation.

5.5.2. Cache Organization

Each way in L2 is implemented in a different subarray in mat for parallelism. The column mux selects the desired BL and sense amplifier senses bit-cell states in either data or tag array. For n-way set-associative cache we use n-comparators to compare the tag bits in Tag Array against input address to detect the set containing the desired data. For fast tag comparison, the Tag array is implemented using SRAM. Next the tag hit signal is routed to the respective mat and the desired cache-line is routed to the I/O ports. The corresponding detailed logical to physical mapping is shown in Fig. 12. The sets are labeled in the NW. Each mat provides 64-bits of data by accessing a subarray. For example, way0 is accessed by enabling SA[0] of Mat[7:0] providing 512 bits of cache line.

5.6. Cash Segregation and Workload Aware Current Boosting

In this section we propose two µarch techniques to exploit DWM circuit knobs at system level namely cache segregation with a novel replacement policy and workload-aware current boosting.

5.6.1. Cache segregation

In proposed design, the L1 cache comprises of traditional SRAM whereas the segmented L2 cache contains DWM. Fig. 5.13 shows different steps in proposed cache replacement

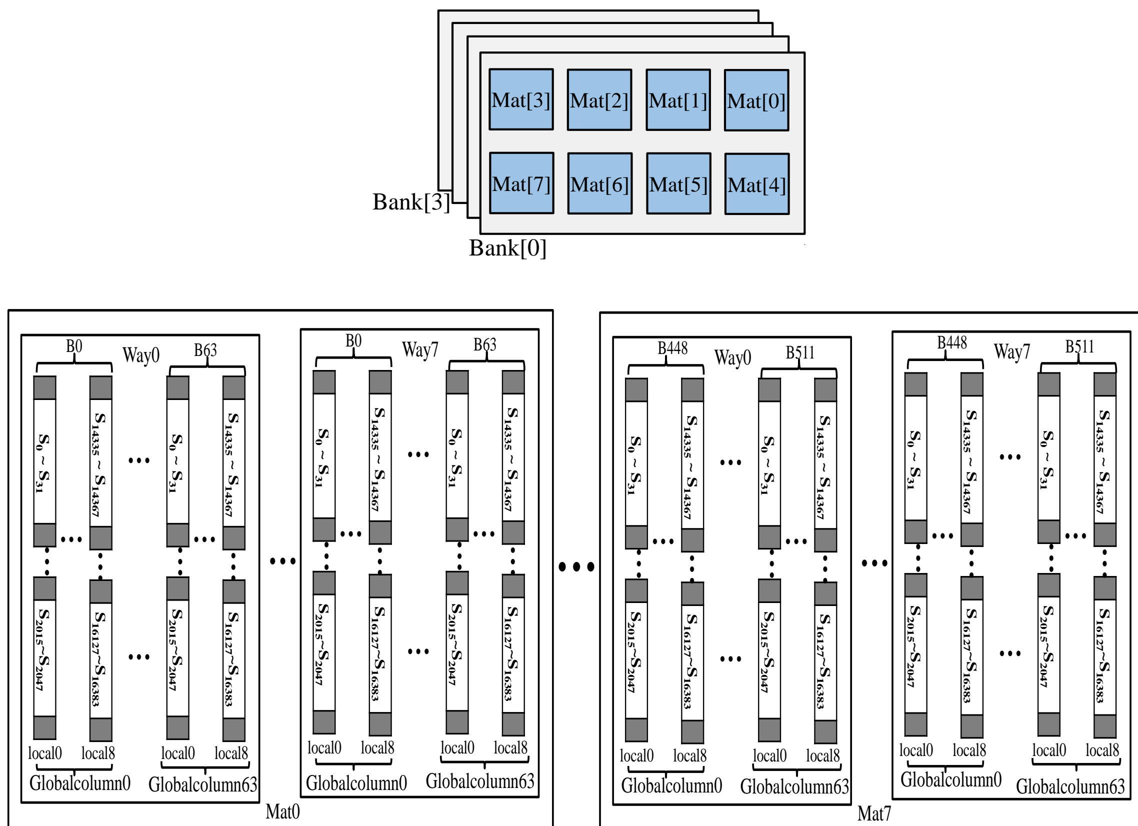

Figure 5.12 Logical to physical mapping of a bank. Shaded ends of NW are buffer bits. The set mapping on the NW is depicted.

policy. If an access to L2 cache is considered as a hit, we check whether this access is to fast way or not. If so, the access is granted, and the way is marked as most recently used (MRU). For the medium way access the block is moved to fast way and marked as MRU after granting the access. LRU block from the fast way is replaced. The block replacement policy in fast way can be explained as follows: During cache access both the tag and data array is accessed simultaneously. The data is temporarily buffered in each mat. In case of hit the content of buffer is routed to I/O ports (Fig. 5.14). The latency from edge of mat to the CPU is longest, and the block can be replaced during that interval by embedding swap-enable (SWE) in each way. A hit signal to a slow and medium way will trigger the SWE. For example, if the desired data is present in way5 and way0 is LRU way in fast ways, the accessed set from way0 is copied to way5 and the corresponding set of way5 from buffer will be placed into way0 (Fig. 5.14). Hence, the latency due to block swapping could be hidden.

5.6.2. Workload-aware current boosting

The cache segregation method presented above requires data migration to achieve energy-efficiency. We propose a dynamic workload monitoring to speed up the write and shift performance by avoiding the costly data migration. The basic idea is illustrated in Fig. 5.15.

Basic idea: The proposed domain wall cache is able to work under three operating modes for shift and write operation. Workload is monitored continuously and L2 caches access profile is extracted for a fixed clock interval during dynamic operation. Two fix access thresholds (Th_H and Th_L) are defined based on L2 access profile for corresponding CPU architecture. These access thresholds are provided as input to the operating current selector. The operating current selector monitors the L2 access profile and compares it with each threshold to select the operating current. The output signal is routed to write driver and shift circuit in L2 cache to determine the operating current.

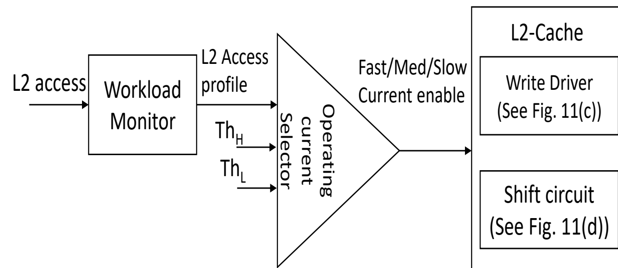

Figure 5.15 Fig. 23 Workload-aware write and shift current boosting.

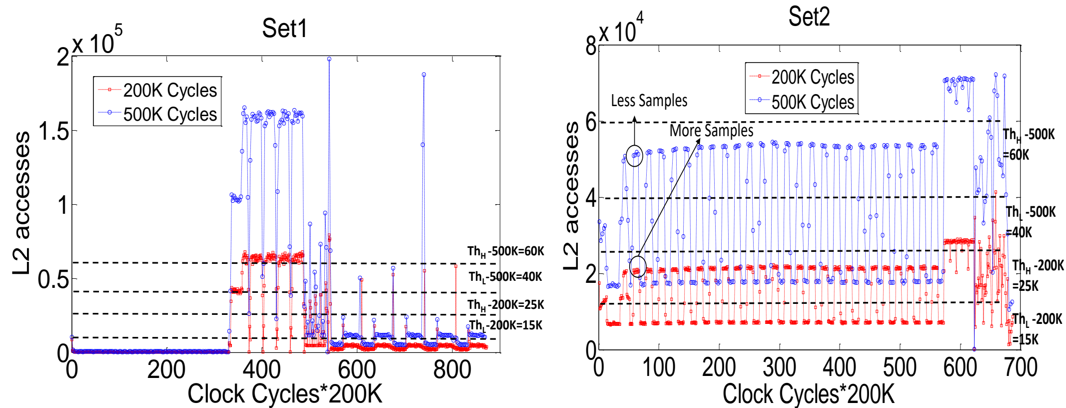

Figure 5.16 Number of L2 accesses for set1 & set2. Access profile for both 200K/500K cycles are shown.

Threshold Selection: To create workload we take the parsec benchmark suite and club 3 benchmarks together called a 'set'. Each set consists of combination of high, medium and low cache access intensive benchmarks. We simulate number of L2 accesses for three access intervals: 50K, 200K and 500K clock cycles as shown in Fig. 5.16. The next objective is to determine the

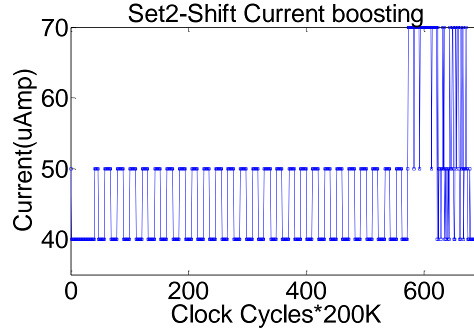

Figure 5.17 Shift-current scaling of set2.

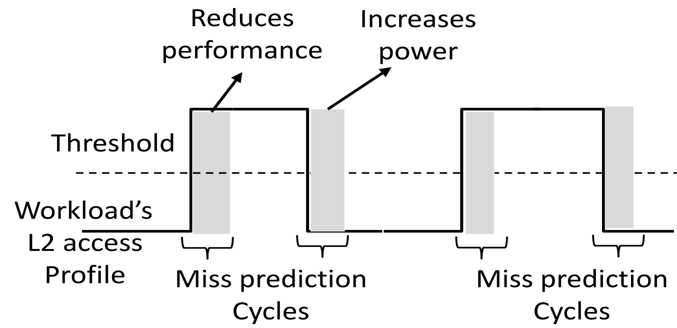

Figure 5.18 Power and performance overhead for proposed workload-aware current boosting.

interval for which the workload is monitored and determine the high and low workload threshold (Th_H and Th_L). The operating current is given by:

$$\text{Operating Current}=\begin{cases} slow & \text{L2 accesses} < Th_L \\ medium & Th_L < \text{L2 accesses} < Th_H \\ fast & \text{L2 accesses} > Th_H \end{cases}$$

The corresponding operating current boosting for set2 for 200K interval is shown in Fig. 5.17.

Note that 200K interval provide better resolution for defining access thresholds. For a coarse interval like 500K if the workload fluctuates rapidly the proposed dynamic current boosting will result in more miss predictions. As shown in Fig. 5.16, 500K case contains a smaller number of samples when workload fluctuates. Since the prediction is based on previous interval's number of accesses, there is a possibility of miss prediction, in each transition between operating currents.

For finer intervals like 50K current boosting might result in frequent boosting up and down which is undesirable for control power overhead. For balanced prediction overhead we choose 200K as the monitoring interval.

The miss predictions cycles during workload monitoring and prediction are depicted in Fig. 5.18. When number of L2 accesses exceed a predefined threshold, current boosting is performed. There are three workload states: low, medium and high based on workload's L2 access profile. The write and shift current are controlled to slow, medium and fast values for the low, medium and high workloads respectively. Workload state is changed when L2 access profile cross the high and low thresholds. Note that workload monitoring and prediction result in two type of overheads: a) performance overhead: -whenever the workload switches from low to high, the predictor unit predicts a high workload which means that the previous N cycles (N=50K, 200K, and 500K) experienced high L2 accesses. However, the shift/write current for the previous N cycles were set to lower current, degrading the performance; b) Power overhead: - when the workload switches from high to low. Predictor unit predicts a low workload for N previous cycles while the shift/write current for the previous N cycles were set to higher operating current. The above-mentioned power and performance overheads can be mitigated by exploiting shorter monitoring interval or using moving average for prediction. The workload threshold selection for each operating point can be performed either by operating system or by a prediction unit inside the processor.

Table 5.1 Processor configuration.

Processor	Alpha,O3,4 cores, 2GHz, 8-way issue
SRAM Cache	L1-Private, Icache=16KB, Dcache=16KB, 64B Cache-line, 2 cycle Read/Write latency, Write back.
LLC Cache	Shared, 32MB, 4 banks, 8 ways, 64B cache-line, writeback, R/W latency based on memory tech.
Main Memory	4GB, DDR3, 200-cycle latency

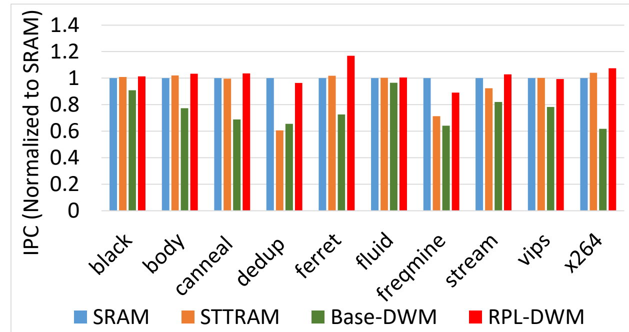

Figure 5.19 Fig. 27 Performance comparison across different memory technologies.

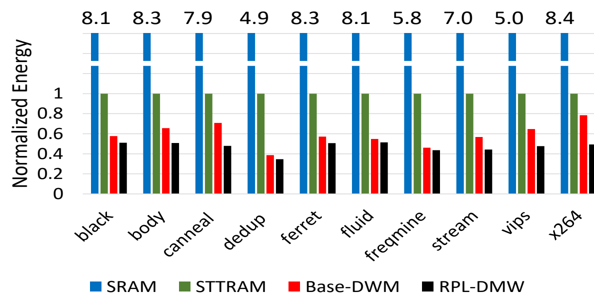

Figure 5.20 Fig. 28 Comparison of energy consumption of L2 cache across different memory technologies.

5.6.3. Simulation Setup and Result

We evaluate and compare 32MB L2 cache for five different cases namely, SRAM, STTRAM, base DWM (with one head and medium shift latency), and RPL-DWM (DWM with proposed replacement policy) and DCB-DWM (DWM with Dynamic current boosting). We performed our evaluation on a 4-core Alpha processor in Gem5 [87] (Table 5.1). Gem5 is modified accordingly to implement cache segmentation and replacement policy and dynamic current scaling. The simulations are performed over a wide range of Parsec Benchmarks [88]. The cache latency and energy is achieved using CACTI [90], NVSIM [132] and Hspice model of DWM (Table 5.2). Base DWM has same parameters as RPL-DWM except it has one head.

For evaluating Domain wall L2 cache with proposed replacement policy we run simulation on each benchmark separately. Fig. 5.19 demonstrates the performance result represented by the normalized instruction per cycle (IPC). It can be observed that RPL-DWM architecture shows ~33% improvement over Base-DWM. We also achieve ~3% (~12%) improvement over SRAM (STTRAM). Even though DWM requires shift operations the small footprint of the bitcell and less routing latency helps in improving the performance. For power simulation we used McPAT [89] multi-core power simulator with modified CACTI which is integrated in Gem5 simulator. Fig. 5.20 shows that the total energy of the proposed DWM-cache is ~14.4X less than SRAM due to small leakage power. Furthermore, it achieves 1.25X less energy compare to Base-DWM due to reduction in number of shift operations.

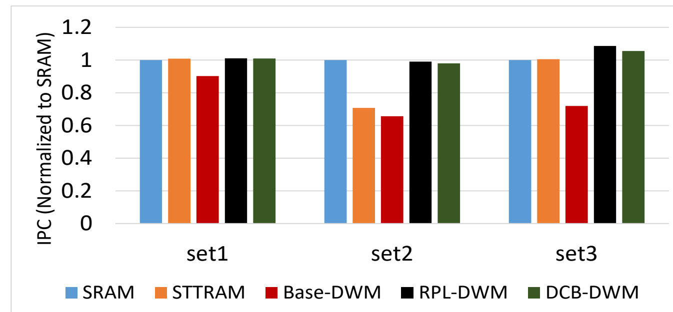

Figure 5.21 Performance comparison across different memory technologies for each workload set.

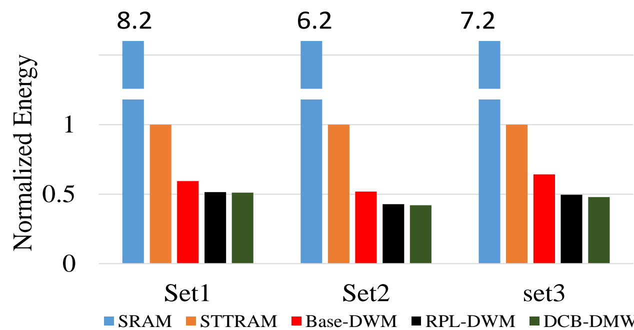

Figure 5.22 Energy comparison across different memory technologies for each workload set.

Table 5.2 Design parameters for different cache configurations (22 nm technology).

Cache Parameters	Cell Size (F^2)	Total Area (mm^2)	Read Latency (nS)	Write Latency (nS)	Read Energy (nJ)	Write Energy (nJ)	Shift Power/Block Fast/medium Slow(mW)	Shift Latency (Fast/medium/ Slow) (nS)	Write Pulse (Fast/medium/ Slow) (nS)	Leakage Power (W)
SRAM	146	57.03	7.1	5	1.1	0.8	-------	-------	------	36.7
STTRAM	40	21.3	5.1	7.1	0.9	1.4	------	-------	3.9	4.5
Base-DWM	6	7.2	2.9	4.9	0.24	0.42	16/8/4	1/1.5/2	3.9	2.4
RPL-DWM	2.5	5.2	2.81	4.63	0.2	0.4	16/8/4	1/1.5/2	3.9	2.31
DVS-DWM	2.5	5.2	2.81	4.63	0.2	0.4	16/8/4	1/1.5/2	5.3/3.9/3	2.31

For evaluation of DCB-DWM parsec benchmark is categorized into set1 (black, body and fluid), set2 (canneal, dedup and freqmine) and set3 (ferret, x264, stream and vips). Normalized IPC and energy for each set is illustrated at Fig. 5.21 and Fig. 5.22 respectively. Furthermore, the IPC results illustrate 2.5% improvement over SRAM. Fig. 30 shows that the total energy of the DCB-DWM is ~14.9X less than SRAM due to small leakage power. Furthermore, it achieves 1.06X less energy compare to RLP-DWM due to dynamic current boosting during write operation.

5.7. Process Variation Analysis

In this Section, we analyze the impact of process variations in the read and write head. We also investigate the modeling of read/write latency distribution and impact of current boosting.

5.7.1. Process Variation in Write Head

Process variation analysis is important due to the size of cache that is employed at the last level. The process variations in the write head is modeled by incorporating variations in MTJ as well as access transistor. For MTJ we have assumed tunnel oxide barrier and surface area variations.

The variations in access transistor is lumped in threshold voltage fluctuation. The mean and standard deviation of these parameters are provided in Table 3.1. The variations in the write head can increase the intrinsic thermal energy barrier and resistance of MTJ which in turn can increase the write time. The write latency is asymmetric in nature. Therefore, we have considered the worst case polarity (high→low transition) for latency analysis.

Fig. 5.23(a) shows the Monte-Carlo analysis for 5000 simulation points at typical process corner. It can be noted that performance analysis with mean write latency assumption can result in significant overestimation. The write latency also shows a long tail and the worst case write head could eventually limit the system performance. In order to gain detailed understanding we use a

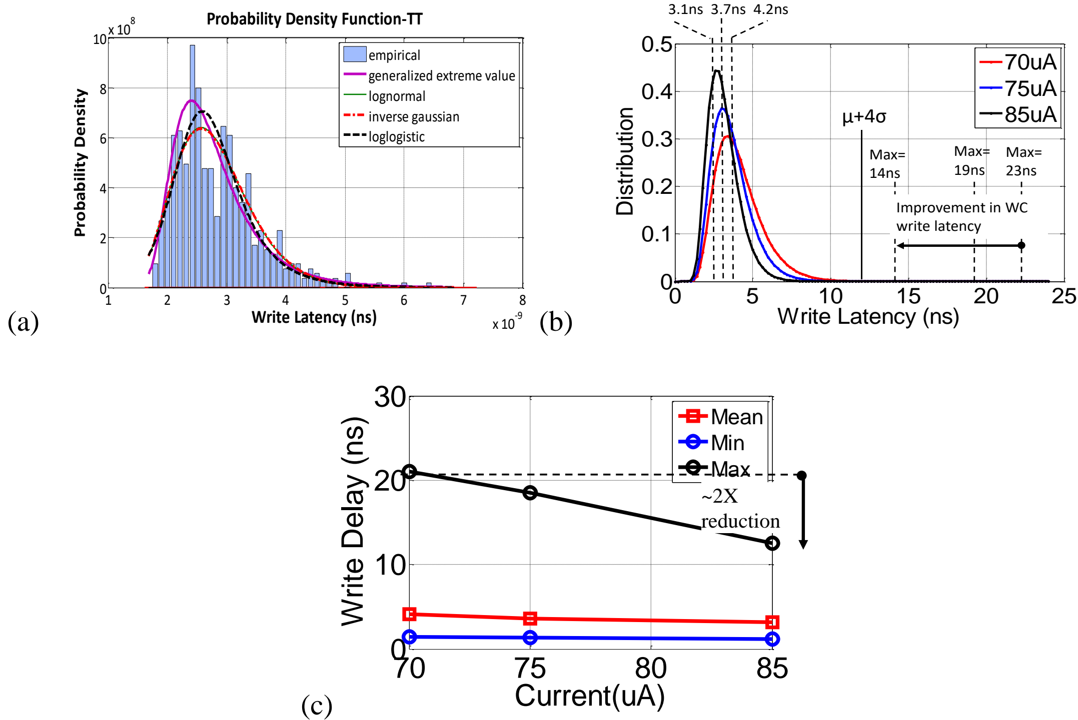

Figure 5.23 Write latency distribution for 5000 Monte Carlo points. The curve fitting to model the tail is also shown; (b) write latency distribution using curve fitting model for three different write currents. The worst-case head can be accelerated through high write current. The 4 sigma delay is also shown. By boosting the current the number of bits beyond 4 sigma delay can be reduced; and, (c) min, mean and max write latency with write current.

curve fitting to model the write latency distribution (especially the tail). Fig. 5.23(a) depicts different models used to fit the distribution in Matlab. Empirical model indicated better match for the tail. Therefore, we used this model for the cache level analysis. Note that the cache size for our study is 32MB which amounts to 32M read/write heads (Section 5.8). The curve fitting model is used to extrapolate the distribution to 32M heads. At 70uA current the worst case write latency is found to be 23ns which is >5X larger than mean value underscoring the need of process variation-aware design (Fig. 5.23(b)). In order to improve the system performance, it is crucial to fix the tail of the write latency. The distribution for boosted write currents are also shown in the plot. It can be observed that write current boosting can be used to speed up tail bits and mitigate the impact of process variation on write latency. The distribution also indicates that the number of heads beyond $\mu+4\sigma$ point is reduced when write current is boosted. Fig. 5.23(c) plots the max, mean and min latency for different write currents. It can be noted that worst case points can gain significant benefit (as much as 2X) although the mean shows minor improvement from boosting.

Effect of process variation on maximum write latency with 50% and 200% of original standard deviation of parameters reported in Table 3.1, is shown in Fig. 5.24. It can be noted that even though in a well-controlled process write latency problem can be solved by proposed current

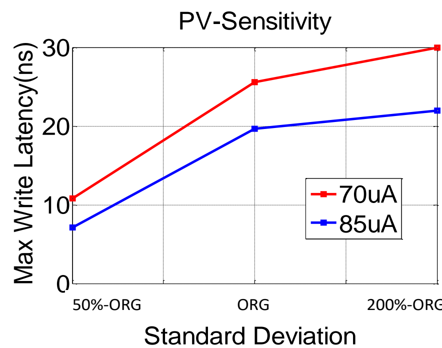

Figure 5.24 Fig. 33 Effect of process variation on maximum write latency by considering 50% and 200% of original standard deviation of parameters reported in Table 3.1.

boosting technique. As shown in Fig. 5.24 even with 50% of original standard deviation, there is 35% improvement in maximum write latency using the proposed current boosting.

5.7.2. Process Variation in Read Head

The process variations in the read head can reduce the TMR and read current which in turn can increase the sense time. We have analyzed the time needed to develop 100mV sense margin (to account for sense amplifier offset due to variations). The simulations are done using the settings described before. Fig. 5.25(a) plots the read latency distribution for 2000 runs of Monte Carlo. Different curve fitting models are also plotted. The read latency distribution for 32M heads is shown in Fig. 5.25(b). It can be noted that process variation can degrade the read latency significantly.

5.7.3. Process Variation Tolerant Design

From the above discussion, it is evident that write current boosting can be used as a knob to mitigate process variation. The serial access nature of the DWM provides another knob namely, shift current that can be exploited for variation tolerance. The total write access time is given by:

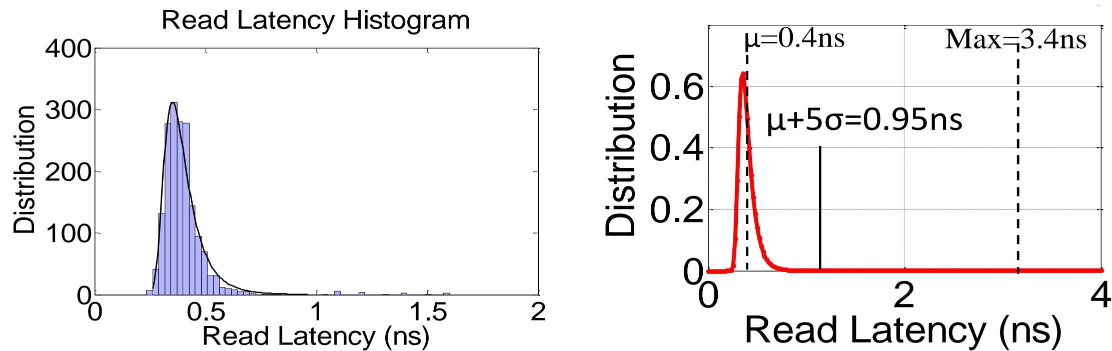

Figure 5.25 Fig. 32 (a) Read latency distribution for 2000 Monte Carlo points. The curve fitting to model the tail is also shown; (b) read latency distribution for 32M heads.

Read/write access latency=read/write latency + shift latency (5.2)

The shift latency depends on the offset of the bit from the head. The worst case read/write latency is experiences by the bit which needs most number of shifts to reach the slowest heads (schematically represented in Fig. 5.26). Therefore, boosting shift speed and write current together can accelerate the worst case bits. As depicted in Fig. 5.23(b), write current boosting reduces the number of heads beyond 4 sigma delay. The remaining heads can be accelerated by employing shift boosting. Modulation of shift speed can also be employed to fix read latency degradation. Since read latency variation is relatively less severe compared to write latency, shift boosting is sufficient to mitigate the delay degradation. Note that the current boosting for write and shift is associated with power consumption. Therefore, these knobs should be used only for the tail bits to improve the performance with minimal impact of dynamic power. The detailed methodology is described in Section 5.8.

5.7.4. Write Driver Design

We propose a novel current mirror based write driver to boost the write current of the column if needed (Fig. 5.27(a)). A reference write current $I_{ref}(WR)$ is mirrored on the leg that is

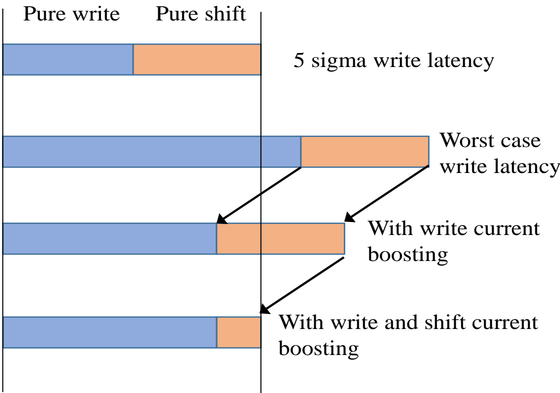

Figure 5.26 Fig. 34 Mitigation of process variation on write latency by write and shift current boosting.

driving BL/SL. The direction of current flow is controlled by the polarity of data to be written (D_{in}). The BL (SL) is connected to current source (VSS) if the data to be written is 1 (0). The sizing of PMOS P_1 is ratioed with respect to to reference leg to generate the required write current. We add an extra PMOS transistor P_2 with size k so that extra current needed for the boosting is generated when boost signal is asserted (i.e., bst=1). For nominal conditions P_2 is disabled by connecting the gate to V_{DD}.

The proposed driver needs 4 transistors for multiplexers and an extra PMOS to generate the boosted current. Considering the fact that gate leakage is negligible and *bst* is a DC signal the

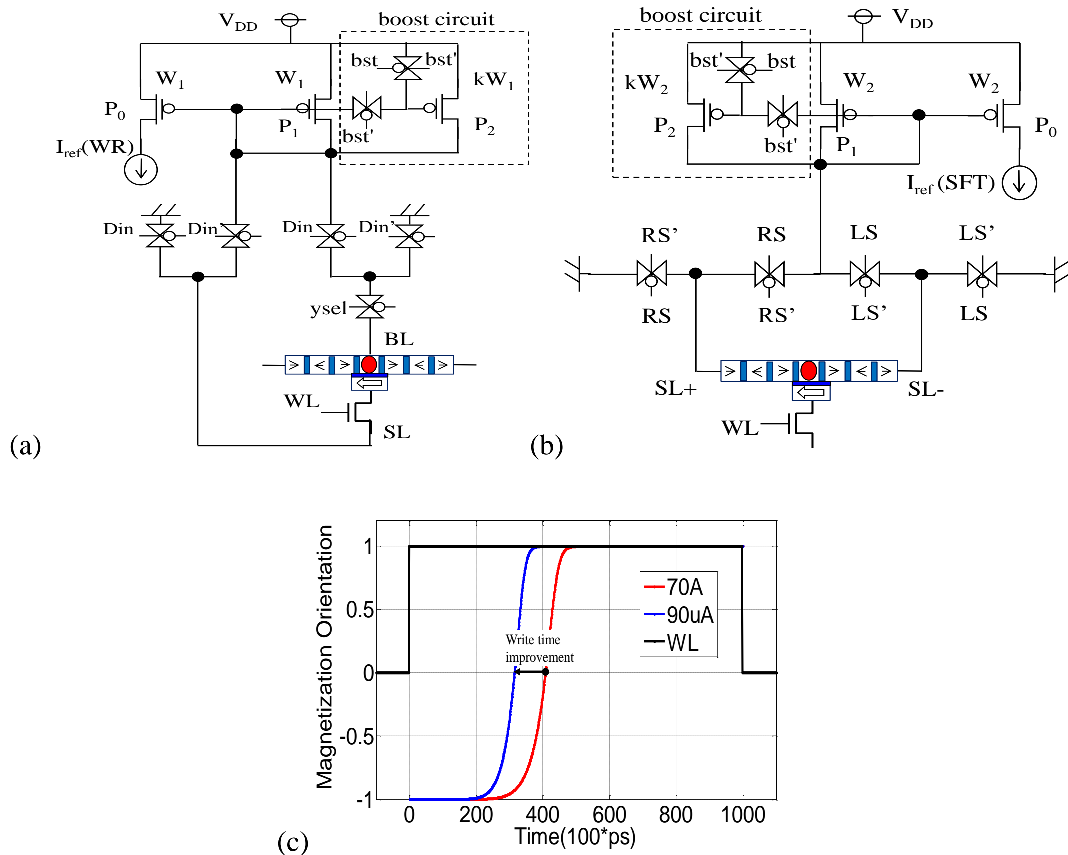

Figure 5.27 (a)& (b) Boost enabled write and shift driver; and (c) simulation results showing write time improvement by enabling write boost.

multiplexers can be designed using minimum sized transistors. Therefore, the area overhead of the proposed boosting can be kept below 1%. Fig. 5.27(c) shows the Hspice simulation waveform of magnetization switching during write process for nominal and boosted current.

5.7.5. Shift Driver Design

Based on the concept described above, we also propose a novel shift circuit to boost the shift current of the column (Fig. 5.27(b)). A reference shift current I_{ref}(SFT) is mirrored on the leg

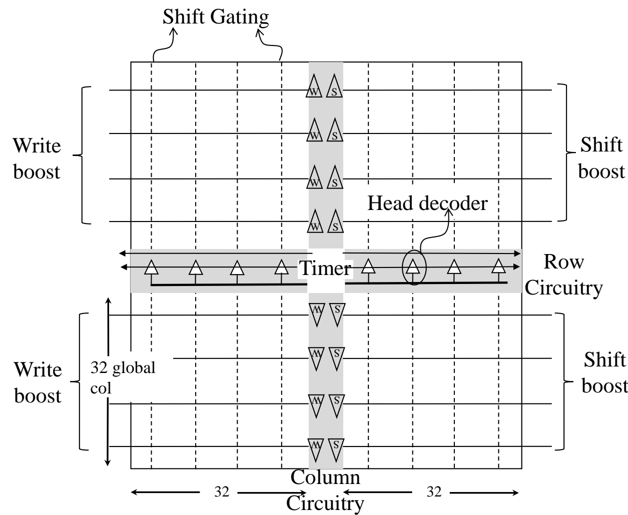

Figure 5.28 Subarray architecture showing boost enabled shift and write drivers, shift gating for low power and head selection.

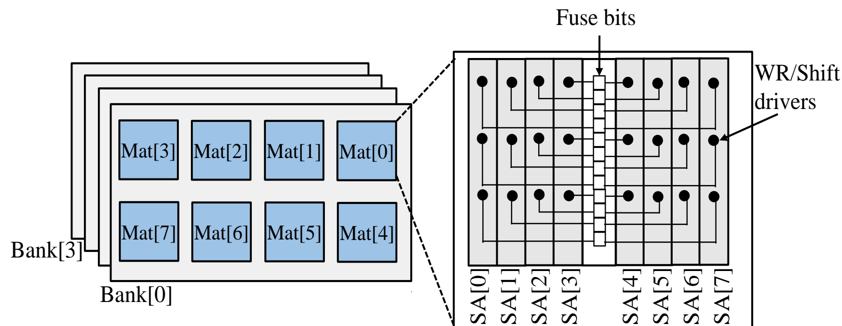

Figure 5.29 Cache organization.

that is driving SL+/SL-. The direction of current flow is controlled by the Left Shift (LS) and Right Shift (RS) signals. The SL+ (SL-) is connected to current source (VSS) if the RS (LS) is asserted. The sizing of PMOS is ratioed with respect to to reference leg to generate the required shift current. PMOS transistor P_2 is sized to provide extra current needed for the boosting when boost signal is asserted (i.e., bst=1). For nominal conditions P_2 is disabled by connecting the gate to V_{DD}. Due to usage of minimum sized transistors in boost circuit, the area overhead is minimal (<1%).

5.7.6. Subarray Architecture

Fig. 5.28 shows the proposed sub-array design with integrated boost enabled write drivers and shift circuit. There are a total of 64 WLs (32 in each sector) and 512 local columns. Column muxing of 8:1 is used for one global column. A total of 64 global columns provide 64 bits of data in/out. The column area holds read/write and shift circuitries. The shift and write drivers are designed per global column basis. Therefore, boosting a write driver will boost the write current for the 8 local columns. Furthermore, the boost signal does not decode the head selection. This particular limitation will boost all heads in the NW even if some of them don't need it. The shift driver is also provided per column basis. Therefore, every local column will be boosted even if one of the read or write heads is slow. *Note that it is possible to disable the boost for fast heads at the cost of decoding complexity*. However, in this work we have not considered head decoding for the sake of simplicity. Furthermore, the power overhead of boosting small number of global columns is found to be minimal (Section 5.8).

5.8. Cache Design for Adaptive Boosting

This section is focused on methodology to identify the slow bits and implementation of current boosting. This is followed by cache organization and simulation results. The limitations and possible improvements are also discussed.

5.8.1. Methodology

The proposed boosting is employed after a test routine that screens the slow write and slow read bits. The test pattern can be any of the conventional March patterns (e.g., March C [40]) that is performed at different frequencies to determine the read and write time of the bits in absence of boosting. The columns containing slow read and slow write are marked individually. In this context it is worth mentioning that the entire global column is marked slow even if one of the local columns are found slow. This is due to the fact that write and shift drivers are shared per global column basis. Next the same patterns are repeated with the boosted write and shift currents to ensure that the bits pass. Since the amount of current boosting is determined statistically through simulations we expect that all bits will pass after this step. If there are still many failing bits the maximum latency is relaxed, and the entire test is performed again from that point. The test time is approximated as below:

$$\text{Test time} = 2N_{Rows} * \text{Maximum_latency} + 2N_{boost} * \text{Maximum_latency} + 2N_{Relaxation} * \text{Relaxed_latency} \quad (5.3)$$

Where N_{Row} is the number of rows, N_{boost} is the number of boosted columns and $N_{relaxation}$ is he number of relaxations. Since each row is written and read subsequently during test its latency is multiplied by two. From our estimates the test time is in order of millisecond.

If after relaxation there are a few failing bits, the existing column or row redundancies can be used to replace the remaining slow bits. It is also possible to provide an extra setting in the drivers during design phase to boost the current further.

Fuses are used to program the individual columns for boost/no-boost. The fuse bits are decoded and loaded in the flip-flops to assert the DC signals controlling boost (Fig. 5.29). Note that fuse-based infrastructure is commonly used in micro- processors for redundancy programming, SRAM assist setting etc. Therefore the proposed technique can be easily incorporated in the system.

5.8.2. Cache Organization

We have used the same cache organization which described in Section 5.7.6. Each subarray contains 64 rows and 512 columns of 32-bit NWs. This amounts to 1Mb data. Each mat is composed of 8 subarrays (SA [7:0]). The write and shift drivers of each subarray receives global column-based boost signal. This will require 128 DC tracks (i.e., two tracks per global column) to be routed for each subarray i.e., 512 DC tracks per mat. Note that minimum pitch metals can be used for routing these signals. Each bank contains 8 mats (mat [7:0]) of total size 8MB. There are four independent banks (bank [3:0]) in the cache

5.8.3. Simulation Setup and Result

We evaluate SRAM, STTRAM and several cases of DWM in terms of power and performance. The evaluations are performed on a 4-core Alpha processor in Gem5 [87]. The processor configuration is provided in Table 5.1. Gem5 is modified accordingly to implement variable read and write latencies for DWM cache. The 32MB cache contains 32 million MTJs. We simulate process variation for 5000 runs of Monte Carlo and find a model to fit the distribution in

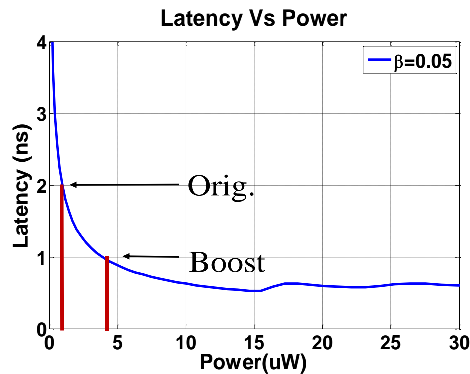

Figure 5.30 Shift current boosting for fast shifting.

Matlab. Next the model is used to estimate the write and read latency distributions for 32 million MTJs. Next the steps described below are followed:

1. The number of heads with write latency greater than 4 sigma (N_{wr}) are determined from the latency distribution obtained from Matlab. Similarly, the number of heads with read latency greater than 4 sigma (N_{rd}) are determined.

2. N_{wr} and N_{rd} are randomly distributed among the 32 million heads. The slow global columns numbers are determined in Matlab and fed to Gem5.

3. Gem5 matches the global columns for each access with the list and finds the number of times the slow global columns are accessed. This information is used to estimate the dynamic power of boosted columns.

We have simulated following cases to evaluate DWM under process variations:

(a) DWM-no-PV: DWM without any process variation.

(b) DWM-WC-PV: DWM with worst-case write and read latency due to process variation.

(c) DWM-bWR: DWM with write boosting of slow columns.

(d) DWM-bWR-bSFT: DWM with write and shift boosting.

(e) DWM-bWR-bSFT-bRD: DWM with write and shift boost for slow write and shift boost for slow read.

(f) DWM-bAll: DWM with write and shift boosting of all columns.

The cache latency and energy is obtained using CACTI [90] and Hspice model of DWM. The parameters used for simulations are provided in Table 4. Mean write latency is considered for DWM-no-PV whereas worst case write latency is considered for DWM-WC-PV (Fig. 5.23(b)). We use write current of 70uA for DWM-no-PV and DWM-WC-PV and 85uA for boosted cases. The shift power is computed from Fig. 5.30. The normal shift (2ns per shift) consumes 4uW per block (512 bits) whereas boosted shift (1ns per shift) consumes 16uW per block. For boosted cases, we assume 4 sigma write and read latencies for normal columns and boosted columns. Without boosting the read and write are assumed to operate with WC latency. The write and read energy with and without boosting is also shown in the Table 4. The cache latency is obtained using NVSim

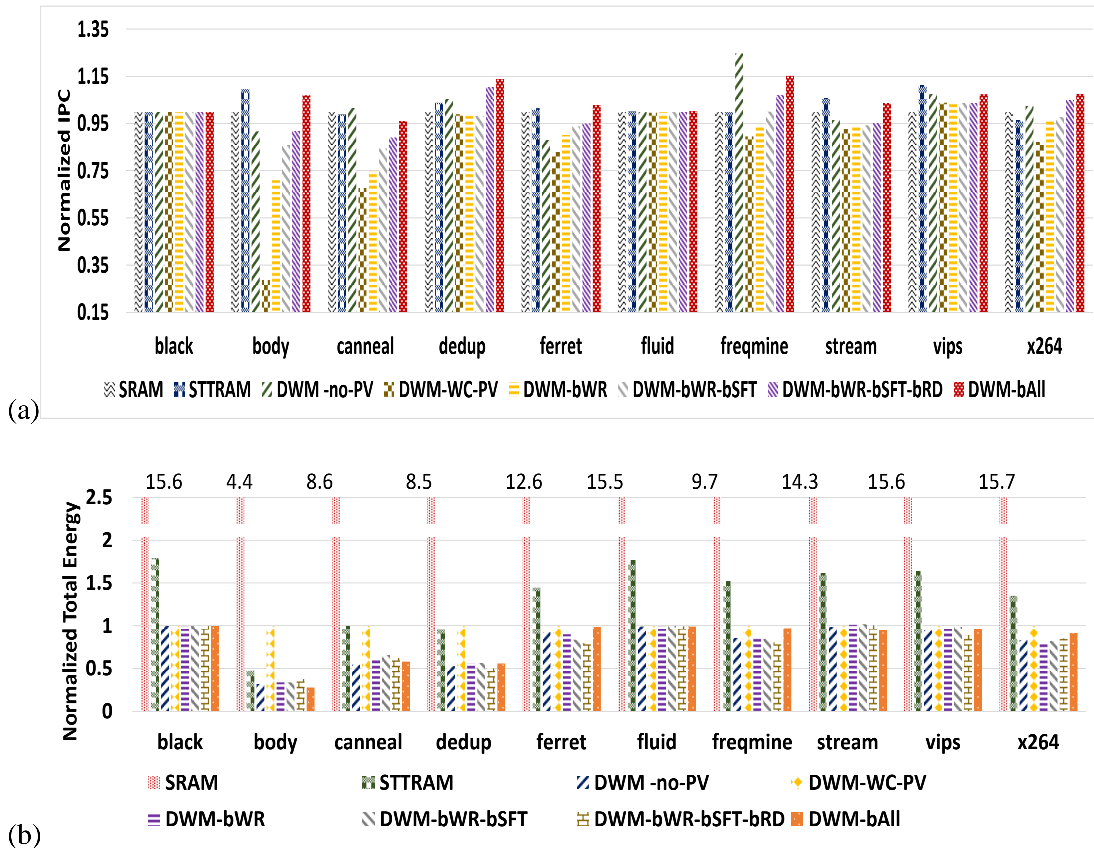

Figure 5.31 (a) IPC; (b) total energy comparison;

[132] by providing write pulse, bitcell footprint, write energy per bit and cache parameters. Read/write/shift energy, leakage power and total area is obtained using CACTI and Hspice model of DWM [37][41]. CACTI is modified for different memory technologies by changing bitcell footprint, bitcell leakage and write energy per access.

Fig. 5.31(a) shows the performance result represented by the normalized instruction per cycle (IPC). DWM-no-PV provides 2% performance improvement over SRAM. However, DWM-WC-PV indicates that process variation can degrade the IPC by 17% on average compared to DWM-no-PV. Boosting the write current (DWM-bWR) can improve the IPC. The maximum benefit is observed for write intensive benchmarks such as dedup, body and freqmine. Boosting both write and shift current (DWM-bWR-bSFT) improves the IPC by 13% compared to DWM-WC-PV. Finally, when slow reads are fixed by boosting the shift current 18% IPC gain is observed. For the sake of benchmarking we also plot the IPC improvement when all global columns are boosted. This case mimics voltage boosting to increase the write current in absence of tuning knobs. This is a power intensive operation which improves the IPC by 24%.

Fig. 5.31(b) shows the normalized energy (normalized to DWM-WC-PV) dissipation. The DWM architecture shows ~12X saving compared to SRAM. This is owing to elimination of bitcell leakage and reduction in peripheral leakage (due to less number of peripherals). DWM-bAll increases the power for benchmarks dedup and freqmine because they are write intensive. The other benchmarks observe power reduction due to lower peripheral leakage as the run-time is faster with boosted write and read.

Fig. 5.32(a)-(b) shows the breakdown of total energy into leakage and dynamic energy. The proposed DWM-bWR-bSFT-bRD reduces the dynamic energy consumption by 40% compared to DWM-WC-PV due to shorter write pulse width. Furthermore, it reduces the dynamic energy by 30% relative to DWM-bAll. Therefore, the proposed read and write boosting shows 30% dynamic energy improvement compared to boosting all bit-cells and 18% performance improvement compared to worst case latency due to process variation.

The total energy is summation of dynamic and leakage energy. Total energy is dominated by the leakage energy due to the large cache. As shown in Fig. 5.32(a) DWM-bAll case result in higher dynamic energy consumption compared to DWM-bWR, DWM-bWR-bSFT and DWM-

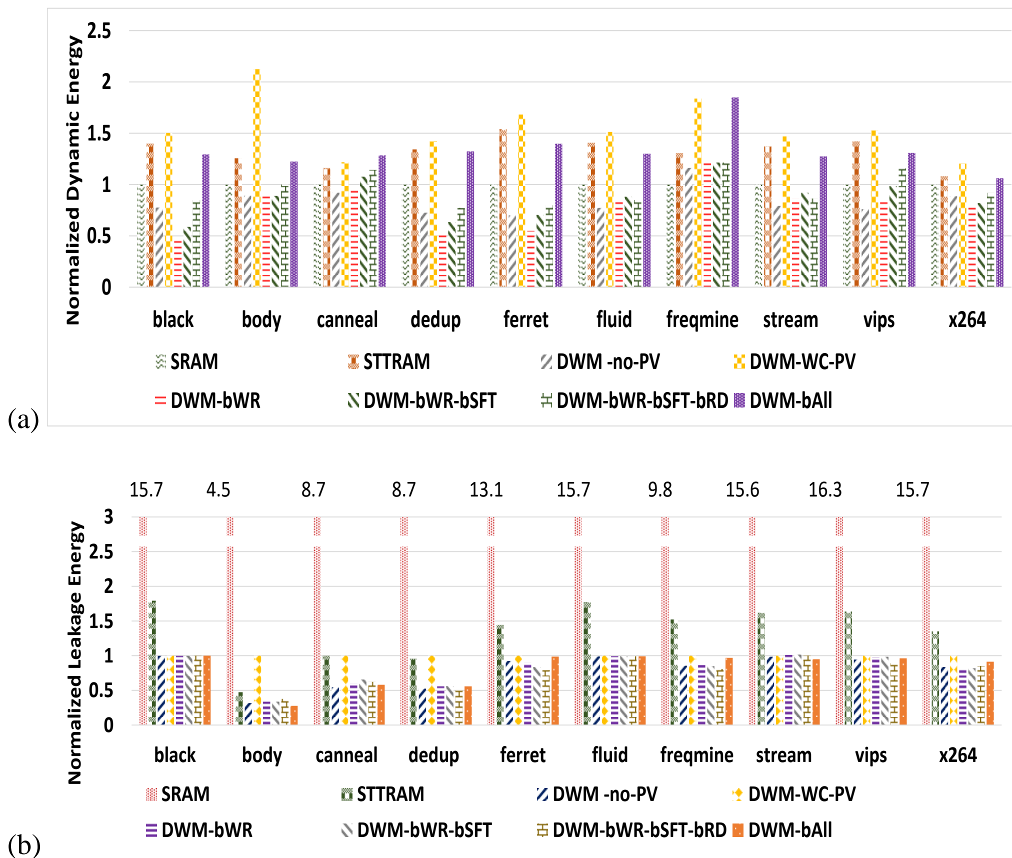

Figure 5.32 (a) Dynamic energy; and, (b) Leakage energy

bWR-bSFT-bRD for all of benchmarks. This is due to boosting of write and shift current for all bitcells during read and write operations which results in higher total energy. However, DWM-bAll case decreases execution time which in turn reduces leakage energy. The two benchmarks (body and stream) are dominated by leakage energy and they get benefitted from significant reduction in execution time for DWM-bAll.

5.9. Summary

DWM is a promising non-volatile memory technology for cache application due to high-density, low standby power, excellent retention, fast access time and good endurance. However it suffers from shift latency and shift power, and area overhead due to aspect ratio mismatch and separate read and write head. It also suffers from severe performance and power degradation due to process variation induced write and read latency variations. We presented a synergistic circuit and micro-architecture cache design using DWM. Our design comprehends several important factors such as bitcell layout for maximizing effective footprint, process requirements to allow seamless integration of DWM, optimization of heads, utilization factor, shift-power and latency. We proposed cache segmentation by controlling the shift current and dynamic shift and write voltage scaling based on workload monitoring and exploited it at the system level for power and performance optimization. Simulations show 3-33% performance and 1.2X-14.4X power consumption improvement for cache segregation and 2.5-31% performance and 1.3X-14.9X power enhancement for dynamic current boosting over a wide range of PARSEC benchmarks.

Furthermore, we proposed a novel low-overhead write and shift current boosting methodology that comprehends circuits and micro-architecture to address process variation induces write latency degradation. The bits experiencing worst-case write latency are fixed through a combination of write and shift boosting whereas worst-case read bits are fixed by shift boosting. The simulations show 30% dynamic energy improvement compared to boosting all bit-cells and

18% performance improvement compared to worst case latency due to process variation over a wide range of PARSEC benchmarks.

Chapter 6

Dynamic Computing in Memory in Resistive Crossbar Arrays

With Von-Neumann computing struggling to match the energy-efficiency of biological systems, there is pressing need to explore alternative computing models. Recent experimental studies have revealed that Resistive Random Access Memory (RRAM) is a promising alternative for DRAM. Resistive crossbar arrays possess many promising features that can not only enable high-density and low-power storage but also non-Von-Neumann computing models. Most recent works focus on dot product operation with RRAM crossbar arrays, and therefore are not flexible to implement various logical functions. We propose a low-power dynamic computing in memory system which can implement various functions in Sum of Product (SOP) form in RRAM crossbar array architecture.

6.1. Introduction

Von-Neumann computing separates memory and processing element resulting in performance and energy bottlenecks due to frequent data transfers. High density crossbar array which employs two terminal RRAM the crosspoint of vertical and horizontal metal wires are proposed [47]. However, these architectures suffer from sneak-path problem which results in poor sense margin, higher power consumption, and limited array size. Crossbar array with a selector diode connected in series to RRAM device has been proposed [133-135] to solve the sneak path issue. Various computing in memory schemes have been proposed to implement dot products in RRAM crossbar array. Digital to analog converter (DAC) and analog to digital converter (ADC)

are required as peripheral circuitry to implement dot product in RRAM crossbar array. These architectures are able to implement matrix multiplication [14] and various computing paradigms such as neuromorphic computing [15-16] and approximate computing [17]. Even though these techniques improve performance and power efficiency they face challenges such as limited application domain and need of power intensive analog circuits such as ADC and DAC.

A computing in memory paradigm is proposed [136] to implement random functions in RRAM crossbar array. This technique offers full programmability across storage and computation. Even though it provides the flexibility of partitioning the hardware resources between computation and storage to achieve optimal performance, the implementation details of arbitrary functions are not discussed. This technique also suffers from poor sense margin (that can limit the array size) as well as increased power consumption, making it impractical for computing in memory applications. Memristor Aided LoGIC (MAGIC) has been proposed [137] where memristors act as an input with previously stored data, and an additional memristor serves as an output to implement logic gates. In this method, the logical operation is associated with write operation leading to higher power and latency overhead. Since the inputs are programmed into memristors the gate must be reprogrammed for new input data incurring substantial power overhead.

In this chapter, we propose a Dynamic Computing in Memory (DCIM) paradigm using RRAM crossbar array which benefits from nonlinear characteristic of selector diode to improve sense margin in order to implement higher fan-in gates. In addition, this technique reduces the power consumption associated with logical operation significantly by eliminating the static current compared to [136]. It also eliminates the need to write into the bitcell to perform logical operations compared to [137].

In summary we make following contributions in this chapter:

- We study computing in memory systems proposed in [9-10] thoroughly and explain their bottlenecks.

- We develop a dynamic computing in memory technique to overcome sense margin limitation to implement higher fan-in AND/OR gates using RRAM crossbar array while reducing power consumption.
- We perform process, voltage and temperature variation analysis to determine optimum reference voltage to maximize read yield.
- We present comparative analysis of proposed technique with respect to other techniques for MCNC benchmarks in terms of power and latency.

6.1. Background

In this section, we explain the basics of crossbar array architecture and read and write operations. We also discuss the state-of-art computing in memory systems using RRAM crossbar and describe its challenges.

6.1.1. Basics of RRAM Crossbar Array

A crossbar memory array consists of wordlines (WL) and bitlines (BL) where memory cell resides at their cross point as shown in Fig. 6.1. In this thesis, we use a bipolar RRAM model [138]

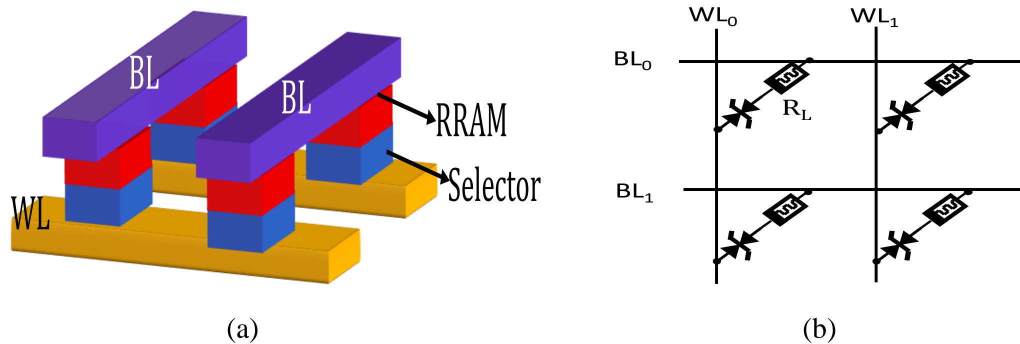

Figure 6.1 Crossbar array with metal oxide RRAM and selector dio each crosspoint; and, (b) schematic of crossbar array with selector diode.

in which RESET/SET is performed at different voltage polarities. The I-R and I-V characteristic of the RRAM is shown in Fig. 6.2(a-b). The memory cell switches from High Resistance State (HRS) to Low Resistance State (LRS) if a positive voltage greater than threshold voltage is applied across the bitcell. Similarly, the bitcell switches from low to high resistance state if negative voltage is applied. Crossbar memory architecture achieves minimal cell size however, the sneak leakage current can reduce sense margin significantly. In order to increase sense margin and eliminate sneak leakage, we employ a memory bitcell which is composed of a RRAM device connected to a symmetric selector diode in series (Fig. 6.1(a-b)). The I-V characteristic of the selector diode is modeled by the following function as discussed in [133]:

$$I_{SEL} = \gamma . \sinh(\alpha . V) \tag{6.1}$$

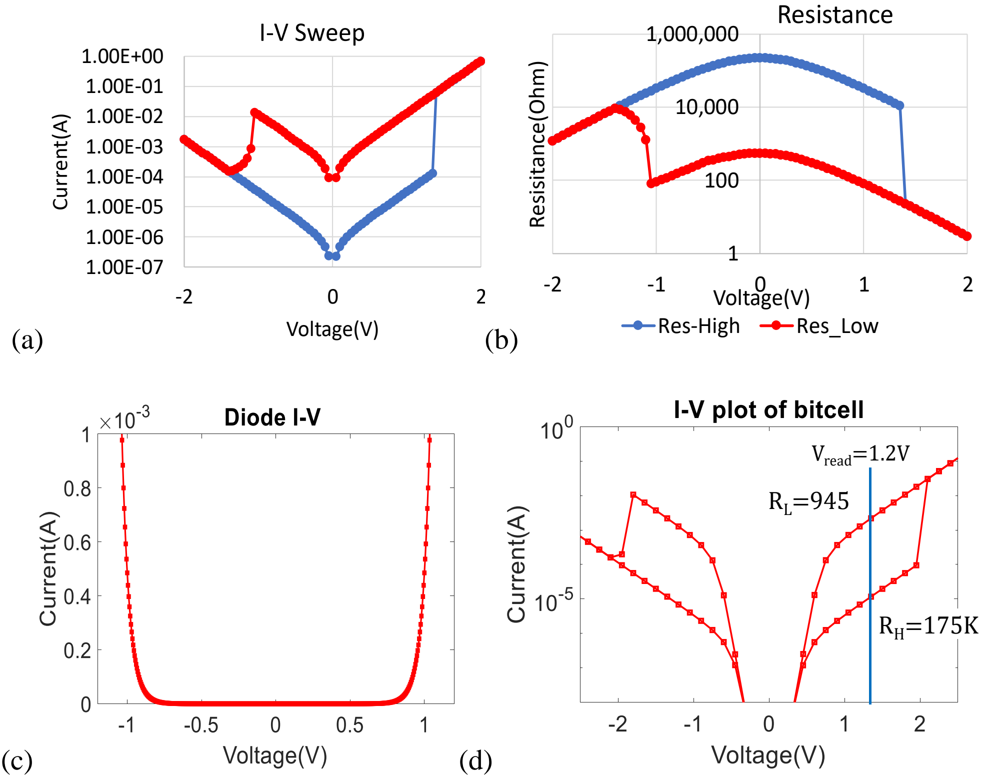

Figure 6.2 I-V curve RRAM model used in this study; (b) I-R characteristic of the RRAM model; (c) I-V curve of selector diode used in this study; and, (d) the I-V characteristic of bitcell composed of RRAM and selector diode.

where γ is a conductance parameter, and α represents the nonlinearity of selector diode. This model fits reasonably with the experimental I-V characteristic for selector devices based on MIM diode and punch through diode [139-140]. The design parameters of RRAM and selector diode are reported in Table 6.1. The I-V curve of selector diode is illustrated in Fig. 6.2(c). Fig. 6.2(d) depicts the I-V curve of the bitcell composed of selector diode and RRAM device. It can be observed that the difference between low and high resistance increases by adding a selector diode which in turn improves the sense margin.

Read Operation: For reading the bitcell, the commonly used ground/ground (GND-GND) scheme is employed. To access the bitcells in the array, the selected WL is connected to V_{READ} and the selected BLs are connected to sense-amplifier (SA) while all unselected BLs and WLs are

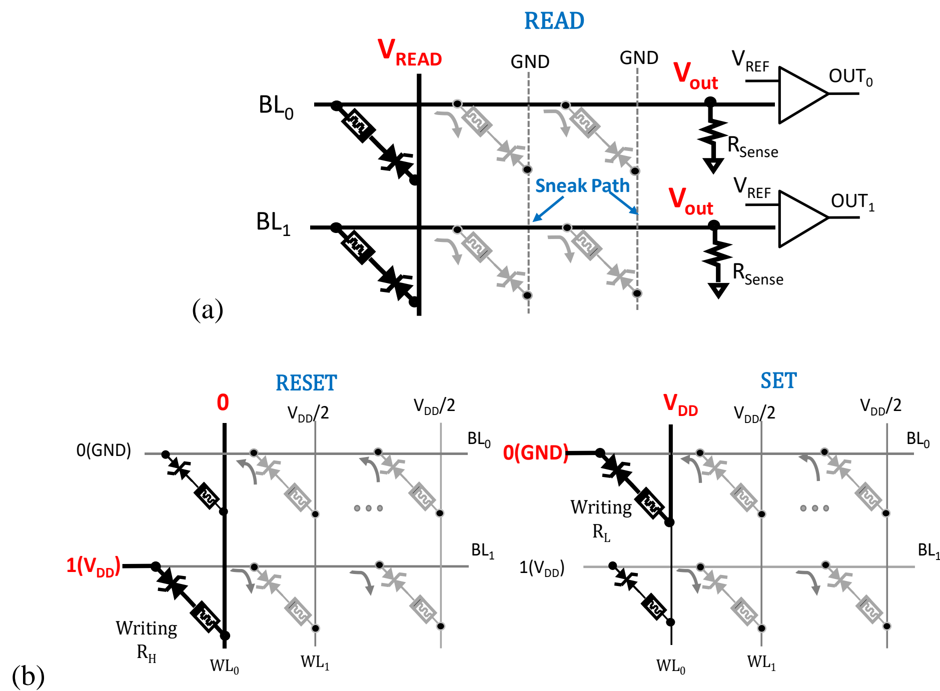

Figure 6.3 RRAM crossbar array (a) GND-GND read scheme; and, (b)VDD/2 write technique. Sneak paths are shown for read and write operations.

biased at GND. Although this read scheme improves the sense margin, it also increases the power

consumption. Other proposed read schemes include FL-FL (floating-floating) and GND-FL [133]. The current through selected bitcell which is generated by applied voltage to the selected WL, is converted to V_{out} by a sense resistance (R_{sense}). Read operation is performed by comparing output voltage (V_{out}) with a reference voltage (V_{REF}) using a SA as shown in Fig. 6.3. Maximum sense margin for both reading '0' (SM0) and reading '1' (SM1) is achieved by setting the $R_{Sense} = \sqrt{R_{OFF}/R_{ON}}$. The state of the unselected bitcells affects the sense margin (as shown in Fig. 6.3(a)). The worst-case sneak path also results in the worst-case SM which occurs when the unselected bitcells are in LRS since the sneak current is at maximum in this case.

Write Operation: We employ the $V_{DD}/2$ writing scheme where the selected WL is connected to V_{DD} and selected BL is connected to GND/V_{DD} (depending on input data) while other unselected BLs and WLs are biased at $V_{DD}/2$ (Fig. 6.3(b)). The write operation is performed in RESET and SET phases. Initially, the desired data is applied to the selected BLs. In the RESET phase the selected WL is connected to ground, hence the logical '0' is written to bitcell (programed to HRS). In the SET phase the selected WL is connected to V_{DD} and the logical '1' is written into bitcell (programed to LRS).

Table 6.1 List of design parameters.

Parameters	Values
RRAM high resistance state (R_H) at 1.2V	18KΩ
RRAM low resistance state (R_L) at 1.2V	440 Ω
RRAM read Latency	0.5ns
RRAM write Latency	22ns
Nonlinear factor of selector (α)[133]	18.4
On-state current of selector (I_{ON})[133]	100uA
Selector Conductance Factor (γ)[133]	$2*10^{-12}$
bitcell high resistance state (R_H) at 1.2V	175KΩ
RRAM low resistance state (R_L) at 1.2V	945Ω
Bitcell write latency at 2.5V	25nS
Bitline Capacitance	30fF

6.1.2. Static Computing in Memory (SCIM) Method

A configurable computing in memory system based on RRAM crossbar architecture which provides full programmability across computation and storage has been proposed in [136]. However, the detailed circuit implementation is not discussed. We extend the idea borrowed from this paper, to implement arbitrary functions in terms of sum of product within RRAM crossbar array for comparative analysis. In this method, the crossbar array is implemented using RRAM without selector diodes. A 2-input AND gate implementation using crossbar array is shown in Fig. 6.4. Each input and its complement are applied to a WL. In order to realize logical A.B, the cells connected to A and B are programmed to LRS and the cells connected to $\bar{A}$ and $\bar{B}$ are programmed to HRS while all other bitcells are programed to HRS (e.g., the bitcells connected to input Z and $\bar{Z}$ as illustrated in Fig. 6.4). The array inputs connected to WLs are applied to different gates implemented on different BLs. All the gates are evaluated concurrently by applying the data input to the array.

AND operation is performed by applying input vector and sensing the BL voltage. For

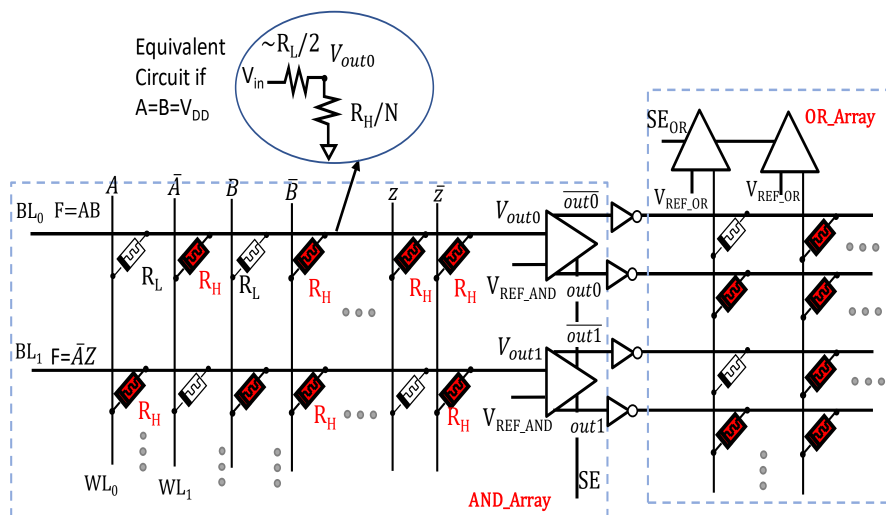

Figure 6.4 Static computing in memory architecture in RRAM crossbar array.

A=B=1, the voltage appearing on the BL_0 is approximately V_{DD} (see the equivalent circuit in the inset of Fig. 6.4). For A=1 and B=0 (or A=0 and B=1), the BL_0 voltage is approximately $V_{DD}/2$. Finally, the voltage generated by applying the input vector is compared against a reference voltage (V_{AND_REF}) using a decoupled SA to determine the output of the AND operation.

As fan-in of the AND gate increases, the difference between voltage representing logical '1' and '0' reduces. The worst-case occurs when only one input is '0' and all remaining inputs are '1'. The difference between bitline voltage when all AND gate inputs are '1' (V_{AND1}) and V_{REF_AND} is defined as sense '1' margin (SM1). Sense '0' margin (SM0) for the AND operation is defined as the difference between bitline voltage when only one input is '0' (V_{AND0}) and V_{AND_REF}. Poor

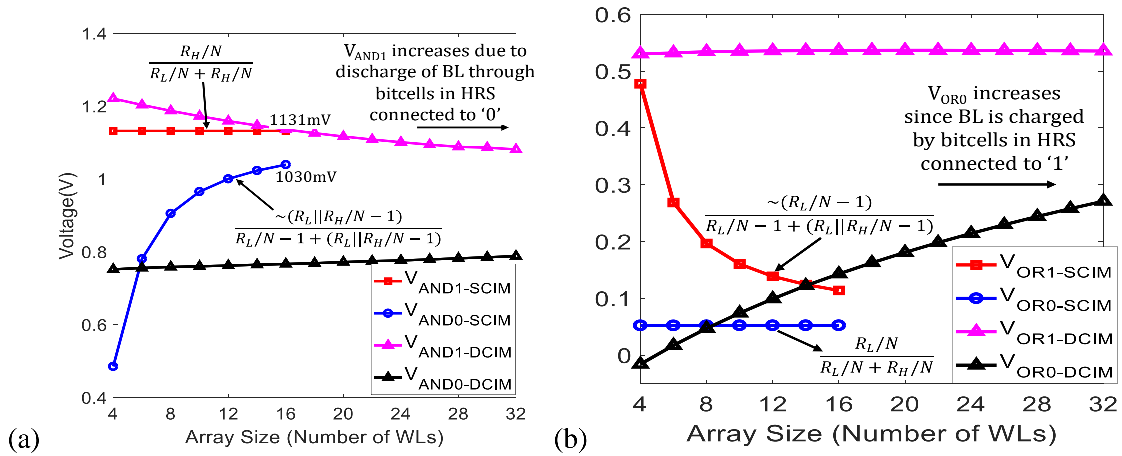

Figure 6.5 V_{AND1} and V_{AND0} versus AND array size; and, (b) V_{OR1} and V_{OR0} versus OR array size in an array of 2N WLs where all WLs are utilized to implement N-input gate.

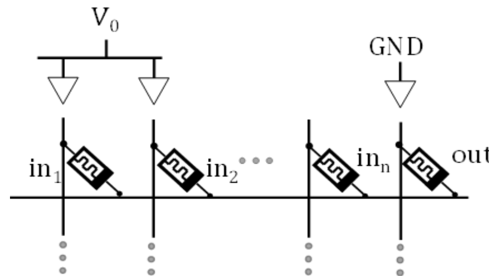

Figure 6.6 MAGIC NOR gate implementation.

sense margin can result in wrong interpretation of the logical AND output. The impact of array size (the number of WLs) on V_{AND1} and V_{AND0} is shown in Fig. 6.5(a). This plot represents the V_{AND0} and V_{AND1} in an array of 2N WLs where all WLs are utilized to implement N-input AND gate. It can be observed that V_{AND1} remains constant with increasing AND gate fan-in. However, V_{AND0} rises with increased number of inputs which in turn degrades the SM. Note that, it is not possible to implement AND gate with more than 8 inputs, since SM reduces below the sense amplifier offset voltage which can result in wrong output.

Any logical function can be implemented in Sum of Product (SOP) form. Therefore, along with implementing AND function in RRAM crossbar array, we need to implement OR function as well. The OR gate implementation is similar to AND gate, except that the bitline voltage is compared against a different reference voltage (V_{REF_OR}). In order to implement the A+B (A OR B), RRAMs connected to A and B are programed to LRS, RRAMs connected to $\bar{A}$ and $\bar{B}$ are programed to HRS, and RRAMs connected to other unused WLs are programed to HRS. By applying A=B=0, the BL is pulled down to '0'. If one of the inputs is '1', a voltage near $V_{DD}/2$ appears on the bitline. The worst-case SM1 for OR array occurs when only one input value is '1' and remaining input values are '0'. The BL voltage in this case is defined as V_{OR1}. Similarly, V_{OR0} is defined as BL voltage when all inputs are '0'. As shown in Fig. 6.5(b), V_{OR1} reduces as the array size increases, which limits the SM.

6.1.3. Memristor Aided LoGIC (MAGIC) [137]

In this CIM architecture, memristors act as an input with previously stored data, and an additional memristor serves as an output to implement logic gates. This technique consists of two sequential stages. As shown in Fig. 6.6, a 2-input NOR gate composed of two RRAMs (in_1 and in_2) is connected to an output RRAM (*out*). In the initial stage, the output RRAM is programed to low resistance state and the input values are written to memristors in_1 and in_2. In the second stage,

voltage V_0 is applied to memristors in_1 and in_2, and the *out* memristor is connected to GND to evaluate the NOR operation. The applied voltage results in a current that flows through RRAMs in_1 and in_2 and appears at RRAM *out*. If both input memristors are logical '0' (high resistance), the voltage appearing across the output RRAM is less than the switching threshold of the output RRAM thus it does not change and remains at logical '1'. For all other input combinations, the voltage across output RRAM is greater than the threshold voltage. Hence, the output memristor switches to high resistance state (logical '0'). Finally, the state of output resistance is sensed using sense amplifier to determine the result of logical NOR operation. Since logical operation is associated with write operation in this method, the latency and power overhead are substantial. The proposed dynamic CIM eliminates the need of a write operation to improve latency and power overhead.

6.2. Proposed Dynamic Computing in memory

In this section, we describe the operation of DCIM and study the impact of fan-in on sense margin and power. 65nm predictive technology [141] is used to perform simulation.

6.2.1. Basic Operation

DCIM aims to overcome sense margin limitation for higher fan-in AND/OR gates using RRAM crossbars. DCIM decreases power consumption due to two reasons: 1) sneak path leakage reduces significantly by employing a selector diode; 2) dynamic-sensing eliminates the static power consumption for performing logical operations. In this technique, each memory cell is composed of a RRAM device connected in series to a selector diode. Computing in memory is accomplished by implementing the functions in SOP form. Thus, both AND and OR operations are required to implement the logical functions. We dedicate separate arrays to perform each function and call them AND-array and OR-array.

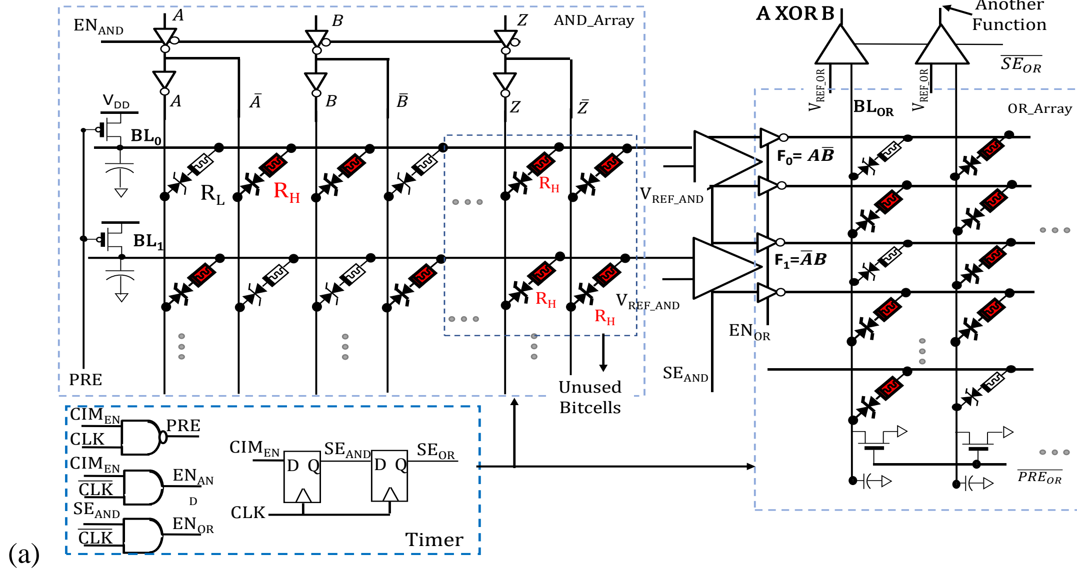

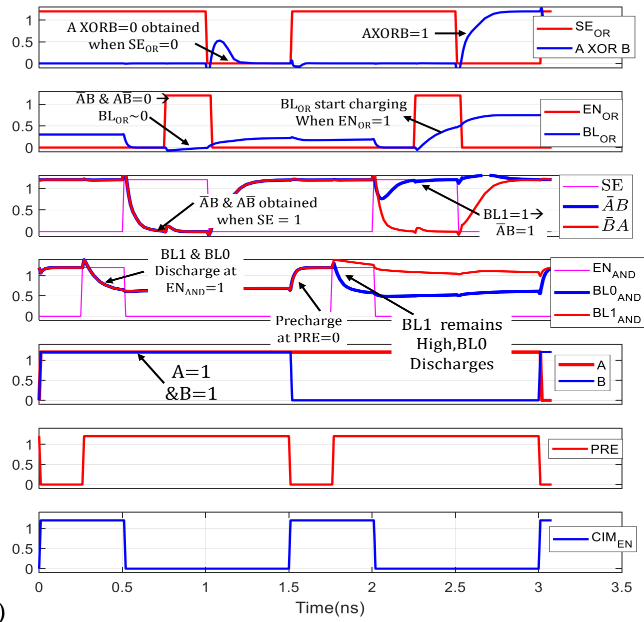

Figure 6.7 XOR implementation using proposed DCIM architecture in RRAM crossbar array; and, (b) timing diagram of logical XOR operation.

In the proposed architecture, the wordlines serve as the inputs and the bitlines are the output of AND functions. Initially both AND and OR arrays are programmed to implement the desired function. The programing is similar to static technique. For instance, in order to implement $A\bar{B}$, the bitcells connected to A and $\bar{B}$ are programed to LRS while the bitcells connected to $\bar{A}$ and B are

programed to HRS (Fig. 6.7(a)). All bitcells connected to other array inputs/WLs which are not part of AND gate inputs are programed to HRS (e.g., the bitcells connected to input Z and $\bar{Z}$). To perform AND operation, the BL is initially precharged to V_{DD}. Once the inputs are applied, the BL either remains precharged or discharges based on the input vector. In the previous example, if V_{DD} (logical '1') is applied to inputs A and $\bar{B}$, the BL remains precharged since these inputs are connected to bitcell in LRS. However, the leakage of HRS bitcells connected to GND discharges the BL negligibly. Any other input combination discharges the BL significantly since GND is connected to a bitcell in LRS. Finally, the BL voltage is compared against the V_{REF_AND} to determine the result of AND operation. The result of the AND function and its complement are provided as input to the OR array to obtain SOP output. Programing of OR array is similar to AND array. However, in OR array BLs are predischarged to '0'. The predischarge of OR array BLs is performed during the AND array evaluation phase, therefore the latency of predischarge phase is hidden. Finally, the voltage generated on the OR array BL is compared against V_{REF_OR} to achieve the result of OR operation.

The effect of array size (number of WLs) on the SM is investigated to determine the best array size (Fig. 6.5). Since two WLs and two bitcells are required for implementing each input of AND gate, the number of WLs is twice the number of AND gate inputs. As depicted in Fig. 6.5(a-b) as array size increases SM for AND/OR operations degrades. It can be observed that proposed DCIM improves SM significantly compared to SCIM, thus larger array size (higher fan-in gates) can be realized.

Fig. 6.7 shows the implementation of XOR function in DCIM. The BL_0 and BL_1 are programmed to implement $A\bar{B}$ and $\bar{A}B$ functions respectively. Note that the bitcells connected to WLs which are not contributing in XOR implementation (called the unused bitcells) are programmed to HRS. Initially, the PRE-signal is activated to precharge AND array BLs to V_{DD}. Next, inputs (A and B) are applied by asserting EN_{AND}. As shown in Fig. 6.7(b), when A, B=1 both

BL_0 and BL_1 fall to 0.65V. Since this voltage is less than V_{REF_AND}=0.74V, outputs of sense amplifiers which determine the results of $A\bar{B}$ and $\bar{A}B$ functions are pulled down to '0' at the edge of SE_{AND}. Since inputs of OR array (F_0=$A\bar{B}$ and F_1=$\bar{A}B$) are '0', the OR array BL (BL_{OR}) remains discharged with voltage of approximately '0' (i.e. A XOR B=0). If A=0 and B=1, BL_0 discharges to 0.65V while BL_1 remains precharged which results in $F_0 = A\bar{B} = 0$ and F_1=$\bar{A}B$=1. Since F_1 is '1' and is connected to a bitcell in LRS, it charges the BL_{OR} to 0.52V while EN_{OR} is asserted. Finally, the voltage of BL_{OR} is compared against V_{REF_OR}=0.38V at the edge of SE_{OR} which produces '1' at the output of SA. Note that OR array sense enable ($\overline{SE_{OR}}$) is an active low signal. Since the voltage generated on bitline of OR array is less than 0.52V, a PMOS based SA with active low sense enable is employed (Section 3.2.4.3).

The PRE, EN and SE signals are generated in the timer (located at the middle of subarray). The duty cycle of EN depends on BL capacitance and the bitcell resistance. In addition, SM depends on the EN pulse width. The EN pulse with is chosen in such a way that V_{OR1} rises to 90% of its steady state voltage. By applying EN, V_{OR0} also rises due to leakage of unused bitcells. Therefore, the EN pulse with must be chosen in such a way to maximize V_{OR1} and minimize the increase of V_{OR0}. The same argument holds true for V_{AND1} and V_{AND0}. Moreover, increasing the EN pulse width results in higher power consumption since both V_{OR0} and V_{OR1} will increase. Thus, there is a tradeoff between power and sense margin. We have swept the EN width from to 0.1nS to 0.5nS in order to optimize both SM and power. The EN pulse width of 0.25ns achieves sufficient sense margin while preserving power consumption. The PRE pulse width depends on the BL capacitance and the width of precharge transistor. Based on simulation result, a PRE pulse width of 0.25nS is sufficient to precharge/predischarge the BL before logical AND/OR operation. The CIM operation starts at the edge CIM_{EM} which is provided as input to the timer (inputs are provided to AND array simultaneously). The timer receives CIM_{EN} and produces PRE, EN and SE signals (clock frequency is 2GHz). The power and area overheard of timer is negligible.

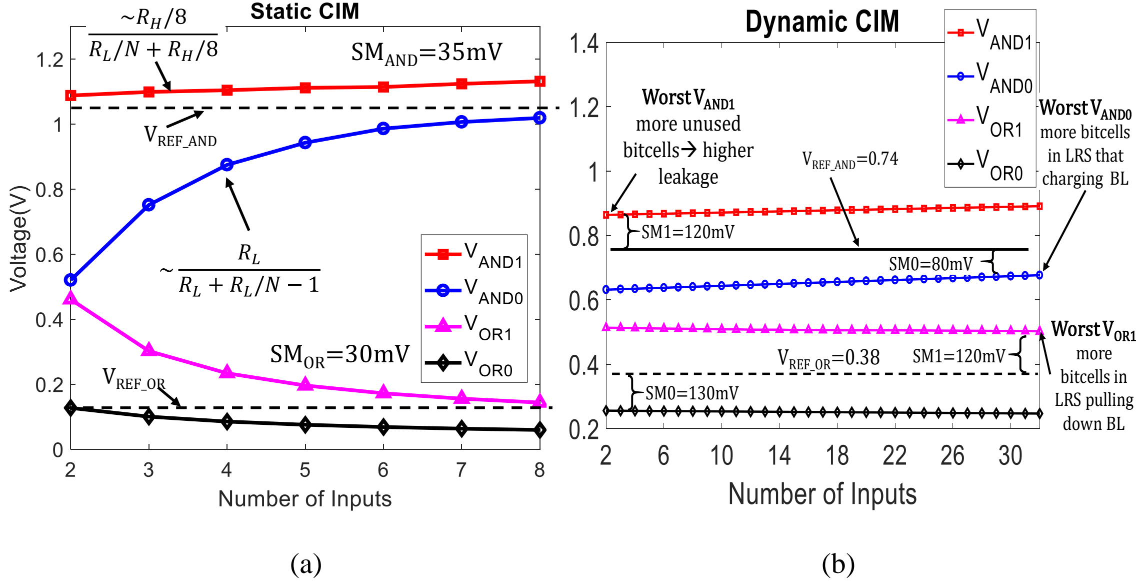

Figure 6.8 $V_{AND,1}$, $V_{AND,0}$, V_{OR1} and V_{OR0} versus gate fan-in for, (a) conventional CIM in array of 16 WLs, (b) DCIM in array of 64 WLs.

6.2.2. Impact of Gate Fan-in on Sense Margin

In the previous section, we investigated the effect of array size on the SM. The purpose of this study is to determine the array size that achieves maximum sense margin while preserving the area efficiency. In other words, it represents the sense margin of AND/OR operation in an array of 2N WLs where all WLs are utilized to implement N inputs AND gate. In this section we study the sense margin with respect to AND gate fan-in. Let us assume that a 4-input AND gate is implemented in an array of 64 WLs. Since 8 WLs are required to implement 4-input AND gate, 8 bitcells are programmed to implement the AND gate while bitcells connected to the rest of WLs are programmed to HRS. The loading effect of unused array inputs connected bitcells in HRS reduces sense margin. Unused array input and its complements are connected to two bitcells in HRS. In case of static CIM, applying inputs to the unused WLs degrade the sense margin. This can be understood by comparing Fig. 6.5 with Fig. 6.8(a). For instance, 2-input OR gate SM is

significantly higher when the array consists of 4 WLs (see Fig. 6.5(b)) versus 16 WLs (see Fig. 6.8(a)).

The impact of unused WLs on sense margin is more severe in DCIM. Suppose input Z value (as depicted in Fig. 6.7) which does not belong to 2-input AND gate implemented on BL_0 is '0'. Since BL_0 is precharged to V_{DD} initially, the voltage across selector diode is VDD, and it is ON initially. As BL voltage discharges through bitcell connected to Z the voltage across selector diode reduces, and it becomes strongly ON to weakly ON. The selector diode is OFF/weakly OFF in the bitcell which is connected to $\bar{Z}$. Therefore, input Z=0 discharges the BL, while input $\bar{Z} = 1$ cannot compensate the effect of Z by charging the BL (since bitcell connected to $\bar{Z}$ is OFF). This result in lower V_{AND1}, leading to SM degradation. As gate fan-in decreases the number of unused bitcells increases. Thus, V_{AND1} reduction increases as fan-in decrease since the leakage through unused bitcells increases. As shown in Fig. 6.8(b), 2-input AND gate achieves worst-case V_{AND1} (higher number of unused bitcells result in higher leakage and lower V_{AND1}).

As mentioned earlier, V_{AND0} is the voltage appears on the BL when only one input is '0'. For 32-input AND gate, V_{AND0} is the BL voltage where 31 inputs connected to bitcells in LRS is pulling up the BL weakly (since selector diode is OFF) while only one input is pulling it down strongly. Thus, as the number of input increases (e.g., from 2 to 32), the number of bitcells in LRS which weakly pulls the BL up increases (e.g. 1 versus 31). Therefore, as depicted in Fig. 6.8(b), 32-inputs AND gate results in the worst-case V_{AND0} (higher V_{AND0}) while 2-inputs AND gate result in the best V_{AND0}. The same argument holds true for V_{OR1} and V_{OR0} . V_{OR1} and V_{OR0} in an array of 64 WLs is also

shown in Fig. 6.8(b). 32-input OR gate results in worst-case V_{OR1} since more bitcells in LRS pulls the BL down.

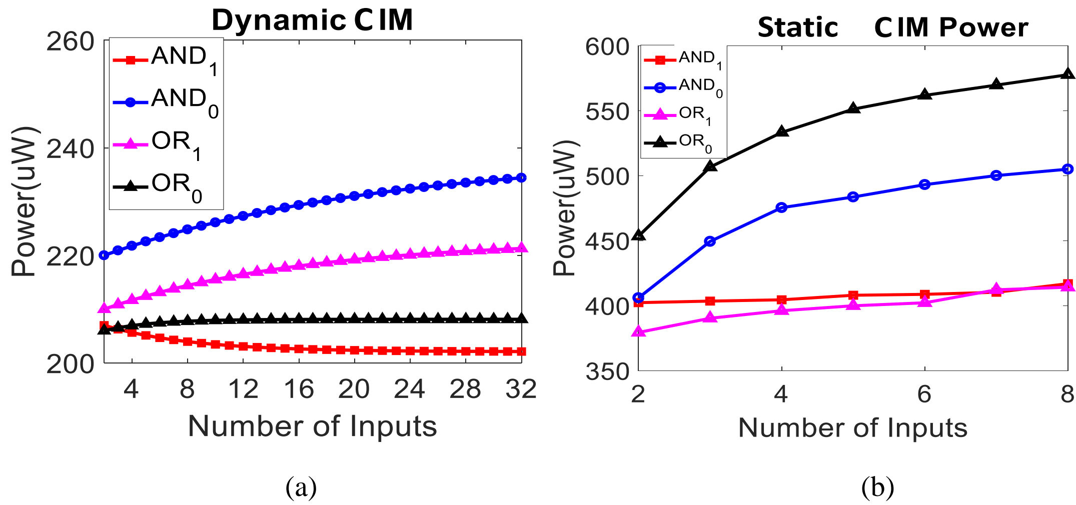

Figure 6.9 Power consumption versus number of inputs; (a) Dynamic CIM and, (b) static CIM.

6.2.3. Impact of Gate Fan-in on Power

The power consumption of proposed DCIM for AND and OR operations are shown in Fig. 6.9(a). In case of AND operation we assume the BL is precharged to V_{DD} and the power consumption is summation of the power drawn from supply after applying inputs, the power consumed by the sense amplifier and the power required to precharge the BL back to V_{DD}. For the OR operation the power consumption is the power drawn from the supply to charge the bitline, and the power consumed by the sense amplifier. It can be noted that as the number of input increases, the power consumption of AND1 operation reduces. As shown in Fig. 6.8(b), V_{AND1} increases with the number of inputs. Hence, less power is consumed to precharge the bitline back to V_{DD}. AND0 operation results in higher power consumption since the bitline discharges to a lower voltage when the result of AND operation is '0'. Therefore, more power is consumed to precharge the BL back to V_{DD}. Fig. 6.9(b) depicts the power consumption of static CIM. It can be noted that static CIM

Table 6.2 Parameters used for process variation study.

Device	Parameter	Mean	Std. Dev.
PMOS	V_{TH}	423mV	$A_{V_T}/\sqrt{wL}$ [(1)]
NMOS	V_{TH}	365mV	$A_{V_T}/\sqrt{wL}$ [(1)]
RRAM	Inial Gap	R_L =0.2nm R_h =1.7nm	7%
RRAM	Oxide Thickness	12nm	5%

[(1)] A_{V_T} *is* Pelgroom coefficient which is ~4.5mV/µm for 65nm technology

power consumption is significantly higher (almost 3X on average) due to static current which flows through the bitcells during logical AND/OR evaluation.

6.3. Process and Temperature Variation Analysis

6.3.1. Impact of Process and Temperature Variation on Sense Margin

The impact of process and temperature variation on V_{AND1} and V_{AND0} are investigated to determine the best V_{REF_AND} to achieve robustness. Process variation analysis is carried out using detailed Monte Carlo simulation in 65nm technology [141]. For RRAM we have assumed oxide thickness and initial filament gap variations. The variations in CMOS circuitry is lumped in threshold voltage fluctuation. The mean and standard deviation of these parameters are provided in Table 6.2. As mentioned earlier, 2-input AND gate results in the worst-case V_{AND1}, and 32-input AND gate results in the worst-case V_{AND0}. Furthermore, higher temperature results in higher bitcell resistance, leading to higher V_{AND0} which in turn degrades the SM0. Whereas, lower temperature leads to lower bitcell resistance and lower V_{AND1} degrading SM1. In order to obtain the worst-case V_{AND0} under process and temperature variation, we run 1000 points Monte-Carlo simulation at 90°C. Similarly, 1000 points Monte-Carlo simulation is performed at -10°C to achieve the worst-

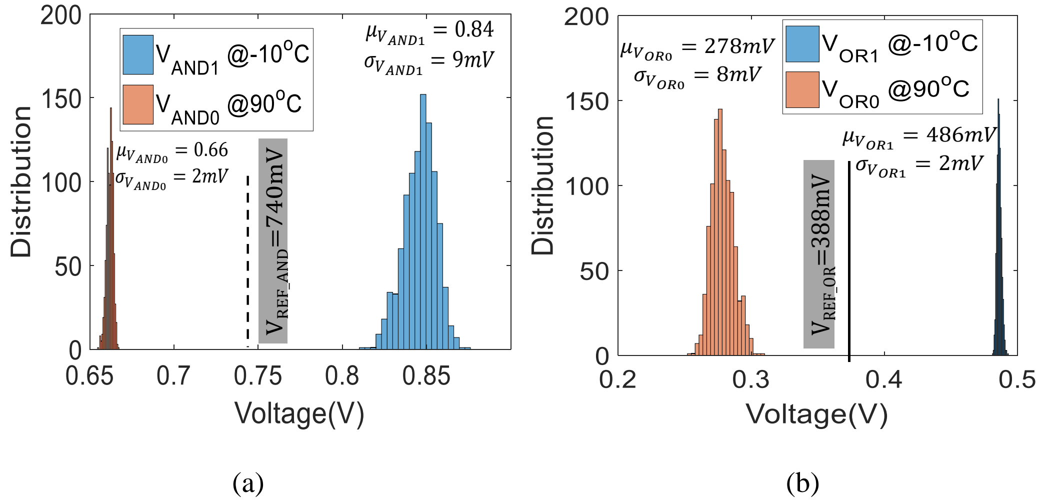

Figure 6.10 (a) V_{AND1} and V_{AND0} distribution for 1000 Monte-Carlo points @ -10°C and 90°C; and, (b) V_{OR0} and V_{OR1} distribution.

case V_{AND1}. The simulation result is shown in Fig. 6.10 (a). Since standard deviation of V_{AND1} ($\sigma_{V_{AND1}}$) is greater than V_{AND0}, a voltage slightly less than $(\mu_{V_{AND0}} + \mu_{V_{AND1}})/2$ is chosen as V_{REF_AND} to maximize the AND operation read yield. We have performed the same analysis to obtain the V_{REF_OR}. The worst-case V_{OR1} occurs at higher temperature (90°C), since higher resistance increase the RC delay, thereby the BL is charged to a lower voltage reducing V_{OR1}. Similarly, the worst V_{OR0} occurs at lower temperature. Monte-Carlo simulation is carried out at different temperatures to determine the optimum V_{REF_OR}. The results are shown in Fig. 6.10(b). Since the $\sigma_{V_{OR0}}$ is greater than $\sigma_{V_{OR1}}$ we pick a voltage greater than $(\mu_{V_{OR0}} + \mu_{V_{OR1}})/2$ as V_{REF_OR} to maximize the OR operation read yield.

The sense-amplifier offset voltage (V_{SA_OFFSET}) depends on the sense time and transistor size since increasing the transistor size decreases the transistor threshold voltage variation. We employed the same sense amplifier we discussed in Section 3.2.4.32 with $\mu_{V_{SA_OFFSET}} = 8mV$ and $\sigma_{V_{SA_OFFSET}} = 16mV$.

The read access pass yield (RAPY) is defined in Section 3.2.4.3.2. To obtain RAPY we assume that V_{REF} is produced by a voltage regulator with negligible variation (5mV). Based on the Monte-Carlo simulation, the RAPY of AND and OR operations are found to be 4.2σ and 4.9σ respectively. The static CIM results in significantly lower yield. The RAPY of AND and OR operations are found to be 1.7σ and 1σ respectively.

6.4. Implementation of Carry Select Adder using DCIM

In order to perform addition, carry select adder is implemented. Fig. 6.11 demonstrate the implementation of 16-bit carry select adder using DCIM. For sake of brevity only low resistance connections are shown. In the carry select addition approach two sets of sum and outgoing carry are computed considering incoming carry is either '0' or '1'. Once the incoming carry is known, we only need to select the correct set of outputs (out of the two sets using multiplexer) without waiting for the carry to propagate further. In Fig. 6.11, S_0^0 and C_1^0 indicate the sum and carry output when incoming carry is '0'. Similarly, S_0^1 and C_1^1 indicate the sum and carry output when incoming carry is '1'. As demonstrated in Fig. 6.11, the carry selection takes place at the adder interface. Based on the C_0 value, $S_0(C_1)$ is selected from the previously computed S_0^0 and S_0^1 (C_1^0 and C_1^1).

Table 6.3 Comparison of 16-bits adder implementation using different CIM schemes.

16-bits Adder	Latency	# of RRAM	Power	# Logical Operations
DCIM (This paper)	2 cycles+carry selection delay =2nS	2*64*48	48mW	64 AND2 32 OR3 32 OR2
SCIM	2nS	64*48	64mW	Same as above
MAGIC	12N+1 (Cycles)=4246ns	177	579mW	193 NOR

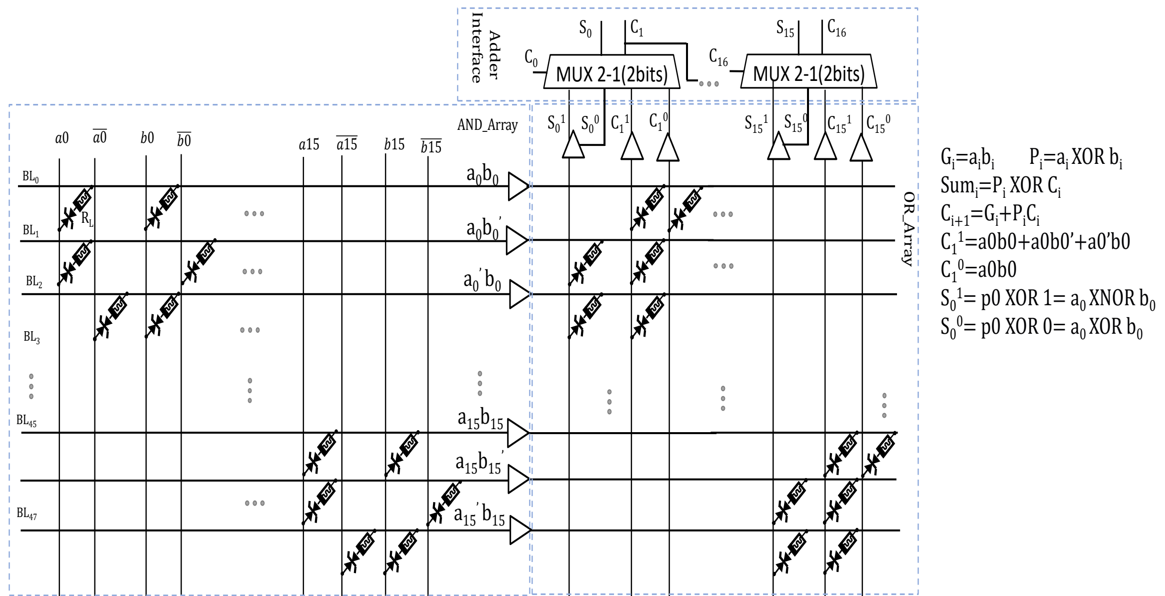

Figure 6.11 Implementation of 16-bit carry select adder using DCIM scheme. For sake of brevity only low resistance connections are shown.

Next, C_1 is propagated to the input select of next multiplexer to determine the value of S_1 and C_2 and so forth. This technique is of great interest since it enables implementing adder in two-level format (in form of SOP) without need of carry propagation. However, it requires multiplexers to perform output selection, which can be done using CMOS MUX in the peripheral. Pass gates are used to implement the MUXs in order to minimize the CMOS area overhead. Larger adders can be implemented by propagating output carry (C_{16}) to the input carry of other arrays that implements another set of 16-bit adder. Table III depicts latency and power of 16-bit adder implemented in three CIM techniques. The SCIM latency and power are obtained from simulation. Since SCIM cannot accommodate more than 8 inputs, we employ two CIM arrays to implement 16-bit adder where the output carry of first CIM array is provided as input to input carry of the second array. Therefore, 16-bit addition latency is identical for both static and dynamic CIM. The MAGIC latency and power are estimated from Table 6.3 in [137] by employing the RRAM model that we used in this work. Even though DCIM requires a greater number of cells (since larger array result

in more unused bitcells) to implement 16-bit adder, it achieves 12X power saving in 16-bit addition and achieves significantly lower latency compared to MAGIC.

6.5. Evaluation and Comparison of different Computing in memory techniques

In this section we compare the proposed DCIM with SCIM and MAGIC in terms of power and latency.

6.5.1. Power

In order to perform comparison, two-level benchmarks of MCNC benchmark suite [142] are used. A script is written in order to extract number of AND/OR gates and their fan-in for each SOP function. Unlike CMOS gates, where power is only consumed during '0' → '1' transition, the power is consumed during both '0' → '1' and '1'→'0' transitions in the CIM techniques. Initially, we assume the probability of each input being '1' as 0.5. In order to obtain power dissipation, the probability of logical AND/OR when output is '0'/'1' is calculated at each stage. Thus, the power consumption of each gate can be expressed as follows:

$$Pr_{AND1}(N) = 1/2^N \tag{6.2}$$

$$Pr_{OR0}(N) = Pr_0(in_1) * Pr_0(in_2) * \ldots * Pr_0(in_N) \tag{6.3}$$

$$P_{AND}(N) = Pr_{AND1}(N) * P_{AND1}(N) + (1 - Pr_1(N)) * P_{AND0}(N) \tag{6.4}$$

$$P_{OR}(N) = Pr_{OR0}(N) * P_{OR0}(N) + Pr_1(N) * P_{OR1}(N) \tag{6.5}$$

Where $P_{OR0}(N)$ and $Pr_{OR0}(N)$ are the power and probability of N-input logical OR gate when the output is '0'. Fig. 6.12(a) shows the power comparison of DCIM with respect to other techniques. Dynamic CIM provides 12.6X and 2.6X power saving compared to static CIM and MAGIC respectively.

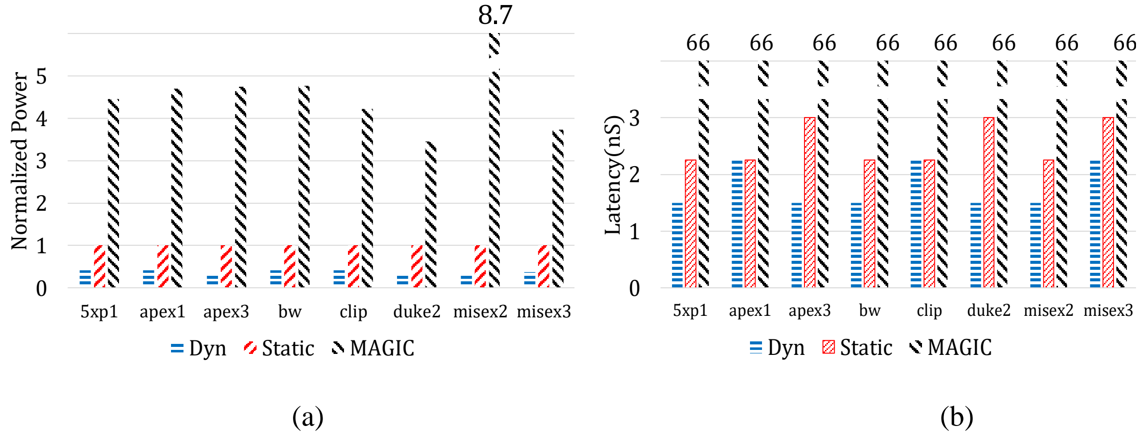

Figure 6.12 (a) Power, and (b) latency comparison of various CIM schemes.

6.5.2. Latency

The latency of logical AND/OR operation for static and dynamic CIM is 0.75nS. Since DCIM support up to 32 input AND/OR gates, the gates with fan-in of more than 32 must be partitioned into lower fain-in gates which is associated with latency and power overhead. For example, a 64-input OR gate is implemented using eight 8-input OR gates. As a result, all outputs of 8-input OR gates must be ORed using another OR array. Hence, increasing the latency by another 0.75nS. The latency results for several benchmarks are shown in Fig. 6.12(b). DCIM achieves 1.42X improvement in latency compared to SCIM since it offers higher fan-in gate implementation. In the SCIM method, the gates with more than 8 inputs must be partitioned into lower fan-in gates. Since many functions in two-level (SOP) form are implemented using high fan-in gates, the SCIM latency is typically one or two sensing cycle longer than DCIM.

In order to obtain the MAGIC power and latency, we implemented each benchmark in two-level NOR-NOR format. In addition, fain-in and number of NOR gates to implement each function is obtained. In order to achieve consistent result, the RRAM model [138] is used where latency of writing ‘0’/‘1’ into RRAM is 22nS (Table 6.1). MAGIC NOR operation associated with two write

operations is described in Section 6.3.1. Since MAGIC does not suffer from limited sense margin, it can implement high fan-in NOR gates. We assume that the array is large enough to accommodate all high fan-in NOR gates required for implementing two-level benchmarks. Therefore, 22nS is needed to program inputs into RRAM array, 22ns to is required to perform first-level NOR operation by writing into output RRAM, and 22nS is required to NOR the first-level NOR outputs to achieve the SOP output. Hence, the total latency of MAGIC scheme is 66nS.

6.6. Summary

In this chapter, we proposed dynamic computing in memory paradigm to overcome sense margin limitation associated with static CIM method in realizing higher fan-in AND/OR gates using RRAM crossbar array. In addition, this technique decreases power consumption significantly by eliminating the static current flow for performing logical operation compared to static CIM and, eliminates the need of writing into the bitcell to perform logical operations compared to MAGIC [137]. DCIM improves read yield of logical operations ~4X compared to SCIM. Simulation results show 1.42X and 20X latency improvement as well as 2.6X and 12.6X power saving compared to static [136] and MAGIC [137] computing in memory methods over a wide range of MCNC benchmarks.

Chapter 7

Future Work

7.1. Improving write performance of Spintronic Memories

In this thesis, we proposed a novel and adaptive write current boosting for STTRAM and write and shift current boosting for DWM to mitigate the process variation induced write and read latency degradation. In this technique, the bits experiencing worst-case write latency are fixed through write current/shift current boosting.

7.1.1. Considerations for inter-die process variations

In this work, simulations are carried out at typical corner. The proposed methodology is equally applicable for dies at other process corners. Our circuit simulation indicates that write latency show similar spread in fast and slow corners. The boost transistors can be designed taking

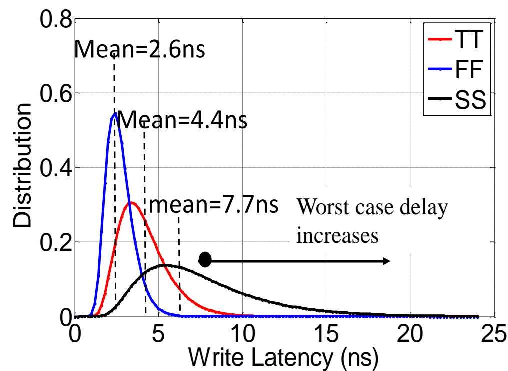

Figure 7.1 Write latency distribution at FF, TT and SS corners. The delay spreads out at SS affecting the performance significantly.

inter- and intra-die process variations into account (Fig. 7.1). Therefore, the boost circuit should be able to provide the current needed for all process corners.

7.1.2. Static vs. dynamic boosting

The proposed adaptive shift current and write current boosting implements static boosting. In order to reduce the impact of process variation on write and shift latency the entire global column is boosted even if only a single head/bitcell in a single local column is slow. This implementation is simple, but it wastes power for fast heads. It is possible to implement dynamic current boosting. The basic idea is to sense the change in the current after switching from p→AP or vice versa. This can be done by employing a circuit to detect the MTJ switching. Let us assume, writing AP is intended. The initial state of MTJ is either P or AP. If its initial state is AP, then the MTJ will not switch. The current difference can be sensed by comparing the MTJ current against a reference current, generated by a reference MTJ in P state using a current subtractor/sense circuit to initiate a write termination signal. However, if MTJ is in P state initially, the current difference between MTJ and reference MTJ in P state is not sufficient to trigger write termination signal. After the MTJ switching, the current difference can be sensed using a current subtractor to trigger the write termination (WT) signal which can be used to disable write enable signal (WE). In such a way, the

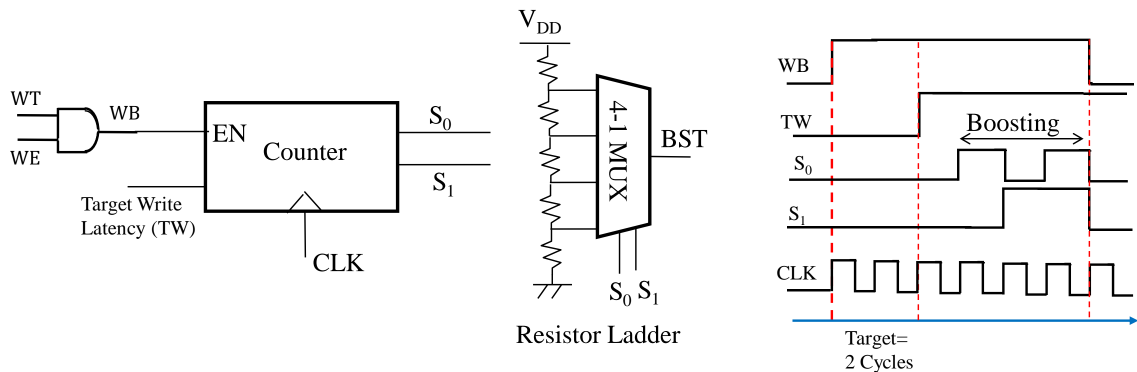

Figure 7.2 Dynamic current boosting circuit. The timing diagram is also shown.

power is saved by terminating the write operation once switching takes place. However, this technique does not improve the write latency of bitcells experiencing worst-case latency. In order to improve the write latency, we can employ a dynamic write current boosting technique as shown in Fig. 7.2. In this technique, an analog boost (BST) signal can be triggered in a step wise fashion, if the write operation takes longer than a target write latency (the mean write latency). This can be achieved by utilizing a counter which receives WE, WT and target write latency signals. This counter starts incrementing after target write time. The counter output can be used as a selector signal for a resistor ladder to generate a boost signal. The boost signal can modulate the gate voltage of PMOS transistor in the write driver (Fig. 3.37) to boost the write current in step wise fashion.

7.2. Security

We have observed that process variation and stochastic switching results in large spread in write latency of STTRAM. This feature can be employed to implement Physically Unclonable Function (PUF) and True Random Number Generator (TRNG).

7.3. Computing in Memory

We proposed a dynamic computing in memory system using RRAM crossbar array and implemented a 16-bit carry select adder. However, this technique can be employed to implement more complex functions such as floating-point adder, multiplier and divider which can opens-up a lot of research opportunity in computing in memory system design. In addition, we have only evaluated the proposed design at circuit level. For future research, we will focus on evaluating this technique at architecture level where we will evaluate the proposed design using GEM5 simulator in terms of energy consumption and performance. In this method, we will implement in-memory

instruction such as *in-memory-addition, in-memory-AND,* and *in-memory-multiplication* to off-load some of processor operations to main memory.

Chapter

Summary

In this chapter we summarize the contributions of this thesis.

The increasing demand for high performance computing (HPC) and integration of multiple cores on a single die have widened the speed gap between logic and memory called the "memory-wall". Process variability and standby power are posing severe obstruction towards SRAM/DRAM scaling to future nodes. Therefore, other emerging memory technologies are investigated to replace CMOS based memories.

STTRAM is a promising non-volatile memory technology for cache application due to high-density, low standby power, excellent retention, fast access time and good endurance. However, it can suffer from poor sense margin, data security issues, and severe performance and power degradation due to process variation induced write and read latency variations.

In this thesis, we proposed two flavors of sensing techniques to improve read yield of STTRAM arrays:

1) To eliminate reference resistance variation, we propose a reference-less, destructive slope detection technique which exploits the MTJ switching from high to low state to detect memory state. We design a proof-of-concept test-chip using 96kb mimicked STTRAM (using passive resistors) bits in 65nm technology to validate the proposed slope sensing circuit. The resistor values are matched with the experimentally calibrated simulated models to capture the process variations in real MTJ.
2) We propose a non-destructive and low-power sensing scheme that exploits a voltage feedback and boosting (VFAB) technique to develop large sense margin. Furthermore,

VFAB sensing does not require a static current to be injected into data and reference STTRAMs which results in significant power saving.

Process variation results in large spread in STTRAM write latency variation. The performance of conventionally designed STTRAM cache can degrade as much as 10% due to process variations. In this work, we model the tail of write lateny for correct estimation of number of failing bits. We also find that write latency can be lowered by boosting the write current. We propose circuit level techniques to implement adaptive write boosting and exploit them at micro-architecture level to mitigate process variation induced performance and power degradation.

STTRAM brings new data security issues that were absent in volatile memory counterparts such as SRAM. This is primarily due to the fundamental dependency of this memory technology on ambient parameters such as magnetic field that can be exploited to tamper with the stored data. The free layer of MTJ flips under the influence of external magnetic field and temperature that can be exploited by the adversary. The magnetic field produced by a horseshoe magnet can be used to flip the bits in a STTRAM memory array. Therefore, magnetic field can be exploited by the adversary to scramble the data in LLC to launch denial of service (DoS) attack or simply increase the miss-rate affecting the overall performance of the system. We investigate data security of STTRAM last level cache under magnetic attack. The magnetic attack could be gradually ramping and/or sudden in nature. We propose three techniques to avoid errors in presence of magnetic attack, (a) stalling where the system is halted during attack; (b) cache bypass during gradually ramping attack where the last level cache (LLC) is bypassed and the upper level caches interact directly with the main memory; and, (c) checkpointing along with bypass during sudden attack where the processor states are saved periodically and the LLC is written back at regular intervals. During attack, the system goes back to the last checkpoint and the computation continues with bypassed cache.

In addition to challenges involved with STTRAM, DWM suffers from shift latency and shift power overhead, aspect ratio mismatch and segregated read and write heads. We propose circuit and architectural techniques to overcome DWM design challenges. We propose layout techniques such as sharing of diffusion, bitlines and shift lines to improve bitcell density. Circuit techniques such as merged read-write head to improve bitcell density, and shift gating to reduce shift power are proposed. Micro-architecture techniques such as cache segregation using a novel replacement policy as well as dynamic current boosting based on workload are proposed to mitigate shift power and shift latency. Finally, adaptive write and shift current boosting is proposed to mitigate process variation induced performance and power degradation.

The speed gap between the processor and memory, impedes the continuous performance improvement of traditional von Neumann architecture. To address this challenge, extensive amount of research is performed to explore alternative non-von Neumann architectures based on the concept of computing in memory. Recent experimental studies have revealed that RRAM is promising alternative to implement main memory due to small footprint and zero stand by power. Therefore, realizing logic operations within RRAM crossbar arrays is a promising approach to implement computing in memory systems. However, RRAM crossbar array suffers from sneak-path problem which results in poor sense margin, higher power consumption, and limited array size. We propose a low-power dynamic computing in memory system which can implement various functions in Sum of Product (SOP) form in RRAM crossbar array architecture. The proposed technique benefits from nonlinear characteristic of selector diode to improve sense margin in order to implement higher fan-in logic gates. In addition, this technique decreases power consumption significantly by eliminating the static current flow for performing logical operation compared to static CIM and, eliminates the need of writing into the bitcell to perform logical operations compared to MAGIC.

Appendix

Publications

Referred Conferences

- **Motaman, Seyedhamidreza**, Anirudh Iyengar, and Swaroop Ghosh. "Synergistic circuit and system design for energy-efficient and robust domain wall caches." In *Proceedings of the 2014 international symposium on Low power electronics and design*, pp. 195-200. ACM, 2014.
- **Motaman, Seyedhamidreza**, and Swaroop Ghosh. "Simultaneous sizing, reference voltage and clamp voltage biasing for robustness, self-calibration and testability of STTRAM arrays." In *Proceedings of the 51st Annual Design Automation Conference*, pp. 1-2. ACM, 2014.
- **Motaman, Seyedhamidreza**, Swaroop Ghosh, and Nitin Rathi. "Impact of process-variations in STTRAM and adaptive boosting for robustness." In *Proceedings of the 2015 Design, Automation & Test in Europe Conference & Exhibition*, pp. 1431-1436. EDA Consortium, 2015.
- **Motaman, Seyedhamidreza**, Swaroop Ghosh, and Jaydeep P. Kulkarni. "A novel slope detection technique for robust STTRAM sensing." In Low Power Electronics and Design (ISLPED), 2015 IEEE/ACM International Symposium on, pp. 7-12. IEEE, 2015.
- **Motaman, Seyedhamidreza**, Mohammad Nasim Imtiaz Khan, and Swaroop Ghosh. "Novel application of spintronics in computing, sensing, storage and cybersecurity." In Design, Automation & Test in Europe Conference & Exhibition (DATE), 2018, pp. 125-130. IEEE, 2018.

- **Motaman, Seyedhamidreza** and Swaroop Ghosh, " Dynamic Computing in Memory (DCIM) in Resistive Crossbar Arrays" ICCD, 2018

Referred Journals

- **Motaman, Seyedhamidreza**, Anirudh Srikant Iyengar, and Swaroop Ghosh. "Domain Wall Memory-Layout, Circuit and Synergistic Systems." *Nanotechnology, IEEE Transactions on* 14, no. 2 (2015): 282-291.
- **Motaman, Seyedhamidreza**, and Swaroop Ghosh. "Adaptive write and shift current modulation for process variation tolerance in domain wall caches." IEEE Transactions on Very Large Scale Integration (VLSI) Systems 24.3 (2016): 944-953.
- Ghosh, Swaroop, Anirudh Iyengar, **Seyedhamidreza Motaman**, Rekha Govindaraj, Jae-Won Jang, Jinil Chung, Jongsun Park, Xin Li, Rajiv Joshi, and Dinesh Somasekhar. "Overview of circuits, systems, and applications of spintronics." IEEE Journal on Emerging and Selected Topics in Circuits and Systems 6, no. 3 (2016): 265-278.
- **Motaman, Seyedhamidreza**, Swaroop Ghosh, and Nitin Rathi. "Cache Bypassing and Checkpointing to Circumvent Data Security Attacks on STTRAM." IEEE Transactions on Emerging Topics in Computing (2017).
- **Motaman, Seyedhamidreza**, Swaroop Ghosh, and Jaydeep P. Kulkarni. "VFAB: A Novel 2-Stage STTRAM Sensing Using Voltage Feedback and Boosting." IEEE Transactions on Circuits and Systems I: Regular Papers 65, no. 6 (2018): 1919-1928.
- **Motaman, Seyedhamidreza**, Swaroop Ghosh, and Jaydeep Kulkarni. "Impact of Process Variation on Self-Reference Sensing Scheme and Adaptive Current Modulation for Robust STTRAM Sensing." ACM Journal on Emerging Technologies in Computing Systems (JETC) 14, no. 1 (2018): 8.

Under review:

- **Motaman, Seyedhamidreza**, Swaroop Ghosh, " A 96kb, 32nS Random Access 1T1R Array at 1.2V in 65nm with Reference-less Slope Sensing Technique." IEEE Journal of solid-state circuits, 2018

Referred Patents

- Ghosh, Swaroop, and **Seyedhamidreza Motaman**. "Robust slope detection technique for STTRAM and MRAM sensing." U.S. Patent 9,818,466, issued November 14, 2017.

Bibliography

[1] Daly, Denis C., Laura C. Fujino, and Kenneth C. Smith. "Through the Looking Glass-The 2018 Edition: Trends in Solid-State Circuits from the 65th ISSCC." *IEEE Solid-State Circuits Magazine* 10, no. 1 (2018): 30-46.

[2] S. Borkar and A. A. Chien, “The future of microprocessors,” Communications of the ACM, vol. 54, no. 5, p. 67, May 2011.

[3] M. Mitchell Waldrop. Nature news feature. http://www.nature.com/news/ the chips are down [for moore’s law. Accessed: 2018-9-01.

[4] Hosomi, M., H. Yamagishi, T. Yamamoto, K. Bessho, Y. Higo, K. Yamane, H. Yamada et al. "A novel nonvolatile memory with spin torque transfer magnetization switching: Spin-RAM." In *Electron Devices Meeting, 2005. IEDM Technical Digest. IEEE International*, pp. 459-462. IEEE, 2005.

[5] Parkin, Stuart SP, Masamitsu Hayashi, and Luc Thomas. "Magnetic domain-wall racetrack memory." Science 320, no. 5873 (2008): 190-194.

[6] Harshfield, Steven T., and David Q. Wright. "PCRAM memory cell and method of making same." U.S. Patent 7,102,150, issued September 5, 2006.

[7] Burr, Geoffrey W., Matthew J. Breitwisch, Michele Franceschini, Davide Garetto, Kailash Gopalakrishnan, Bryan Jackson, Bülent Kurdi et al. "Phase change memory technology." Journal of Vacuum Science & Technology B, Nanotechnology and Microelectronics: Materials, Processing, Measurement, and Phenomena 28, no. 2 (2010): 223-262.

[8] Choi, Ja Moon. "Ferroelectric RAM device." U.S. Patent 6,044,008, issued March 28, 2000.

[9] Govoreanu, B., G. S. Kar, Y. Y. Chen, V. Paraschiv, S. Kubicek, A. Fantini, I. P. Radu et al. "10× 10nm 2 Hf/HfO x crossbar resistive RAM with excellent performance, reliability and

low-energy operation." In *Electron Devices Meeting (IEDM), 2011 IEEE International*, pp. 31-6. IEEE, 2011.

[10] Sousa, Ricardo C., and I. Lucian Prejbeanu. "Non-volatile magnetic random access memories (MRAM)." Comptes Rendus Physique 6, no. 9 (2005): 1013-1021.

[11] Sun, Guangyu, Jishen Zhao, Matt Poremba, Cong Xu, and Yuan Xie. "Memory that Never Forgets: Emerging Non-volatile Memory and the Implication for Architecture Design." National Science Review (2017).

[12] Nomura, Kumiko, Keiko Abe, Hiroaki Yoda, and Shinobu Fujita. "Ultra low power processor using perpendicular-STT-MRAM/SRAM based hybrid cache toward next generation normally-off computers." Journal of Applied Physics 111, no. 7 (2012): 07E330.

[13] Everspin throws first ST-MRAM chips down, launches commercial spin-torque memory era, https://www.engadget.com/2012/11/14/everspin-throws-first-st-mram-chips-down/, 2012.

[14] Ni, Leibin, et al. "An energy-efficient matrix multiplication accelerator by distributed in-memory computing on binary RRAM crossbar." Design Automation Conference (ASP-DAC), 2016 21st Asia and South Pacific. IEEE, 2016.

[15] G. W. Burr, et al. "Experimental demonstration and tolerancing of a large-scale neural network (165 000 synapses) using phase-change memory as the synaptic weight element." TED, 2015.

[16] S. Yu, et al. "A neuromorphic visual system using RRAM synaptic devices with Sub-pJ energy and tolerance to variability: Experimental characterization and large-scale modeling." IEDM, 2012.

[17] B. Li, Y. Shan, et al. Memristor-based approximated computation. In ISLPED, pages 242{247, Sept 2013.

[18] W. Zhao, et al. "Synchronous non-volatile logic gate design based on resistive switching memories." TCAS I: 2014.

[19] A. Sengupta, et al. "Spin-transfer torque magnetic neuron for low power neuromorphic computing." Neural Networks (IJCNN), 2015 International Joint Conference on. IEEE, 2015.

[20] M. Sharad, et al. "Boolean and non-Boolean computation with spin devices." IEDM, 2012.

[21] M. Sharad, et al. "Spin-neurons: A possible path to energy-efficient neuromorphic computers." JAP, 2013.

[22] A. F. Vincent, et al. "Spin-transfer torque magnetic memory as a stochastic memristive synapse for neuromorphic systems." IEEE transactions on biomedical circuits and systems, (2015).

[23] S. Lequeux, et al. "A magnetic synapse: multilevel spin-torque memristor with perpendicular anisotropy." Scientific reports 6, 2016.

[24] M. Sharad, et al. "Spin-based neuron model with domain-wall magnets as synapse." IEEE TNano, 2012.

[25] Sun, Guangyu, Jishen Zhao, Matt Poremba, Cong Xu, and Yuan Xie. "Memory that never forgets: emerging nonvolatile memory and the implication for architecture design." National Science Review (2017).

[26] Meena, Jagan Singh, Simon Min Sze, Umesh Chand, and Tseung-Yuen Tseng. "Overview of emerging nonvolatile memory technologies." Nanoscale research letters 9, no. 1 (2014): 526.

[27] Zhang, Jianwei, et al. "Identification of transverse spin currents in noncollinear magnetic structures." Physical review letters, 2004.

[28] LALE Landau and Evgeny Lifshitz. On the theory of the dispersion of magnetic permeability in ferromagnetic bodies. Phys. Z. Sowjetunion, 8(153):101–114, 1935.

[29] M. Julliere, “Tunneling between ferromagnetic films,” Physics letters A, vol. 54, no. 3, pp. 225–226, 1975.

[30] Zhang, Yue, Weisheng Zhao, Guillaume Prenat, Thibaut Devolder, Jacques-Olivier Klein, Claude Chappert, Bernard Dieny, and Dafiné Ravelosona. "Electrical modeling of stochastic

spin transfer torque writing in magnetic tunnel junctions for memory and logic applications." IEEE Transactions on Magnetics 49, no. 7 (2013): 4375-4378.

[31] Zaleski, A., J. Wrona, M. Czapkiewicz, W. Skowroński, J. Kanak, and T. Stobiecki. "The study of conductance in magnetic tunnel junctions with a thin MgO barrier: The effect of Ar pressure on tunnel magnetoresistance and resistance area product." Journal of Applied Physics 111, no. 3 (2012): 033903.

[32] Yoshida, Chikako, and Toshihiro Sugii. "Reliability study of magnetic tunnel junction with naturally oxidized MgO barrier." In Reliability Physics Symposium (IRPS), 2012 IEEE International, pp. 2A-3. IEEE, 2012.

[33] Yoshida, Chikako, Masaki Kurasawa, Young Min Lee, Koji Tsunoda, Masaki Aoki, and Yoshihiro Sugiyama. "A study of dielectric breakdown mechanism in CoFeB/MgO/CoFeB magnetic tunnel junction." In Reliability Physics Symposium, 2009 IEEE International, pp. 139-142. IEEE, 2009.

[34] Koch, R. H., J. A. Katine, and J. Z. Sun. "Time-resolved reversal of spin-transfer switching in a nanomagnet." Physical review letters 92, no. 8 (2004): 088302.

[35] Apalkov, Dmytro, Alexey Khvalkovskiy, Steven Watts, Vladimir Nikitin, Xueti Tang, Daniel Lottis, Kiseok Moon et al. "Spin-transfer torque magnetic random access memory (STT-MRAM)." ACM Journal on Emerging Technologies in Computing Systems (JETC) 9, no. 2 (2013): 13.

[36] Apalkov, Dmytro, Alexey Khvalkovskiy, Steven Watts, Vladimir Nikitin, Xueti Tang, Daniel Lottis, Kiseok Moon et al. "Spin-transfer torque magnetic random access memory (STT-MRAM)." ACM Journal on Emerging Technologies in Computing Systems (JETC) 9, no. 2 (2013): 13.

[37] Xuanyao Fong; Sri Harsha Choday; Panagopoulos Georgios; Charles Augustine; Kaushik Roy (2013), "SPICE Models for Magnetic Tunnel Junctions Based on Monodomain Approximation," https://nanohub.org/resources/19048.

[38] Diao, Zhitao, et al. "Spin-transfer torque switching in magnetic tunnel junctions and spin-transfer torque random access memory." Journal of Physics: Condensed Matter 19.16 (2007): 165209.

[39] Raychowdhury, Arijit, et al. "Design space and scalability exploration of 1T-1STT STTRAM memory arrays in the presence of variability and disturbances." IEEE International Electron Devices Meeting (IEDM). 2009.

[40] Jang, Jae-Won, Jongsun Park, Swaroop Ghosh, and Swarup Bhunia. "Self-correcting STTRAM under magnetic field attacks." In Proceedings of the 52nd Annual Design Automation Conference, p. 77. ACM, 2015.

[41] M. Hayashi, "Current driven dynamics of magnetic domain walls in permalloy nanowires." PhD diss., Stanford University, 2006.

[42] Yu, Shimeng, and H-S. Philip Wong. "A phenomenological model for the reset mechanism of metal oxide RRAM." IEEE Electron Device Letters 31, no. 12 (2010): 1455-1457.

[43] Fujimoto, Masayuki, Hiroshi Koyama, Masashi Konagai, Yasunari Hosoi, Kazuya Ishihara, Shigeo Ohnishi, and Nobuyoshi Awaya. "Ti O 2 anatase nanolayer on TiN thin film exhibiting high-speed bipolar resistive switching." Applied physics letters 89, no. 22 (2006): 223509.

[44] Lee, H. Y., P. S. Chen, T. Y. Wu, Y. S. Chen, C. C. Wang, P. J. Tzeng, C. H. Lin, F. Chen, C. H. Lien, and M-J. Tsai. "Low power and high speed bipolar switching with a thin reactive Ti buffer layer in robust HfO2 based RRAM." In Electron Devices Meeting, 2008. IEDM 2008. IEEE International, pp. 1-4. IEEE, 2008.

[45] Lee, H. Y., P. S. Chen, T. Y. Wu, Y. S. Chen, C. C. Wang, P. J. Tzeng, C. H. Lin, F. Chen, C. H. Lien, and M-J. Tsai. "Low power and high speed bipolar switching with a thin reactive Ti buffer layer in robust HfO2 based RRAM." In Electron Devices Meeting, 2008. IEDM 2008. IEEE International, pp. 1-4. IEEE, 2008.

[46] Yu, Shimeng, Ximeng Guan, and H-S. Philip Wong. "On the stochastic nature of resistive switching in metal oxide RRAM: Physical modeling, Monte Carlo simulation, and experimental characterization." In Electron Devices Meeting (IEDM), 2011 IEEE International, pp. 17-3. IEEE, 2011.

[47] Liang, Jiale, and H-S. Philip Wong. "Cross-point memory array without cell selectors—Device characteristics and data storage pattern dependencies." IEEE Transactions on Electron Devices 57.10 (2010): 2531-2538.

[48] Xu, Wei, et al. "Design of last-level on-chip cache using spin-torque transfer RAM (STT RAM)." IEEE Transactions on Very Large Scale Integration (VLSI) Systems 19.3 (2011): 483-493.

[49] Dong, Xiangyu, Xiaoxia Wu, Guangyu Sun, Yuan Xie, Helen Li, and Yiran Chen. "Circuit and microarchitecture evaluation of 3D stacking magnetic RAM (MRAM) as a universal memory replacement." In Design Automation Conference, 2008. DAC 2008. 45th ACM/IEEE, pp. 554-559. IEEE, 2008.

[50] Desikan, Rajagopalan, Charles R. Lefurgy, Stephen W. Keckler, and Doug Burger. "On-chip MRAM as a high-bandwidth, low-latency replacement for DRAM physical memories." (2002).

[51] Sun, Guangyu, Xiangyu Dong, Yuan Xie, Jian Li, and Yiran Chen. "A novel architecture of the 3D stacked MRAM L2 cache for CMPs." In High Performance Computer Architecture, 2009. HPCA 2009. IEEE 15th International Symposium on, pp. 239-249. IEEE, 2009.

[52] Smullen, Clinton W., Vidyabhushan Mohan, Anurag Nigam, Sudhanva Gurumurthi, and Mircea R. Stan. "Relaxing non-volatility for fast and energy-efficient STT-RAM caches." In High Performance Computer Architecture (HPCA), 2011 IEEE 17th International Symposium on, pp. 50-61. IEEE, 2011.

[53] Xu, Wei, Hongbin Sun, Xiaobin Wang, Yiran Chen, and Tong Zhang. "Design of last-level on-chip cache using spin-torque transfer RAM (STT RAM)." IEEE Transactions on Very Large Scale Integration (VLSI) Systems 19, no. 3 (2011): 483-493.

[54] Jog, Adwait, Asit K. Mishra, Cong Xu, Yuan Xie, Vijaykrishnan Narayanan, Ravishankar Iyer, and Chita R. Das. "Cache revive: architecting volatile STT-RAM caches for enhanced performance in CMPs." In Proceedings of the 49th Annual Design Automation Conference, pp. 243-252. ACM, 2012.

[55] Z. Sun, X. Bi, H. Li, W.-F. Wong, Z.-L. Ong, X. Zhu, and W. Wu. "Multi retention level STT-RAM cache designs with a dynamic refresh scheme." In Proceedings of the 44th Annual IEEE/ACM International Symposium on Microarchitecture, pp. 329-338. ACM, 2011.

[56] K. Swaminathan, R. Pisolkar, C. Xu, and V. Narayanan. "When to forget: A system-level perspective on STT-RAMs." In Design Automation Conference (ASP-DAC), 2012 17th Asia and South Pacific, pp. 311-316. IEEE, 2012.

[57] C. Xu, D. Niu, X. Zhu, S. H. Kang, M. Nowak, and Y. Xie. "Device-architecture co-optimization of STT-RAM based memory for low power embedded systems." In Proceedings of the International Conference on Computer-Aided Design, pp. 463-470. IEEE Press, 2010.

[58] Rasquinha, Mitchelle, Dhruv Choudhary, Subho Chatterjee, Saibal Mukhopadhyay, and Sudhakar Yalamanchili. "An energy efficient cache design using spin torque transfer (STT) RAM." In Proceedings of the 16th ACM/IEEE international symposium on Low power electronics and design, pp. 389-394. ACM, 2010.

[59] Song, Jee-Hwan, Jisu Kim, Seung H. Kang, Sei-Seung Yoon, and Seong-Ook Jung. "Sensing margin trend with technology scaling in MRAM." International Journal of Circuit Theory and Applications 39, no. 3 (2011): 313-325.

[60] Jung, Seong-Ook, Jisu Kim, Jee-Hwan Song, Seung H. Kang, Sei Seung Yoon, and Mehdi Hamidi Sani. "Balancing a signal margin of a resistance based memory circuit." U.S. Patent 7,889,585, issued February 15, 2011.

[61] Kim, Jisu, Kyungho Ryu, Jung Pill Kim, Seung H. Kang, and Seong-Ook Jung. "STT-MRAM sensing circuit with self-body biasing in deep submicron technologies." IEEE Transactions on Very Large Scale Integration (VLSI) Systems 22, no. 7 (2014): 1630-1634.

[62] Halupka, David, Safeen Huda, William Song, Ali Sheikholeslami, Koji Tsunoda, Chikako Yoshida, and Masaki Aoki. "Negative-resistance read and write schemes for STT-MRAM in 0.13 μm CMOS." In Solid-State Circuits Conference Digest of Technical Papers (ISSCC), 2010 IEEE International, pp. 256-257. IEEE, 2010.

[63] Ren, Fengbo, Henry Park, Richard Dorrance, Yuta Toriyama, C-K. Ken Yang, and Dejan Marković. "A body-voltage-sensing-based short pulse reading circuit for spin-torque transfer RAMs (STT-RAMs)." In Quality Electronic Design (ISQED), 2012 13th International Symposium on, pp. 275-282. IEEE, 2012.

[64] Au, Edward KS, Wing-Hung Ki, Wai Ho Mow, Silas T. Hung, and Catherine Y. Wong. "A novel current-mode sensing scheme for magnetic tunnel junction MRAM." IEEE transactions on magnetics 40, no. 2 (2004): 483-488.

[65] Sun, Zhenyu, Hai Li, Yiran Chen, and Xiaobin Wang. "Voltage driven nondestructive self-reference sensing scheme of spin-transfer torque memory." IEEE Transactions on Very Large Scale Integration (VLSI) Systems 20, no. 11 (2012): 2020-2030.

[66] Chen, Yiran, Hai Li, Xiaobin Wang, Wenzhong Zhu, Wei Xu, and Tong Zhang. "A 130 nm 1.2 V/3.3 V 16 Kb spin-transfer torque random access memory with nondestructive self-reference sensing scheme." IEEE Journal of Solid-State Circuits 47, no. 2 (2012): 560-573.

[67] Jeong, Gitae, Wooyoung Cho, Sujin Ahn, Hongsik Jeong, Gwanhyeob Koh, Youngnam Hwang, and Kinam Kim. "A 0.24-mum 2.0-V 1T1MTJ 16-kb Nonvolatile Magnetoresistance RAM With Self-Reference Sensing Scheme." IEEE Journal of solid-state circuits 38, no. 11 (2003): 1906-1910.

[68] Pelgrom, Marcel JM, Aad CJ Duinmaijer, and Anton PG Welbers. "Matching properties of MOS transistors." IEEE Journal of solid-state circuits 24, no. 5 (1989): 1433-1439.

[69] Lee, Dongsoo, and Kaushik Roy. "Energy-delay optimization of the STT MRAM write operation under process variations." IEEE Transactions on Nanotechnology 13, no. 4 (2014): 714-723.

[70] Li, Jing, Haixin Liu, Sayeef Salahuddin, and Kaushik Roy. "Variation-tolerant Spin-Torque Transfer (STT) MRAM array for yield enhancement." In Custom Integrated Circuits Conference, 2008. CICC 2008. IEEE, pp. 193-196. IEEE, 2008.

[71] T. Andre, "Embedded MRAM: Technology and applications," in Proc. Embed. Memory Design for Nano-Scale VLSI Syst. Forum With IEEE Int. Solid-State Circuits Conf., 2008.

[72] Kim, Jisu, Taehui Na, Jung Pill Kim, Seung H. Kang, and Seong-Ook Jung. "A split-path sensing circuit for spin torque transfer MRAM." IEEE Transactions on Circuits and Systems II: Express Briefs 61, no. 3 (2014): 193-197.

[73] Nho, Hyunwoo, Sei-Seung Yoon, S. Simon Wong, and Seong-Ook Jung. "Numerical estimation of yield in sub-100-nm SRAM design using Monte Carlo simulation." IEEE Transactions on Circuits and Systems II: Express Briefs 55, no. 9 (2008): 907-911.

[74] Sun, Hongbin, Chuanyin Liu, Nanning Zheng, Tai Min, and Tong Zhang. "Design techniques to improve the device write margin for MRAM-based cache memory." In

Proceedings of the 21st edition of the great lakes symposium on Great lakes symposium on VLSI, pp. 97-102. ACM, 2011.

[75] Bi, Xiuyuan, Zhenyu Sun, Hai Li, and Wenqing Wu. "Probabilistic design methodology to improve run-time stability and performance of STT-RAM caches." In Proceedings of the International Conference on Computer-Aided Design, pp. 88-94. ACM, 2012.

[76] J. Li, P. Ndai, A. Goel, S. Salahuddin, and K. Roy. "Design paradigm for robust spin-torque transfer magnetic RAM (STT MRAM) from circuit/architecture perspective." Very Large Scale Integration (VLSI) Systems, IEEE Transactions on 18, no. 12 (2010): 1710-1723.

[77] S. P. Park, S. Gupta, N. Mojumder, A. Raghunathan, and K. Roy. "Future cache design using STT MRAMs for improved energy efficiency: devices, circuits and architecture." In Proceedings of the 49th Annual Design Automation Conference, pp. 492-497. ACM, 2012.

[78] Y. Kim, S. K. Gupta, S. P. Park, G. Panagopoulos, and K. Roy. "Write-optimized reliable design of STT MRAM." In Proceedings of the 2012 ACM/IEEE international symposium on Low power electronics and design, pp. 3-8. ACM, 2012.

[79] D. Lee, S. K. Gupta, and K. Roy. "High-performance low-energy STT MRAM based on balanced write scheme." In Proceedings of the 2012 ACM/IEEE international symposium on Low power electronics and design, pp. 9-14. ACM, 2012.

[80] Mutyam, Madhu, Feng Wang, Ramakrishnan Krishnan, Vijaykrishnan Narayanan, Mahmut Kandemir, Yuan Xie, and Mary Jane Irwin. "Process-variation-aware adaptive cache architecture and management." IEEE Transactions on Computers 7 (2009): 865-877.

[81] Joo, Yongsoo, Dimin Niu, Xiangyu Dong, Guangyu Sun, Naehyuck Chang, and Yuan Xie. "Energy-and endurance-aware design of phase change memory caches." In Proceedings of the Conference on Design, Automation and Test in Europe, pp. 136-141. European Design and Automation Association, 2010.

[82] M.K. Qureshi, M. M. Franceschini, and L. A. Lastras-Montaño. "Improving read performance of phase change memories via write cancellation and write pausing." In High Performance Computer Architecture (HPCA), 2010 IEEE 16th International Symposium on, pp. 1-11. IEEE, 2010.

[83] M.K. Qureshi, M. M. Franceschini, A. Jagmohan, and L. A. Lastras. "PreSET: improving performance of phase change memories by exploiting asymmetry in write times." In Computer Architecture (ISCA), 2012 39th Annual International Symposium on, pp. 380-391. IEEE, 2012.

[84] M.K. Qureshi, M. M. Franceschini, L. A. Lastras-Montaño, and J. P. Karidis. "Morphable memory system: a robust architecture for exploiting multi-level phase change memories." In ACM SIGARCH Computer Architecture News, vol. 38, no. 3, pp. 153-162. ACM, 2010.

[85] Zhou, Ping, Bo Zhao, Jun Yang, and Youtao Zhang. "Energy reduction for STT-RAM using early write termination." In Computer-Aided Design-Digest of Technical Papers, 2009. ICCAD 2009. IEEE/ACM International Conference on, pp. 264-268. IEEE, 2009.

[86] Bushnell, Michael, and Vishwani D. Agrawal. Essentials of electronic testing for digital, memory, and mixed-signal VLSI circuits. Vol. 17. Springer, 2000.

[87] Gem5, http://www.gem5.org.

[88] Parsec, http://parsec.cs.princeton.edu/index.htm.

[89] McPAT, http://www.hpl.hp.com/research/mcpat

[90] CACTI. http://www.hpl.hp.com/research/cacti/.

[91] Kim, Jisu, Kyungho Ryu, Seung H. Kang, and Seong-Ook Jung. "A novel sensing circuit for deep submicron spin transfer torque MRAM (STT-MRAM)." IEEE Transactions on very large scale integration (VLSI) systems 20, no. 1 (2012): 181-186.

[92] Rathi, Nitin, Swaroop Ghosh, Anirudh Iyengar, and Helia Naeimi. "Data privacy in non-volatile cache: Challenges, attack models and solutions." In Design Automation Conference (ASP-DAC), 2016 21st Asia and South Pacific, pp. 348-353. IEEE, 2016.

[93] Bi, Xiuyuan, Hai Li, and Jae-Joon Kim. "Analysis and optimization of thermal effect on STT-RAM Based 3-D stacked cache design." In VLSI (ISVLSI), 2012 IEEE Computer Society Annual Symposium on, pp. 374-379. IEEE, 2012.

[94] Ding, Yunfei, and Zhanjie Li. "Magnetic shielding in magnetic multilayer structures." U.S. Patent 8,213,221, issued July 3, 2012.

[95] Gu, Shiqun, Rongtian Zhang, Vidhya Ramachandran, and Dong Wook Kim. "Small form factor magnetic shield for magnetorestrictive random access memory (MRAM)." U.S. Patent 8,952,504, issued February 10, 2015.

[96] Gupta, Saurabh, Hongliang Gao, and Huiyang Zhou. "Adaptive cache bypassing for inclusive last level caches." In Parallel & Distributed Processing (IPDPS), 2013 IEEE 27th International Symposium on, pp. 1243-1253. IEEE, 2013.

[97] Gao, Hongliang, and Chris Wilkerson. "A dueling segmented LRU replacement algorithm with adaptive bypassing." In JWAC 2010-1st JILP Worshop on Computer Architecture Competitions: cache replacement Championship. 2010.

[98] Atkins, Mark. "Performance and the i860 microprocessor." IEEE Micro 11, no. 5 (1991): 24-27.

[99] Wang, Jue, Xiangyu Dong, and Yuan Xie. "OAP: An obstruction-aware cache management policy for STT-RAM last-level caches." In Proceedings of the Conference on Design, Automation and Test in Europe, pp. 847-852. EDA Consortium, 2013.

[100] Huangfu, Yijie, and Wei Zhang. "Real-Time GPU Computing: Cache or No Cache?." In Real-Time Distributed Computing (ISORC), 2015 IEEE 18th International Symposium on, pp. 182-189. IEEE, 2015.

[101] Kothari, Love, and Nicholas P. Carter. "Architecture of a self-checkpointing microprocessor that incorporates nanomagnetic devices." IEEE Transactions on Computers 56, no. 2 (2007): 161-173.

[102] Shyam, Smitha, et al. "Ultra low-cost defect protection for microprocessor pipelines." In ACM Sigplan Notices, 2006.

[103] Martínez, José F., Jose Renau, Michael C. Huang, and Milos Prvulovic. "Cherry: Checkpointed early resource recycling in out-of-order microprocessors." In Microarchitecture, 2002.(MICRO-35). Proceedings. 35th Annual IEEE/ACM International Symposium on, pp. 3-14. IEEE, 2002.

[104] Schulz, Martin, Greg Bronevetsky, Rohit Fernandes, Daniel Marques, Keshav Pingali, and Paul Stodghill. "Implementation and evaluation of a scalable application-level checkpoint-recovery scheme for MPI programs." In Proceedings of the 2004 ACM/IEEE conference on Supercomputing, p. 38. IEEE Computer Society, 2004.

[105] Bronevetsky, Greg, Daniel Marques, Keshav Pingali, and Paul Stodghill. "Automated application-level checkpointing of MPI programs." In ACM Sigplan Notices, vol. 38, no. 10, pp. 84-94. ACM, 2003.

[106] J. Handy, The Cache Memory Book. New York: Academic, 1993, pp. 39-46.

[107] Schulz, Martin, Greg Bronevetsky, Rohit Fernandes, Daniel Marques, Keshav Pingali, and Paul Stodghill. "Implementation and evaluation of a scalable application-level checkpoint-recovery scheme for MPI programs." In Proceedings of the 2004 ACM/IEEE conference on Supercomputing, p. 38. IEEE Computer Society, 2004.

[108] Borup, Craig A., and Joseph P. Miller. "Circuit for enabling a cache using a flush input to circumvent a late noncachable address input." U.S. Patent 5,097,532, issued March 17, 1992.

[109] Splash, http://kbarr.net/splash2.

[110] Diodato, Philip W. "Embedded DRAM: more than just a memory." IEEE Communications Magazine 38, no. 7 (2000): 118-126.

[111] Allwood, Dan A., Gang Xiong, C. C. Faulkner, D. Atkinson, D. Petit, and R. P. Cowburn. "Magnetic domain-wall logic." Science 309, no. 5741 (2005): 1688-1692.

[112] Hrkac, G., J. Dean, and D. A. Allwood. "Nanowire spintronics for storage class memories and logic." Philosophical Transactions of the Royal Society A: Mathematical, Physical and Engineering Sciences 369, no. 1948 (2011): 3214-3228.

[113] A. J. Annunziata, M.C. Gaidis, L. Thomas, C. W. Chien, C-C Hung, P. Chevalier, E.J. O'Sullivan, J.P Hummel, E.A. Joseph, Y. Zhu, T. Topuria, E. Delenia, P.M. Rice, S.S.P. Parkin, W.J. Gallagher. "Racetrack memory cell array with integrated magnetic tunnel junction readout." Electron Devices Meeting (IEDM), 2011 IEEE International, pp. 24-3. IEEE, 2011.

[114] L. Thomas, S.-H. Yang, K.-S. Ryu, B. Hughes, C. Rettner, D.-S. Wang, C.-H. Tsai, K.-H. Shen, and S.S.P. Parkin. "Racetrack Memory: A high-performance, low-cost, non-volatile memory based on magnetic domain walls." In Electron Devices Meeting (IEDM), 2011 IEEE International, pp. 24-2. IEEE, 2011.

[115] L. Thomas, M. Hayashi, X. Jiang, R. Moriya, C. Rettner, and S.S.P. Parkin,"Oscillatory dependence of current-driven magnetic domain wall motion on current pulse length", Nature. 443, pp. 197-200, 2006.

[116] Annunziata, A. J., M. C. Gaidis, L. Thomas, C. W. Chien, C. C. Hung, P. Chevalier, E. J. O'Sullivan, J.P. Hummel, E.A. Joseph, Y. Zhu, T. Topuria, E. Delenia, P.M. Rice, S.S.P Parkin, W.J. Gallagher, "Racetrack memory cell array with integrated magnetic tunnel junction readout." In Electron Devices Meeting (IEDM), 2011 IEEE International, pp. 24-3. IEEE, 2011.

[117] S. Ghosh, "Path to a TeraByte of on-chip memory for petabit per second bandwidth with< 5watts of power." In Proceedings of the 50th Annual Design Automation Conference, p. 145. ACM, 2013.

[118] Annunziata, A. J., M. C. Gaidis, L. Thomas, C. W. Chien, C. C. Hung, P. Chevalier, E. J. O'Sullivan et al. "Racetrack memory cell array with integrated magnetic tunnel junction

readout." In Electron Devices Meeting (IEDM), 2011 IEEE International, pp. 24-3. IEEE, 2011.

[119] Parkin, Stuart SP, Masamitsu Hayashi, and Luc Thomas. "Magnetic domain-wall racetrack memory." Science 320, no. 5873 (2008): 190-194.

[120] Kryder, Mark H., and Chang Soo Kim. "After hard drives—What comes next?." Magnetics, IEEE Transactions on 45, no. 10 (2009): 3406-3413.

[121] Venkatesan, Rangharajan, Vivek Kozhikkottu, Charles Augustine, Arijit Raychowdhury, Kaushik Roy, and Anand Raghunathan. "TapeCache: a high density, energy efficient cache based on domain wall memory." In Proceedings of the 2012 ACM/IEEE international symposium on Low power electronics and design, pp. 185-190. ACM, 2012.

[122] Venkatesan, Rangharajan, Mrigank Sharad, Kaushik Roy, and Anand Raghunathan. "DWM-TAPESTRI-an energy efficient all-spin cache using domain wall shift based writes." In Proceedings of the Conference on Design, Automation and Test in Europe, pp. 1825-1830. EDA Consortium, 2013.

[123] S. Ghosh, "Design methodologies for high density domain wall memory." NANOARCH, 2013.

[124] Anirudh Iyengar and Swaroop Ghosh, “Modeling and analysis of domain wall dynamics for robust and low-power embedded memory”, IEEE Design Automation Conference (DAC), 2014.

[125] Sun, Zhenyu, Wenqing Wu, and Hai Li. "Cross-layer racetrack memory design for ultra high density and low power consumption." In Design Automation Conference (DAC), 2013 50th ACM/EDAC/IEEE, pp. 1-6. IEEE, 2013.

[126] Venkatesan, Rangharajan, Vivek Kozhikkottu, Charles Augustine, Arijit Raychowdhury, Kaushik Roy, and Anand Raghunathan. "TapeCache: a high density, energy efficient cache

based on domain wall memory." In Proceedings of the 2012 ACM/IEEE international symposium on Low power electronics and design, pp. 185-190. ACM, 2012.

[127] Venkatesan, Rangharajan, Mrigank Sharad, Kaushik Roy, and Anand Raghunathan. "DWM-TAPESTRI-an energy efficient all-spin cache using domain wall shift based writes." In Proceedings of the Conference on Design, Automation and Test in Europe, pp. 1825-1830. EDA Consortium, 2013.

[128] Roohi, Arman, Ramtin Zand, and Ronald F. DeMara. "A tunable majority gate-based full adder using current-induced domain wall nanomagnets." IEEE Transactions on Magnetics 52, no. 8 (2016): 1-7.

[129] Chen, Xianzhang, Edwin H-M. Sha, Qingfeng Zhuge, Penglin Dai, and Weiwen Jiang. "Optimizing data placement for reducing shift operations on domain wall memories." In Design Automation Conference (DAC), 2015 52nd ACM/EDAC/IEEE, pp. 1-6. IEEE, 2015.

[130] Zhang, Xianwei, Lei Zhao, Youtao Zhang, and Jun Yang. "Exploit common source-line to construct energy efficient domain wall memory based caches." In Computer Design (ICCD), 2015 33rd IEEE International Conference on, pp. 157-163. IEEE, 2015.

[131] www.chipworks.com, for information regarding the 22nm SoC.

[132] NVSim, http://www.nvsim.org.

[133] Zhou, Jiantao, et al. "Crossbar RRAM arrays: Selector device requirements during read operation." IEEE Transactions on Electron Devices 61.5 (2014): 1369-1376.

[134] Huang, Jiun-Jia, et al. "One selector-one resistor (1S1R) crossbar array for high-density flexible memory applications." Electron Devices Meeting (IEDM), 2011 IEEE International. IEEE, 2011.

[135] Deng, Yexin, et al. "RRAM crossbar array with cell selection device: A device and circuit interaction study." IEEE Transactions on Electron Devices 60.2 (2013): 719-726.

[136] Zha, Yue, and Jing Li. "Reconfigurable in-memory computing with resistive memory crossbar." Proceedings of the 35th International Conference on Computer-Aided Design. ACM, 2016.

[137] Talati, Nishil, et al. "Logic design within memristive memories using memristor-aided loGIC (MAGIC)." IEEE Transactions on Nanotechnology 15.4 (2016): 635-650.

[138] Jiang, Z., Wong, H. P. (2014). Stanford University Resistive-Switching Random Access Memory (RRAM) Verilog-A Model. nanoHUB. doi:10.4231/D37H1DN48

[139] Govoreanu, Bogdan, et al. "High-performance metal-insulator-metal tunnel diode selectors." IEEE Electron Device Letters 35.1 (2014): 63-65.

[140] Srinivasan, V. S. S., et al. "Punchthrough-diode-based bipolar RRAM selector by Si epitaxy." IEEE Electron Device Letters 33.10 (2012): 1396-1398.

[141] Predictive technology model, ASU, http://www.asu.edu/~ptm.

[142] Yang, Saeyang. Logic synthesis and optimization benchmarks user guide: version 3.0. Microelectronics Center of North Carolina (MCNC), 1991.

[143] "As Nodes Advance, So Must Power Analysis [Online]." Available: http://semiengineering.com/as-nodes-advance-so-must-power-analysis/, [accessed September 2018].

[144] https://nanohub.org/courses/ss2014/01a/outline/unit8anandraghunathanmemorysystems/l82cachebasics#

Vita

Seyedhamidreza Motaman

Seyedhamidreza Motaman received his Bachelor's degree in Electrical Engineering in 2011 from K. N. Toosi University of Technology, Tehran, Iran, and his Master's degree in Electrical Engineering in 2013 from Amir Kabir University of technology, Tehran, Iran. He is currently pursuing his Ph.D. degree in Computer Science and Engineering department of the Pennsylvania State University after transferring from USF in 2016.

His primary research interests include low-power, robust and secure circuit and microarchitecture design of emerging non-volatile memories. During his doctoral studies, he also investigated topics such as data security and privacy of spintronic memories and computing in memory using emerging non-volatile memory technologies.

His research work has culminated in several peer-reviewed journal and conference publications as well as best poster awards. Additionally, he holds one patents for his work on Robust Slope Detection Technique for STTRAM and MRAM Sensing. He has served as a technical reviewer for journals and conferences including IEEE TCAS-I, IEEE TNANO, Journal of Low Power Electronics, and Integration, the VLSI Journal.